Achieving OER Selectivity in the Electrolysis of Seawater through Shielded Carbon- Supported Iridium Nanoclusters

Catherine Harvey

INSTITUT POLYTECHNIQUE DE PARIS

NNT : 2024IPPAX030

Thèse de doctorat

Achieving OER Selectivity in the Electrolysis of Seawater through Shielded Carbon-Supported Iridium Nanoclusters

Thèse de doctorat de l'Institut Polytechnique de Paris
préparée à l'École Polytechnique

n°626 : École Doctorale de l'Institut Polytechnique de Paris (ED IP Paris)
Spécialité de doctorat : Chimie

Thèse présentée et soutenue à Palaiseau, 24 juin, 2024, par

Catherine Harvey

Composition du Jury :

Mme. Anne Bleuzen Professeure, Université Paris-Saclay	Présidente
Mme. Elena Savinova Professeure, Université de Strasbourg	Rapportrice
M. Bruno Fabre, Directeur de Recherche, Université de Rennes	Rapporteur
M. Loïc Assaud Enseignant-Chercheur, Université Paris-Saclay	Examinateur
M. Cédric Tard Directeur de Recherche, École Polytechnique	Directeur de thèse
M. Thierry Gacoin Directeur de Recherche, École Polytechnique	Co-Directeur de thèse
M. Simon Delacroix Professeur Assistant, École Polytechnique	Co-Directeur de thèse

INSTITUT POLYTECHNIQUE DE PARIS

Institut Polytechnique de Paris
91120 Palaiseau, France

Remerciements

Cherished with the sacredness of a precious pearl are the family, advisors, jury members, professors, colleagues, and roommates who endowed their love, guidance, teaching, support, encouragement, and presence. It is only with these pillars that the enduring effort to complete a dissertation can be surmounted. The forging of these crucial pillars was complemented, reinforced, and elaborated by the very sincere consideration and kind concern that was bestowed each rising day with a thoughtfulness that I only hope could be conveyed in the redaction of this dissertation. It was the dear await of our encounters that I yearned for and blessed my day with the enthusiasm to complete the studies and contrive the redaction of this thesis.

I hope the very benevolent act of the jury members to review the dissertation and preside over the defense can be met with an effort and passion that seeps through the following redaction with an eagerness that entices your passions and interests. It is with my most thoughtful consideration that I thank Professor Anne Bleuzen, Professor Elena Savinova, Director Bruno Fabre, and Professor Loïc Assaud for their very sincere kindness to review the account that follows. Yearning to improve the quality of the dissertation with your expertise, it is my wish that your insights may be adequately denotated in the final composition that this dissertation may become.

The support of my family was sincerely felt even an ocean away from home. The nurturing concern of my mother, Debby, my father, Mac, my sister Jill, my sister Claire and her husband Joseph, and our newest addition James, was touched through their loving wishes over the holidays, their frequent phone calls, and their momentous visits across a continent. Growing experience with living in this unforgiving world has made me eternally grateful for the very thoughtful devotion with which my parents bestowed upon my sisters and I throughout our childhood and as we've matured a loving, moral, and secure home, I'm sincerely beholden. I only hope that I can embody and personify a character that can adequately represent the upbringing that they so sincerely instilled in me.

The caring guidance of my advisors, Professor Cédric Tard, Professor Thierry Gacoin, and Dr. Simon Delacroix here at Ecole Polytechnique and the members of the Comité de suivi de thèse, Professor Marion Giraud and Professor Subhash Risbud encouraged my inspiration to aspire to new spheres of erudition. They instilled a sense of confidence to create, to coalescence a new color scheme, while synchronously painting a horizon to which would incarnate a glimmer of perseverance to achieve distinction within our sincere efforts. Being graced each day with Cédric's cheerful persona only reminded me of his very kindhearted and benevolent thought to take me in as we embarked in the very enduring effort to grasp the complexity of his chosen disciple with an inviting eagerness and very kind patience. The incredible insights given by Thierry during our meetings very sincerely complement his innate thoughtfulness and charisma with a balance attainable only by a person such as himself who is able to thrive in the crucial role that he plays, please accept my most respectful sentiments. I only hope that the very gracious attentiveness with which Simon gave towards the efforts of this work can be gleamed in the following pages, his dependable support and prudent guidance was so sincerely cherished. Professor Giraud very considerately supported the progress of this dissertation with an altruism

that I envy, it was with her very devoted effort that we together prepared for the XPS analysis. I hope to one day be able to learn even a morsel of her wisdom, ingenuity, and gracefulness, and endeavor to implement these qualities into the redaction of this thesis. Captivated by the incredible efficiency, devotion, and concern with which they give their work, I'm honored to have been blessed by their teachings, and strive to emulate their efforts and enrich my knowledge to one day make it within a role that they've so dearly earned.

The onset of this enduring quest to complete a dissertation began with very humble beginnings at Rensselaer Polytechnic Institute and the University of California, Davis. I very sincerely strive to emulate the devoted philosophies towards the passionate pursuits that were so considerately exemplified to me. For most of my young life, the turning of the leaves during the autumn season was witnessed from the viewpoint of the playing field. The challenges and hardships of the soccer season required an endurance, a manifestation of the effort that was made during the rest of the year to prepare for the season ahead. I first witnessed this necessary commitment in my coach, Cord Farmer. Cord instilled a sense of pride in my teammates and I; he inspired us to be better players through diligence, commitment, and perseverance. After those early morning soccer trainings devoted to developing these skills, I would run to the laboratory and see those traits perfected in my research advisor, Professor Robert Linhardt. His incredible effort and commitment enabled us to work autonomously, pursuing our ideas and creative thoughts; his very considerate guidance encouraged our independence and responsibility.

It is with a sincereness I only hope can commemorate the pure delight I felt within our encounters that I thank Professor Anita Oberholster and Professor David Block. It was with Professor Sebastian Wachsmann-Hogiu that I was first able to recognize my interest in scientific reduction, the compassion and concern that he showed for his students gave us the confidence and morale needed to create a distinction within the intricacy of his profession. Leading with a very gentle hand that very much encouraged us to pursue our passions and interests, I most graciously hope that Professor Subhash Risbud will accept my very sincere appreciation and admiration for his attentive guidance and very kind concern. Professor Yayoi Takamura and her very thoughtful advisement throughout my tenure in the program at UC Davis accompanied and encouraged me to excel through very new and challenging concepts. I often reflect with nostalgia about the Fulbright Year and am so honored to have had the opportunity to meet the Fulbright Commission, their critical support created a very dear experience within the benevolent laboratory of Professor María Vallet-Regí. The insightful thoughts for the fellowship writing by Professor Isabel Izquierdo Barba and Professor Antonio Jesus Salinas Sanchez, and the gracious teachings of Professor Blanca González Ortiz have taught me so much and are qualities that are very often reflected upon during my conduct throughout the working day. Welcoming me into his laboratory devoted to research in cancer therapeutics, Professor Kit Lam with the help of Dr. Lucas Solano led us with a profound knowledge and conceptual erudition of the malady fortified with a very sincere work ethic and commitment that provided us graduate and postdoctoral scholars with the guidance, literacy, and means to informatively pursue our creative conceptions towards effective solutions that could relieve our communities of this onerous disease.

It is indeed the welcoming morning greetings at the laboratory each day amongst a group of very kindhearted individuals that instilled my sense of happiness and an eagerness to accomplish the daunting tasks to come. The sincerity with which the professors, postdoctoral scholars, and my fellow doctoral students in the Laboratoire de Chimie Moléculaire concern ourselves for each another creates a touching ambience that evokes our sense of compassion and fortifies our spirits. Complemented with the lead of Cédric's very kind and attentive direction, this compassion vitalizes the earnest efforts and intent with which the group complete their daily objectives, instilling a passionate morale amongst the members that enliven each day. I will forever cherish the morning salutations in the office with Edith, Sylvaine, and Marie. They couldn't have created a more conducive environment for writing a thesis. Being also blessed with the support of the Chemistry Group within the Laboratoire de Physique de la Matière Condensée, I hope I can show my most sincere gratitude to Rabei for his commendable devotion towards helping us with our efforts to complete the necessities of our projects. Dr. Jongwook Kim was so kind in his gracious efforts to organize the monthly meetings. Having the chance to work with Dr. Sandrine Tusseau-Nenez and learn from her very profonde comprehension of X-Ray Diffraction was an honor. The very earnest efforts of Dr. Clement Marchat to image the inks and nanosheets were met with a pleasure to work with such a thoughtful person. It was lovely to be alongside Lilian and Jisoo and console each other with the troubles of our research efforts.

I was struck by the charisma and altruism of Dr. Nicolas Casaretto and most sincerely enjoyed the moments with Dr. Grégory Danoun at the gatherings. I thank Dr. Sophie Bourcier, Mr. Gilles Alla, Ms. Elodie Dubois, Mr. Christophe Genty, and Dr. Véronique Girard, she was so considerate to take care of the momentous tasks ensuring our research progress could be made. Professor Audrey Auffrant is an incredibly adept chemist; it was quite a thrilling experience to learn from her during the complementary teaching activity. I hope that Dr. Duncan Carmichael, Dr. Corinne Gosmini, Dr. Covadonga Lucas Torres, Professor Gregory Nocton, Dr. Thomas Simler, Professor Gilles Ohanessian, Professor David Touboul and Mr. Karim Hammad will accept my most sincerest respects for their very considerate and thoughtful presence.

I was greeted and initially guided through the experiments in this laboratory with Dr. Silvia Duran, her advice has been so crucial to the experiments that were conducted. I thank Pauline and Nolwenn for the wonderful conversations at lunch and the kindness of Thibault to welcome us into his home. It's been a lovely experience to work with Marie-Sophie, Syed, and Linghui in the laboratory and Anna was an incredibly helpful and kind intern, I wish her and her family my most sincerest respects. I learned so much from María in planning the Hydrogen Winter School, and Sebastian was so fun to work with. The warm greetings and supportive charismas of Ingrid, Laureen, Lucie, Adrien, Linda, Angus, Claire, Doug, and Linda in the halls and at the lunches were fervently cherished each day.

I came home each evening to Joël, his support and companionship throughout these years gave this effort and life a meaning that was so sincerely valued and endeared. I hope the owners of the home, Ms. Hélène Fourreau and Mr. Antoine Goupilleau will accept my most thoughtful consideration and sincerest respects for their kindness to create such a lovely home for us. They also welcomed the wonderful

Luka, Anatole, Wallerand, Marie, and Emma into our humble abode, who were such pleasurable companions to share with and learn from.

I most humbly thank the Doctoral School for enabling me with the means of working with and learning from these gifted individuals. Accepting me into this renown institution is such an honor that I strived each arising day to fulfill their intentions. I hope that this redaction may adequately exemplify the distinction that the members of this institution have strived so dearly to conceive.

Reflecting on these memorable moments with such honorable characters is quite complicated without evoking a tear, may the spread of these teardrops not wipe the words from this page and the resilience of our cherished memories endure. I hope that you may discover the gift of happiness. I wish everybody in both my worst and at my very best, my most thoughtful care and concern,

With my most sincerest regards,

Cate

Table of Contents

Abbreviation	Meaning	Section
1D	One Dimensional	I.1.2.1
2D	Two Dimensional	I.1.2.1
3D	Three Dimensional	I.3.2.2
AEM	Adsorbate Evolution Mechanism	I.1.2
AEMWE	Anion Exchange Membrane Water Electrolyser	I.1.2
ATR-IR	Attenuated Total Reflection Infrared Spectroscopy	I.4.2.3
AWE	Alkaline Water Electrolyser	I.2.2.2
c-SACs	Correlated Single Atom Catalysts	I.4.2.3
CER	Chlorine Evolution Reaction	I.1.1
CHE	Computational Hydrogen Electrode	I.3.2.1.2
CIF	Crystallographic Information File	III.3.1
COF	Covalent Organic Framework	IV.2.2.1
CTAB	Cetyl-trimethylammonium Bromide	II.2.1.1
CUS	Coordinately Unsaturated Site	I.3.2.1.2
DC	Direct Current	I.2.2.2
DFT	Density Functional Theory	I.3.2.1
DSA	Dimensionally Stable Anodes	I.3.2.3
EDS	Energy Dispersive X-Ray Spectroscopy	II.2.1.1
FFT	Fast Fourier Transform	II.2.1.1
FO	Forward Osmosis	I.4.6
FTIR	Fourier Transform Infrared Spectroscopy	II.2.1.2
FTO	Florine Doped Tin Oxide	I.4.5
HAADF-HRSTEM	High-Angle Annular Dark Field Scanning High Resolution Transmission Electron Microscopy	I.4.2.3
HER	Hydrogen Evolution Reaction	I.1.4
HR	High Resolution	II.2.1.1
IM	Imidazolate	III.2.1
ISO	International Organization for Standardization	I.1.3
KOH	Potassium Hydroxide	I.1.2
LDH	Double Layered Hydroxide	I.1.2
LOM	Lattice Oxygen Oxidation Mechanism	I.3.2
LSV	Linear Sweep Voltammetry	II.2.4.1
LUMO	Lowest Unoccupied Molecular Orbital	III.2.3
MOFs	Metal Organic Frameworks	II.1.4
NF	Nanofiltration	II.1.4
NM	Nafion Membrane	IV.2.1
NS	Nafion Solution	IV.2.1
NZES	Net Zero Emissions Scenario	I.1.1
OER	Oxygen Evolution Reaction	I.1.2
OLEMS	Online Electrochemical Mass Spectrometry	I.3.2.1.3
PCET	Proton Concerted Electron Transfer	I.3.2.1.2
PEMWE	Proton Exchange Membrane Water Electrolyser	I.1.2
PGM	Platinum Group Metals	I.1.2
pH	-log10[H+]	I.1.2.1

RHE	Reversible Hydrogen Electrode	I.1.2
RPM	Rotations per Minute	II.2.4.1
RRDE	Rotating Ring Disk Electrode	III.3.4.1
SACs	Single Atom Catalysts	I.4.2.3
SAM	Single Atom Moieties	I.4.2.3
SDS	Sodium Dodecyl Sulfate	III.2.2
SEM	Scanning Electron Microscopy	I.1.2.1
TEM	Transmission Electron Microscopy	II.2.1.1
TEOS	Tetraethyl Orthosilicate	II.2.1.1
TFCPA	Thin Film Composite Polyamide Membrane	II.1.4
TGA	Thermogravimetric Analysis	II.2.3.1
TOF	Turnover Frequency	I.4.2.3
TON	Turnover Number	I.1.2.1
UV	Ultraviolet	II.1.5
VC	Vulcan Carbon	II.2.1.1
XAFS	X-Ray Adsorption Fine Structure	I.4.2.3
XPS	X-Ray Photoelectron Spectroscopy	I.3.2.1
XRD	X-Ray Diffraction	II.2.1.1
ZIF-8	Zeolitic Imidazolate Framework	III.2.1

€	Euro
A	Ampere
Å	Angstroms
C	Celsius
eV	Electronvolt
g	Grams
h	Hours
kWh	kilowatt-hours
l	Liter
m	Meter
M	Molarity
min	Minute
Mol	Moles
S	Siemens
sec	Second
V	Volts
W	Watt
w/w	weight by weight
wt.%	weight percent

Roman Symbol	Denotation
a_{H_2O}	Activity of Water
A	Area of the Electrode
C	Concentration
C_d	Double Layer Capacitance
D	Diffusion Coefficient
d	Adsorbate Distance Above the Solid Surface
	Distance between the Electrodes
d_{um}	Molecular Sieve Material Pore Aperture
d_m	Window Dimension of Molecular Sieve Material
e_0	Elementary Charge
E	Electrode Potential
E°	Standard Electrode Potential
$\mathcal{E}$	Faradaic Selectivity
F	Constant of Faraday
$\mathcal{F}$	Flux
$\Delta G^\ddagger$	Free Energy of Activation
h	Plank constant
I	Current
J	Current Density
	Joules
K	Partition Coefficient
	Electrolyte Permeability
K_s	Specific Conductance
$\mathcal{K}$	Force Constant
k	rate constant
k_H	Henry's Law constant
k_b	Boltzmann Constant
m	Stoichiometry
m	Number of Jumps within the Membrane
m_{SiO_2}	Calculated Mass of Silica
$m_{c\bullet m}$	Precursor Material Mass
N	Collection Efficiency
n	Quantity of Electrons
p	Pressure
p_w	Vapor Pressure
Δp	Partial Pressure Difference between the Cathode and Anode
$p_{H_2}^c$	Hydrogen Partial Pressure at the Cathodic Outlet
$p_{O_2}^A$	Oxygen Partial Pressure at the Anodic Outlet
R	Standard Gas Constant
	Nanoparticle Radius
R_t	Total DC solution resistance between Cathode and Anode
r	Spacial Coordinate
	Radius

S_{H_2}	Hydrogen Solubility
S_{O_2}	Oxygen Solubility
S^*	Absolute Surface Area of the Precursor Material
ΔS	Change in Entropy
s	Number of Jumps to (+) and from (-) the Bulk solution
T	Temperature
t	Time
t_{ZIF-8}	Thickness of Nanosheet Overlayer
$U^{\circ}_{rev,T}$	Standard Reversible Voltage of a Water Electrolytic Cell
U_{cell}	Applied Voltage
$V^{\circ}_{w(l)}$	Standard Volume of Liquid Water
V_0	Limiting Velocity
w	Work
x	Nuclear Coordinate
z	Charge
ΔZPE	Zero-Point Energy

Greek Symbols

Greek Symbol	Denotation
δ	Thickness of Film
	Thickness of Permselective Membrane
$\Delta\varepsilon$	Chemisorption Energy
$\Delta\varepsilon_{pot}$	Potential Energy of the Adsorbate-Catalyst System
ϵ_s	Dielectric constant of the solvent
ϵ_0	Permittivity of free space
η	Overpotential
$\tilde{\eta}_C$	Current Efficiency
$\tilde{\eta}_U$	Voltage Efficiency
κ	Transmission Coefficient
ν	Viscosity
ϕ	Potential
	Film thickness
ρ	Density
υ	Scan rate
ξ	Diffusion Layer Thickness

Résumé

Obtenir une sélectivité optimale à l'anode pour la production d'oxygène lors de l'électrolyse de l'eau de mer est un défi crucial afin de permettre la production d'hydrogène décarboné. Cela nécessite le développement de matériaux permsélectifs qui dépassent les limites de perméabilité et de sélectivité des membranes de dessalement classiques. En utilisant une membrane de tamisage moléculaire rigide, on obtient une meilleure capacité de sélection des molécules en comparaison avec les membranes de dessalement en polymère, qui se basent principalement sur un processus de séparation dépendant de l'énergie, dû au mouvement des chaînes polymériques constitutives. Au cours de cette thèse, une encapsulation de nanoparticules d'iridium greffées sur du carbone dans une matrice de silice a été réalisée afin de bloquer le transport des ions chlorure hydratés. L'analyse thermogravimétrique et la microscopie électronique à transmission ont confirmé un recouvrement complet du matériau électrocatalytique après cinq heures de réaction, avec une épaisseur moyenne de 34 nm. La caractérisation structurale par diffraction des rayons X a montré la présence de pores autour des agrégats de silice amorphe d'une taille d'environ 9 nm, bien supérieur au diamètre de l'ion chlorure hydraté. L'incorporation ultérieure de l'électrocatalyseur encapsulé dans une encre de carbone et de Nafion, puis déposée sur une électrode de carbone vitreux et analysée par voltammétrie à balayage linéaire, a révélé que le transport des électrons des nanoparticules électrocatalytiques encapsulées vers l'électrode de travail était une étape limitante dans ces processus. Il est aussi apparu que la diffusion directe de des ions chlorures vers l'électrode en vue d'une oxydation ultérieure était également apparente. Une autre approche exploitant la synthèse de nanofeuilles de MOF de type ZIF-8 avec un diamètre de pore contrôlé, rigidifié par leur croissance dans la phase monoclinique, a été étudié. L'hypothèse envisagée souhaitait conférer une perméabilité sélective à l'eau par exclusion de taille afin de bloquer le transport des ions chlorures hydratés dans le film électrocatalytique, tout en améliorant la conductivité du matériau grâce aux propriétés conductrices des MOF. L'architecture des nanofeuilles a été conçue pour optimiser leur disposition afin de bloquer sélectivement les multiples voies de transport à travers le film électrocatalytique. La reproductibilité des analyses a été au cœur des expériences menées en utilisant une électrode de travail de type RRDE (rotating ring-disk electrode), et a permis la détection sélective de la production de dichlore non souhaitée tout en facilitant l'approche intégrée avec un rapport Zn/Ir de 160/1 dans le film électrocatalytique. Nous avons pu démontrer une efficacité réduite de ~65% dans la réaction de production de dichlore à des concentrations de 10 à 150 mM en ions chlorures en présence de perchlorate comme électrolyte support. La surtension requise pour arriver à une densité de courante de 3 mA/cm^2 sur le disque de l'électrode a été observée comme augmentant légèrement également. L'évaluation du degré de contrôle cinétique et de contrôle diffusionnel auquel les courants OER et CER comprenant l'évaluation de la sélectivité CER peuvent être soumis est proposée pour vérifier ce contrôle diffusionnel qui pouvait être transmis par les nanofeuilles sur le courant CER. Ensuite, les perspectives sont discutées en élucidant les modes de transport des ions chlorures qui pouvaient être susceptible d'être empêchés par la

présence des nanofeuilles dans le film électrocatalytique. Une étude des paramètres diffusionnels pourrait de plus permettre d'estimer l'efficacité des nanofeuilles en la présence des autres éléments qui sont en abondance dans l'eau de mer. La question de la stabilité des nanofeuilles de MOF dans le film a également été adressée afin de créer un matériau électrocatalytique favorisant la production sélective d'oxygène en présence d'ions chlorures en milieu acide. Ces propositions renforcent l'intérêt de l'utilisation de l'eau de mer comme électrolyte pour l'électrolyse de l'eau dans le contexte de l'utilisation de l'hydrogène comme solution durable pour répondre aux besoins critiques de nos sociétés.

Chapter 1

Unraveling the Competition between the Oxygen and Chlorine Evolution Reactions in Seawater Electrolysis: Enhancing Selectivity for Green Hydrogen Production.

"Une chose domine chez moi, l’entraînement et l’ardeur la plus grande vers l’abstraction.”

-Gustave Moreau

I.1 Introduction

I.1.1 The Social-Technological Crisis

Energy consumption is expected to reach 100,000 terawatt-hours (TWh) in the Net-Zero Emissions Scenario (NZES), outlined at the 2015 Paris agreement to minimize global temperature increases to 1.5 °C by the year 2050[1,2]. This NZES expects water electrolysis to adsorb about 15,000 TWh to produce the required 520 mega tons of hydrogen to sustainably power our world[1,2]. Indeed, the generation of a hydrogen energy vector that is derived from renewable energy sources ("green hydrogen") would fulfill the world's energy shortage while also evading these climatically harmful carbon emissions that warm the planet.[3,4] Water electrolysis was initially discovered by two Dutchmen, Adriann Paets van Troostwijk (1752-1837) and Johan Rudolph Deiman (1743-1808), who connected two gold wires to an electrostatic generator that were each placed at either end of a glass tube filled with water[5]. The electric discharges of the generator produced evolved gases on both wires. Those evolved gases were interpreted to be oxygen at the anode and hydrogen at the cathode, shown in the reactions below under acidic conditions.

$$2H_2O \rightarrow 4H^+ + O_2 + 4e^- \ (OER, anode) \tag{1a}$$

$$2H^+ + 2e^- \rightarrow H_2 \ (HER, cathode) \tag{1b}$$

Considering that the production of one ton of hydrogen requires about 10 m^3 of water, there will become an exigency to source and also transport upwards of 5,2 km^3 of water[6]. With total global renewable freshwater resources estimated at 49,809 x 10^9 m^3 in 2020, exclusive withdrawals would dry up our critical freshwater resources within 100 years[7]. Moreover, utilizing freshwater to power electrolysis would heighten the emerging social-technological crisis inherent in the water-energy nexus[8]. More than two billion people live in countries experiencing water stress and an estimated 1.6 billion people live in regions with water availability though without the infrastructure to access it[9]. Alleviating that social-technological crisis and propelling the sustainability of our society requires unlocking the other 96.5% of the 1.69 x 10^9 km^3 of seawater water on earth portrayed in *Figure 1a*.

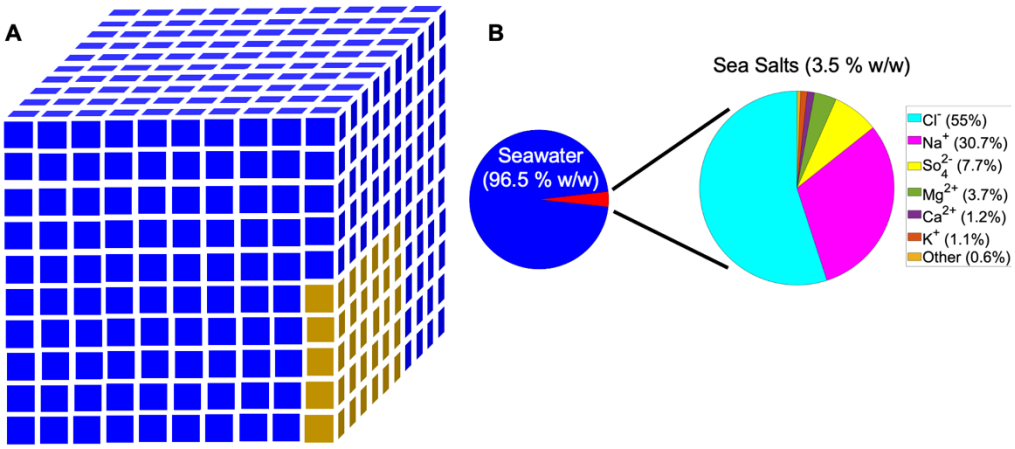

Figure 1: (A) Graphical representation of the volumetric percentages of ice and seawater (97% v/v) on the Earth represented by blue squares and freshwater (3% v/v) represented by gold squares, adapted from Urban[8]. (B) Diagram of the major chemical constituents of seawater, sea salt percentages were adapted from the seawater reference composition defined by Millero et. al. and represent the mass fractions of the solute with respect to the total mass of solutes at pH 8[10].

However, there is plethora of chemical constituents in seawater including sea salts, small organic molecules, living organisms, and polymers(*Figure 1b*) which create complications during the electrolysis[10,11]. Especially, one of the major challenges during the seawater electrolysis is the presence of chlorine anions which induces a competition between oxygen and chlorine production (CER).

I.1.2 State-of-the-Art Water Electrolyser Technologies

Undergoing the preferential oxygen evolution reaction (OER) at the anode and the hydrogen evolution reaction (HER) at the cathode leads to local acidification at the anode as water or hydroxide ions are consumed under acidic or neutral/basic conditions and protons or water are produced (*Reaction 2a* and *Reaction 2b*), and a local basification at the cathode as protons or water molecules are consumed under acidic or neutral/basic conditions and water or hydroxide ions are produced (*Reaction 3a* and *Reaction 3b*).

$$2H_2O \rightarrow 4H^+ + O_2 + 4e^- \quad (Anode\ in\ acid) \qquad (2a)$$

$$4OH^- \rightarrow 2H_2O + O_2 + 4e^- \quad (Anode\ at\ neutral\ or\ alkaline) \qquad (2b)$$

$$H^+ + 2e^- \rightarrow H_2 \quad (Cathode\ in\ acid) \qquad (3a)$$

$$2H_2O + 2e^- \rightarrow H_2 + 2OH^- \quad (Cathode\ at\ neutral\ or\ alkaline) \qquad (3b)$$

The pH dependence of the OER enables the reaction at the anode to evolve at voltages below its characteristic reversible potential of 1.23 V – 0.059·pH vs. RHE in alkaline solutions in accordance with the Nernst relation. Alkaline water electrolysis (AWE) utilizes a cell with two compartments continuously fed with a highly

concentrated, corrosive alkaline supporting electrolyte (often 20-30 wt % (ca. 7M) KOH solution), though this design is subject to leakages and require periodic replenishment *(Figure 2a)*. The electrodes are separated by a porous diaphragm to prevent gas crossover, though this diaphragm has been shown to poorly operate, causing low Faradaic efficiencies, and limiting the maximum AWE current densities to about 0.2 - 0.4 A/cm^2 despite the use of the highly concentrated supporting electrolyte[12]. The device must also be operated at ambient pressures, making the produced hydrogen significantly wet and increasing the cost of drying and compression. Moreover, electrolysis of seawater under alkaline conditions can induce hydroxide precipitation and reduce the lifetime durability of the electrolyser and the active surface area of the electrocatalyst[13].

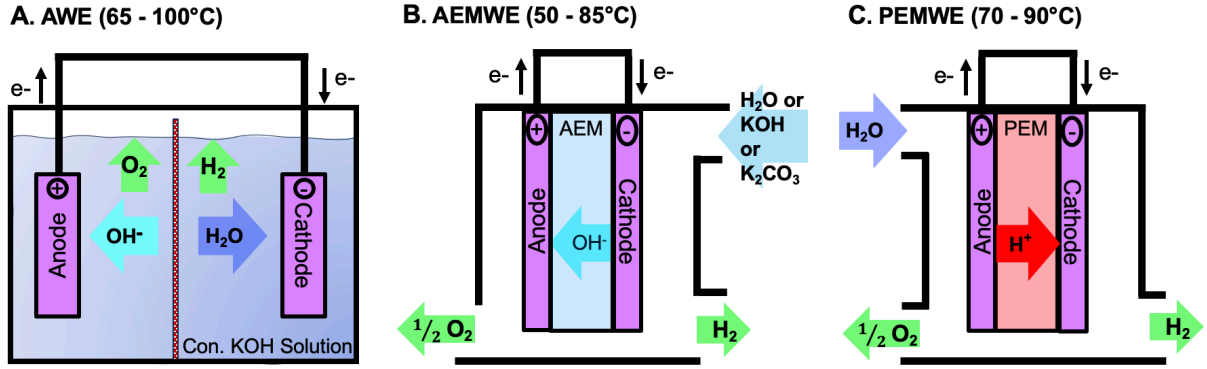

Figure 2: (A) An alkaline water electrolyser with a concentrated KOH liquid supporting electrolyte pumped on both sides of the cell with a porous diaphragm that impedes gas crossover while promoting the migration of the hydroxide ions generated at the cathode toward the anode. (B) An anion exchange membrane water electrolyser consisting of a solid cationic polymer promoting migration of hydroxide ions from the cathode to the anode where oxidation occurs; water with or without a dilute supporting electrolyte such as potassium hydroxide or potassium carbonate is shown being supplied to the cathode. (C) A proton exchange membrane water electrolyser with water being supplied to the anode; the evolution of oxygen promotes the generation of protons that then migrate through the solid poly-sulfonic membrane towards the cathode to evolve hydrogen. Reproduced from Li et. al.[14]

Anion exchange membrane water electrolysis (AEMWE) utilizes an anion exchange solid polymer electrolyte (< 50 μm in thickness). This membrane facilitates the transport of hydroxide ions from the cathode to the anode and separates the evolved gases while decreasing the ionic resistance. Thus AEMWE can operate at higher pressures with more efficient current densities *(Figure 2b)*. Indeed, Li et. al. reported current densities of 2.7 A/cm^2 using an ammonium-enriched anion exchange ionomer embedding both the cathode and the anode[15]. To improve the ionic conductivity, dilute solutions of KOH (< 1M) supporting electrolyte or potassium carbonate are often needed, though pure water is preferred to minimize chemical and device maintenance. Water is indeed a feasible electrolyte solution with an ionomer of sufficient cationic functionality and electrode binding ability[12,14]. Moreover, the non-

acidic environment enables the use of non-precious metals electrocatalysts such as first-row transition metal oxides, nitrides, and sulfides decreasing the capital expenditure, and increasing the scalability. Anion exchange membranes can also enable the design of asymmetric electrolysers with independent electrolyte feeds to promote the selectivity for the OER at the anode[16]. Dresp et. al developed an electrolyser where 0.5 M KOH anolyte circulate in the anode compartment which was separated from natural seawater catholyte by an AEM membrane. Only few millimole of chloride ion can cross over in the anolyte, unaffecting the NiFe-LDH electrocatalyst. In another study, a custom made biphenyl-based ionomer showed high anion exchange capacities contributing to low overpotential at high current densities[17].

The highest current densities are achieved with proton-exchange membrane water electrolysers (PEMWE). In PEMWE, a solid polymer electrolyte membrane between the anode and the cathode such as Nafion is used to facilitate migration of the protons generated at the anode towards the cathode where their reduction occurs *(Figure 2c)*. This solid polymer allows for high operating pressures. However, it is especially vulnerable to water impurities, which can become trapped and concentrated, reducing the proton conductivity. Moreover, the harshly acidic conditions require the use of platinum group metals (PGM) such as iridium or ruthenium at the anode to catalyze the OER, and platinum or palladium HER catalysts at the cathode. The local acidification of the anode caused by the OER at high current densities may moreover increase the degradation of the electrode materials. Thus, it is crucial to develop acidic resistant catalysts to avoid continuous buffer additions [18-21]. Unfortunately, the thermodynamic potential difference between the OER and the parasitic CER when electrolyzing seawater is the lowest under acidic conditions. To avoid the chlorine production, Rossi et. al. use an asymmetric design electrolyte feed in which a humidified gas stream is introduced at the anode, while the chloride ions in the seawater catholyte were prevented from crossover by the electrostatic repulsions presented from the anionic functionalities of the membrane[22]. The vapor anolyte further reduced the occurrence of sodium ion transport and decreased the observed overpotentials of the cell[22]. Kumari et. al. went one step further to introduce seawater humidified air at the anode and a nitrogen gas stream in the cathode compartment; the solar hydrogen conversion efficiency calculated before and after 50 h of continuous operation was found to increase from 6% to 6.3% compared to the decrease of 6.6% to 0.5% observed when liquid seawater electrolytes feeds were used[23].

I.1.2.1 Abating the Use of Precious Metals in PEMWE

Krishnan et. al. calculated an 82% price reduction in the PEMWE stack design through alternative materials utilization and lower loadings of PGM electrocatalysts. Unfortunately, the high overpotential for the OER, the low pH contributed by the ionic membrane, and the highly oxygenated environment at the anode necessitates an electrocatalyst with a durability currently only characteristically found in iridium[24]. Though with loadings of 2 mg/cm^2 required to achieve typical operating conditions of 2 A/cm^2 and 2 V, only a capacity of > 1 GW per year of PEMWE production technology can be achieved by tapping almost 10% of the annually mined production[24]. Though to meet the NZES for 2050, upwards of 3600 GW must be realized[24], thus ensuing an

iridium shortage[25]. On the other hand, costing a sixth to a fifteenth of the price of the extremely rare iridium metal with 0.001 ppm in the Earth's crust, both DFT studies and experimental measurements of its overpotential have rendered ruthenium as the precious metal with remarkable OER electrocatalytic activity under acidic conditions[26,27]. However, its preferential utilization must address its characteristically low stability.

Therefore, there exists a challenge to reduce the precious metal loadings without however sacrificing the performance and durability of the electrocatalyst. Alia et. al. indeed showed that reduced metal loadings can degrade the current density over the long term[28]. Thus coherent strategies to diminish the precious metal loading are exigent. Improving the catalytic interface by incorporating supportive substrates with improved electrical conductivity; optimizing the surface area of the catalyst structure and iridium packing density by implementing the design of 1D and 2D nanomaterials; utilizing reactive spray deposition technologies with a self-assembly mechanism proceeding through volatile solvent evaporation that creates a porous hierarchical structure with low Ir loadings[29] are some methodologies that have been explored and discussed in the literature. Techniques that improve catalyst recycling such as ultrasonication and alcoholic delamination have also been reported[30,31].

Development of non-PGM catalysts would evidently alleviate the cost burden of current PEM technology and the taxing utilization of precious natural resources. However, the lacking level of performance and durability of these alternatives when compared to Ir have continually rendered this feat elusive[24]. Towards assuaging this predicament, Wang et. al. identified 68 nonbinary acid-stable oxides as electrocatalysts at the anode for PEMWE from the data of the Material Project through computation of Pourbaix decomposition free energies. For example, Sb, Ti, Sn, Ge, Mo, and W-based oxides were indicated to have high corrosion resistance in strong acids[32]. Moreover, Li et. al. identified a stable potential window in which γ-MnO_2 showed no signs of deactivation after 8000 h of electrolysis at 10 mA/cm^2 and pH = 2[33]. Hernandez et. al. reported a nickel-manganese antimonate electrocatalyst that performed the OER in 1 M sulfuric acid, though required an overpotential of 735 mV operating at 10 mA/cm^2 for 168 h[34]. Thorarinsdottir et. al. elucidated the OER catalytic mechanism of bismuth oxide (BiO_x) films electrodeposited on fluorine-doped tin oxide-coated glass working electrodes and posited that two $Bi^{3+}O_x$ centers undergo two sequential two-electron oxidations to form the symmetric peroxo $Bi^{4+}O_xBi^{4+}O_x$ entity, which then disproportionates intermolecularly to form a mixed valence $Bi^{3+}O_xBi^{5+}O_x$ peroxo species[35]. Upon oxidation to form $Bi^{5+}O_xBi^{5+}O_x$, oxygen is subsequently released. No distinctive changes in film morphology were evident through SEM following chronopotentiometry testing; an OER current density of 1-5 mA/cm^2 was sustained at moderate overpotentials for 110 h at pH 1.82, acidified with sulfuric acid[35]. These results further demonstrated that the p-block metal oxides often used as the stabilizing embedding matrices may indeed play a catalytic role in acidic OER electrocatalysis. On the other hand, an overpotential of 189 mV at 1 mA/cm^2 was recorded for a metal molecular cluster anion, a barium salt of cobalt polyoxometalate blended with a commercial carbon paste support; this design showed a stable current density for one day that was 10 times higher than that of iridium oxide (IrO_2) blended with the carbon paste support, producing a TON of 47 compared to 0.1 for IrO_2 when

corrected for the metal content. This was the first instance in which a low-cost, earth abundant material reached comparable activities to the commercial IrO_2 standard[36].

I.1.3 Indirect Seawater Electrolysis Technologies

The complexity of seawater instigates the development of new strategies to electrolyze this abundant resource to produce hydrogen. Desalinization of seawater is currently used in electrolyser technologies and called indirect seawater electrolysis. Current desalination technologies include forward osmosis[37,38] and reverse osmosis (RO). RO occupied 66% of the global water desalination in 2016 and utilizes polyamide membranes capable of 99.7% salt rejection[39-42]. These relatively easy single reverse osmosis technologies can produce water with conductivities of 5-20 µS/cm. However, the European Union recommends low temperature water electrolysis to be conducted according to ISO 3696 Grade 2 water with a conductivity of < 1.0 µS/cm[43-46]. Thus, the infrastructure for additional purification is required. Reverse osmosis membranes could be placed in series, though each of these high pressure pumps require 2 to 4 kWh of energy to produce 1 m^3 of freshwater[47]. Purifying the needed 5.2 km^3 of water to meet the NZES could thus require 20.8 TWh of energy as highlighted in *Figure 3*. Thus it is of a fundamental importance to continue scientific advancement into the development of direct seawater electrolysis to spare energy.

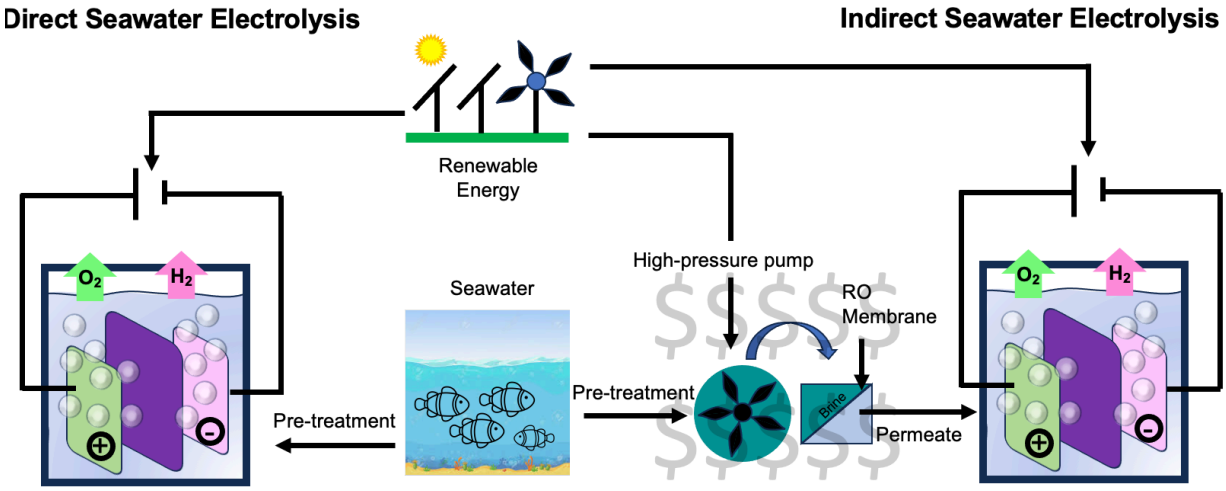

Figure 3: Schematic comparison of Direct and Indirect Seawater Electrolysis highlighting the additional energy costs required to power the high-pressure pump module. Figure adapted from Farràs et. al.[48]

I.2 Mitigating Seawater Electrolyser Performance

It is therefore crucial to be able to produce green hydrogen with direct electrolysis starting from seawater. However, the presence of salts induces drop in performances.

I.2.1 Parasite Reactions in Seawater Electrolysers

The electrolysis of non-purified seawater has been shown to degrade the electrolyser system performance. The carbonate and borate ions in seawater are present, though at concentrations too low to buffer a seawater electrolyte from these dramatic pH shifts that occur upon the preferential evolution of oxygen and hydrogen at the anode and the cathode. The local acidification that occurs at the anode enables seawater constituents such as the chlorine chemistry to promotes the corrosion and toxicity. The local basification that occurs at the cathode causes hydroxide precipitation and the blockage of the electrode surfaces and the membrane materials. This convoluted composition can thus affect the chemical and mechanical robustness of the electrolyzer, the electrochemically active dimensions of the electrode, and the specific operating conditions (voltage, current density, solution feed rate, response time to reach steady-state operation)[49].

Furthermore, the presence of additional chemical constituents into the electrolyte of the electrolyser can create competition among the substrate at the active site of the electrocatalyst[11,50]. In particular, the chloride ion can be oxidized at the anode (**Reaction 3** of *Figure 4)* in place of water to create toxic chlorine gas. After the CER, the evolved chlorine or its disproportioned species can then travel to the cathode and be reduced as shown in **Reaction 4** of *Figure 4* corroding the cathode. The chloride ions can also replace the oxygen atoms in a passivated surface and cause pitting corrosion along the anode, as shown in **Reaction 5** of *Figure 4*[51-54]. The catalysts can also become poisoned by the presence of these noninnocent ions, **Reaction 6** of *Figure 4*. [55,56].

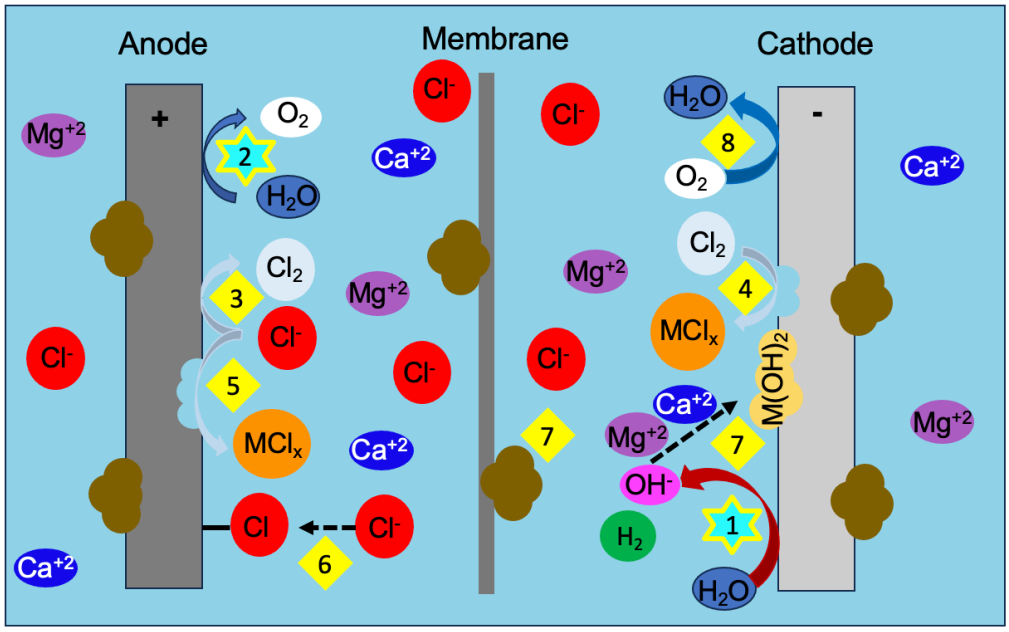

Figure 4: Depictive representation of the inherent complications of seawater electrolysis. The desired efficiencies for the HER (Reaction 1) and OER reactions (Reaction 2) can be undermined by the presence of antagonistic ions in the electrolyte such as the chloride ion, which can compete with water to undergoes oxidation at the

anode (Reaction 3). The toxic chlorine gas and its disproportionation species can then undergo reduction at the cathode and corrode the electrode (Reaction 4). The chloride ion can also corrode the anode by replacing the oxygens along the passivated surface (Reaction 5). The ions can also inhibit the catalysts at the anode and cathode by affecting their functionality and promoting dissolution (Reaction 6). The local basic environment of the cathode can also cause magnesium and calcium hydroxides to precipitate and block the functionality of the electrocatalysts; these deposits can also become trapped along the electrolyser membrane (Reaction 7). Parasitic oxygen reduction reactions can also occur at the cathode (Reaction 8).

Other ions present in seawater can also affect the electrode integrity. The precipitation of magnesium and calcium hydroxides, shown in **Reaction 7** of *Figure 4*, lead to depositions on the electrode surface that inhibit the functionality of the electrocatalysts[57,58]. These magnesium and calcium hydroxide precipitates can also become trapped and concentrated in electrolyser membranes, causing deactivation and reducing the lifetime durabilities of these essential components[59]. Han et. al. utilized a bipolar membrane consisting of an anion exchange layer and a cation exchange layer under reverse bias to promote local acidification in the catholyte to inhibit this inorganic precipitation[60]. Sadly, this novel design decreases the susceptibility towards evolved O_2 which can cross toward the membrane and induced aa parasitic oxygen reduction reaction (**Reaction 8**, *Figure 4)* [11,50]. Finally, membranes could be subject to significant microbial fouling in presence of seawater [61]. For example, Belila et. al. found that 0.25% of the bacterial operational taxonomic units were present at all stages within a water desalination plant, and further indicated that that chlorination was not effective at inactivating all bacteria and preventing microbial growth[62]. Though Debiemme-Chouvy and Cachet do suggest that electrochemical methods such as the generation of hydrogen bubbles and a low-intensity electrical potential may prevent the formation of a biofilm[63].

It worth to mention that all these precipitates and deposits decreases logically the electrochemically active surface of the cell and stack components. In addition, gas bubbles generated during the electrolysis of seawater may also be less prone to coalesce than the ones in freshwater (Figure 5)[64,65]. Tourneur et. al. have however recently found that the introducing cylindrical micropatterns at the surface of the electrode can promote gas bubble release[66].

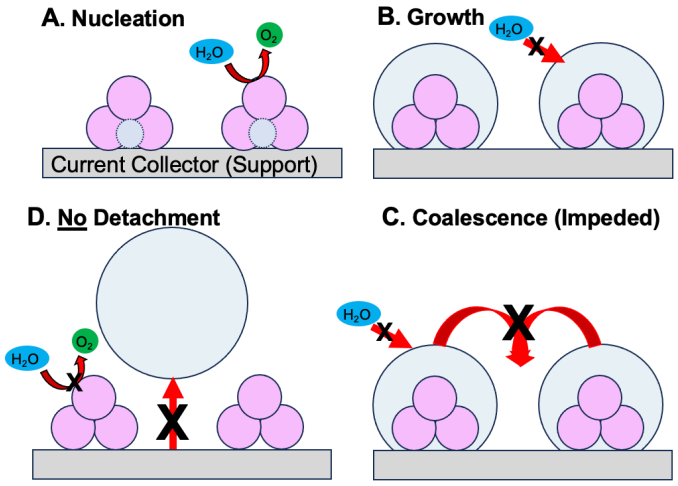

Figure 5: Stages of gas bubble (grey) formation on an electrocatalytic nanoparticle (pink) along a conductive support beginning with (A) nucleation followed by (B) growth. Seawater impedes the coalescence of the bubbles (C) preventing the electrocatalytic material from oxidizing (or reducing) adjacent water molecules (D).

I.2.2 Drop in the Electrolyzer Efficiency using Seawater

The efficiency of the individual cells may be determined as a product of the current efficiency ($\tilde{\eta}_C$) and the voltage efficiency ($\tilde{\eta}_U$), which includes the power consumption to maintain the heat balance during endothermic and exothermic electrode processes and prevent potential electrolyte freezing and elevated temperatures[67]. All the parameters influencing the efficiency are listed in Table 1 (adapted from Schalenbach et. Al) [77].

$$\tilde{\eta}_{cell} = \tilde{\eta}_C * \tilde{\eta}_U \quad (4)$$

Table 1. Classification of the operational parameters, electrolyte characteristics, and properties of the electrocatalyst and the electrodes that affect the voltage efficiency, the current efficiency, the heat balance, and thus the overall cell efficiency. Adapted from the work of Schalenbach et. al.[67]

	Cell efficiency		
	Voltage efficiency	Current efficiency	Heat balance
Operation parameters	Temperature Pressure Cell current	Temperature Pressure Cell current	Temperature Pressure Cell current
Electrolyte	Membrane thickness Conductivity	Membrane thickness Diffusivities Permeabilities	Membrane thickness Vapor pressure
Catalyst and electrodes	Morphology Permeability Activity Surface area Conductivity	Morphology Permeability	

I.2.2.1 The Current Efficiency

The current efficiency ($\tilde{\eta}_c$) also known as a faradaic efficiency, is the ratio between the moles of hydrogen produced (Δn_{H_2}) to the moles of electrons used during the electrolysis process (Δn_{e^-}). The current efficiency can be given by the following equation:

$$\tilde{\eta}_c = \frac{\Delta n_{H_2}}{\Delta n_{e^-}} = \frac{\frac{I\Delta t}{2F} - \Delta n_{loss}}{\frac{I\Delta t}{2F}} = \frac{I - 2F\left(\frac{\Delta n_{loss}}{\Delta t}\right)}{I} = \frac{I - I_{loss}}{I} \quad (5)$$

Where (I) is the current, (t) is the time, and (F) is Faraday's constant.

Current efficiencies at the anode and cathode are affected by two major losses. The first one is the recombination of H_2 and O_2 in H_2O and the second one is the current loss caused by the parasitic CER. The recombination of H_2 and O_2 is caused by the diffusion of the gases through the membrane and the convection insured by the electrolyte of the solubilized gases through the membrane [67]. Thus, I_{loss} can be written as following:

$$I_{loss} = I_{loss}^{recombination} + I_{loss}^{CER} \quad (6a)$$

$$I_{loss} = 2F\left(\frac{K}{\nu}p_c^{H_2} - D_{H_2}\right)S_{H_2}\frac{\Delta p}{d} + 4F\left(\frac{K}{\nu}p_a^{O_2} - D_{O_2}\right)S_{O_2}\frac{\Delta p}{d} + I_{loss}^{CER} \quad (6b)$$

Gordon et. al. reported the solubility of hydrogen at various salinities of local seawater samples. They found the hydrogen solubility to decrease with increasing salinity[68]. Thus, differences in hydrogen diffusivity and permeability through the membrane are expected to affect the cross-permeation flux densities.

I.2.2.2 The Voltage Efficiency

The voltage efficiency, $\tilde{\eta}_U$, can be defined with respect to the reversible voltage of a water electrolytic cell ($U_{rev,T}$) and the applied voltage (U_{cell}). These two parameters are affected by the use of seawater.

$$\tilde{\eta}_U = \frac{U_{rev,T}}{U_{cell}} \quad (7)$$

The reversible voltage ($U_{rev,T}$) is affected by the presence of salts in water. Indeed, increasing the salinity of the aqueous electrolyte solution is known to lower its characteristic vapor pressure (p_w) at a total pressure (p) [69]. By assuming that the water vapor is ideal and in equilibrium with the water in its electrolyte solution at a vapor pressure (p_{w^*}), the effect of this vapor pressure on the reversible voltage of a water electrolytic cell $U_{rev,T,p}$ at temperature (T) may be defined as following [70]:

$$nFU_{rev,T,p} = nFU_{rev,T}^{\circ} + RT\ln\left[\frac{(p - p_w)^{3/2} \bullet p_{w^*}}{p_w p^{1/2}}\right] \quad (8)$$

Where the Nernst relation with the standard reversible voltage ($U^{\circ}_{rev,t}$) may be equated to the standard free energy of formation of liquid water, which at 25°C is -2.37 x 10^5 J, giving ($U^{\circ}_{rev,t}$) a value of 1.229 V.

The applied cell voltage (U_{cell}) is also modified by the use of seawater. Indeed, (U_{cell}) is defined as the sum of the Nernst voltage U_N, the ohmic drop U_Ω ,and the kinetic overpotential U_{kin} [67].

$$U_{cell} = U_N + U_\Omega + U_{kin} \tag{9}$$

U_N is affected by the partial pressure ($p^c_{H_2}$) and ($p^A_{O_2}$) at the cathode and anode, respectively. Assuming that the gaseous hydrogen and oxygen produced at the electrodes are saturated with the water vapor, we obtained the following expression for U_N.

$$U_N = U^{\circ}_{rev,T} + \frac{RT}{2F}\ln\left(\frac{p^C_{H_2}\sqrt{p^A_{O_2}}}{p^{3/2}a_{H_2O}}\right) \tag{10}$$

Where *R* is the universal gas constant, *T* is the temperature, (a_{H_2O}) is the activity of water, ($p^c_{H_2}$) and ($p^A_{O_2}$) represent the partial pressures of hydrogen and oxygen at the cathode and anode, respectively, and (*p)* denotes the ambient total pressure as used above.

However, depending on the pH of the solution, only the proton and/or hydroxide ions involved in the oxidation and reduction reactions of water electrolysis that evolve the measured stationary currents at the anode and the cathode can contribute to the specific conductance (K_s) of the electrolyte[67]. Seawater alone is known to have a lower specific conductance than the buffered osmotic water used in PEMWE or AWE technologies. Electrolyzing seawater alone will thus require a greater applied cell voltage (U_{cell}) due the increase in the Ohmic drop (U_Ω), of the cell by increasing the total DC resistance between the cathode and the anode (R_t), which affects the overall voltage efficiency of the electrolyzer[71].

$$U_\Omega = R_t j \tag{11a}$$

$$R_t = \frac{1}{K_s} \tag{11b}$$

I.2.2.2.1 A Consideration for the Heat Flow.

It is desirable for electrolysers to operate at a fixed temperature. Leroy et. al. defined the thermobalanced voltage (U_{TB}) by considering the heat of vaporization ($T\Delta S$) caused by the phase transition of liquid water to gaseous oxygen and hydrogen, the heat of vaporization (H^{gas}_{ev}) that accounts for the phase transition of liquid water into gaseous water vapor, and the energy required to increase the temperature of the supply water at ambient temperature (20°C) to typical cell temperatures of 80°C (E_{Supply}),

$$U_{TB} = U^{\circ}_{rev,T} + \frac{T\Delta S}{2F} + \frac{E_{Supply}}{2F} + \frac{H^{gas}_{ev}}{2F} \quad (12)$$

The voltage efficiency can thus be further defined.

$$\tilde{n}_U = \frac{U_{rev}}{U_{TB}} \; for \; U_{cell} \leq U_{TB} \quad (13a)$$

$$\tilde{n}_U = \frac{U_{rev}}{U_{cell}} \; for \; U_{cell} > U_{TB} \quad (13b)$$

To conclude, the decreases of the vapor pressure (p_w) and the specific conductance of the electrolyte with the use of seawater will increase the reversible voltage ($U_{rev,T,p}$), the thermobalanced voltage (U_{TB}), and the applied cell voltage (U_{cell}) decreasing the efficiency.

I.3 Critical Challenges at the Anode

The strategic exigency for a design at the anode that mitigates the chemical and mechanical degradation of the overall electrolyser performance during seawater electrolysis in particular is convoluted in part by the chlorine species that can form upon perturbing the solution pH and adjusting the potential applied at the anode.

I.3.1 Thermodynamic Constraints of the OER and CER

The reduction-oxidation equilibria of the predominate chloride species at certain pH and electrical potential is given by the Pourbaix diagram in *Figure 6*[20,72,73].

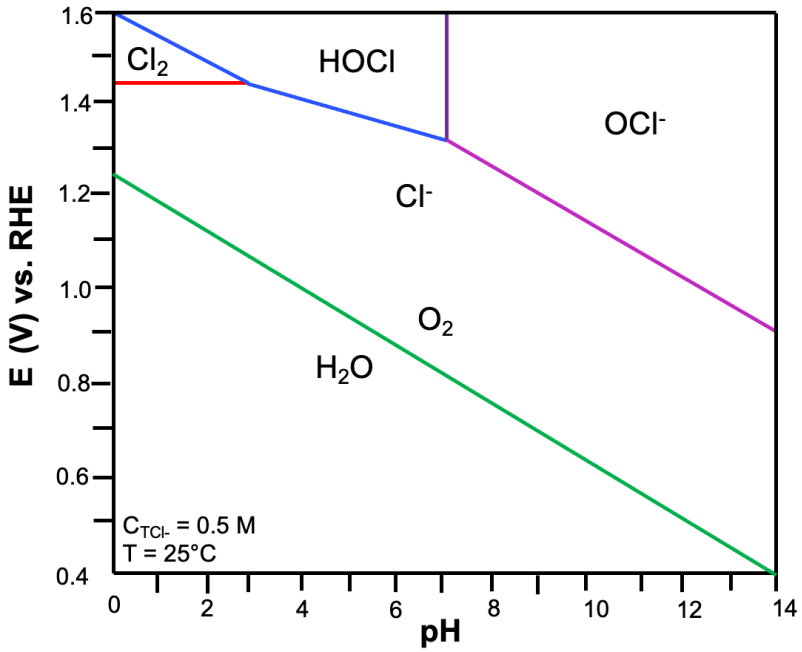

Figure 6: Pourbaix diagram of a salinated aqueous electrolyte (0.5 M NaCl) indicating the stable chemical species that are evolved as the pH and electrode potential are varied. The green line represents the pH and electrode potential values at which a thermodynamic equilibrium between water and oxygen exists; pH and electrode potential combinations above this line indicate regions at which oxygen can be evolved from water. The red line similarly indicates the electrode potentials and pH values where chlorine gas is evolved. The blue line and the magenta line indicate the onset of the hypochlorous acid and hypochlorite ion, respectively. The purple line indicates the pH and electrode potentials at which a thermodynamic equilibrium exists between the hypochlorous acid and hypochlorite.

Different chemical species can be electrochemically generated from the parasitic oxidations of the chloride ion including Cl_2, HClO, and ClO^- in acidic, neutral, and basic pH conditions. Specifically, under acidic conditions,

$$2Cl^- \longrightarrow Cl_2(aq) + 2e^- \qquad E^0 = 1.36\,V\ vs.SHE \tag{14}$$

Moreover, it is apparent that the voltage difference between the OER and the thermodynamically unpreferred formation of hypochlorite is largest under basic conditions (480 mV). This difference promotes the high OER selectivity evident in alkaline seawater electrolysis[72]. Non-PGM catalysts stable in these basic conditions have been reported with OER faradaic efficiencies approaching 100% [72,74,75].

I.3.2 Heterogeneous Mechanisms of the OER and the CER

Present in a phase different from the reactants, heterogenous catalysts are easily separable from the reactants and the products after the reaction. Thus they are very desirable for high volume transformations such as those within the energy sector. The heterogeneous catalysts interact strongly with the reactants, intermediates, and products in what is known as an inner sphere electrode reaction, or the electron

transfer can occur through a monolayer of solvent in between the solid catalyst and the reactants, products, and intermediates in what is known as an outer sphere electrode reaction[76]. Indeed, the characteristics of the interface can greatly influence the rate of electron transfer, the required overpotential, and the resulting faradaic current. Three different major mechanisms are referenced in the literature: the electrochemical oxide mechanism (EOM), the adsorbate evolution mechanism (AEM), and the lattice oxygen oxidation mechanism (LOM).

I.3.2.1 Elucidated Mechanisms for the Oxygen Evolution Reaction

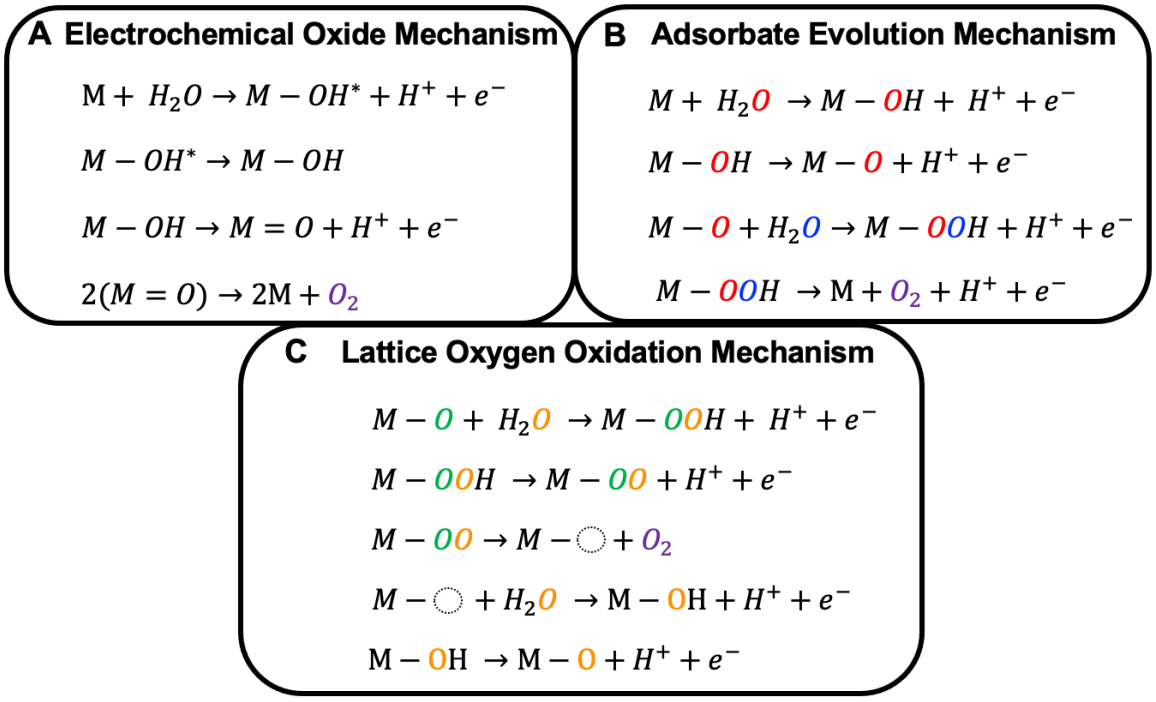

Figure 7: Proposed reaction pathways for the oxygen evolution reaction elucidated (a) from Tafel kinetics and DFT studies, (b) through DFT studies, and (c) by a combination of DFT, OLEMS, XPS, and XAS.

I.3.2.1.1 Electrochemical Oxide Mechanism

Initial evidence demonstrating the effect that the solid electrocatalyst can have on the kinetic rate of the reaction was first mounted by Bockris et. al., who found the rate of electron transfer to be dependent on the work function of the metal[77,78]. J. O'M. Bockris was also the first to calculate the corresponding Tafel slope for different considered reaction mechanisms in the oxygen evolution reaction. The approach assumed only one step in the mechanism was rate determining. Thus, the produced intermediates from the non-rate determining steps were present in only small concentrations and the saturation of the surface was only appreciable with the reactants of the rate determining step[79]. These calculations were compared to Tafel slopes obtained from experimental analysis of the log current vs. overpotential data and an electrochemical oxide path was proposed. The EOM was later refined by Over and Castelli et. al. with DFT calculations. They propose an additional structural

rearrangement of the bound oxide (step 2) to be the rate determining step as shown in Figure 7a [80,81]. [82]. By further studying the relative stabilities of the most pertinent spin states through DFT, Busch et. al. modeled the OER reaction cycle of a biomimetic catalyst, a μ-OH Mn(III-V) dimer bridged through hydroxide entities and truncated with acetylacetonate-type ligands [83]. The electrochemical oxide mechanism was confirmed with an oxidation of Mn-OH to Mn=O prior to the generation of O2, which was found to occur through a chemical step in which the two Mn=O moieties recombine in what has become known as a binuclear mechanism[83,84].

I.3.2.1.2 Adsorbate Evolution Mechanism

The proposed proton concerted electron transfer (PCET) mechanism shown in *Figure* 7b, known as both the adsorbate evolving mechanism and the mononuclear mechanism, is thought to initiate with an acid-base nucleophilic attack[85,86].

To theoretically study this mechanism, the (ΔG_{RX}) of each intermediate formed in the pathway has to be computed. It requires the computing of the chemisorption ($\Delta\epsilon$), the zero-point energy adjustment (ΔZPE), and the entropy (ΔS) as shown in *Equation 15*, though also corrected for the total energy of the gases[87,88],

$$\Delta G_{RX} = \Delta\epsilon(d) + \Delta ZPE - T\Delta S \qquad (15)$$

The chemisorption energy is quantified by measuring the change in potential energy of the adsorbate-catalyst system ($\Delta\epsilon_{pot}$) as a function of the adsorbate distance (d) above the solid surface [89]. To calculate (Δε), Norskov et. al. developed the computational hydrogen electrode (CHE) method. Rather than computing the solvation energies of the electrons and protons, Norskov et. al. assumed a chemical equilibrium between gaseous hydrogen molecules and solvated protons and electrons[90]. Thus, a simple computation of the free energy of the H_2 molecule in the gas phase can be conducted and the free energy (ΔG_{RX}) of each intermediate reaction (i.e. $M-OH \rightarrow M-O+H^+ + e^-$) can be calculated as the free energy of the reaction $M-OH \rightarrow M-O+\frac{1}{2}H_2(g)$.

One example of the calculated chemisorption energies ($\Delta\epsilon$) of each intermediate onto active surface sites was made by Rossmeisl et. al. on a (110) RuO_2 surface[91]. The active surface sites consisted of either a bridge site between two fourfold coordinated metal ions (in purple), or a coordinately unsaturated site (CUS) located on top of a fivefold coordinated metal at the surface (in light orange) in *Figure 8*.

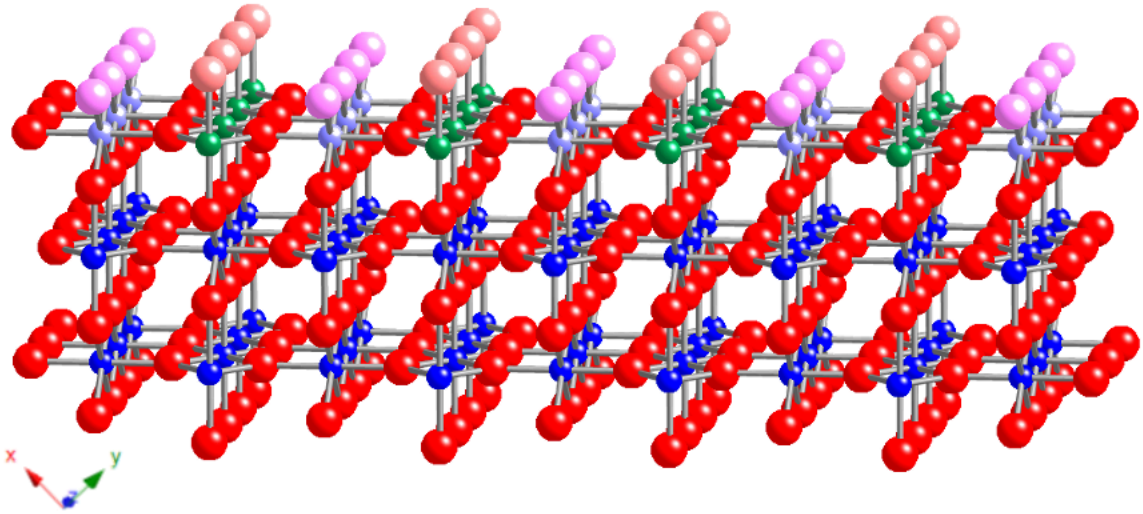

Figure 8: Representation of the bulk Ru and O atoms in blue and red, respectively, and the surface atoms, consisting of bridging Ru sites in purple and CUS Ru sites in green. Oxygen adsorbates on the electrochemically active Ru CUS sites are shown in light orange and the pink atoms on the Ru bridge sites represent surface oxygens.

The mononuclear mechanism considers the CUS sites to be the primary active site on the surface of the rutile metal oxide structure[92]. The activation of bridge sites, that can occur by doping the metal oxide, creates a proton donor-acceptor moiety. This modification can initiate the bifunctional OER mechanism [92] and the bifunctional OER mechanism 2. These mechanisms differ only in that the splitting of the water during the formation of the peroxide adsorbate occurs electrochemically in the first and chemically in the second[93,94].

The chemisorption energies of these intermediates can be utilized to calculate the Gibbs Free Energy ($\Delta G_{RX}(U)$) of each reaction step (X) in the mechanism as a function of the electrode potential (U) [91].

$$\Delta G_{RX}(U) = \Delta G_{RX} - ne_0U + k_bTpH\ln 10 \qquad (16)$$

The potential determining step is the formation of the intermediate peroxide. Assuming that the rate determining step is determining by the potential determining step, the reaction mechanism may be deduced on a thermodynamic basis[95-99]. To minimize the overpotential required to complete the reaction, the energies of the three intermediates must be tuned. However, Rossmeisl and coworkers further found that the energies of the different intermediates are linearly correlated and are thus unable to be varied independently. It further limited the ability to optimize the electrocatalyst towards catalyzing the reaction at the minimum reversable potential value (U_{rev}) of the overall reaction[95,96,100].

Thus computing the chemisorption energy of the second intermediate of the pathway depicted in Figure 7.b ($M - O_{ads}$) enables the ΔG_{RX} value for the $M - OH_{ads}$ and $M - OOH_{ads}$ intermediates to be determined. Indeed, this constant difference of 3.2 eV between the $\Delta G(M - OH_{ads})$ and $\Delta G(M - OOH_{ads})$ rather than the ideal 2.46 eV indicates an inherent overpotential[101]. Further optimizing the proton

donor/acceptor functionality of the bridge sites along the ruthenia catalyst surface and activating the bifunctional mechanisms has been proposed to break that scaling relation[92]. Finally, by modeling (Δε), the ability of the catalytic surface to form the chemical bond with the $M - O_{ads}$ intermediate, the reaction rate, the catalytic activity, of electrocatalyst for the OER can be calculated[102]. By thus plotting the catalytic activity as a function of the $\Delta\epsilon_{M-O_{ads}}$, a volcano-shaped curve can be obtained, as shown in *Figure 9*.

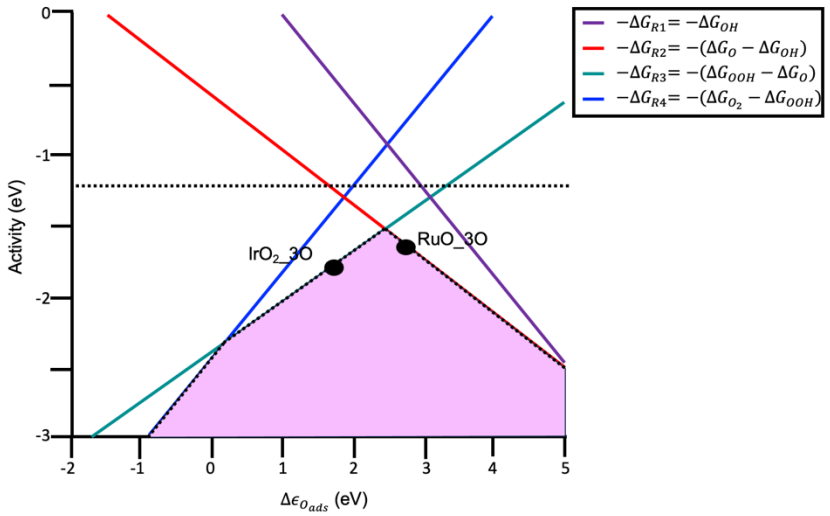

Figure 9: The theoretical activity of the four charge transfer steps of the proposed AEM oxygen evolution reaction on a metal oxide surface. Along the y axis are the activities of each step along the proposed reaction pathway, which are shown to be linearly coordinated with the oxygen dissociative chemisorption energies plotted on the x axis along the oxide surface. The resulting volcano curve is highlighted in pink and outlined in dotted lines with the position of two potent catalysts, iridium dioxide and ruthenium dioxide with saturated bridge sites and vacancies at the CUS sites. The best possible catalyst would catalyze the reaction at the horizontal dotted line indicating the equilibrium potential of 1.23eV. Figure adapted from Rossmeisl et. al.[103].

The apex of the volcano plot, known as the Sabatier maximum, is defined at the oxygen interaction energy at which the oxygen coverage is constant and the formation of the $(M - OOH_{ads})$ peroxide intermediate becomes possible[91]. This maximum illustrates the Sabatier principle, which states that the reaction rate is maximum at an optimum interaction strength of the adsorbates with the catalyst. A stronger interaction inhibits the release of the O_2 molecules and poisons the surface and a too weak interaction is indicative of an incomplete surface site coverage of the $M - O_{ads}$ and an inability to promote the formation of the peroxide intermediate[104].

This Sabatier maximum of *Figure 9* has a characteristic activity along the y axis smaller than the ideal equilibrium value of 1.23 eV (horizontal dashed line). In the AEM, there is an inherent thermodynamic impediment to the maximum activity of a catalyst coming from the observed linear scaling relationship previously discussed. Indeed, the competition between the -OH bond cleavage (step 2, Figure 7.b) and the

formation of the $(M - OOH_{ads})$ peroxide intermediate renders a minimum theoretical overpotential of 0.4 eV. Thus catalyzing the mechanism with an applied potential of just 1.23 V when the system is at equilibrium is considered thermodynamically unrealizable[96]. Additional energy, or driving force, is required to promote the rate and observed current of the water splitting reaction in the direction of oxygen evolution.

Lastly, it was shown that the mechanism at the apex of the volcano plot is highly dependent on the applied potential[93]. By applying an overpotential of 200 to 400 mV, Exner demonstrated the prominence of a Walden inversion mechanism, similar to the AEM with the concurrent formation of gaseous oxygen and adsorption of a water molecule in the final step of the pathway[105]. It worth noting that this inversion contributes to the degradation of rutile RuO_2 electrodes[106]. Binninger further found that at applied potentials close to the equilibrium potential, crystalline IrO_2 (110) preferentially catalyzes the OER through the availability of an Ir*OO surface entity. The active sites were found to be the oxygen atoms at the crystalline IrO_2 (110) surface, avoiding Ir-O bond breaking and justifying the evidenced stability of crystalline IrO_2 towards the OER[107]. The applied potential was further shown to affect the electrocatalytically produced current through the amount of oxidative (rather than capacitive) charge accumulated within the catalyst. This indicate a decrease in the activation free energy of the rate determining step with the amount of charge stored[108].

I.3.2.1.2.1 Descriptor Development. The slope of the volcano curve, which assumes a single elementary reaction governs the rate of the reaction, has been shown to change both at the legs and at the apex of the curve as the preferred mechanism adjusts or another elementary step begins to dictate the rate[109]. These phenomena add complexity of predicting selective catalysts for the OER and CER. Adequate descriptors, such as the energetic span[110] and the electrochemical step symmetry index[111] have been developed. Utilizing heuristic tools which incorporate the overpotential into the volcano-based analysis allow to assess the performance of electrode compositions[109,112-115]. As previously shown, the volcano curve is resolved from calculations of the potential determining steps, which may indeed differ from the rate determining step. Exner determined that for small overpotentials the potential determining step may differ from the rate determining step and only approach the rate determining step at large overpotentials[21,112]. The descriptor $G_{max}(\eta)$ was proposed to replace the thermodynamic overpotential (η) and the use of the potential determining step as a classification for catalytic activity as it can approach the rate determining step for typical reaction conditions. The use of $G_{max}(\eta)$ can elucidate the chemical steps of a reaction pathway and can be coupled with a microkinetic approach to approximate current densities. It can resolve discrepancies in the rate determining steps of a reaction pathway with a predetermined Tafel slope[116]. Furthermore, it was shown to be an effective approach towards predicting the selectivity between the OER and peroxide formation as the effect of the applied overpotential on the surface coverage could be accounted for and an evaluation of the evolved current densities could be made[116,117].

Many other OER activity descriptors such as the e_g orbital filling of transition metal ions[118], the shifting of the redox potentials through the inductive effect of foreign metal substitution[119], the covalence of the oxygen-metal bonds[120], and structural

factors such as the lattice spacing of the metal electrodes[121], the M-O-M bond angle and the ability of the crystal structure to accommodate the ion size (Goldschmidt tolerance factor) have been proposed[122]. Though if in-situ surface reconstruction induced by the OER is indeed appreciable including loss of the crystal matrix and variable densities of the electrocatalytic active sites, the utility of these descriptors may be limited[121,123].

I.3.2.1.3 Lattice Oxygen Oxidation Mechanism

The lattice oxygen oxidation pathway depicted in *Figure 7c*, is similar to a Mars-Van Krevelen mechanism. It has the potential to surpass the inherent limitation (scaling relationship) of the AEM by the lattice oxygen participation through direct O-O coupling in the oxygen evolution pathways. Therefore, the inevitable catalyst instability must be addressed[124,125].

Initial observation of the drastic surface reconstruction that occurs in many OER catalysts led Grimaud et. al. to study the influence of the substitution of a monovalent alkaline metal in La_2LiIrO_6 perovskite. By doing this, higher Ir oxidation states are stabilized and they can prove unambiguously that the metallic t2g-like π^* states are inactive for the OER [126]. Instead, the active surface sites on highly oxidized Ir-based catalysts are shown to be the lattice surface oxygen species that become more electrophilic upon oxidation. The computation of the Fukui function to render electron density maps indicated the participation of non-bonding oxygen states at the Fermi level upon Li removal and Ir oxidation, creating electrophilic oxygen radicals susceptible to nucleophilic attack by water oxygen lone pairs[126]. Grimaud et. al. combined online electrochemical mass spectroscopy (OLEMS) and DFT calculations to reveal that the O_2 generated by catalytic oxides with high activity towards the OER can derive from the oxygens within the lattice[120,125,127]. Furthermore, these oxides exhibited pH dependent OER activity which indicated that the proton transfers in the OER mechanism (step 2) are nonconcerted[120,125]. This pH dependency provides a lever to increase the efficiency of water electrolysis in the electrolysers. Saveleva et. al. furthermore confirmed that the generation of the electrophilic oxygen anion reactive intermediate can occur on both electrochemical iridium oxides (hydrated and amorphous) and thermally generated iridium oxides (of the crystalline rutile structure) through DFT analysis and operando studies using soft X-ray absorption spectroscopy at the O-K edge and near atmospheric pressure-XPS at the core levels of Ir 4f and O 1s[128].

I.3.2.2 Stability Predicament at the Anode

The LOM may affect the stability of the material and enhance its susceptibility towards degradation. Indeed, disruption of the catalytic surface was evidenced to promote dissolution. Cherevko et. al. found Ru to have the highest rate of dissolution among six different noble metals including Ir indicated for acidic water electrolysis as shown in *Figure 10*[129].

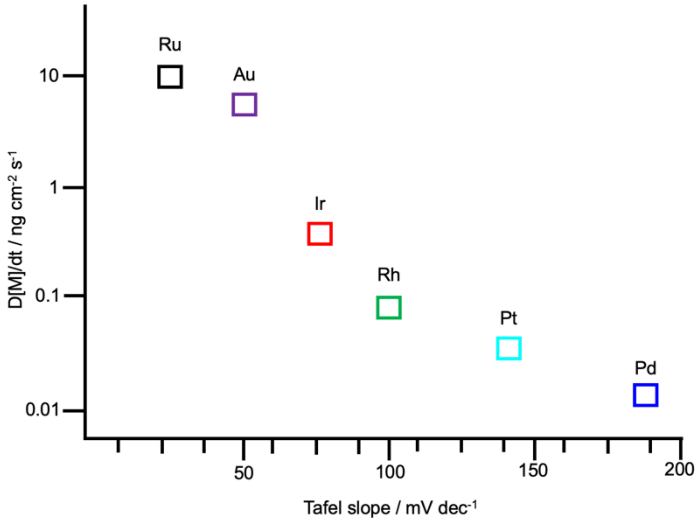

Figure 10: A scatter plot of the dissolution rate at j = 5 mA cm^{-2} determined through scanning flow cell/inductively coupled plasma mass spectrometry as a function of the Tafel slope taken from ohmic drop compensate current-potential curves scanned at 2mV s^{-1}. Reproduced from Cherevko et. al.[129]

Shown in their respective Pourbaix diagrams, both the Ir and Ru metals become passivated at pH = 0 at a voltage of ~0.9 V. The IrO_2 oxide layer is further indicated to be stable up to a potential of 2 V under acidic conditions, whereas RuO_2 begins to electrochemically dissolve to volatile RuO_4 under acidic conditions at a mere 1.4 V[130]. More specifically, the intermediate specie Ru (IV) is proposed to be the substrate for oxygen evolution and corrosion reactions[131]. Both of these processes were determined by Kötz et. al. to proceed towards Ru (VIII) through two single-electron transfer steps as shown in *Figure 11a*, with the relative stability of Ru(VI) determining whether the Ru (VIII) corrodes or volatilizes, or dissociates to Ru (VI)[131]. Kasian et. al. found the dissolution products of IrO_2 to be potential dependent as shown in *Figure 11b* with the formation of Ir(V) occurring regardless of the starting electrode material and the potential[132].

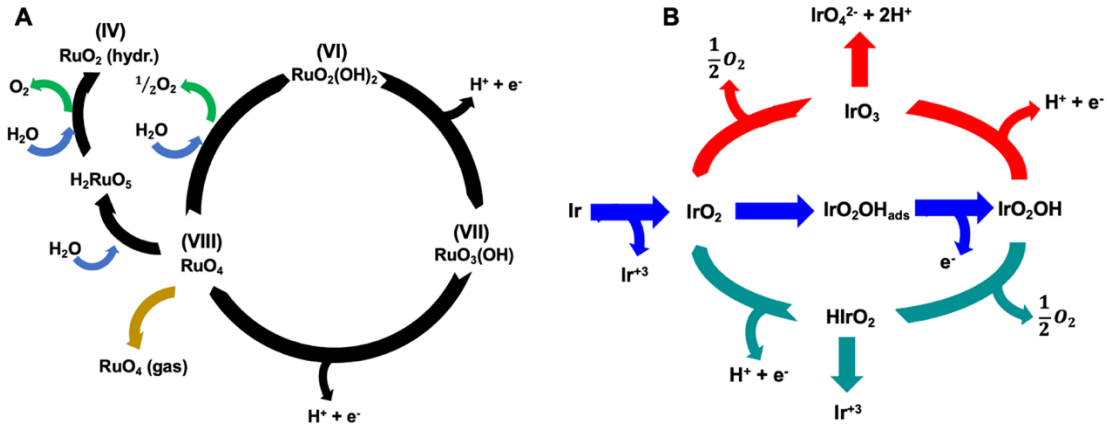

Figure 11: (A) Depiction of the Ru metal oxidation state during the oxygen evolution and corrosion processes on Ru and RuO_2 electrodes reproduced from Kötz et. al.[131]

(B) Ir dissolution scheme at higher anode potentials indicated in red arrows, at lower anode potentials indicated in green arrows. The blue arrows indicate the pathway of dissolution intermediates that occur irrespective of the potential and electrode material. Figure adapted from Kasian et. al.[132]

Ir and Pt were found to have lower steady-state dissolution rates [129]. Their however higher rate of transient dissolution was proposed to be caused by the higher kinetic rate of initial iridium oxide formation. Furthermore, amorphous iridium oxides were shown to be more sensitive to transient dissolution processes though also showed a superior activity towards the OER. [133,134]. This high recorded activity is thought to be independent of the increase in surface area. Evidence shown by Schweiner et.al. of O atom exchange between the oxide lattice and water of up to 2.5 nm below the catalytic surface suggests that all the atoms in these smaller particles sizes can be enabled[135,136]. Indeed, Willinger et.al found IrO_x samples with high electrochemical activity towards the OER to consist of a hollandite-like structural motif with a IrO_6 structural distortion creating a ratio between corner- and edge- sharing units; mixed Ir-oxidation states were moreover found[137]. This open three-dimensional network of short range order is proposed to encourage a redox mechanism that enables the uptake and release of oxygen atoms through the rotating corner-sharing and edge-sharing units, uninhibited by concerted motions that would be required of long-range ordered structures as shown in *Figure 12*[137].

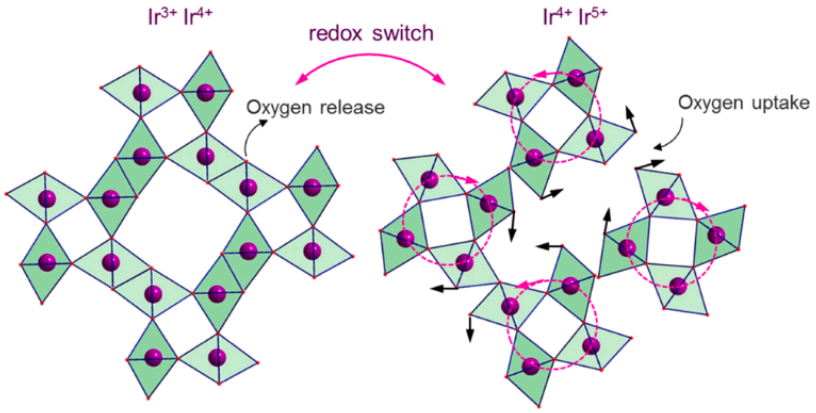

Figure 12: Proposed redox mechanism of hollandite-like structural motifs of amorphous iridium oxides.

Mom. et. al. further found that amorphous iridium oxides contained more CUS sites and O-bridge sites than crystalline rutile type IrO_2 that can be deprotonated upon the application of a potential[133]. This deprotonation increases the electrophilicity of the active sites and decreases the activation barrier for O-O coupling as indicated in *Figure 13*. Thus, a higher density of CUS and bridge sites in amorphous iridium oxides increase the electrochemical activity[133]. However, this activity was simultaneously shown to lower the barrier for Ir dissolution[133]. Thus strategies centered on the design of amorphous iridium oxide anodes may aid in improved selectivity between the OER and CER; however, the stability of the electrode may still be questionable.

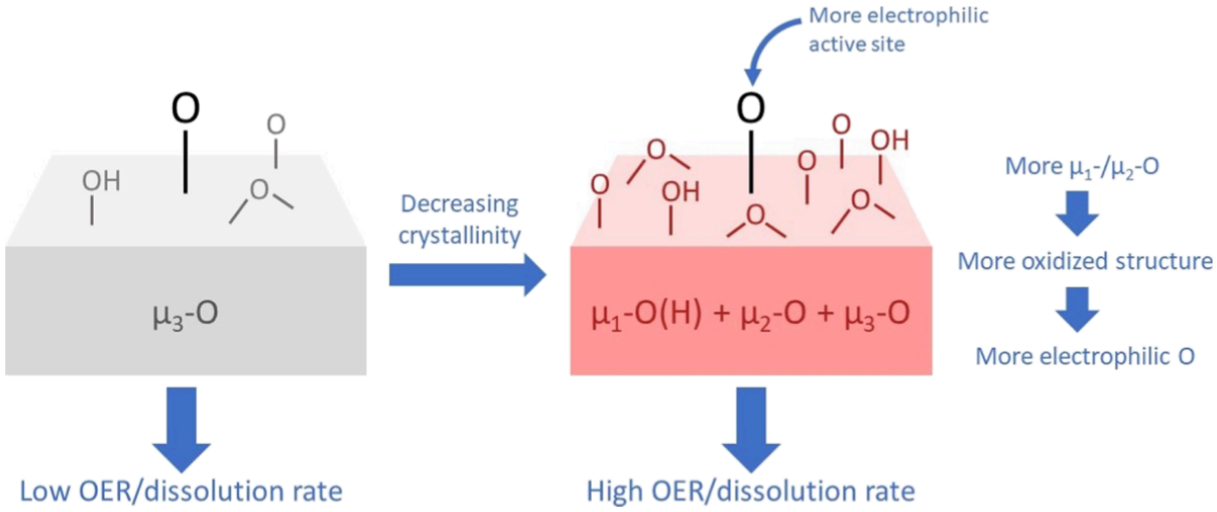

Figure 13: Representative depiction of the adverse effect of decreasing the crystallinity of iridium oxide. Amorphous iridium oxides were shown to consist of more CUS sites (μ_1) and bridge sites (μ_2) in addition to bulk oxygen sites (μ_3) that were susceptible to deprotonation under anodic potentials, creating electrophilic oxygen atoms on the electrode surface that lowered the rate-limiting barrier for O-O coupling. Figure of Mom et. al.[133]

Interestingly, Willinger et. al. had found that the residual K ions localized in the large tunnels of the hollandite-like open structure of amorphous IrO_x could stabilize the catalyst[137]. Thus, Xu. et. al. prepared an IrO_x catalyst with incorporated hydronium ions through rapid oxidation of $IrCl_3.nH_2O$ in molten salts. It achieved negligible degradation after 8 months of hydrogen production in a three-electrode cell test in 0.1 M $HClO_4$. [138]. OLEMS with isotopic labeling further indicated that the lattice water accommodates into the IrO_x framework as hydronium ions that undergo nucleophilic attack by the water adsorbed on the electrocatalytic surface at anodic potentials, initiating a modified AEM mechanism[138].

Encouraging the AEM mechanism for OER electrocatalysis may indeed improve the stabilities of the materials. Lu et. al. found that the OER mechanism could be switched from AEM to LOM to AEM by manipulating the oxygen defect content of $La_xSr_{1-x}CoO_{3-\delta}$ perovskites. They exhibit a volcano-type activity variation as the oxygen defect concentration increased[139]. The mechanistic manipulation and volcano activity variation was proposed to be caused by a concentration lockup of the generated Co^0 with increasing O vacancies. DFT simulation found this lockup to be caused by a coupling between the p and d orbitals. This coupling induces interionic $p\pi$ compensation, which can maintain the oxidation activities by the tailband of localized O-2p orbitals, and preserve the stability of the material through the transition back to the AEM mechanism[139]. A metal defect trapping technique was also utilized to synthesize Ru single atoms within the Co-O-Co skeleton of Co_3O_4. This configuration shifted the Co-O hybridized orbitals away from the Fermi level discouraging the removal of valence electrons and the activation of the lattice oxygen. In addition, the local geometry of the active centers was shifted from planar to a 3D local orientation. This change facilitates the proton transfer from the OER reaction intermediates to the

bridging oxygen sites and broke the intermediate adsorption energy limitation as shown in the proposed mechanism of the study of *Figure 14*[140]. Thus, both the stability of the material was improved and an overpotential of a mere 198.5 mV under acidic conditions was required to catalyze the OER.

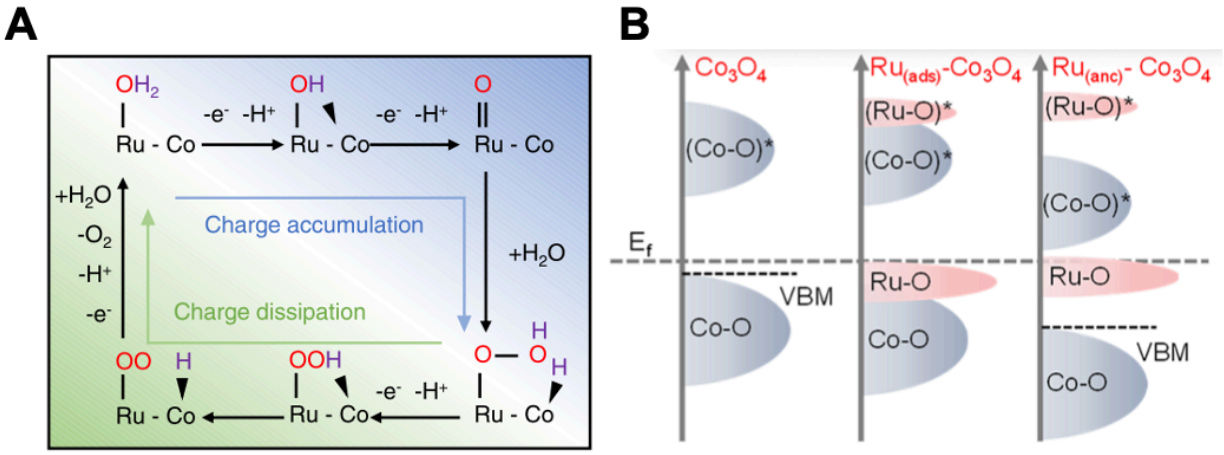

Figure 14: (A) The proposed OER mechanism of an atomically disperse Ru atom under a lattice anchored (Ru_{anc}) steric configuration. (B) DFT calculations comparing the band centers of the Ru-O-Co system indicating downshifted Co-O hybridization in the $Ru_{(anc)}$ – Co_3O_4 steric configuration, which decreased the tendency to loose valence electrons at the Co sites and the participation of the lattice oxygen. Figure of Hao et. al.[140]

I.3.2.3 Elucidated Mechanisms for the Chlorine Evolution Reaction

Understanding how the chlorine evolution reaction takes place was at first discussed through calculations of indirect experimental Tafel slopes and reaction orders. Three main mechanisms are reported in the literature. First, Krishtalik and Rotenberg initially deduced the mechanism for chlorine evolution shown in *Figure 15a* on graphite electrodes. They proceed through the identification of a low Tafel slope on the anodic polarization curve and a first order reaction with respect to the chloride ion that created a univalent positive chlorine state. This result was later confirmed on RuO_2 and RuO_2-TiO_2 electrodes[141-143]. Though Janssen and Hoogland argued that the electrode doesn't behave as a porous material. Thus the electrochemical active surface area is nearly equal to its external surface area, and found the chlorine evolution pathway to follow a Volmer-Heyrovsky mechanism on a graphite anode. According to their analysis, the rate determining step should dependent on the degree of electrode aging[144]. Finally, Faita et. al. found evidence for the Volmer-Tafel mechanism of *Figure 15c* on an electrode made of a Pt-Ir alloy on a titanium substrate[145].

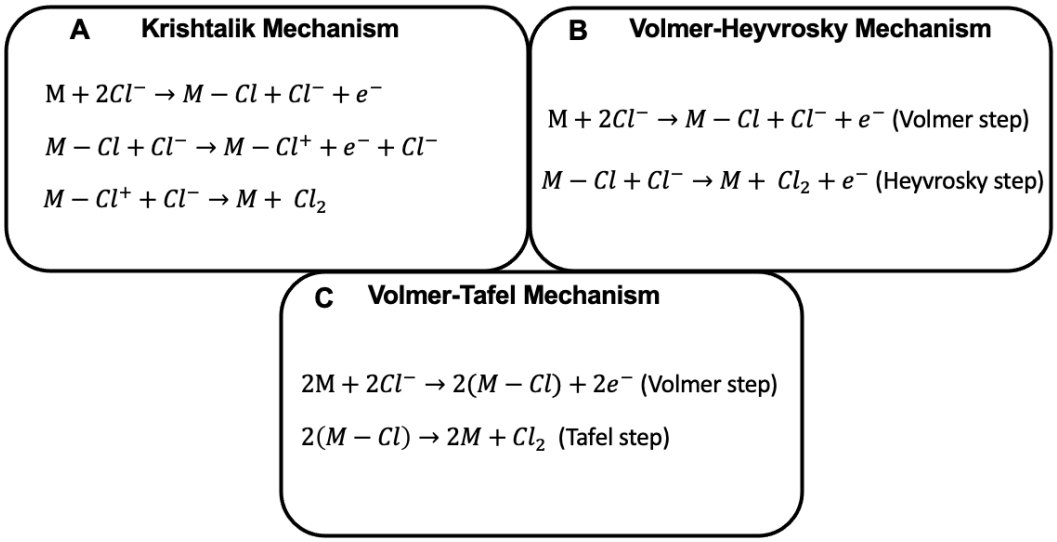

Figure 15: Classical chlorine evolution mechanisms derived by kinetic studies.

It was the discovery of the dimensionally stable anode (DSA), designed with a titanium substrate and a mixed metal oxide composed of ruthenium dioxide and titanium dioxide, that cut the energy consumed per ton of chlorine produced to nearly half[53]. Developed initially by Beer, who patented the material in 1965, these DSA anodes replaced the carbon electrodes, which are highly susceptible to corrosion under any crystalline structure or morphology ($C + 2H_2O \rightarrow CO_2 + 4H^+ + 4e^-$)[53,146,147]. Tethered with more than 50% of the entire global chemical production turnover, brine electrolysis produces the globally demanded 90 million tons of chlorine and 100 million tons of sodium hydroxide, positioning the industry as one of the largest chemical sectors, just behind sulfuric acid and ethylene production[53]. As expected, the industry demands a large consumption of electricity to power the voltage demands required to produce the current densities for the evolution of chlorine at the anode and sodium hydroxide at the cathode. These hydrophilic anodes designed by Beer could be engineered in the form of meshes with a mud-cracking morphological pattern that enabled greater escape of gas bubbles, decreasing the inner electrode gap and the gaseous oversaturation of the inner electrode solution, reducing the ohmic drop[53,148]. Reducing the gas bubble size and the average residence time at the electrode surface also promoted deblocking of the electrode active sites; coverage of the active sites can increase the local overpotential and accelerate corrosion[53,148]. Though the actual electrocatalytic properties of the material showed only a modest improvement over the electrocatalytic properties of the carbon electrode that was due to their powder-like consistency, which increased the surface area and roughness factor[148]. It is the versatile nature of these highly conductive, active oxides that promote their potentiality and robustness towards decreasing the activation energies of critical electrochemical reactions[148].

I.4 Facilitating the Electrocatalytic Performance at the Anode

Enhancing the selectivity of seawater electrolysis with appreciable faradaic efficiencies for oxygen and hydrogen evolution is convoluted by the multifarious complexity of the competition between CER and OER at the anode. Beginning to unravel that complexity enables strategies to be designed that break the scaling relationships select for the most active facet of the electrocatalyst, modulate the electrocatalytic surfaces with substitutions and vacancies, and augment the conductivity. Incorporating filtration approaches and taking inspiration from the observed self-healing properties of molecular electrocatalysts may lead to a heterogeneous electrocatalysts with a characteristic penchant for OER selectivity crucially needed to utilize the abundancy of seawater reserves to generate the hydrogen energy carrier.

I.4.1 OER vs. CER Mechanistic Competition

Usually in brine electrolysis, the oxygen evolution reaction is considered a parasitic side reaction hampering the selectivity for the chlorine evolution reaction at the DSA rutile-type anodes[149]. Under the aqueous NaCl or HCl conditions, the surface of the electrode can interact with water, chloride ions, or other ionic constituents of the electrolyte solution. Within the potential region of the chlorine evolution reaction that occurs beginning at 1.36 V, there is a strong occurrence for the oxidation of water considering that the reversible voltage of water begins at 1.23 V. In further considering this contention by examining the adsorbate evolution mechanism for the OER, two electrons are transferred to form the adsorbed oxygen species whereas only one electron is transferred to form a chlorine intermediate. Thus the energy gained ($= zeE$) for the adsorption of oxygen is double the energy gained for the adsorption of a chlorine intermediate. Therefore thermodynamics dictates that the electrode surface is effectively covered with the $M - O_{ads}$ adsorbate under the potentials at which chlorine begins to evolve[150].

Trasatti conjectured that the chloride ion adsorbed onto the surface by binding the same single oxygen species ($M - O_{ads}$). The slope of unity in the graph of *Figure 16* indicates that the AEM ($-OH_{ads}$) adsorbate of the OER and the (-Cl) adsorbate of CER bind the catalytic surface through the same $M - O_{ads}$ atom. Indeed each of these adsorbates adsorb onto the $M - O_{ads}$ populating the surface with a one-to-one linear correlation[89,151]. Thus Trasatti observed that good oxygen evolving catalysts were also chlorine evolving catalysts. Trasatti also revealed that an additional overpotential is required for those catalysts to catalyze the oxygen evolution reaction[151]. This overpotential comparison indicates that the prevalent mechanism on these catalysts is indeed the AEM.

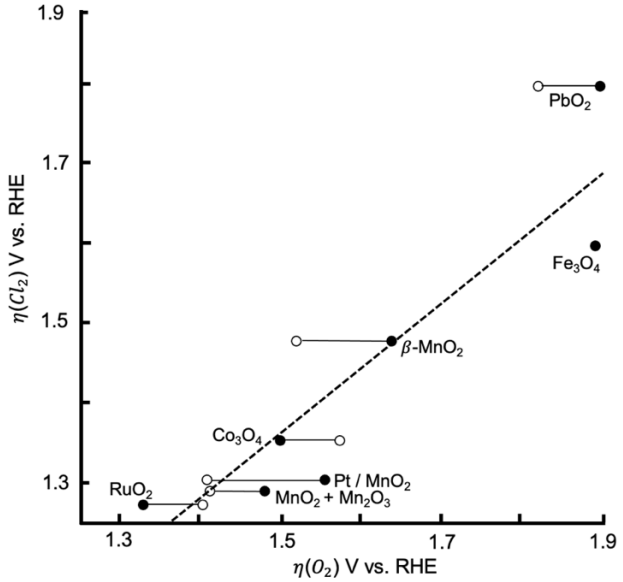

Figure 16: Plot of the overpotential for chlorine evolution against the overpotential for oxygen evolution recorded for various oxides at the same current density in acidic solution (●) and basic solutions (O). Figure adapted from Trasatti et. al.[151]

The initial density functional theory (DFT) studies to elucidate the potential, pH regions, chloride concentrations, and electrode materials in which this O_{ads} species was adsorbed on the electrode surface were conducted by Hansen et. al.. They analyzed the surface structure and the activity trends underlying the electrocatalysis of chlorine evolution over rutile oxides[152]. Further considerations for the effects of the solvent, the bridging lattice oxygen atoms, and the uncertainties of the DFT calculations were also studied[115,153,154]. The unit cell surface consisted of two bridge sites (^{b}) and two CUS sites (^{c}) and the adsorbates were found to strongly bind the bridge sites. Thus the adsorbate binding stabilities at the CUS sites were probed. It was assumed that the activation energies (E_A) of the reactions were linearly correlated to the reaction chemisorption energies ($\Delta\epsilon$) as previously described. It was found that adsorption of the CER adsorbates directly onto the CUS sites required a pH < -3 and formation of CER adsorbates directly on the bridge sites required an even lower pH[98,152]. Plots of the Cl^c and ClO^c chemisorption energies against the O^c_{ads} chemisorption energies showed a similar trend seen in the plot of *Figure 16* and thus indicated that the chemisorption energies are linearly correlated. This phenomenon was thought to be caused by the identical valency of one found in both the chloride species and the oxygen atom of the hydroxide adsorbate precursor. Thus, a plot of the potential against the O_{ads} binding energy was generated and depicts the potential and O_{ads} chemisorption energy regions in which the most stable adsorbates can be found on the surface, as shown in *Figure 17*. The three Sabatier volcano curves indicate chlorine evolution through the mechanistic pathway consisting of the ClO^c, the $Cl(O^c)_2$, or the Cl^c intermediates. The blue line represents a combined Sabatier volcano that takes the stability of the initial adsorbate on the surface into account; the intermediate is only expected to form at active sites that are indeed stable and abundant.

The three metal oxides indicated in *Figure 17* each bind to the O^c_{ads} with a different binding energy and thus stabilize a different adsorbate and a different chlorine intermediate. Along the surface of IrO_2, the O^c_{ads} initiates the formation of the ClO^c intermediate, which was further determined to follow a Volmer-Heyrovsky mechanism[152,155,156].

$$O^c_{ads} + 2Cl^-(aq) \rightarrow ClO^c + Cl^- + e^- \rightarrow O^c_{ads} + Cl_2(g) + 2e^- \quad (17)$$

Along the RuO_2 (110) surface, the most stable adsorbate populating the CUS sites in the potential regions of chlorine evolution is the O_2^{cc} adsorbate, enabling the formation of the chlorine intermediate through the Krishtalik mechanism[152].

$$O_2^{cc} + 2Cl^-(aq) \rightarrow Cl(O^c)_2 + Cl^-(aq) + e^- \rightarrow O^c + Cl_2(g) + 2e^- \quad (18)$$

This analysis indicates that chlorine will evolve on IrO_2 and RuO_2 through the formed ClO^c and the $Cl(O^c)_2$ intermediates at the CUS sites. Exner et. al. later proposed however that the ClO^c adsorbate is also indeed the precursor for the CER on RuO_2 (110)[153]. When the combined Sabatier volcano curve for the chlorine evolution of *Figure* 17 *(Blue Curve)* is compared to the Sabatier volcano curve for oxygen evolution, as shown in *Figure 17 (Green Curve)*, it is apparent that in accordance with the initial work by Trasatti, the CER will evolve at lower potentials than the oxygen evolution reaction on oxides with characteristic oxygen chemisorption energies. The CER occurs through a single intermediate, and thus the mechanism isn't subjected to the linear scaling relationships between the three intermediates inherent in the OER undergoing the AEM. Moreover, CER selectivity is highly favored under conditions in which the Cl^c intermediate, rather than the ClO^c intermediate is

formed at the rutile surface, even in only slightly acidic or even neutral pH conditions[155].

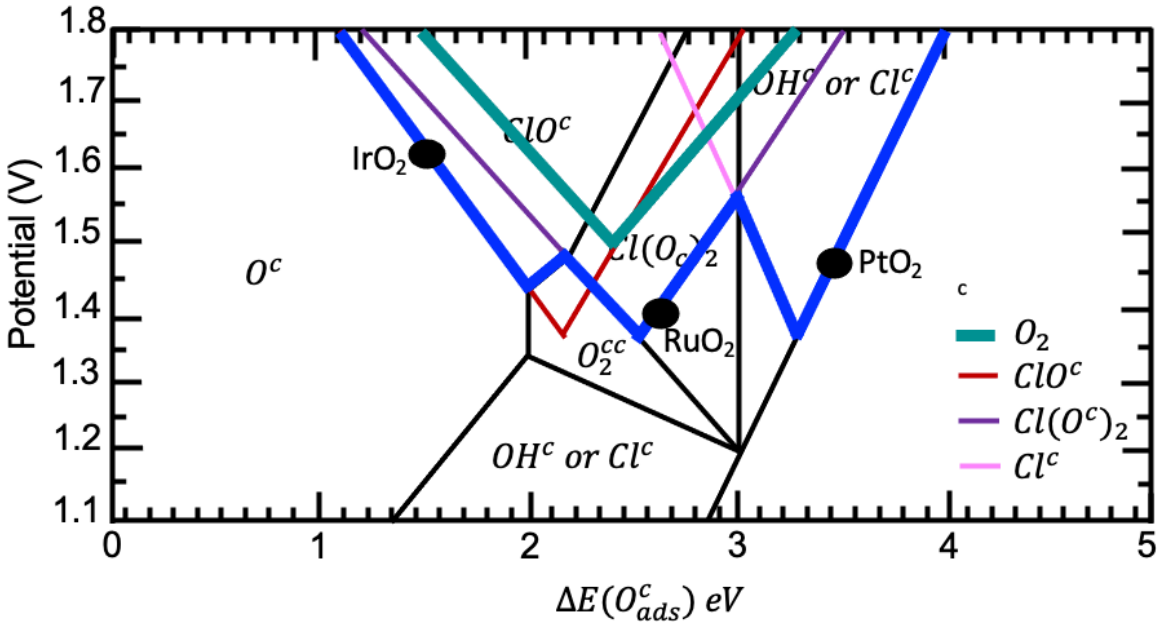

Figure 17: (Blue Curve) Combined Sabatier volcano curve that indicates the most stable adsorbate and formed intermediate at a given O_{ads} binding energy and potential at pH = 0 and $a_{Cl^-} = 1$. (Green Curve) The Sabatier volcano for the OER indicating that greater potentials are required to catalyze the reaction along IrO_2, RuO_2, and PtO_2. Reproduced from Hansen et. al.[152]

I.4.1.1 Confronting Competitive Adsorption

Vos et. al. indicated that the OER reaction is suppressed in the presence of chloride ions through competitive adsorption and active site blocking[55]. Graphs in solutions showed decreasing OER activity as the concentration of the chloride ion (and the bromide ion) increased as shown in *Figure 18*. The CER was further found to proceed through the Volmer-Heyrovsky mechanism, similar to the Rideal-Eley mechanism for gaseous reagents.

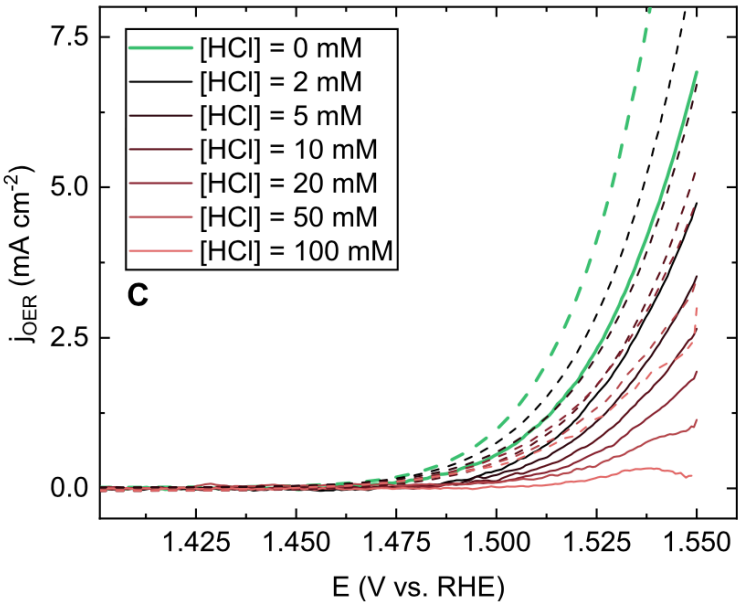

Figure 18: OER current density as a function of potential vs. RHE in the presence of bromide (solid curves) and without bromide (dashed curves) at increasing chloride ion concentrations. Figure of Vos. et. al.[55]

If a Langmuir adsorption model with a lack of lateral interactions among adsorption sites is assumed, the surface coverage of water at the active sites is thus expected to diminish in the presence of the chloride ion, though its presence at an approximately consistent concentration enables a small amount of oxygen to form, at the dismay of the chloro-alkali industry. Therefore, improving the selectivity at the anode is an inevitable challenge.

I.4.1.2 Identifying the Rate Determining Step

Efforts have been proposed to develop new electrocatalysts that maximize the free energy difference between the respective CER and OER intermediates. With the assumption of quasi-equilibrium of the reaction intermediates preceding the rate determining step in place, the free energies of the transition states corresponding to the rate determining step can be found, enabling the rate determining step to be identified[150,157]. With the desire to discover an electrocatalyst that stabilizes the oxygen transition state, the intrinsic catalytic characteristics of an electrocatalyst may be regarded through measurements of the exchange current density. Exner et.al. proposed that the linear regions of the Tafel plot may each be extrapolated to $\eta = 0$ to measure the exchange current densities. They could then be utilized in the generalized Butler-Volmer equations discussed by Parsons to determine the free energy of the corresponding transition state, enabling the rate determining step to be determined with respect to the overpotential applied[150,158].

The free energies of the reaction intermediates must be determined to enable a critical assessment of the intermediates and transitions states to stabilize and thus promote CER or OER selectivity. Quasi-equilibrium implies inaccessible values of reaction intermediates free energies. Though, advancement of transient experiments

like cyclic voltammetry[159] and operando spectroscopic methods[160] can aid in their identification. However, with small surface area coverages due to their higher Gibbs Free energies, in-situ intermediate detection is generally difficult. A particular attention should be made to verify the reaction intermediates and their corresponding free energies determined through DFT theory and the construction of ab initio surface Pourbaix diagrams. The free energies in function of potential of reaction intermediates can be *ab initio* calculated and correlated with the respective free energies of their transition states determined through the Tafel plots. This work enables a free energy surface model of an electrocatalyzed reaction to be deduced and the dependence of the free energies of the transition states and reaction intermediates on the overpotential to be depicted. Understanding the characteristic rate determining step of a designed electrocatalyst with respect to the overpotential could enable optimization of an electrocatalyst that, for instance, stabilizes the $(M-OOH_{ads})$ transition state with respect to the $M-Cl_{ads}$ and $M-OCl_{ads}$ transition states, making the OER the kinetic product by increasing the speed of the reaction step as delineated in *Figure 19*[161].

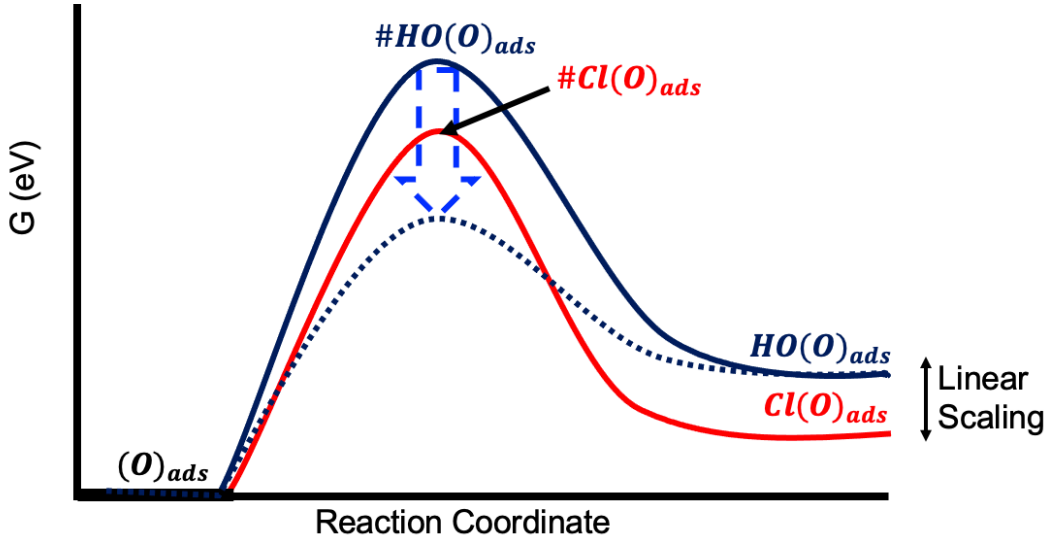

Figure 19: The free energy diagram along the reaction coordinate of the OER and the CER over a single-crystalline RuO_2 (110) electrode at $\eta_{CER} > 0.1\,\mathrm{V}$ and constant pH indicating the relative energies of the transition states (#) of the rate limiting steps for the OER and CER. The thermodynamic stabilities of the $\mathrm{HO(O)_{abs}}$ and the $\mathrm{Cl(O)_{abs}}$ intermediates are determined by the linear scaling relationships. Figure adapted from Exner[162].

I.4.2 Modulating the Structure of the Electrocatalyst

Initial thoughts by Taylor implicated that unsaturation within an active site at the atomic level can control surface reactivity[163]. Refinement of the local structure can optimize the functionality of the active site. A challenge of heterogenous electrocatalysis is maximizing the exposed active sites and enhancing their intrinsic mass activity by stabilizing the transition state while maintaining stability. Refining the size and the dispersion, and moreover the crystal facet orientation, has been shown

to improve the amount of exposed active sites[164]. Moreover, dispersing the active centers among various types of substrates such as metal oxides[165], metals sulfides[166], and carbons[167] can influence the ionic and electronic defects within the material and encourage electron transfer capabilities of the active centers, manipulating the valence of the active site and the coordinating bond lengths[168]. These refinements can influence the stability of the intermediates and the activation energies of the transition states electronically, geometrically, and through confinement effects enabling selective seawater electrolysis to be achieved[169,170].

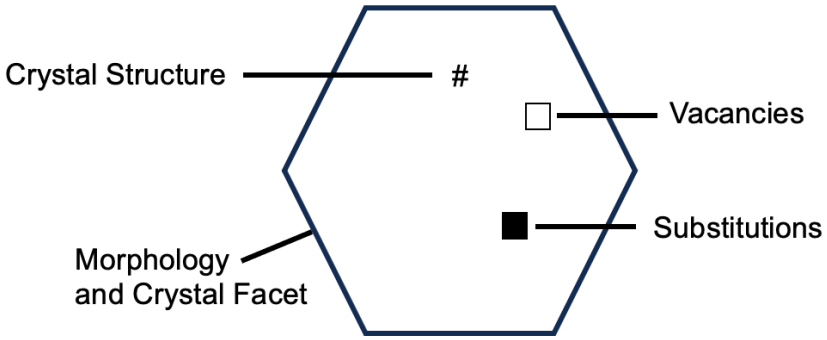

Figure 20: Means of manipulating the active site to improve the activity and selectively of the electrocatalyst.

I.4.2.1 Manipulating the Morphology and Crystal Facet

The D-band centers of late transition metals with low coordination numbers, consisting of edges, steps, and kinks are thought to be more diffuse, residing further from the nucleus and interacting more strongly with adsorbates than metal atoms on close packed surfaces with higher metal coordination numbers and more compact, tightly-bound d-states[169]. Dickens and Norskov projected the density of states onto an Ru atom CUS-terminated single kink site along the (110) plane and found shifted D-band centers with significant higher energies, which result in less filling of the Ru-O adsorbate antibonding states and a stronger Ru-O adsorbate bond, promoting the OER[171]. Indeed, the structure of the catalytic surface has been shown to affect the catalytic activity of the material towards the OER through a linear correlation with the density of coordinatively undersaturated metal sites (CUS) along each crystallographic face[172]. The (100) facet of epitaxial grown RuO_2 supported on a single crystal (001) facet of $SrTiO_2$ was found to more easily oxide the reagent substrate than the corresponding (110) facet in a basic 0.1 M KOH solution as shown in *Figure 21*. Measurements of the cathodic pseudocapacitive charge further enabled a charge ratio between the two surfaces to be determined that was found to mimic the CUS ratio between the two facets[172].

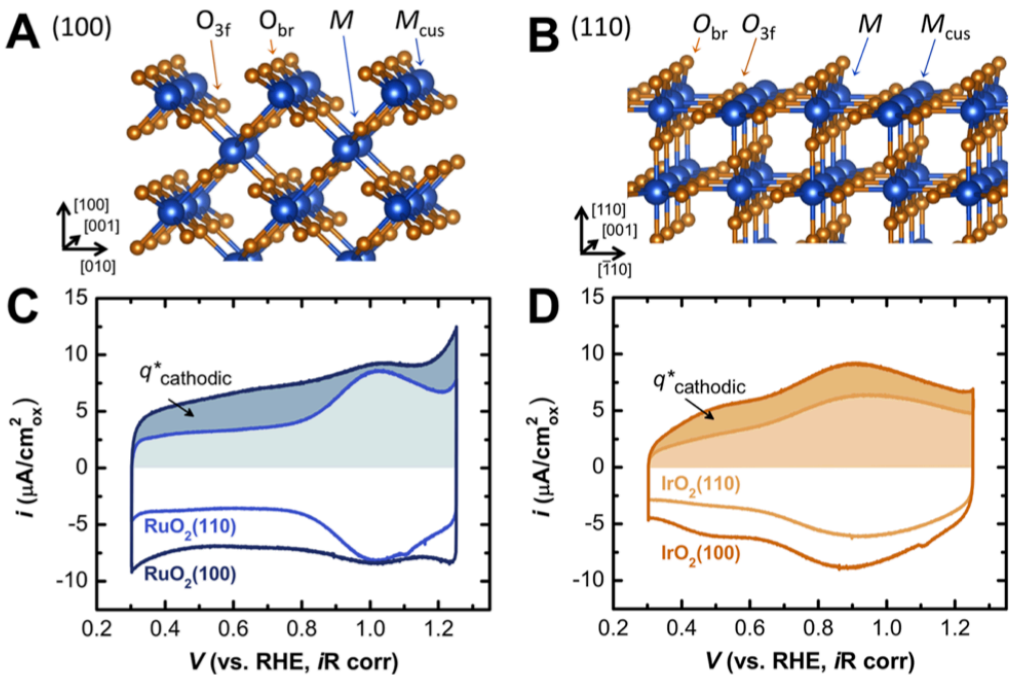

Figure 21: (A) Schematic depiction of the (100) facet and (B) the (110) facet of RuO_2 and IrO_2. Fully coordinated metal centers (M) and coordinately undersaturated metal sites (M_{cus}) are indicated in blue, bridging oxygens (O_{br}) and three-fold coordinated oxygen (O_{3f}) are shown in orange. Analysis of the pseudocapacitive charge ($q^*_{cathodic}$) shown in (C) and (D) for RuO_2 and IrO_2 gave an indication of the electrochemically active metal site density on the electrode surface, the ratio of the calculated charge between each orientation indicating the undercoordinated metal site density. Figure of Stoerzinger et. al.[172]

The stepped nature of the (230) facet of RuO_2 was further proposed to explain the greater Cl^- evolution; the (230) facet possesses an activity with a greater susceptibility to changes in the pH because of the abundant pre-oxidation occurring through proton removal of the hydroxide adsorbates along the surface active sites [173,174]. This (230) surface was indeed proposed to be more hydrophilic, possibly due to its unique binding energies with the -H_2O and -OH adsorbates, enabling different degrees of hydrogen bonding amongst the adsorbate groups along the surface[175]. The mechanism of chlorine evolution was further proposed to proceed without pre-oxidation on more hydrophobic surfaces such as the (100) facet with less local functional group motion that facilitates proton exchange[173]. Facilitating proton exchange may indeed be more facile on faceted surfaces. Adiga et. al. epitaxially grew a (101) surface of RuO_2 on r-Al_2O_3 and TiO_2 substrates, a surface which is known to possess a large degree of strain due to the large lattice mismatch between the film and the substrate [176]. This strain was shown to relax as the film thickness increased through the introduction of facets and defect formation. This faceting was shown to dramatically decrease the activity towards the OER, which was shown to be perpetuated through the LOM evidenced by exposing the thicker films to solutions of varying pH, the AEM mechanism is conjectured to independent of solution pH due to the proposed concerted proton-electron transfers. Interestingly, the CER activity was

minimally affected. Strain relaxation and the resulting faceting may thus induce a mechanistic change in the OER[176]. The study moreover found the thicker films to be more selective for the CER.

Indeed, mitigating the elucidated mechanisms of the CER and the OER to select for one evolved product is convoluted by the disparities between the single intermediate and the multiple intermediate reactions. Interpretation of the most thermodynamically stable intermediate, initially addressed by the DFT studies by Hansen et. al. has aided in the utilization of potential and pH manipulations to promote the evolution of the CER or the OER[152]. *Figure 22* highlights the potential and pH conditions that promote the evolution of the CER or the OER.

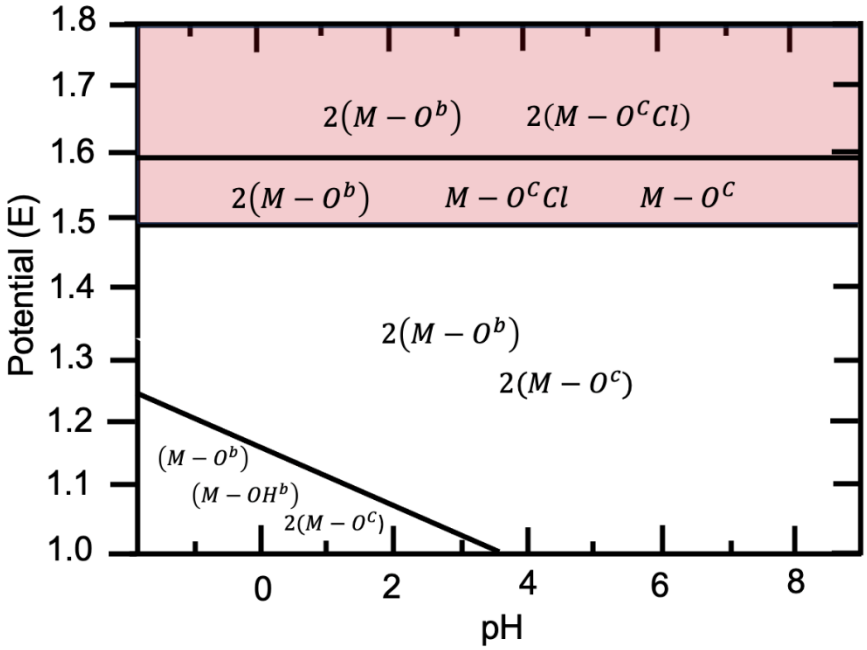

Figure 22: Pourbaix diagram depicting the most stable adsorbates along the RuO_2 (110) catalytic surface corrected for solvent effects at Activity Cl^- = 1. Denoted adsorbate structures were further found to be stable with respect to the gas phase molecular species. Potential and pH regions highlighted in red indicate the conditions promoting the CER; the $2(M-O^b)+2(M-O^C)$ structure is expected to serve as the catalytic active phase for the OER. Figure reproduced from Exner et. al.[153]

However, with the high current densities afforded by PEM electrolysers, achieving OER selectivity under acidic conditions is critical, requiring surface engineering that controls the nature and abundance of the active sites that catalyze the desired reaction. Saha et. al. utilized ab-initio studies to further find the (101) and the (001) to be the most selective facets at pH = 0 along RuO_2 for the CER and the OER, respectively[98]. The difference in selectivity was attributed to the variation in the adsorption energies of the CER and OER intermediates along each facet, which is caused by the disparities in the ligand coordination symmetry around each active site that affects the charge distribution and the bond length between the adsorbate and active site[98,177].

I.4.2.2 Introducing Point Defects into the Local Chemical Environment

I.4.2.2.1 Lattice Substitution

Exner et. al. found in an ab initio thermodynamic study that the activity towards the OER could be improved by 0.8 to 1.0 eV by reducing the adsorption energy of oxygen to the catalytic Ru_{cus} when the ruthenium atoms of the second coordination shell were substituted by Ir or Cr[177]. To further their investigation of the OER vs. CER selectivity, Exner et. al. found in another study that replacement of the top most monolayer of RuO_2 (110) with TiO_2 improved the CER selectivity by adjusting the bonding strength of the oxygen to optimize the strength of the chloride adsorption in the Heyrovsky step[178]. Karlsson et. al. found that monolayers of TiO_2 on RuO_2 improved selectivity for the CER while maintaining the characteristically high activity of pure RuO_2, and that by moreover doping TiO_2 with Ru, the Ti_{CUS} sites could be activated with optimal oxygen adsorption descriptor values for active and selective chlorine evolution[179]. Ru has been indeed proposed to influence the electronic state of TiO_2[180]. Deactivation of DSA electrodes was further noted by Karlsson et. al. to be caused by the removal of Ru from the surface[179,181]. Macounová et. al. went one step further to employ a systematic study of spray-freeze freeze drying prepared nanocrystalline $Ru_{1-x}Ti_xO_2$ ($0<x<0.2$) in chloride containing acidic media to dissect the ambiguity surrounding the compositional roles of these catalysts within DSA electrodes[182]. The authors found the selectivity towards the CER to increase with greater Ti content that relieves Ti clustering along the z axis and promotes Ti-Ti pairing between CUS and bridge sites, as shown when comparing *Figure 23a* and *Figure 23c*; these structural shifts were furthermore indicated to cause an increased oxygen deficiency within the Ti environment[182]. Moreover, this increased oxygen deficiency was indicated to promote the LOM, as evident in the comparison of *Figure 23b* and *Figure 23d*. Thus, the variability in the chlorine selectivity was ascribed to the differences in the mechanisms used by the catalyst to evolve oxygen, with catalytic structures that promote the LOM having an increased selectivity for the CER[182].

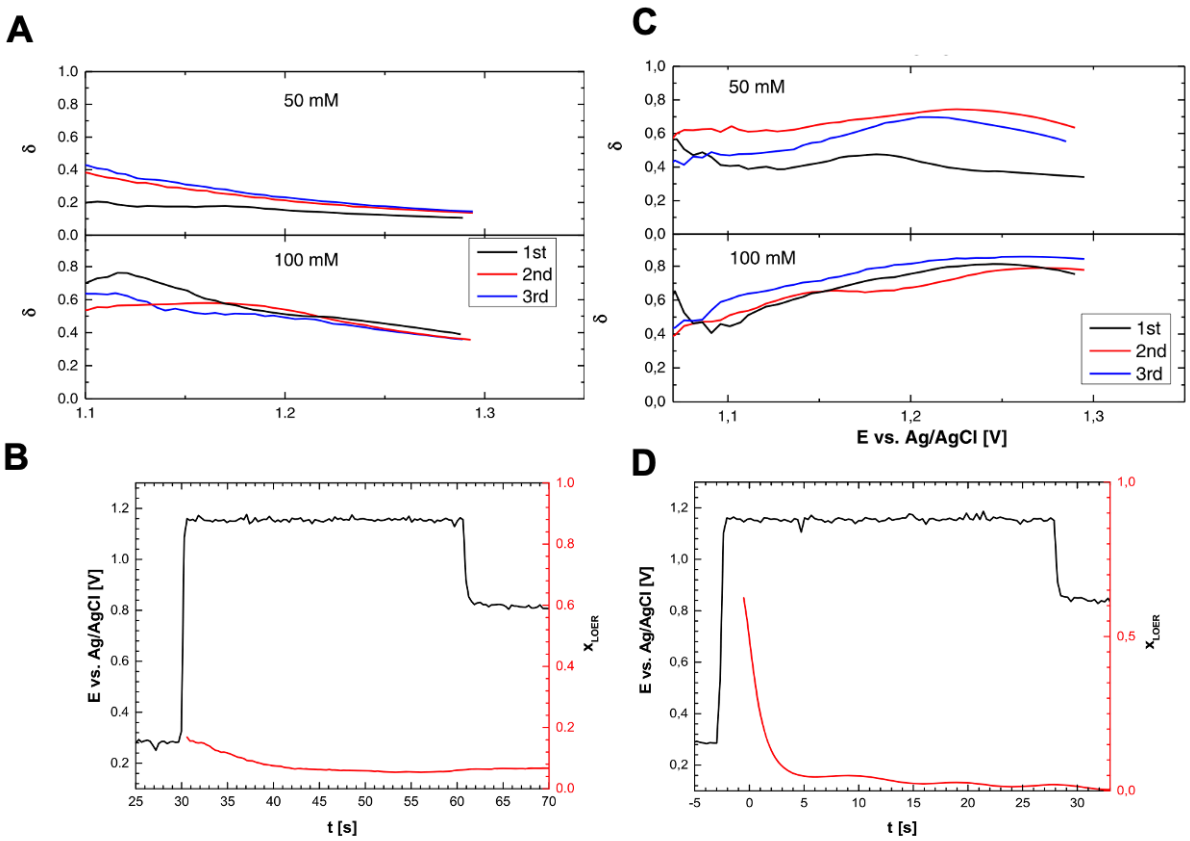

Figure 23: (A) and (B) represent the selectivity (δ) towards chlorine evolution and the tendency to evolve oxygen via the LOM determined through differential electrochemical mass spectrometry isotopic labeling for $Ru_{0.95}Ti_{0.05}O_2$. (C) and (D) represent the results obtain for the structural composition $Ru_{0.80}Ti_{0.20}O_2$. Figure of Macounová et. al.[182]

In another study, Astudillo et. al. found through detection by differential electrochemical mass spectroscopy that the LOM in acidic, chloride containing aqueous solutions electrocatalyzed by Ru-Mn-O oxides coincided with greater CER selectivity [183]. However, ab-initio studies indicated that an Ru-Mn-O surface behaves similarly to pure RuO_2 surface in that the adsorption of oxygen into any conceivable surface site is unlikely to result in its immobilization that promotes the LOM: the surfaces are rendered too stable[183]. The binding of oxygen adsorbates at the Mn_{cus} sites was however found to be weaker, which may promote the migration of a proton towards the bridge sites for the -OH and -OOH reaction intermediates, and explain the observed experimental trend of higher OER activity with increasing Mn content[183,184]. However, it must be noted that spectroscopic confirmation of the CUS and bridge sites in the prepared Ru-Mn-O oxides remained elusive throughout the study and low dimensionality sites, such as crystal edges and vertices, were mentioned by the authors to not be taken into account, which may indeed influence the perceived mechanism of the OER and an understanding of the observed selectivity[176].

Interestingly, substituting RuO_2 materials with Zn was found to increase selectivity towards the OER at more positive potentials[185]. The authors suggested that

the substitution resulted in rearrangement of the metal atoms along the [111] that created more oxygen vacancies on the surface that affected the adsorbate binding of the chlorine evolution precursors and enhanced the oxygen evolution via the LOM at more positive potentials[185]. However, the chemical constituent which is substituted into the lattice may affect the OER mechanism. An overpotential of 214 mV was achieved by Wu et. al. who incorporated Ni into the RuO_2 lattice; DFT studies and operando electrochemical mass spectrometry analysis indicated that the Ni replaced Ru in the bridge sites, which both stabilized the lattice oxygen and promoted the AEM mechanism while achieving impressive stabilities of >1,000 h under a current density of 200 mA/cm^2[186]. Interestingly, the oxidation state of the Ru catalyst with Ni embedment was shown through X-ray photoelectron spectroscopy to be slightly up-shifted compared to RuO_2; higher Ru oxidation states have been shown to enhance OER electrocatalysis[187]. Moreover, the number of dopants on the electrocatalytic surface may affect the OER mechanism that predominates. Zagalskaya and Alexandrov found that substituting the surface of RiO_2 (110) with only two nickel atoms wasn't enough to induce a mechanistic shift from the AEM to the LOM[188]. The formation of metal vacancies that were caused by catalyst dissolution were further proposed to have a synergistic effect with the introduced dopants to lower the OER overpotential via the LOM[188]. Zagalskaya and Alexandrov further found defective IrO_2 to be less LOM active than defective RuO_2 through simulations suggesting that by creating two surface vacancies in the high energy 211 facets of RuO_2 and IrO_2, the mechanism could be switched from AEM to LOM in RuO_2 though not in IrO_2, indicative of the greater structural stability of IrO_2 under OER conditions[188].

I.4.2.2.2 Generating Vacancies within the Lattice

Incorporating the Ru into a mixed metal oxide such as the pyrochlore $Pb_2Ru_2O_{7-x}$ structure increased the concentration Ru(V) indicated through XPS measurements and was further shown to improve its stability even after being subjected to a 2h stability test in alkaline conditions[189]. The high Ru oxidation state and high concentration of oxygen vacancies characteristically present in pyrochlore $A_2B_2O_{7-x}$ structures that form upon a cationic radii mismatch of >1.46 was proposed to promote an improvement in the activity and selectively towards the OER during simulated seawater electrolysis under alkaline conditions[190-193]. Oxygen vacancies shifted the O-2p orbitals upwards, increasing the density of states around the Fermi level and promoting both metallic character and potential interaction with AEM adsorbates[190]. Another means of generating vacancies within the lattice is through leaching. Though deemed thermodynamically unstable under acidic conditions and prone to dissolution through cation A-site leaching according to in-situ Pourbaix analysis, an increase in electrocatalytic activity with A-site dissolution was found for Ru incorporated into $A_2Ru_2O_7$ (A = Y, Nd, Gd, Bi) pyrochlores [194]. Weaker interactions between the Ru 4d and O 2p orbitals of the OER intermediates of the AEM with longer Ru-O bond lengths were shown to improve activity in the materials when compared to RuO_2 [194]. This increase in activity was shown to be correlated with both the increase in the density of Ru active sites promoted by leaching and an increase in the oxygen 2p-state energy for adsorbed oxygen density of states, as shown in **Figure 24** [194]. Moreover, the bulk phase of $Y_2Ru_2O_7$ was shown to be maintained after

chronoamperometry testing by XRD and also that the surfaces evolves during OER catalysis[194]. The surface coverage of the active sites is indeed critical. Gayen et. al. found the apparent OER activity of $Pb_2Ru_2O_{7-x}$ pyrochlores to decrease upon being subjected to annealing at elevated temperatures regardless of the annealing environment; this effect was attributed to the observed increase in crystallinity that lowered the density of under-coordinated active sites, which decreased their surface coverage on the catalytic surface[189].

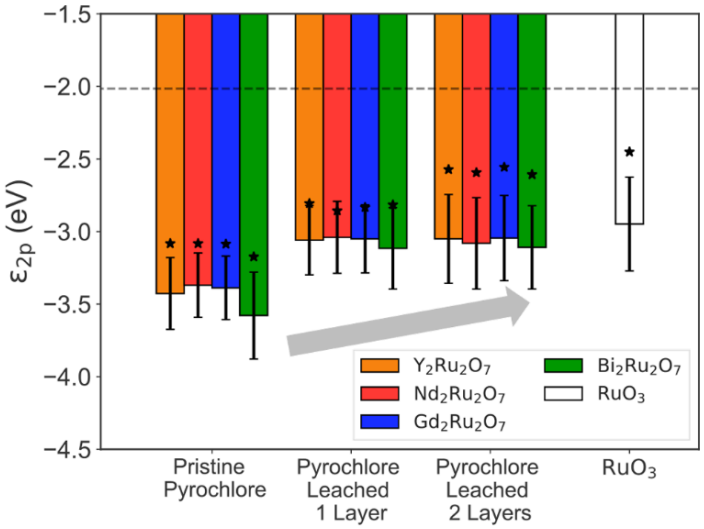

Figure 24: Computed oxygen 2p-state energy comparison of pristine pyrochlore, one and two layer leached pyrochlore, and the fully leached pyrochlore-like RuO_3 structure, showing an increasing trend that approaches the computationally determined optimal OER activity value of -2.0 eV shown by the dashed line. Figure of Hubert et. al.[194]

Nong et. al. also found that leaching nickel from their $IrNi@IrO_x$ core-shell nanoparticles could achieve uniquely high activities in OER electrocatalysis [195]. The leaching produced significantly shorted Ir-O bond lengths at the shell surface with a covalent character that created electrophilic oxygens, highly conductive and more susceptible to the nucleophilic attack inherent in the O-O bond formation of the LOM mechanism as shown in **Figure 25**b. Conclusions from XANES measurements indicated that the iridium atoms adjacent to the vacancies formed through nickel leaching had a greater number of d-band holes. Moreover, the occupied projected density of states indicated that the iridium 5d-states were concomitantly lowered below the oxygen 2p states, producing oxygen hole formation, with significant Ir character, that was reflected by the appearance of an unoccupied, narrow band just above the Fermi level [195].

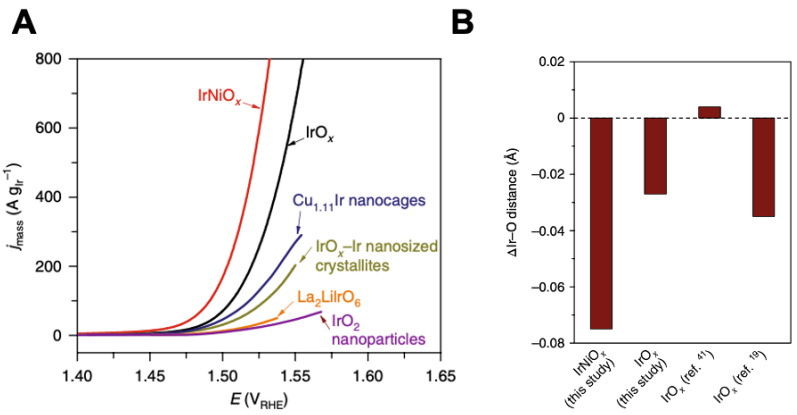

Figure 25: (A) Comparison of the activity towards the OER in an acidic electrolyte amongst the investigated IrNi@IrO_x, the benchmark IrO_2, and electrocatalysts of high recorded intrinsic activity divulged from the literature. (B) Degree of change in the Ir-O bond length along the surface of the IrNi@IrO_x nanoparticles, IrO_x nanoparticles, an IrO_x film, and standard IrO_x nanoparticles. Figure of Nong et.al.[195]

I.4.2.3 Use of Single-Atom Catalysts

The number and type of atoms within the first and second coordination shell can significantly affect the local geometry and charge density of the metal active sites[196] Ji. et. al. incorporated Ru atoms into a low crystallinity 2D TiO_x substrate that promoted sub-nano ruthenium clusters through a cationic defect adsorption-oxidation anchoring method, creating partially oxidized, high valence, and lowly coordinated ruthenium atoms[197]. DFT simulations predicted that the CER proceeded through stabilization of the -Cl adsorbate by the ruthenium clusters, similar to the results of Lu et. al. discussed above, avoiding the -OCl intermediate and improving the mass activity, selectivity, and stability towards the CER[197]. Though, the close-packed geometries adopted by these supported metallic cluster/nanoparticles may limit, as previously indicated, their achievable activities and desired selectivities[198].

Embedding a metal atom with a heteroatom support as in the case of single-atom catalysts (SACs) or amongst adjacent metal atoms, known as correlated SACs (c-SACs) may provide greater flexibilities in the structural design to tune the atomic structure and the local coordination of the active site to achieve optimal electronic structures for selective adsorbate binding with high activities and verified stability[164,198]. Cho et. al. identified the critical role of the three-coordinated Pt^{II} with broken D_{4h} symmetry in a platinum single atom catalyst with reported CER selectivities approaching 100% under acidic conditions[199]. It must however be understood that the study illustrated the significant degree of heterogeneity present at the active sites of SACs and the complexity of discriminating the authentic active sites and the quantifying the intrinsic activity of the catalysts through metrics such as the turnover frequency (TOF)[199]. These lowly coordinated active sites were deemed more active in the CER than the Pt-N_4 sites previously reported with a preferential binding of the -OCl intermediate[199,200]. On the other hand, the design and successful synthesis of single atoms that exhibit spatial correlation within a sublattice substrate have the potential to exhibit identical structural motifs within those substrates. Accommodating

iridium single atoms into the cationic sites of a cobalt spinel oxide through an ion exchange-pyrolysis procedure produced Ir sites that were shown to possess short range order though the partial projected pair distribution function profiles derived from multiple high-angle annular dark field scanning high resolution transmission electron microscopy (HAADF-HRSTEM) images[201,202]. These Ir cluster sites exhibited a spatial correlation with the Co_3O_4 host lattice with the majority of the Ir sites exhibiting short range order rather than being isolated within the cationic lattice of the Co_3O_4[201]. The electrocatalytic active sites were shown to be comprised of these short range Ir octahedral spatially correlated sites enclosed by Co sites. Electronic structural analysis showed a downshift valence band maximum edge and d-band centers of these Ir-Co_{oct} nanodomains at the Fermi energy, as shown in *Figure 26d* that could modulate the oxygen intermediate adsorption energies. An overpotential of 300mV at 6 mA/cm^2 was exhibited with a mass activity two orders of magnitude greater than commercial IrO_2 catalysts.

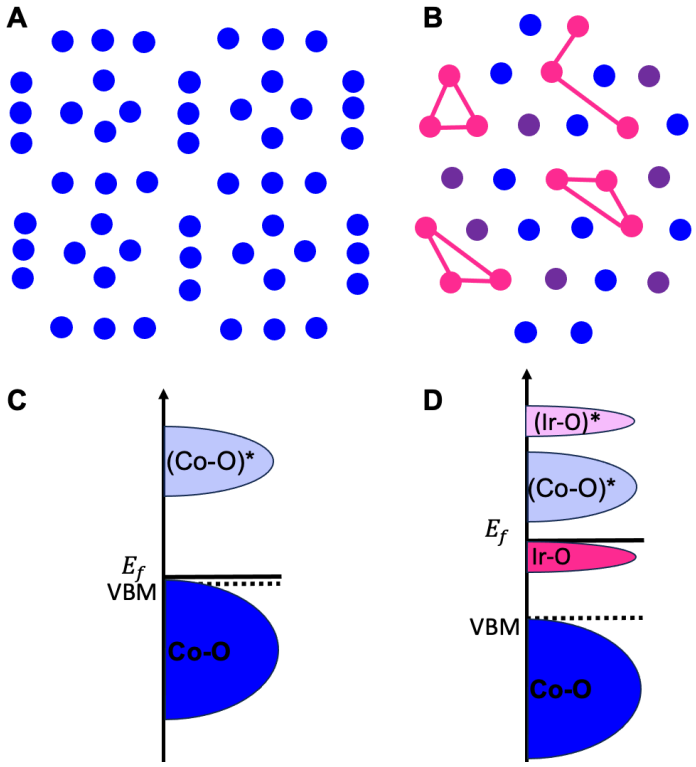

Figure 26: The schematics of (A) represent the precursor cobalt based zeolitic imidazole framework and (B) the structural modification through Ir ion incorporation with correlated sites indicated. The corresponding Density of States diagrams are shown in (C) and (D) and reveal the formation of Ir 5d-O 2p states near the Fermi level upon Ir substitution. Figures of Shan et. al.[201]

The activity was also found to be greater than Ir single atoms adsorbed onto a Co_3O_4 support without spatial correlation. Moreover, the electrocatalysis was proposed to proceed through the electrochemical oxide path mechanism, proposed by Antolini[203]. Chronopotentiometry at a current density of 10 mA/cm^2 showed 200hrs of continuous OER electrocatalysis. Liang et. al. further showed that incorporating

iridium dopants into strontium titanate perovskites could activate the titanium electronic states towards surface oxygen adsorption[204]. The intrinsic activity of the catalyst, calculated by normalizing the catalytic current by the electrochemical surface area, was found to be 26 times that of commercial IrO_2 under acidic conditions. Thus the structural flexibility afforded by correlated single atom catalysts could provide an additional metal-metal interaction with the means to manipulate the electronic states of the active site to promote selective adsorbate binding. The novelty of these discovered electrocatalytic topologies enriches the potential development of potent electrocatalysts and requires an ingenuity to tailor the active sites with a coordination environment that can achieve the desired selectivity by preferentially stabilizing the intermediates and the respective transition states of the adsorbate evolution mechanism of the OER for improved stability of the catalyst, or promote the -Cl adsorbate pathway of the CER to achieve the desired selectivity at the anode to advance the potential of direct seawater electrolysis.

The characteristically high OER activity of Ru catalysts is thought to arise from its modulable redox state. The electrocatalytic activity of single atom Ru sites were shown to be electronically augmented by incorporating a compressive strain induced by the lattice mismatch of the surrounding Pt-rich coordination environment, which shifted the d-band center εRu-d towards the Fermi level, optimizing the binding the OER reaction intermediates as shown in Figure 27[26].

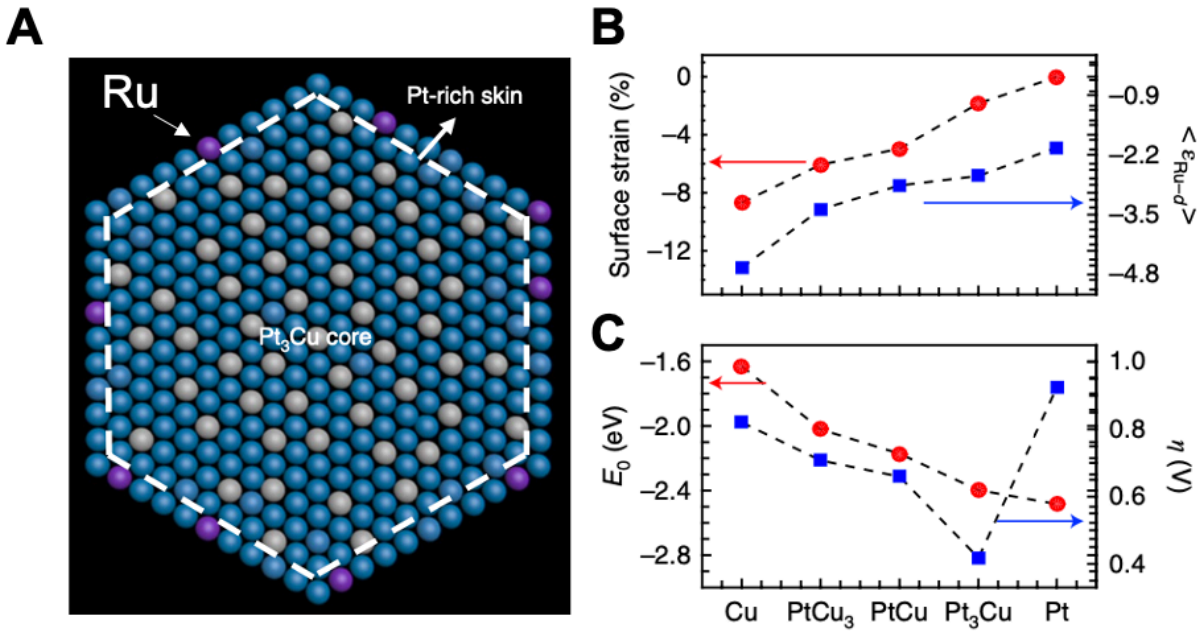

Figure 27: (A) Representative atomic schematic of the most potent Ru_1-Pt_3Cu electrocatalyst in a series of PtCu alloys with the position of the Pt in blue, the Cu in grey, and the Ru in purple determined through elemental mapping of the HAADF image. (B) indicates the shifting of the $\varepsilon_{Ru\text{-}d}$ towards the Fermi level in blue squares as the in-plane lattice contraction relative to a pristine Pt (111) surface in red circles decreases. (C) Indicates the corresponding absorption energy (E_0) of the oxygen

adsorbate and the overpotential (η) resolved through DFT theoretical analysis. Figures of Yao et. al.[26]

ATR-IR measurements further detected the presence of the -OOH intermediate suggesting the Ru sites catalyzed the OER through the AEM mechanism, which ensured stability while also requiring an overpotential of just 220 mV to achieve the metric current density of 10mA / cm^2 under acidic conditions[26]. In situ XAFS and XPS measurements also revealed the transfer of electrons towards the Ru atom, indicating possible charge compensation that prevented the over oxidation of the Ru atom and its subsequent dissolution[26]. Similar redox shifts were seen by Liu et. al. who embedded Ru single atoms in an oxygen coordinated metal organic framework nanosheet shown in, which downshifted the bonding Ru_{3d} band center towards the bonding O_{2p} band and weakened the chemical bonding between the Ru active sites and the -Cl^- adsorbate of the CER more so than the -OH adsorbate of the OER[205]. This refinement decreased the Gibbs Free Energy change of the potential determining step of the proposed CER mechanism, the second Heyrovsky step accompanying the formation of the molecular chlorine, which enabled the reaction to proceed with a lower overpotential than the OER[205]. The material demonstrated an overpotential of just 30mV to catalyze the CER at a current density of 10 mA/cm^2 in 1M NaCl and pH = 1, current densities of 1000mA/cm^2 were further shown to be maintained for >1000 h with a Cl_2 selectivity of >98% in simulated seawater[205].

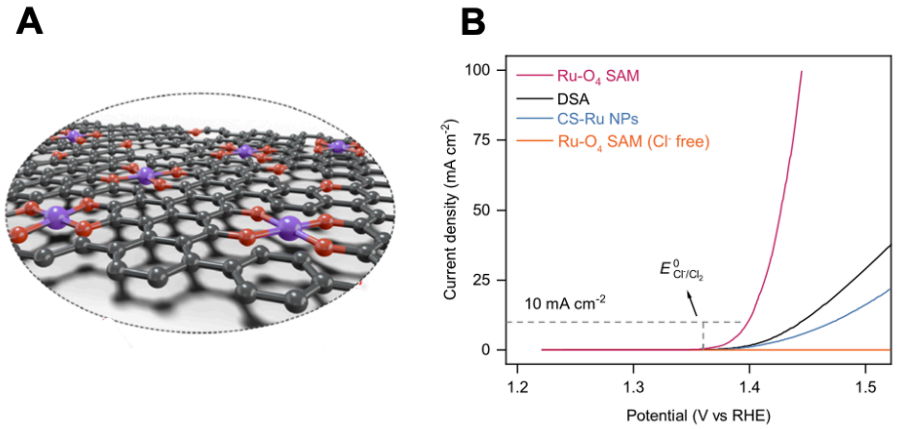

Figure 28: (A) Schematic of the synthesized RuO_4 single atom moieties (SAM) with ruthenium in purple, oxygen in red, and carbon in grey. (B) Polarization curves of the Ru-O_4 SAM, the commercial DSA, carbon-supported Ru nanoparticles, and the Ru-O_4 SAM in a solution free of chloride ions. The scan rate was 5 mV/sec and the rotation rate was 1600 rpm within a 1 M NaCl solution at pH = 1. The DSA wasn't stirred, and the chloride free solution consisted of 1 M $NaClO_4$. Figure of Liu et. al. [205]

Moreover, this overpotential is less than the 85 mV reported for commercial DSA, which also has a recorded Cl_2 selectivity of 95.5%. Thus a strategy that modulates the valence of single atom Ru and the relative energies of its d-band centers through optimization of the coordination environment could enable selective binding of the CER or OER intermediates and the preferred gas evolving reaction at the anode.

Table 2: Studied electrocatalysts probed for respective CER and OER activities. (NS) indicates not specified, (UD) is undetermined, (N/A) is not applicable, (K) is Khrishtalik, (V-H) is Volmer Heyrosky, (AEM) is Adsorbate Evolution Mechanism, (LOM) is Lattice Oxygen Mechanism.

Active Site	Crystal Structure	Probed Plane	(+) Substitution (-) Vacancies	Probed Reaction	Preferred Mechanism	Ref.
Ru (CUS)	Rutile RuO_2	101	N/A	OER and CER	V-H (-OCl)	165
Ru (CUS)	Rutile RuO_2	101	N/A	OER and CER	V-H (-OCl)	91
Ru (CUS)	Rutile RuO_2	001	N/A	OER and CER	AEM	91
Ru (CUS)	Rutile RuO_2	110	(+) Ir or Cr	OER	AEM	166
Ru (CUS)	Rutile RuO_2	110	Top Layer TiO_2	OER and CER	V-H (-OCl)	167
Ti (CUS)	Rutile TiO_2	110	(+) Ru	CER	V-H (-OCl)	168
UD	Rutile RuO_2	NS	(+) Ti	CER	NS	172
Ru (CUS) and Mn (CUS)	Rutile RuO_2	NS	(+) Mn	OER	AEM	173
NS	Rutile RuO_2	NS	(+) Zn	OER	LOM	175
Ru (CUS)	Rutile RuO_2	NS	(+) Ni	OER	AEM	176
Ru (CUS)	Rutile RuO_2	110	(+) 2 Ni	OER	AEM	119
Ru (CUS)	Rutile RuO_2	110	(+) 6 Ni	OER	LOM	119
Ru	$Pb_2Ru_2O_{7-x}$	NS	(-) O	OER	AEM	179
Ru	$A_2Ru_2O_7$	NS	(-) A = Y, Nd, Gd, Bi	OER	AEM	183
Ir-O	IrNi@IrO_x	N/A	(-) Ni	OER	LOM	184
Ru	2D TiO_x	N/A	N/A	OER and CER	V-H (-Cl)	186
Pt-N_4	CNT	N/A	N/A	OER and CER	V-H (-OCl)	189
Ir	Co_3O_4	N/A	N/A	OER	ECOP by Antolini [213]	191
Ru	Pt_3Cu	N/A	N/A	OER	AEM	47
Ru	MOF	N/A	N/A	OER and CER	V-H (-Cl)	195

I.4.3 In-Situ Filtration

The evolution of chlorine may also be impeded by arresting the species transport of the chloride ions towards the anode. Strategies such as the application of an electrochemically inert coating layer with an optimized thickness that selectivity

mitigates the respective concentrations of the desired reactants and products at the buried interface, and renders a physical stability resistant to delamination; the incorporation and synthetic linkage of electrostatic repelling polyanion moieties; the degree of crystallinity of electrocatalytic surfaces; and the placement of a gas-permeable, hydrophobic membrane between the seawater and the anode have all been designed to impede the species transport of the chloride ion and selectively evolve oxygen at the anode during seawater electrolysis.

Initially implemented by Bennett, a layer of MnO_2 was electrochemical deposited onto a DSA substrate and shown to evolve oxygen from seawater with 99+% efficiency[206]. He further proposed that the coating layer prevented the diffusion of chloride ions, creating a polarized concentration gradient. Subsequent studies by Fujimura et.al. deposited MnO_2 on an IrO_2-coated titanium plate with 13 mol % molybdenum; the film was found to consist of a single phase of δ-MnO_2 that only slightly reduced the activity towards oxygen evolution while improving the durability of the material to reach an OER efficiency of 98.5% for over 1,500 h in pH = 12 at 1,000 A/m[274]. Further additions of tungsten were conducted by Habazaki et. al., who found the manganese-molybdenum-tungsten oxide anodically deposited on an IrO_2-coated titanium improved the activity of the electrode towards the OER [207]. Moreover, additions of iron by Ghany et.al. to an Mn-Mo oxide anodically deposited on an IrO_2 coated Ti substrate was shown to improve the stability of the material at higher temperatures while maintaining 100% OER efficiency[208].

Intrigued by the impressive OER selectivity characteristic of these manganese oxide based overlayers, Vos et. al. electrochemically grew a thin film (5 - 20nm) of MnO_x on a GC disk electrode with a IrO_x catalytic layer and used rotating ring-disk electrode voltammetry to discover that the selectivity for the CER at 30mM Cl^- decreased from 86% to 7% in the presence of the MnO_x overlayer, though with a 45% drop in activity for the OER[209]. The morphology of the overlayer consisted of a porous structure of intertwined, amorphous sheets of δ-MnO_2 with a thickness of 8 - 10nm that were thought to be electrochemically inert and instead impeded the species transport of the chloride ion while remaining permeable to H_2O, H^+, and O_2 as shown in *Figure 29*[209]. Thus at the buried interface between the MnO_x and the IrO_x catalytic layer, the diffusion coefficient and concentration gradient of the chloride ion are decreased, increasing the diffusion layer thickness and the overpotential required for the chlorine evolution.

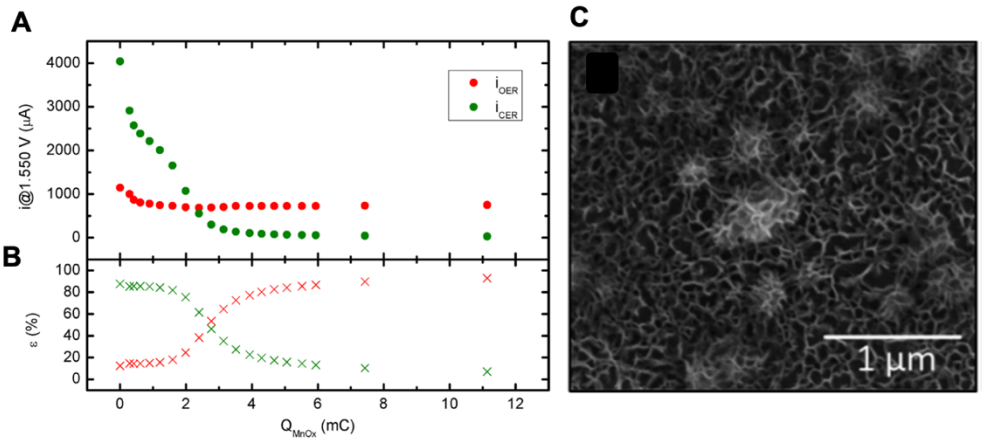

Figure 29: (A) OER and CER recorded currents at 1.550 V calculated with the rotating ring disk electrode indicating a drop in CER currents as the charge (Q) characteristic of the MnO_x layer thickness is increased, a 45% decrease in the OER activity is also evident. (B) The equivalent selectivities of the OER and the CER as a function of the charge of the MnO_x layer. (C) SEM image of thin, porous sheets of MnO_x deposited on the IrO_x / GC electrode. Figure of Vos et. al.[209]

Beatty et. al. initiated a study of the structure-property relation of the buried interface; the induced confinement effects may indeed affect the steric, chemical, and electronic properties of the mechanistic intermediates and may enable an addition means of tuning the activity and selectivity of the desired reaction[210]. Different thicknesses of SiO_2 overlayers were grown on Pt substrates of varying thicknesses. Silica is considered more thermodynamically stable in acidic and neutral solutions under a wider range of applied potentials than manganese oxide[211]. Through measurements of the hydrogen underpotential deposition (H_{upd}) by cyclic voltammetry, the peak in the voltammogram at +0.26 V RHE typically associated with Pt (100) terraces could be found for the 4.6 nm SiO_x overlayer on thick Pt substrate, though was greatly suppressed in the voltammograms of the bare Pt control and the 1.4 nm SiO_x overlayer thickness, and skewed in the 10.3 nm SiO_x overlayer due to slow proton diffusion through the overlayer, indicating that the Pt crystal orientation and densities of the crystalline defects can be modulated by the thickness of the overlayer, providing a potential means to select for the CER or OER[210]. Moreover, the thickness and composition of the Pt oxide interlayer, shown to be grown between the SiO_x overlayer and the Pt thin film through XPS measurements, was found to be tunable by adjusting the thicknesses of the SiO_x overlayer and Pt/Ti substrates; these characteristics were furthermore found to dictate electrochemical properties, the stability of the SiO_x overlayers, and the HER performance[210]. Indeed, a reduction in the thickness of the interlayer can rupture the steric environment between the interlayer and the silica overlayer, even affecting the potential mechanism. Robinson et. al. moreover found that application of SiO_x overlayers on a platinum thin film disposes adjacent silanol groups at the Pt active centers that can facilitate the oxidation of the CO intermediates that have adsorbed onto Pt to CO_2, advancing the potential of fuel cells that directly utilize alcohols[212].

To thus further the applicability of silica overlayers towards selective OER catalysts, Bhardwaj et.al. applied a SiO_x overlayer on a thin Pt film electrode; the 4.8-8.7 nm overlayer thicknesses demonstrated a three order of magnitude decrease in the Cl^- permittivity when compared to aromatic polyamide membranes utilized in reverse osmosis water desalination membranes as shown in **Figure 30**[21].

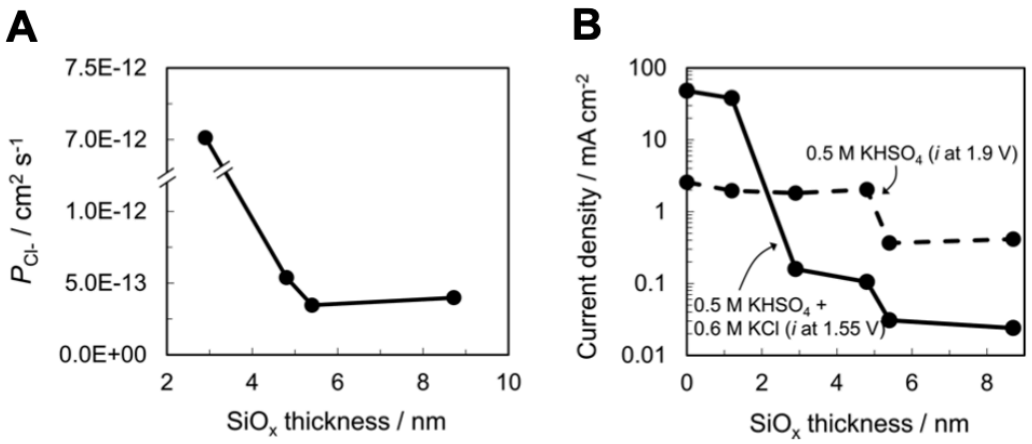

Figure 30: (A) Calculated permeability of Cl- through an SiO_x overlayer deposited on Pt thin film electrocatalyst as a function of the SiO_x overlayer thickness as determined through linear scanning voltammetry in 0.5 M $KHSO_4$ + 0.6 M KCl. (B) The current densities recorded during linear scanning voltammetry at +1.90 V vs. RHE in 0.5 M $KHSO_4$ in the dotted curve and at +1.55 V vs. RHE in 0.5 M KHSO4 + 0.6 M KCl in the solid curve. Figure of Bhardwaj et. al.[21]

The selective transport arresting mechanism was proposed to be the additional energy required to rearrange the bonds of the hydration sphere surrounding the chloride ion, which required removal to permeate the free volume elements within the SiO_x overlayer, determined by ellipsometric porosimetry measurements and XPS analysis to have Si-Si nearest neighbor distances of ~4.6 Å[21]. Indeed, the hydrated diameters of the Cl^- ion has been measured to be 6.5 Å[213]. Vos et. al. furthered this study by also applying the SiO_x overlayers on amorphous iridium oxide nanoparticles and iridium mixed-metal oxides deposited on a Ti support and found the morphology of the underlayer and its synergy with the overlayer to be of crucial importance towards achieving both a selective and stable electrocatalytic design[214]. Microscopic defects and irregularities in the IrO_x nanoparticle substrate indeed affected the electrocatalytic selectivity towards the OER and no correlation between the overlayer thickness and OER selectivity could be found[214]. Silica overlayers applied on the mixed metal substrate appeared to decrease the activity for both the CER and the OER, though were more favorable towards the OER with prolonged integrity maintained during a potentiodynamic electrolysis evaluation[214].

Iridium oxide coated titanium substrates have also been hot pressed with the cation selective perfluorosulfonic acid polymer Nafion®[215]. Though achieving lower current densities, applying a Nafion-117 membrane (H^+-form) onto the coated electrode allowed water to permeate while electrostatically repelling the chloride ions and led to nearly 100% oxygen selectivity at pH = 8.3. A similar sieving mechanism

with the use of the anionic backbone of sulfonated polystyrene-block-(ethylene-ran-buylene)-block- polystyrene polymer (S-PSEBS) was applied to coat an IrO_2/Ti anode with an electrostatically Cl^- repelling layer[216]. The sulfonated form of the S-PSEBS polymer, with a hydrophilicity that enables the species transport of water molecules, was shown to increase the oxygen evolution efficiency to 94% and decrease the chlorine evolution efficiency to 6% at 100 mA/cm^2 at pH = 8.3.

Selective electrocatalysts have also been designed for alkaline conditions with a graphene oxide overlayer that was electrodeposited with iron hydroxide onto an annealed, porous nickel foam that had been subjected to a hydrothermal deposition of Ni-Co hydroxide as shown in *Figure 31*[217]. The electrocatalyst was able to reach current densities of 1 A / cm^2 under alkaline conditions below overpotentials reaching 480 mV and thus before the evolution of hypochlorite becomes thermodynamically possible[217]. The graphene oxide overlayer was shown to improve the resistance to corrosion caused by the chloride ion, and moreover improve the OER activity both by decreasing the size of the FeOOH nanoparticles, and thus improving their interaction with the Ni-Co hydroxide underlayer, and by decreasing the charge transfer resistance of the material, and thus improving its electrical conductivity[217].

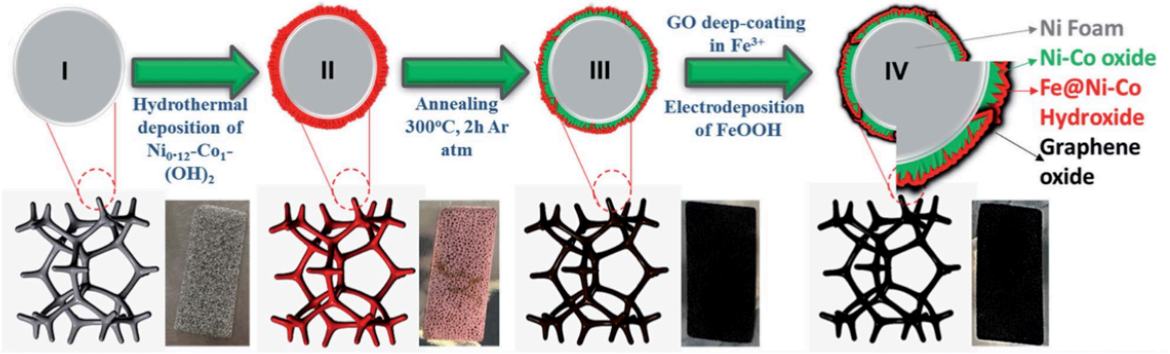

Figure 31: Schematic depiction of the FeOOH deposited on β-Ni-Co hydroxide with a graphene oxide outer layer. Figure of Jadhav et.al.[217]

Kitiphatpiboon et. al. found that by submerging a nickel foam that had been oxidized to form $NiFe(OH)_x$ along its surface into an 0.1M Na_2S solution for sulfur integration, the stability of the electrode could be improved by the intercalation of sulfate ions, which could block the species transport of the chloride anions[218]. The sulfur doping was also shown to improve the conductivity between the active sites on $FeNiS_x$ and $NiFe(OH)_x$[218]. A strategy that prepared porous N-$NiMo_3P$ sheets with negatively charged surface polyanions such as nitrates and phosphates also protected the electrode from the chlorine chemistry[219]. Alternatively, Obata et. al. utilized anodic deposition to apply a CeO_x overlayer onto an Au substrate that had been coated with $NiFeO_x$ through conventional cathodic deposition and found that the overlayer prevented dissolution of the active Fe species and selectively impeded the chloride ion through an electrostatic interaction [220]. With an isoelectric point of 7, CeO_x is expected to be negatively charged under alkaline conditions[220]. Its hydrous, disordered structure was proposed to enable the diffusion of OH^- to the $NiFeO_x$ catalyst on the Au substrate, promoting an OER overpotential shown to be less than the onset of the hypochlorite redox potential[220,221].

Interestingly, a hollow nanocubic electrocatalyst composed of Ir-doped Ni-Fe-Zn Prussian blue analogs was demonstrated to manifest abundant amorphous-crystalline interfaces (ACI) that were indicated to be in-situ passivated with carbonate anions after prolonged electrolysis in an alkaline seawater electrolyte[222]. These carbonate anions were proposed to protect the electrocatalyst against chloride corrosion by repelling the negatively charged chloride anions. The synthesized hollow nanocubes were further shown to have a higher catalytic activity than commercial IrO_2 in alkaline, alkaline seawater, and acidic electrolytes that was proposed to be facilitated by the heterogeneity of atomic arrangements at the ACI surface as shown in *Figure 32*[222]. The Zn was however shown to be completely leached out under acidic conditions, though a synergy between the Ni, Fe, and Ir at the surface of the nanocubes was supposed to preserve the ACI during water oxidation.

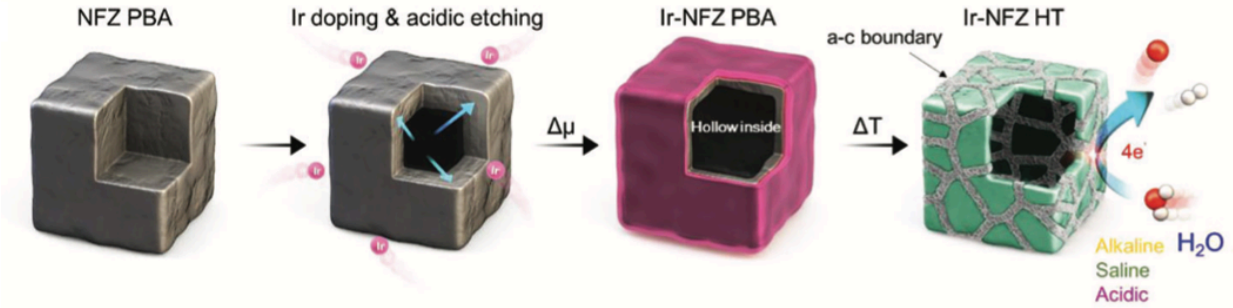

Figure 32: Schematic representation of the synthetic route utilized to generate the numerous amorphous-crystalline interfaces on the Ir-NFZ HT nanocube. Figure of Han et. al.[222]

Xie et. al. further designed a hydrophobic, porous polytetrafluoroethylene (PTFE) based membrane permeable only to gases that encompassed the anode and sandwiched a concentrated KOH solution, termed a self-dampening electrolyte, that provided a water vapor pressure gradient driving the evaporation and diffusion of water vapor from the seawater across the PTFE membrane towards the catalyst at the anode as shown in *Figure 33*[223]. Current densities of 250 mA/cm^2 with an operational lifetime of over 3,200 h were achieved[223].

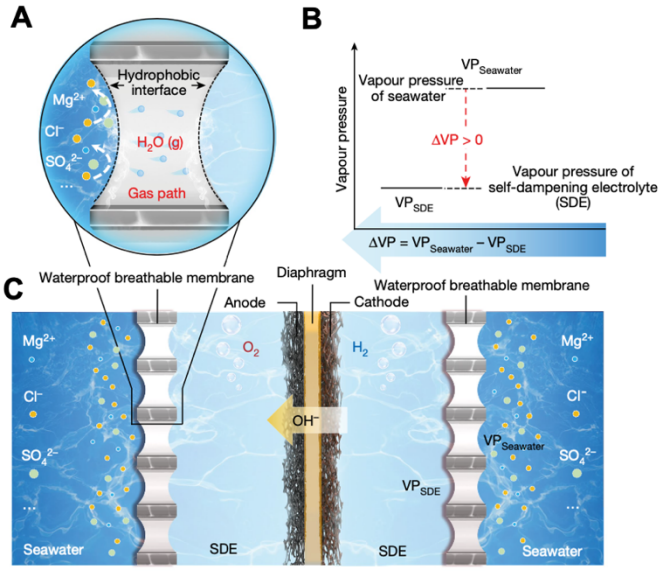

Figure 33: (A) Schematic of the hydrophobic porous polytetrafluoroethylene (PTFE)-based waterproof breathable membrane permitting the selective diffusion of water vapor while remaining impermeable to impurity ions and seawater. (B) Representation of the driving force created for water vapor diffusion through application of a self-dampening electrolyte. (C) Depiction of the orientation of the membrane and the electrolyte with respect to the anode and the cathode. Figure of Xie et. al.[223]

The use of the membrane within the electrolyzer unit itself could moreover act as a filtering mechanism to prevent the movement of the chloride ion towards the anode. Though an asymmetric electrolyzer design, Shi et. al. introduced natural seawater into the cathode compartment and a hydroxide solution into the anode compartment; the species transport of the chloride ion was impeded from approaching the anode through the placement of a sodium ion exchange membrane[224]. The Ni-Fe-P nanowires anchored with atomically dispersed Pt at the cathode accelerated hydrogen evolution through a DFT calculated energy barrier reduction of 0.26 eV in natural seawater[224].

I.4.4 Augmenting the Conductivity

By manipulating the surface structure of the catalyst, an augmentation in the conductivity may be realized, which may indeed lower the overpotential required to effectuate the OER and enable selectivity against the CER to be achieved under acidic conditions. Conductivity is related to the concentration of mobile electronic carriers such as electrons, holes, and ionic point defects occupying lattice atomic positions such as vacancies, interstitials, and substitutional solutes as well as impurities[225]. Indeed, removing oxygen atoms through mechanisms such as the Mars-van Krevelen leaves excess electrons either delocalized through a metallic state or localized within a polaronic state[226]. The mobility of these electronic carriers is defined as the velocity of the entity per unit driving force and is directly proportional to the diffusion coefficient according to the Nernst-Einstein relation. In addition, electrons and holes in metals, semiconductors, and high-mobility ceramics are subject to a drift velocity that is much

less than the instantaneous velocity of random particle movements. Their mobility is inversely proportional to their effective mass, which considers the interaction between the charge carrier and the lattice potential[225]. This polaronic interaction may be large, which indicates a weak interaction between the carrier and the ion and a small effective mass, or strong resulting in large polarons in which the motion of electrons and holes must occur through a thermally activated hopping mechanism and can reduce mobility[225]. Kim et. al. synthesized an IrO_2 shell encasing a metallic iridium core by rapidly dealloying osmium from an $Ir_{25}Os_{75}$ alloy under highly acidic conditions[121]. A decrease in overpotential for the $Ir_{25}Os_{75}$ core-shell thin film when compared to a synthesized $Ir_{50}Os_{50}$ nanoparticle at high current densities is shown in *Figure 34a*, which was attributed to the measured increase in conductivity [121]. The conductivities of the 3D-interconnected, porous $Ir_{25}Os_{75}$ core-shell thin film and the $Ir_{50}Os_{50}$ nanoparticles, proposed to be highly oxidized and consisting of many insulating oxide interfaces, were quantified through measurements of the carrier mobility and carrier density with 4-probe van der Pauw measurements[121]. The interconnected heterogeneity of a metallic core oxide shell structure could indeed create additional undercoordinated sites that induce alterations in the local geometries, the electronic structures, and additional defect sites that can be manipulated to tailor the electrocatalytic properties of the surface[226].

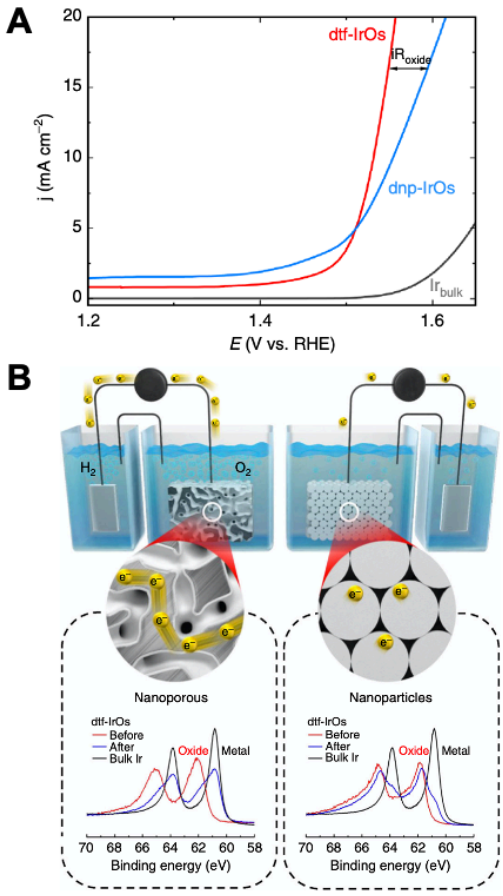

Figure 34: (A) Linear sweep voltammogram with a rotating disk electrode in 0.1 M $HClO_4$ showing the polarization curves of the $Ir_{25}Os_{75}$ core-shell material (dtf-IrOs) and

$Ir_{50}Os_{50}$ nanoparticle (dnp-IrOs). (B) A depiction of the effect of numerous, insulating oxide interfaces on the conductivity of the material; the oxides layers were quantified through XPS sputter etching experiments. The XPS experiments for the dtf-IrOs material indicated on the other hand the presence of an Ir-metallic core. Figure of Kim et. al.[121]

Indeed, induction of polaronic interactions with the CO adsorbate in the rutile titanium dioxide (110) was shown to significantly affect its adsorption energy and the polaronic ground state of the system; CO adsorption was shown to promote polaron transfer from subsurface to surface sites[227]. Probed through analysis of the polaron formation energy, or the electronic energy gained by phonon-electron coupling balanced the energy lost to local lattice distortions, the CO adsorbate was shown to not only reduce the energy cost to form the polaron though also was found to bind most favorably at a titanium atom site with a polaron just below[227].

Stoerzinger et. al. manipulated the degree of epitaxial strain within a $LaCoO_3$ thin film grown through pulsed layer deposition on insulating substrates of different thicknesses and found the degree of tensile strain to influence the electrical conductivity and observed activity towards the OER; deviations in the local symmetry were proposed to affect the number of defects sites and the charge transfer resistance, and moreover to decrease the Co-O bond distance and increase the strength of the adsorbed bond to oxygen[228]. Engineering these defects were moreover shown to dramatically improve the OER performance of a Co-doped nanorod-like RuO_2 electrocatalyst; the low oxidation state of the Co dopant required less O^{2-} in the RuO_2 lattice and thus yielded oxygen vacancies, as evidenced through X-ray photoelectron spectroscopy analysis[229]. The oxygen vacancies were proposed to improve not only the electrical conductivity of the materials though also augment the number of active sites, and moreover participate in the LOM mechanism, calculated to be the lowest free energy path according to DFT simulations[229]. Overpotentials of 169 mV for the OER under acidic conditions were achieved with stable chronopotentiometry measurements for over 50 h at 10 mA/cm[2229]. Thus strategies that implement designs to elevate the conductivity of the electrocatalyst at the active site through formation of point defects and manipulation of the electronic structure have the potential to tune the binding of the preferential intermediate and moreover promote the activity of the material without depreciating the inherent stability.

I.4.5 Self-Healing Catalysts

Tuning the catalytic active site and the reaction mechanism selectivity is indicated within to be quite challenging through heterogeneous electrocatalysis of PGM metals. Though the high anodic potentials required to effectuate the OER and the resulting harshly acidic environment has generally required a characteristically robust catalyst such as a heterogeneous catalyst composed of PGM metals in PEMWE technology[230]. Indeed, oxides of earth-abundant metals are basic according to the Lux classification of bases, and thus readily react with acid and corrode through leaching and dissolution[231]. Implementation of molecular electrocatalysts to facilitate the OER can on the other hand enable the structure-activity relationships and reaction mechanisms to be finely tuned through manipulation of the ligand design[230]. However, most of the ligand design optimizations to impart selective activity of the metal center

such as metathesis, transfer dehydrogenation, C-H activation and functionalization, and cross coupling bond formation have been developed under reductive conditions, requiring the development of ligands stable to oxidative transformations[232].

One approach to catalyst design can be the development of molecular electrocatalysts which undergo self-healing, the characteristic ability to reform from a self-assembly process[233]. If the equilibrium for self-assembly energetically lies within that of the OER catalysis, overall corrosion of the catalyst can be avoided[233]. Indeed, regeneration will occur if the catalyst can self-assemble at applied potentials lower than the potentials required to effectuate the OER. If a greater dependence on the proton concentration through calculation of its reaction order within the mechanism is moreover found for the self-healing catalyst than for the catalysis of the OER, pH adjustments can be utilized to selectively tune the propensity towards self-assembly while maintaining catalytic functionality[233]. Huynh et. al. electrodeposited manganese oxide (MnO_x) onto an FTO working electrode and determined its catalytic rate law for the OER through assessments of the Tafel slopes and the reaction order with respect to the proton concentration at acidic and basic pH values[234]. Reformulations of the Tafel plots to a single potential (E) vs. pH plot, shown in **Figure 35**, with an additional MnO_x deposition trace under acidic[235] and slightly basic conditions[236] enabled a prediction of the pH conditions in which catalyst regeneration subsides and a net dissolution of the film commences[234]. The self-healing property of the MnO_x catalytic film, shown to evolve through the disproportionation reaction of two Mn^{+3} ions, was indeed indicated to uphold until a pH of 0 was approached.

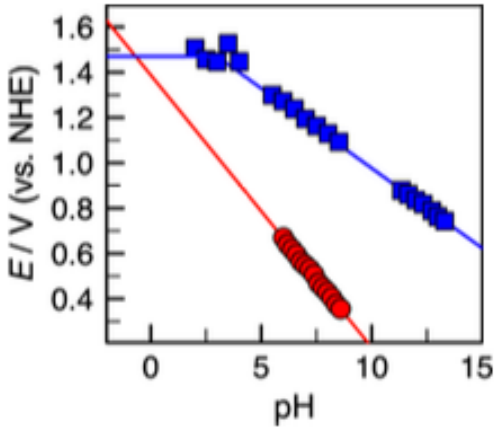

Figure 35: The potential required for the evolution of oxygen on MnO_x (blue squares) as a function of the pH showing a zero-order dependence on the proton concentration under acidic conditions and the inverse first-order dependence in the alkaline regime. The red trace indicates the fourth-order dependence of MnO_x deposition on the proton concentration under acidic and near neutral pH regimes that were divulged from the literature. The concentrations of Mn^{+2} under both measurements are comparable. Figure of Huynh et. al.[234]

Surendranath et. al. further showed that cobalt phosphate (CoP_i) was capable of self-healing; electrodeposition of the oxidic metallate onto a FTO electrode achieved an O_2 faradaic efficiency of near 100% in neutral salt water[237]. The high

activity of this catalyst towards the OER in neutral pH conditions was further proposed to improve the selectivity against the CER, which according to the Pourbaix analysis discussed above, becomes thermodynamically unfavored as the pH increases and the OER becomes more thermodynamically preferred[238]. Though more importantly, selectivity against the CER was shown to be achieved by engaging the kinetic competition between the water and chloride ion through exposure of the catalytic edge sites of the metallate cluster present in the CoP_i complexes[238]. The large disparity between the concentration of water and that of chloride ions in solution can promote the substitution of P_i for water to initiate the O-O bond formation. The effectiveness of this strategy to achieve selectivity is seen in *Figure 36*, where differential electrochemical mass spectrometry (DEMS) was used to determine the quantities of oxygen and chlorine evolved at pH = 7.

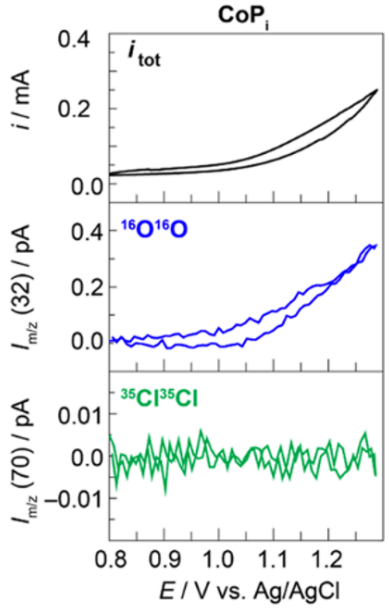

Figure 36: The top panel is a cyclic voltammogram of CoP_i in an aqueous solution of 100mM KP_i and 500mM NaCl at a scan rate of 5mV/s. The middle and bottom panels are the DEMS results for the evolved oxygen and the evolved chlorine, respectively. Figure of Kean and Nocera[238].

The presence of phosphate in the solution was moreover shown to decrease the faradaic efficiency for the CER through both its buffering effect and ability to associate with oxide surfaces through an inner-sphere mechanism and form a negatively-charged electrically repelling layer[239]. Applying the ingenuity of this advancement towards the design of heterogeneous electrocatalysts selective for the OER that are imbued with the propensity for self-healing under acidic conditions would engender a robust solution for PEMWE technology.

I.4.6 Modifying Seawater Electrolyser Designs

Implementing the use of seawater into current water electrolyser designs has been facilitated at present both through indirect methodologies and direct, asymmetric electrolyser designs. Veroneau and Nocera discussed an initial forward osmosis (FO)

step in which the splitting of water would provide the concentration gradient and driving force for the selective movement of water through a membrane impermeable to sea salts[38]. Further operating at the elevated temperatures of solid oxide water electrolysers enables the sea salts to remain while water vapor is split into its hydrogen and oxygen constituents; Liu et. al. reported no significant degradation to the cell after 400 hr of operation with the use of untreated seawater[240].

Direct seawater electrolysis at present relies on a design ingenuity that considers the limitations of untreated seawater and anticipates the predicaments that become apparent with the presence of the additional sea salts. Untreated seawater is subjected to local basification at the cathode as water is reduced hydrogen, and the presence of the additional cations in seawater promote local precipitation at the cathode under these basic conditions. Han et. al. utilized a bipolar membrane that provided local acidification within the catholyte, enabling the use of seawater at the catholyte and a 0.1 M NaOH solution at the anolyte within this asymmetric design[60]. Shi et. al. furthered the use of a Na^+ exchange membrane that prevented the transport of the chloride ion dissolved in the seawater catholyte into a 0.1 M NaOH analyte solution, preventing the competition between the CER and the OER at the anode[224]. However, there remains the challenge to address that competition and enable the solicit use of seawater within both compartments of the electrolyser design.

1.5 Conclusions of the Literature

A social-technological crisis has emerged as the energy demands of our increscent societies encroach on limited freshwater reserves. It is urgent to develop the capability of utilizing the abundant reserves of seawater in sustainably driven water electrolysers for the generation of hydrogen. While indirect electrolysis may provide the needed short-term solution, the inevitable additional energy costs will prove absorbent over the long term. The advancement of direct seawater technologies that further the selectivity of the anode may improve wastewater treatments, appeasing the exigencies for water conservation imperative for an increasing percentage of our inhabited world. Though utilizing seawater directly in the current state-of-the-art electrolyser technologies can affect its performance both at the system and stack level by degrading the electrolyser durability. Specifically, the presence of the chloride ion enables the evolution of the toxic and corrosive chlorine gas. Using seawater as an electrolyte can also affect the electrochemically active dimensions of the catalyst and perturb the electrolyte permeabilities, diffusivities, conductivities, and vapor pressure, impacting the current and voltage efficiencies.

Thermodynamic analysis of the Pourbaix diagram for artificial seawater indicates that the competition between the oxygen evolution and chlorine evolution is exacerbated in the acidic medium of PEM electrolysers. Nonetheless, in this condition the highest current densities have been achieved. Butler-Volmer kinetics and Marcus theory clarifies the relation between the thermodynamics and the kinetics of electrochemical reactions, enabling an understanding of the observed chlorine gas evolution at the anode. Despite the greater standard potential of the CER, the reaction proceeds through a single intermediate that enables chlorine evolution to be the kinetic product during seawater electrolysis. The proposed mechanisms of the OER were elucidated and indicated that the LOM mechanism can affect the stability of the

anode. Thus, designing strategies that can promote the AEM mechanism were proposed. However, the elucidated mechanisms of the CER indicated that the relationship between the key intermediates of the CER pathway and the AEM pathway of the OER are linearly correlated. The need to dissect the rate determining step of the preferred pathway is crucial to stabilize transition states to select for the preferred intermediate. This feat could be accomplished perhaps through the development of descriptors that moreover incorporate stability parameters to derive a catalyst at the apex of the volcano curve possessing realistic potency. Indeed, predictions of the best catalysts must thus be developed with a robustness that accounts for the multi-faceted complexity involved in heterogeneous electrocatalysis to devise the most effective system. Overcoming the inherent linear correlations that the proposed AEM pathway of the OER are subjected to is another potential though challenging means of achieving selectivity. The water and chloride reagents were moreover shown to competitively adsorb onto the electrocatalyst surface; the concentration discrepancy between the water and chloride reagents in solution can thus influence the observed evolved gaseous product.

Achieving selectivity at the anode is therefore a formidable challenge. Design strategies that modulate the structure of the electrocatalyst such as optimizing the exposure of the facet with the greatest OER selectivity, introducing point defects in the local chemical environment, and improving the active site density are ongoing. Indeed, further implementing the design of correlated single atom catalysts could afford the structural flexibility to manipulate the type of atom and its proportion within the first and second coordination shell and optimize the electronic state of the active site to promote selective adsorbate binding. Ruthenium and its modulable redox state greatly diversifies the potential coordination environments and the relative energies of its d-band centers, enabling the optimization of the adsorbate binding. The design of catalysts with greater conductivities may further decrease the observed OER overpotentials. Indeed, the development of heterogeneous electrocatalytic systems with a penchant for self-healing would facilitate the needed stability under the harsh acidic conditions within PEMWE. The most realizable solution may moreover be found to be an in-situ filtration of the chloride ion that arrests its transport and decreases its concentration at the active site of the electrocatalyst. Further insights into the effects of the electrified double layer, and the structural sensitivity of adsorbate binding on the electrocatalysis of the evolved gaseous products may further the efforts to achieve selectivity for the OER at the anode under the perilous acidic conditions and provide a solution as serendipitous as the abundancy of a natural resource such as seawater.

1.6 The State of the Art

The perilous acidic conditions created at the anode by the evolution of the oxygen requires the use of a robust electrocatalyst that can catalyze the intensive, four-step reaction of the OER. An iridium catalyst was thus chosen with a nanocluster morphology consisting of 2-4 nm diameters that increased its active surface area while decreasing the noble metal loading. These nanoclusters are interwoven on a Vulcan carbon support; this electrocatalyst consisted of 10% w/w iridium and 90% w/w Vulcan carbon and is termed Ir10 in the following work. The Vulcan carbon support both

prevents nanocluster aggregation and enables electron conduction. Indeed, this 3D electrocatalytic system is incorporated into an electrocatalytic film consisting of this Ir10 material with a 5% w/w solution of Nafion in 1-propanol and water and additional Vulcan carbon to improve the electrical conduction towards the glassy carbon electrode on which the film is drop casted.

Careful contemplation of the three-dimensional nature of this electrocatalytic system encourages an in-situ filtration design of the chloride ion to prevent its species transport towards the catalytic nanoclusters. Consideration of the materials that enable in-situ filtration reveals a spectrum that ranges from flexible polymeric membranes towards rigid molecular sieving materials. Recognizing that rigid molecular sieving materials impart additional latitude in the separation through their imposed rigid confinements that suppress rotational and even vibrational degrees of freedoms within the coordinating transition state, enabling additional entropic selectivity to be induced. Two molecular sieving materials were considered, silica and Zeolite Imidazole Framework-8 (ZIF-8). Initial morphologies consider a core-shell type structures in which the molecular sieving material encompasses the electrocatalytic Ir10 nanocluster, as shown below in Figure 37.

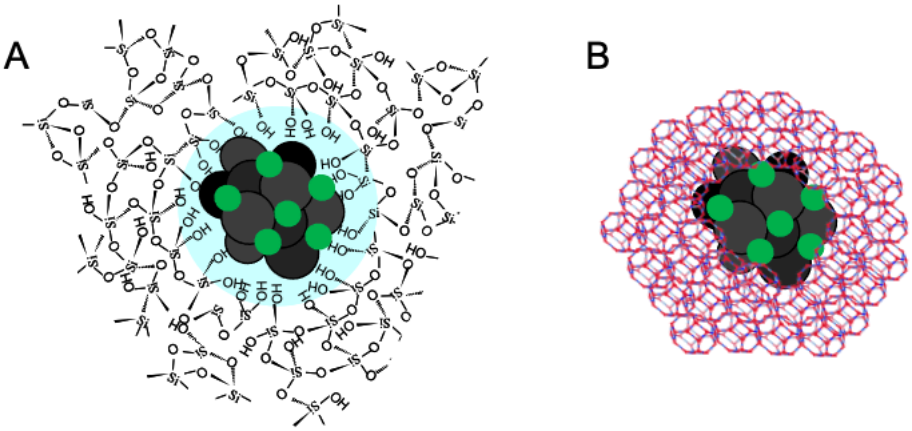

Figure 37: Two proposed core-shell morphologies consisting of (A) a silica and (B) a ZIF-8 molecular sieving overlayer that encompass the electrocatalytic Ir10 nanoclusters.

The following chapters will delineate the effects of the overlayers on the electrocatalytic oxidation of the preferred water reactant and evidenced suppression of the chlorine evolution reaction. Optimization of the consistency of the electrocatalytic ink that is drop casted onto the electrode to create the film, augmentation to the chloride ion concentrations that are probed, and development of the electroanalytical protocol to analyze the films will be dissected through subsequent results and discussions. Interpretations proposing the elucidation of the kinetically or diffusional control to which the OER and CER currents that comprise the CER selectivity may be subject upon nanosheet integration further their implementation. These insights instigate perspectives that unravel the major modes of species transport within the electrocatalytic film to improve the integration design of the nanosheets and their synthesis strategy to optimize the long-term stability and robustness towards other ionic constituents within seawater.

I.7 References

1 IEA. Comparison of total final consumption in the IPCC scenarios and in the Net Zero Scenario, 2020-2050. (International Energy Agency, Paris, 2021).

2 IEA. Net Zero by 2050: A Roadmap for the Global Energy Sector. (International Energy Agency, Paris, 2021).

3 Decker, G. L., Gouse, W.S., Gregory, D.P., Hirsch, R.L., Hoffman, K.C., Hoos, I.R., Johnson, J.E., Longwell,J.P., Siri, W.E., Sliepcevich, C.M., Smelt, R. *Hydrogen as a Fuel: A Report*. National Academies Press.(1979).

4 Crisp, D. *et al.* How Well Do We Understand the Land-Ocean-Atmosphere Carbon Cycle? *Rev. Geophys.* **60**, e2021RG000736 (2022). https://doi.org/10.1029/2021RG000736

5 de Levie, R. The electrolysis of water. *J. Electroanal. Chem.* **476**, 92-93 (1999). https://doi.org/10.1016/S0022-0728(99)00365-4

6 Service, R. F. Seawater splitting could help green hydrogen grow. *Science* **379**, 1075 (2023). http://doi:10.1126/science.adh8151

7 Organization, F. a. A. Renewable internal freshwater resources. (2020).

8 Urban, J. J. Emerging Scientific and Engineering Opportunities within the Water-Energy Nexus. *Joule* **1**, 665-688 (2017). https://www.sciencedirect.com/science/article/pii/S2542435117300971

9 Nations, U. United Nations World Water Development Report 2021: Valuing Water. UNESCO 2021. 7, place de Fontenoy, 75352 Paris 07 SP, France. (2021).

10 Millero, F. J., Feistel, R., Wright, D. G. & McDougall, T. J. The composition of Standard Seawater and the definition of the Reference-Composition Salinity Scale. *Deep Sea Res. Part I Oceanogr. Res.* **55**, 50-72 (2008). https://doi.org/10.1016/j.dsr.2007.10.001

11 Yu, H., Wan, J., Goodsite, M. & Jin, H. Advancing direct seawater electrocatalysis for green and affordable hydrogen. *One Earth* **6**, 267-277 (2023). https://doi.org/10.1016/j.oneear.2023.02.003

12 Li, Q. *et al.* Anion Exchange Membrane Water Electrolysis: The Future of Green Hydrogen. *J. Phys. Chem. C* **127**, 7901-7912 (2023). https://doi.org/10.1021/acs.jpcc.3c00319

13 Hausmann, J. N., Schlögl, R., Menezes, P. W. & Driess, M. Is direct seawater splitting economically meaningful? *Energy Environ. Sci.* **14**, 3679-3685 (2021). http://dx.doi.org/10.1039/D0EE03659E

14 Li, D. *et al.* Durability of anion exchange membrane water electrolyzers. *Energy Environ. Sci.* **14**, 3393-3419 (2021). http://dx.doi.org/10.1039/D0EE04086J

15 Li, D. *et al.* Highly quaternized polystyrene ionomers for high performance anion exchange membrane water electrolysers. *Nat. Energy* **5**, 378-385 (2020). https://doi.org/10.1038/s41560-020-0577-x

16 Dresp, S. *et al.* Efficient direct seawater electrolysers using selective alkaline NiFe-LDH as OER catalyst in asymmetric electrolyte feeds. *Energy Environ. Sci.* **13**, 1725-1729 (2020). http://dx.doi.org/10.1039/D0EE01125H

17 Frisch, M. L. *et al.* Seawater Electrolysis Using All-PGM-Free Catalysts and Cell Components in an Asymmetric Feed. *ACS Energy Lett.* **8**, 2387-2394 (2023). https://doi.org/10.1021/acsenergylett.3c00492

18 Carneiro-Neto, E. B., Lopes, M. C. & Pereira, E. C. Simulation of interfacial pH changes during hydrogen evolution reaction. *J. Electroanal. Chem.* **765**, 92-99 (2016). https://doi.org/10.1016/j.jelechem.2015.09.029

19 Katsounaros, I. *et al.* The effective surface pH during reactions at the solid–liquid interface. *Electrochem. Commun.* **13**, 634-637 (2011). https://doi.org/10.1016/j.elecom.2011.03.032

20 Tong, W. *et al.* Electrolysis of low-grade and saline surface water. *Nat. Energy* **5**, 367-377 (2020). https://doi.org/10.1038/s41560-020-0550-8

21 Bhardwaj, A. A. *et al.* Ultrathin Silicon Oxide Overlayers Enable Selective Oxygen Evolution from Acidic and Unbuffered pH-Neutral Seawater. *ACS Catal.* **11**, 1316-1330 (2021). https://doi.org/10.1021/acscatal.0c04343

22 Rossi, R. *et al.* Using a vapor-fed anode and saline catholyte to manage ion transport in a proton exchange membrane electrolyzer. *Energy Environ. Sci.* **14**, 6041-6049 (2021). http://dx.doi.org/10.1039/D1EE02265B

23 Kumari, S., Turner White, R., Kumar, B. & Spurgeon, J. M. Solar hydrogen production from seawater vapor electrolysis. *Energy Environ. Sci.* **9**, 1725-1733 (2016). http://dx.doi.org/10.1039/C5EE03568F

24 Ouimet, R. J. *et al.* The Role of Electrocatalysts in the Development of Gigawatt-Scale PEM Electrolyzers. *ACS Catal.* **12**, 6159-6171 (2022). https://doi.org/10.1021/acscatal.2c00570

25 Minke, C., Suermann, M., Bensmann, B. & Hanke-Rauschenbach, R. Is iridium demand a potential bottleneck in the realization of large-scale PEM water electrolysis? *Int. J. Hydrog. Energy.* **46**, 23581-23590 (2021). https://doi.org/10.1016/j.ijhydene.2021.04.174

26 Yao, Y. *et al.* Engineering the electronic structure of single atom Ru sites via compressive strain boosts acidic water oxidation electrocatalysis. *Nat. Catal.* **2**, 304-313 (2019). https://doi.org/10.1038/s41929-019-0246-2

27 Sohail, M., Lv, W. & Mei, Z. Recent Progress in Ruthenium-Based Electrocatalysts for Water Oxidation under Acidic Condition. *ACS Sustain. Chem. Eng.* **11**, 17564-17594 (2023). https://doi.org/10.1021/acssuschemeng.3c05415

28 Alia, S. M., Stariha, S. & Borup, R. L. Electrolyzer Durability at Low Catalyst Loading and with Dynamic Operation. *J. Electrochem. Soc.* **166**, F1164 (2019). https://dx.doi.org/10.1149/2.0231915jes

29 Faustini, M. *et al.* Hierarchically Structured Ultraporous Iridium-Based Materials: A Novel Catalyst Architecture for Proton Exchange Membrane Water Electrolyzers. *Adv. Energy Mater.* **9**, 1802136 (2019). https://doi.org/10.1002/aenm.201802136

30 Carmo, M. *et al.* PEM water electrolysis: Innovative approaches towards catalyst separation, recovery and recycling. *Int. J. Hydrog. Energy.* **44**, 3450-3455 (2019). https://doi.org/10.1016/j.ijhydene.2018.12.030

31 Shore, L. E. C. Process for recycling components of a PEM fuel cell membrane electrode assembly. (2012).

32 Wang, Z., Zheng, Y.-R., Chorkendorff, I. & Nørskov, J. K. Acid-Stable Oxides for Oxygen Electrocatalysis. *ACS Energy Lett.* **5**, 2905-2908 (2020). https://doi.org/10.1021/acsenergylett.0c01625

33 Ailong Li, H. O., Nadège Bonnet, Toru Hayashi, Yimeng Sun, Qike Jiang, Can Li, Hongxian Han, Ryuhei Nakamura. Stable Potential Windows for Long-Term Electrocatalysis by Manganese Oxides Under Acidci Conditions. *Angew. Chem. Int. Ed.* **58**, 5054-5058 (2019). https://doi.org/10.1002/anie.201813361

34 Moreno-Hernandez, I. A. *et al.* Crystalline nickel manganese antimonate as a stable water-oxidation catalyst in aqueous 1.0 M H2SO4. *Energy Environ. Sci.* **10**, 2103-2108 (2017). http://dx.doi.org/10.1039/C7EE01486D

35 Thorarinsdottir, A. E., Costentin, C., Veroneau, S. S. & Nocera, D. G. p-Block Metal Oxide Noninnocence in the Oxygen Evolution Reaction in Acid: The Case of Bismuth Oxide. *Chem. Mater.* **34**, 826-835 (2022). https://doi.org/10.1021/acs.chemmater.1c03801

36 Blasco-Ahicart, M., Soriano-López, J., Carbó, J. J., Poblet, J. M. & Galan-Mascaros, J. R. Polyoxometalate electrocatalysts based on earth-abundant metals for efficient water oxidation in acidic media. *Nat. Chem.* **10**, 24-30 (2018). https://doi.org/10.1038/nchem.2874

37 Veroneau, S. S., Hartnett, A. C., Thorarinsdottir, A. E. & Nocera, D. G. Direct Seawater Splitting by Forward Osmosis Coupled to Water Electrolysis. *ACS Appl. Energy Mater.* **5**, 1403-1408 (2022). https://doi.org/10.1021/acsaem.1c03998

38 Veroneau, S. S. & Nocera, D. G. Continuous electrochemical water splitting from natural water sources via forward osmosis. *Proc. Natl. Acad. Sci.* **118**, e2024855118 (2021). https://doi.org/10.1073/pnas.2024855118

39 Yang, Z. *et al.* A Critical Review on Thin-Film Nanocomposite Membranes with Interlayered Structure: Mechanisms, Recent Developments, and Environmental Applications. *Environ. Sci. Technol.* **54**, 15563-15583 (2020). https://doi.org/10.1021/acs.est.0c05377

40 Park, H. B., Kamcev, J., Robeson, L. M., Elimelech, M. & Freeman, B. D. Maximizing the right stuff: The trade-off between membrane permeability and selectivity. *Science* **356**, eaab0530 (2017). https://doi.org/10.1126/science.aab0530

41 Geise, G. M., Park, H. B., Sagle, A. C., Freeman, B. D. & McGrath, J. E. Water permeability and water/salt selectivity tradeoff in polymers for desalination. *J. Membr. Sci.* **369**, 130-138 (2011). https://doi.org/10.1016/j.memsci.2010.11.054

42 Caldera, U. & Breyer, C. Learning Curve for Seawater Reverse Osmosis Desalination Plants: Capital Cost Trend of the Past, Present, and Future. *Water Resour. Res.* **53**, 10523-10538 (2017). https://doi.org/10.1002/2017WR021402

43 Becker, H. *et al.* Impact of impurities on water electrolysis: a review. *Sustain. Energy Fuels* **7**, 1565-1603 (2023). http://dx.doi.org/10.1039/D2SE01517J

44 Azevedo, C. D. R. *et al.* Design, setup and routine operation of a water treatment system for the monitoring of low activities of tritium in water. *Nucl. Eng. Technol.* **55**, 2349-2355 (2023). https://doi.org/10.1016/j.net.2023.03.037

45 G. Tsotridis, A. P. EU harmonized protocols for testing of low temperature water electrolysis. European Union.(2021).

46 ISO3696. Water for Analytical Laboratory Use - Specification and Test Methods. 1987).

47 Okampo, E. J. & Nwulu, N. Optimisation of renewable energy powered reverse osmosis desalination systems: A state-of-the-art review. *Renew. Sust. Energ. Rev.* **140**, 110712 (2021). https://doi.org/10.1016/j.rser.2021.110712

48 Farràs, P., Strasser, P. & Cowan, A. J. Water electrolysis: Direct from the sea or not to be? *Joule* **5**, 1921-1923 (2021). https://doi.org/10.1016/j.joule.2021.07.014

49 Lagadec, M. F. & Grimaud, A. Water electrolysers with closed and open electrochemical systems. *Nat. Mater.* **19**, 1140-1150 (2020). https://doi.org/10.1038/s41563-020-0788-3

50 Zheng, W., Lee, L. Y. S. & Wong, K.-Y. Improving the performance stability of direct seawater electrolysis: from catalyst design to electrode engineering. *Nanoscale* **13**, 15177-15187 (2021). http://dx.doi.org/10.1039/D1NR03294A

51 Natishan, P. M. & O'Grady, W. E. Chloride Ion Interactions with Oxide-Covered Aluminum Leading to Pitting Corrosion: A Review. *J. Electrochem. Soc.* **161**, C421 (2014). https://dx.doi.org/10.1149/2.1011409jes

52 Haq, T. u. & Haik, Y. Strategies of Anode Design for Seawater Electrolysis: Recent Development and Future Perspective. *Small Science* **2**, 2200030 (2022). https://doi.org/10.1002/smsc.202200030

53 Zeradjanin, A. R. The era of stable electrocatalysis. *Nat. Catal.* **6**, 458-459 (2023). https://doi.org/10.1038/s41929-023-00973-w

54 Ives, M. B., Lu, Y. C. & Luo, J. L. Cathodic reactions involved in metallic corrosion in chlorinated saline environments. *Corros. Sci.* **32**, 91-102 (1991). https://doi.org/10.1016/0010-938X(91)90065-W

55 Vos, J. G., Venugopal, A., Smith, W. A. & Koper, M. T. M. Competition and selectivity during parallel evolution of bromine, chlorine and oxygen on IrOx electrodes. *J. Catal.* **389**, 99-110 (2020). https://doi.org/10.1016/j.jcat.2020.05.024

56 Geiger, S., Cherevko, S. & Mayrhofer, K. J. J. Dissolution of Platinum in Presence of Chloride Traces. *Electrochim. Acta* **179**, 24-31 (2015). https://doi.org/10.1016/j.electacta.2015.03.059

57 Maril, M. *et al.* Critical aspects in the development of anodes for use in seawater electrolysis. *Int. J. Hydrog. Energy.* **47**, 3532-3549 (2022). https://doi.org/10.1016/j.ijhydene.2021.11.002

58 Kirk, D. W. & Ledas, A. E. Precipitate formation during sea water electrolysis. *Int. J. Hydrog. Energy.* **7**, 925-932 (1982). https://doi.org/10.1016/0360-3199(82)90160-4

59 Dresp, S., Dionigi, F., Klingenhof, M. & Strasser, P. Direct Electrolytic Splitting of Seawater: Opportunities and Challenges. *ACS Energy Lett.* **4**, 933-942 (2019). https://doi.org/10.1021/acsenergylett.9b00220

60 Han, J.-H. *et al.* Direct seawater electrolysis via synergistic acidification by inorganic precipitation and proton flux from bipolar membrane. *J. Chem. Eng.* **429**, 132383 (2022). https://doi.org/10.1016/j.cej.2021.132383

61 Kumaravel, V. & Abdel-Wahab, A. A Short Review on Hydrogen, Biofuel, and Electricity Production Using Seawater as a Medium. *Energy Fuels* **32**, 6423-6437 (2018). https://doi.org/10.1021/acs.energyfuels.8b00995

62 Belila, A. *et al.* Bacterial community structure and variation in a full-scale seawater desalination plant for drinking water production. *Water Research* **94**, 62-72 (2016). https://doi.org/10.1016/j.watres.2016.02.039

63 Debiemme-Chouvy, C. & Cachet, H. Electrochemical (pre)treatments to prevent biofouling. *Curr. Opin. Electrochem.* **11**, 48-54 (2018). https://doi.org/10.1016/j.coelec.2018.07.006

64 Slauenwhite, D. E. & Johnson, B. D. Bubble shattering: Differences in bubble formation in fresh water and seawater. *Journal of Geophysical Research: Oceans* **104**, 3265-3275 (1999). https://doi.org/10.1029/1998JC900064

65 Zhang, Z., Liu, W. & Free, M. L. Phase-Field Modeling and Simulation of Gas Bubble Coalescence and Detachment in a Gas-Liquid Two-Phase Electrochemical System. *J. Electrochem. Soc.* **167**, 013532 (2020). https://dx.doi.org/10.1149/2.0322001JES

66 Tourneur, J., Joanny, L., Perrin, L., Paul, S. & Fabre, B. Efficient and Highly Stable 3D-Printed NiFe and NiCo Bifunctional Electrodes for Practical HER and OER. *ACS Applied Engineering Materials* **1**, 2676-2684 (2023). https://doi.org/10.1021/acsaenm.3c00417

67 Schalenbach, M. *et al.* Acidic or Alkaline? Towards a New Perspective on the Efficiency of Water Electrolysis. *J. Electrochem. Soc.* **163**, F3197 (2016). https://dx.doi.org/10.1149/2.0271611jes

68 Gordon, L. I., Cohen, Y. & Standley, D. R. The solubility of molecular hydrogen in seawater. *Deep Sea Res.* **24**, 937-941 (1977). https://doi.org/10.1016/0146-6291(77)90563-X

69 Nayar, K. G., Sharqawy, M. H., Banchik, L. D. & Lienhard V, J. H. Thermophysical properties of seawater: A review and new correlations that include pressure dependence. *Desalination* **390**, 1-24 (2016). https://doi.org/10.1016/j.desal.2016.02.024

70 LeRoy, R. L., Bowen, C. T. & LeRoy, D. J. The Thermodynamics of Aqueous Water Electrolysis. *J. Electrochem. Soc.* **127**, 1954-1962 (1980). http://dx.doi.org/10.1149/1.2130044

71 de Jonge, R. M., Barendrecht, E., Janssen, L. J. J. & van Stralen, S. J. D. Gas bubble behaviour and electrolyte resistance during water electrolysis. *Int. J. Hydrog. Energy.* **7**, 883-894 (1982). https://doi.org/10.1016/0360-3199(82)90007-6

72 Dionigi, F., Reier, T., Pawolek, Z., Gliech, M. & Strasser, P. Design Criteria, Operating Conditions, and Nickel–Iron Hydroxide Catalyst Materials for Selective Seawater Electrolysis. *ChemSusChem* **9**, 962-972 (2016). https://doi.org/10.1002/cssc.201501581

73 John C. Crittenden, R. R. T., Davis W. Hand, Kerry J. Howe and George Tchobanoglous. *MWH's Water Treatment: Principles and Design*. 3rd edn. 457-539. John Wiley & Sons, Inc.(2012).

74 Fujimura, K. *et al.* Anodically deposited manganese-molybdenum oxide anodes with high selectivity for evolving oxygen in electrolysis of seawater. *J.*

Appl. Electrochem. **29**, 769-775 (1999). https://doi.org/10.1023/A:1003492009263

75 Yu, L. *et al.* Non-noble metal-nitride based electrocatalysts for high-performance alkaline seawater electrolysis. *Nat. Commun.* **10**, 5106 (2019). https://doi.org/10.1038/s41467-019-13092-7

76 Bard, A. J. Inner-Sphere Heterogeneous Electrode Reactions. Electrocatalysis and Photocatalysis: The Challenge. *J. Am. Chem. Soc.* **132**, 7559-7567 (2010). https://doi.org/10.1021/ja101578m

77 Bockris, J. O. M., Mannan, R. J. & Damjanovic, A. Dependence of the Rate of Electrodic Redox Reactions on the Substrate. *J. Chem. Phys.* **48**, 1898-1904 (2003). https://doi.org/10.1063/1.1668987

78 Fierro, S., Nagel, T., Baltruschat, H. & Comninellis, C. Investigation of the oxygen evolution reaction on Ti/IrO2 electrodes using isotope labelling and on-line mass spectrometry. *Electrochem. Commun.* **9**, 1969-1974 (2007). https://doi.org/10.1016/j.elecom.2007.05.008

79 Bockris, J. O. M. Kinetics of Activation Controlled Consecutive Electrochemical Reactions: Anodic Evolution of Oxygen. *J. Chem. Phys.* **24**, 817-827 (2004). https://doi.org/10.1063/1.1742616

80 Castelli, P., Trasatti, S., Pollak, F. H. & O'Grady, W. E. Single crystals as model electrocatalysts: Oxygen evolution on RuO2 (110). *J. Electroanal. Chem.* **210**, 189-194 (1986). https://doi.org/10.1016/0022-0728(86)90325-6

81 Over, H. Surface Chemistry of Ruthenium Dioxide in Heterogeneous Catalysis and Electrocatalysis: From Fundamental to Applied Research. *Chem. Rev.* **112**, 3356-3426 (2012). https://doi.org/10.1021/cr200247n

82 B. Hammer, J. K. N. Theoretical Surface Science and Catalysis - Calculations and Concepts. *Adv. Catal.* **45**, 71 (2000). https://doi.org/10.1016/S0360-0564(02)45013-4

83 Busch, M., Ahlberg, E. & Panas, I. Electrocatalytic oxygen evolution from water on a Mn(iii–v) dimer model catalyst—A DFT perspective. *Phys. Chem. Chem. Phys.* **13**, 15069-15076 (2011). http://dx.doi.org/10.1039/C0CP02132F

84 Busch, M. Water oxidation: From mechanisms to limitations. *Curr. Opin. Electrochem.* **9**, 278-284 (2018). https://doi.org/10.1016/j.coelec.2018.06.007

85 Geiger, S. *et al.* The stability number as a metric for electrocatalyst stability benchmarking. *Nat. Catal.* **1**, 508-515 (2018). https://doi.org/10.1038/s41929-018-0085-6

86 Pfeifer, V. *et al.* In situ observation of reactive oxygen species forming on oxygen-evolving iridium surfaces. *Chem. Sci.* **8**, 2143-2149 (2017). http://dx.doi.org/10.1039/C6SC04622C

87 Sargeant, E., Illas, F., Rodríguez, P. & Calle-Vallejo, F. Importance of the gas-phase error correction for O2 when using DFT to model the oxygen reduction and evolution reactions. *J. Electroanal. Chem.* **896**, 115178 (2021). https://doi.org/10.1016/j.jelechem.2021.115178

88 Urrego-Ortiz, R., Builes, S., Illas, F. & Calle-Vallejo, F. Gas-phase errors in computational electrocatalysis: a review. *EES Catalysis* **2**, 157-179 (2024). http://dx.doi.org/10.1039/D3EY00126A

89 Jens K. Nørskov, F. S., Frank Abild-Pedersen, and Thomas Bligaard. *Fundamental Concepts in Heterogeneous Catalysis*. First edn. John Wiley and Sons.(2014).
90 Abidi, N., Lim, K. R. G., Seh, Z. W. & Steinmann, S. N. Atomistic modeling of electrocatalysis: Are we there yet? *Wiley interdisciplinary reviews. Computational molecular science* **11**, e1499 (2021). https://doi.org/10.1002/wcms.1499
91 Rossmeisl, J., Logadottir, A. & Nørskov, J. K. Electrolysis of water on (oxidized) metal surfaces. *Chem. Phys.* **319**, 178-184 (2005). https://doi.org/10.1016/j.chemphys.2005.05.038
92 Halck, N. B., Petrykin, V., Krtil, P. & Rossmeisl, J. Beyond the volcano limitations in electrocatalysis – oxygen evolution reaction. *Phys. Chem. Chem. Phys.* **16**, 13682-13688 (2014). http://dx.doi.org/10.1039/C4CP00571F
93 Exner, K. S. On the mechanistic complexity of oxygen evolution: potential-dependent switching of the mechanism at the volcano apex. *Materials Horizons* **10**, 2086-2095 (2023). http://dx.doi.org/10.1039/D3MH00047H
94 Fang, Y.-H. & Liu, Z.-P. Mechanism and Tafel Lines of Electro-Oxidation of Water to Oxygen on RuO2(110). *J. Am. Chem. Soc.* **132**, 18214-18222 (2010). https://doi.org/10.1021/ja1069272
95 Reier, T., Nong, H. N., Teschner, D., Schlögl, R. & Strasser, P. Electrocatalytic Oxygen Evolution Reaction in Acidic Environments – Reaction Mechanisms and Catalysts. *Adv. Energy Mater.* **7**, 1601275 (2017). https://doi.org/10.1002/aenm.201601275
96 Koper, M. T. M. Thermodynamic theory of multi-electron transfer reactions: Implications for electrocatalysis. *J. Electroanal. Chem.* **660**, 254-260 (2011). https://doi.org/10.1016/j.jelechem.2010.10.004
97 Dau, H. *et al.* The Mechanism of Water Oxidation: From Electrolysis via Homogeneous to Biological Catalysis. *ChemCatChem* **2**, 724-761 (2010). https://doi.org/10.1002/cctc.201000126
98 Saha, S., Gayen, P. & Ramani, V. K. Facet-dependent Chlorine and Oxygen Evolution Selectivity on RuO2: An Ab initio Atomistic Thermodynamic Study. *ChemCatChem* **12**, 4922-4929 (2020). https://doi.org/10.1002/cctc.202000617
99 Seh, Z. W. *et al.* Combining theory and experiment in electrocatalysis: Insights into materials design. *Science* **355**, eaad4998 (2017). https://doi.org/10.1126/science.aad4998
100 Calle-Vallejo, F., Martínez, J. I., García-Lastra, J. M., Rossmeisl, J. & Koper, M. T. M. Physical and Chemical Nature of the Scaling Relations between Adsorption Energies of Atoms on Metal Surfaces. *Phys. Rev. Lett.* **108**, 116103 (2012). https://link.aps.org/doi/10.1103/PhysRevLett.108.116103
101 Man, I. C. *et al.* Universality in Oxygen Evolution Electrocatalysis on Oxide Surfaces. *ChemCatChem* **3**, 1159-1165 (2011). https://doi.org/10.1002/cctc.201000397
102 Bligaard, T. *et al.* The Brønsted–Evans–Polanyi relation and the volcano curve in heterogeneous catalysis. *J. Catal.* **224**, 206-217 (2004). https://doi.org/10.1016/j.jcat.2004.02.034

103 Rossmeisl, J., Qu, Z. W., Zhu, H., Kroes, G. J. & Nørskov, J. K. Electrolysis of water on oxide surfaces. *J. Electroanal. Chem.* **607**, 83-89 (2007). https://doi.org/10.1016/j.jelechem.2006.11.008

104 R.A. van Santen, M. N. *Molecular Heterogeneous Catalysis: A Conceptual and Computational Approach*. Wiley-VCH Verlag GmbH & Co. KGaA.(2006).

105 Exner, K. S. Importance of the Walden Inversion for the Activity Volcano Plot of Oxygen Evolution. *Advanced Science* **10**, 2305505 (2023). https://doi.org/10.1002/advs.202305505

106 Hess, F. & Over, H. Coordination Inversion of the Tetrahedrally Coordinated Ru4f Surface Complex on RuO2(100) and Its Decisive Role in the Anodic Corrosion Process. *ACS Catal.* **13**, 3433-3443 (2023). https://doi.org/10.1021/acscatal.2c06260

107 Binninger, T. & Doublet, M.-L. The Ir–OOOO–Ir transition state and the mechanism of the oxygen evolution reaction on IrO2(110). *Energy Environ. Sci.* **15**, 2519-2528 (2022). http://dx.doi.org/10.1039/D2EE00158F

108 Nong, H. N. *et al.* Key role of chemistry versus bias in electrocatalytic oxygen evolution. *Nature* **587**, 408-413 (2020). https://doi.org/10.1038/s41586-020-2908-2

109 Exner, K. S. Importance of the volcano slope to comprehend activity and selectivity trends in electrocatalysis. *Curr. Opin. Electrochem.* **39**, 101284 (2023). https://doi.org/10.1016/j.coelec.2023.101284

110 Chen, J., Chen, Y., Li, P., Wen, Z. & Chen, S. Energetic Span as a Rate-Determining Term for Electrocatalytic Volcanos. *ACS Catal.* **8**, 10590-10598 (2018). https://doi.org/10.1021/acscatal.8b03008

111 Piqué, O., Illas, F. & Calle-Vallejo, F. Designing water splitting catalysts using rules of thumb: advantages, dangers and alternatives. *Phys. Chem. Chem. Phys.* **22**, 6797-6803 (2020). http://dx.doi.org/10.1039/D0CP00896F

112 Exner, K. S. A Universal Descriptor for the Screening of Electrode Materials for Multiple-Electron Processes: Beyond the Thermodynamic Overpotential. *ACS Catal.* **10**, 12607-12617 (2020). https://doi.org/10.1021/acscatal.0c03865

113 Exner, K. S. Recent Progress in the Development of Screening Methods to Identify Electrode Materials for the Oxygen Evolution Reaction. *Adv. Funct. Mater.* **30**, 2005060 (2020). https://doi.org/10.1002/adfm.202005060

114 Exner, K. S. Universality in Oxygen Evolution Electrocatalysis: High-Throughput Screening and a Priori Determination of the Rate-Determining Reaction Step. *ChemCatChem* **12**, 2000-2003 (2020). https://doi.org/10.1002/cctc.201902363

115 Exner, K. S. Beyond the Traditional Volcano Concept: Overpotential-Dependent Volcano Plots Exemplified by the Chlorine Evolution Reaction over Transition-Metal Oxides. *J. Phys. Chem. C* **123**, 16921-16928 (2019). https://doi.org/10.1021/acs.jpcc.9b05364

116 Razzaq, S. & Exner, K. S. Materials Screening by the Descriptor Gmax(η): The Free-Energy Span Model in Electrocatalysis. *ACS Catal.* **13**, 1740-1758 (2023). https://doi.org/10.1021/acscatal.2c03997

117 Mavrikis, S., Göltz, M., Rosiwal, S., Wang, L. & Ponce de León, C. Boron-Doped Diamond Electrocatalyst for Enhanced Anodic H_2O_2 Production. *ACS Appl. Energy Mater.* **3**, 3169-3173 (2020). https://doi.org/10.1021/acsaem.0c00093

118 Suntivich, J., May, K. J., Gasteiger, H. A., Goodenough, J. B. & Shao-Horn, Y. A Perovskite Oxide Optimized for Oxygen Evolution Catalysis from Molecular Orbital Principles. *Science* **334**, 1383-1385 (2011). https://doi.org/10.1126/science.1212858

119 Kuznetsov, D. A. *et al.* Tuning Redox Transitions via Inductive Effect in Metal Oxides and Complexes, and Implications in Oxygen Electrocatalysis. *Joule* **2**, 225-244 (2018). https://doi.org/10.1016/j.joule.2017.11.014

120 Grimaud, A. *et al.* Activating lattice oxygen redox reactions in metal oxides to catalyse oxygen evolution. *Nat. Chem.* **9**, 457-465 (2017). https://doi.org/10.1038/nchem.2695

121 Kim, Y.-T. *et al.* Balancing activity, stability and conductivity of nanoporous core-shell iridium/iridium oxide oxygen evolution catalysts. *Nat. Commun.* **8**, 1449 (2017). https://doi.org/10.1038/s41467-017-01734-7

122 Hong, W. T., Welsch, R. E. & Shao-Horn, Y. Descriptors of Oxygen-Evolution Activity for Oxides: A Statistical Evaluation. *J. Phys. Chem. C* **120**, 78-86 (2016). https://doi.org/10.1021/acs.jpcc.5b10071

123 Wu, L. *et al.* High-Efficiency Oxygen Evolution Reaction: Controllable Reconstruction of Surface Interface. *Small* **19**, 2304007 (2023). https://doi.org/10.1002/smll.202304007

124 Binninger, T. *et al.* Thermodynamic explanation of the universal correlation between oxygen evolution activity and corrosion of oxide catalysts. *Sci. Rep.* **5**, 12167 (2015). https://doi.org/10.1038/srep12167

125 Chen, F.-Y., Wu, Z.-Y., Adler, Z. & Wang, H. Stability challenges of electrocatalytic oxygen evolution reaction: From mechanistic understanding to reactor design. *Joule* **5**, 1704-1731 (2021). https://doi.org/10.1016/j.joule.2021.05.005

126 Grimaud, A. *et al.* Activation of surface oxygen sites on an iridium-based model catalyst for the oxygen evolution reaction. *Nat. Energy* **2**, 16189 (2016). https://doi.org/10.1038/nenergy.2016.189

127 Zhang, N. & Chai, Y. Lattice oxygen redox chemistry in solid-state electrocatalysts for water oxidation. *Energy Environ. Sci.* **14**, 4647-4671 (2021). http://dx.doi.org/10.1039/D1EE01277K

128 Saveleva, V. A. *et al.* Operando Evidence for a Universal Oxygen Evolution Mechanism on Thermal and Electrochemical Iridium Oxides. *J. Phys. Chem. Lett.* **9**, 3154-3160 (2018). https://doi.org/10.1021/acs.jpclett.8b00810

129 Cherevko, S. *et al.* Dissolution of Noble Metals during Oxygen Evolution in Acidic Media. *ChemCatChem* **6**, 2219-2223 (2014). https://doi.org/10.1002/cctc.201402194

130 Pourbaix, M. *Atlas of Electrochemical Equilibria in Aqueous Solutions*. National Association of Corrosion Engineers.(1974).

131 Kötz, R., Lewerenz, H. J. & Stucki, S. XPS Studies of Oxygen Evolution on Ru and RuO2 Anodes. *J. Electrochem. Soc.* **130**, 825 (1983). https://dx.doi.org/10.1149/1.2119829

132 Kasian, O., Grote, J.-P., Geiger, S., Cherevko, S. & Mayrhofer, K. J. J. The Common Intermediates of Oxygen Evolution and Dissolution Reactions during Water Electrolysis on Iridium. *Angew. Chem. Int. Ed.* **57**, 2488-2491 (2018). https://doi.org/10.1002/anie.201709652

133 Mom, R. V. *et al.* Operando Structure–Activity–Stability Relationship of Iridium Oxides during the Oxygen Evolution Reaction. *ACS Catal.* **12**, 5174-5184 (2022). https://doi.org/10.1021/acscatal.1c05951

134 Elmaalouf, M. *et al.* The origin of the high electrochemical activity of pseudo-amorphous iridium oxides. *Nat. Commun.* **12**, 3935 (2021). https://doi.org/10.1038/s41467-021-24181-x

135 Kevin, S., Baptiste, G., Isabelle, M. & Olga, K. Lattice Oxygen Exchange in Rutile IrO2 during the Oxygen Evolution Reaction. *J. Phys. Chem. Lett.* **11**, 5008-5014 (2020). https://doi.org/10.1021/acs.jpclett.0c01258

136 She, L. *et al.* On the Durability of Iridium-Based Electrocatalysts toward the Oxygen Evolution Reaction under Acid Environment. *Adv. Funct. Mater.* **32**, 2108465 (2022). https://doi.org/10.1002/adfm.202108465

137 Willinger, E., Massué, C., Schlögl, R. & Willinger, M. G. Identifying Key Structural Features of IrOx Water Splitting Catalysts. *J. Am. Chem. Soc.* **139**, 12093-12101 (2017). https://doi.org/10.1021/jacs.7b07079

138 Xu, J. *et al.* IrOx·nH2O with lattice water–assisted oxygen exchange for high-performance proton exchange membrane water electrolyzers. *Sci. Adv.* **9**, eadh1718 (2023). https://doi.org/10.1126/sciadv.adh1718

139 Lu, M. *et al.* Artificially steering electrocatalytic oxygen evolution reaction mechanism by regulating oxygen defect contents in perovskites. *Sci. Adv.* **8**, eabq3563 (2022). https://doi.org/10.1126/sciadv.abq3563

140 Hao, Y. *et al.* Switching the Oxygen Evolution Mechanism on Atomically Dispersed Ru for Enhanced Acidic Reaction Kinetics. *J. Am. Chem. Soc.* **145**, 23659-23669 (2023). https://doi.org/10.1021/jacs.3c07777

141 Krishtalik, L. I. Kinetics and mechanism of anodic chlorine and oxygen evolution reactions on transition metal oxide electrodes. *Electrochim. Acta* **26**, 329-337 (1981). https://doi.org/10.1016/0013-4686(81)85019-0

142 Krishtalik, L. & Rotenberg, Z. Overvoltage in the anodic evolution of chlorine on graphite. II. Kinetic dependence in different regions of potentials. *Zh. Fiz. Khim.* **39**, 907 (1965).

143 Krishtalik, L. & Rotenberg, Z. Overpotential of the anodic evolution of chlorine on graphite. I. Influence of pH. *Zh. Fiz. Khim.* **39**, 328-334 (1965).

144 Janssen, L. J. J. & Hoogland, J. G. The electrolysis of an acidic NaCl solution with a graphite anode—III. Mechanism of chlorine evolution. *Electrochim. Acta* **15**, 941-951 (1970). https://doi.org/10.1016/0013-4686(70)80036-6

145 Faita, G., Fiori, G. & Augustynski, J. W. Electrochemical Processes of the Chlorine-Chloride System on Platinum-Iridium-Coated Titanium Electrodes. *J. Electrochem. Soc.* **116**, 928 (1969). https://dx.doi.org/10.1149/1.2412172

146 Beer, H. B. The Invention and Industrial Development of Metal Anodes. *J. Electrochem. Soc.* **127**, 303C (1980). https://dx.doi.org/10.1149/1.2130021
147 Beer, H. B. Brit. Patent 1147442. (1965).
148 Trasatti, S. Electrocatalysis: understanding the success of DSA®. *Electrochim. Acta* **45**, 2377-2385 (2000). https://doi.org/10.1016/S0013-4686(00)00338-8
149 Dong, H., Yu, W. & Hoffmann, M. R. Mixed Metal Oxide Electrodes and the Chlorine Evolution Reaction. *J. Phys. Chem. C* **125**, 20745-20761 (2021). https://doi.org/10.1021/acs.jpcc.1c05671
150 Exner, K. S., Sohrabnejad-Eskan, I. & Over, H. A Universal Approach To Determine the Free Energy Diagram of an Electrocatalytic Reaction. *ACS Catal.* **8**, 1864-1879 (2018). https://doi.org/10.1021/acscatal.7b03142
151 Trasatti, S. Electrocatalysis in the anodic evolution of oxygen and chlorine. *Electrochim. Acta* **29**, 1503-1512 (1984). https://doi.org/10.1016/0013-4686(84)85004-5
152 Hansen, H. A. *et al.* Electrochemical chlorine evolution at rutile oxide (110) surfaces. *Phys. Chem. Chem. Phys.* **12**, 283-290 (2010). http://dx.doi.org/10.1039/B917459A
153 Exner, K. S., Anton, J., Jacob, T. & Over, H. Chlorine Evolution Reaction on RuO2(110): Ab initio Atomistic Thermodynamics Study - Pourbaix Diagrams. *Electrochim. Acta* **120**, 460-466 (2014). https://doi.org/10.1016/j.electacta.2013.11.027
154 Exner, K. S., Anton, J., Jacob, T. & Over, H. Microscopic Insights into the Chlorine Evolution Reaction on RuO2(110): a Mechanistic Ab Initio Atomistic Thermodynamics Study. *Electrocatalysis* **6**, 163-172 (2015). https://doi.org/10.1007/s12678-014-0220-3
155 Exner, K. S. Design criteria for the competing chlorine and oxygen evolution reactions: avoid the OCl adsorbate to enhance chlorine selectivity. *Phys. Chem. Chem. Phys.* **22**, 22451-22458 (2020). http://dx.doi.org/10.1039/D0CP03667F
156 Exner, K. S., Anton, J., Jacob, T. & Over, H. Full Kinetics from First Principles of the Chlorine Evolution Reaction over a RuO2(110) Model Electrode. *Angew. Chem. Int. Ed.* **55**, 7501-7504 (2016). https://doi.org/10.1002/anie.201511804
157 Over, H. Fundamental Studies of Planar Single-Crystalline Oxide Model Electrodes (RuO2, IrO2) for Acidic Water Splitting. *ACS Catal.* **11**, 8848-8871 (2021). https://doi.org/10.1021/acscatal.1c01973
158 Parsons, R. General equations for the kinetics of electrode processes. *Trans. Faraday Soc.* **47**, 1332-1344 (1951). http://dx.doi.org/10.1039/TF9514701332
159 Kuo, D.-Y. *et al.* Influence of Surface Adsorption on the Oxygen Evolution Reaction on IrO2(110). *J. Am. Chem. Soc.* **139**, 3473-3479 (2017). https://doi.org/10.1021/jacs.6b11932
160 Jovanovič, P. *et al.* Electrochemical Dissolution of Iridium and Iridium Oxide Particles in Acidic Media: Transmission Electron Microscopy, Electrochemical Flow Cell Coupled to Inductively Coupled Plasma Mass Spectrometry, and X-

ray Absorption Spectroscopy Study. *J. Am. Chem. Soc.* **139**, 12837-12846 (2017). https://doi.org/10.1021/jacs.7b08071

161 Dickens, C. F., Kirk, C. & Nørskov, J. K. Insights into the Electrochemical Oxygen Evolution Reaction with ab Initio Calculations and Microkinetic Modeling: Beyond the Limiting Potential Volcano. *J. Phys. Chem. C* **123**, 18960-18977 (2019). https://doi.org/10.1021/acs.jpcc.9b03830

162 Exner, K. S. Controlling Stability and Selectivity in the Competing Chlorine and Oxygen Evolution Reaction over Transition Metal Oxide Electrodes. *ChemElectroChem* **6**, 3401-3409 (2019). https://doi.org/10.1002/celc.201900834

163 Taylor, H. S. & Armstrong, E. F. A theory of the catalytic surface. *Proc. R. Soc. Lond. Ser. A-Contain. Pap. Math. Phys. Character* **108**, 105-111 (1925). https://doi.org/10.1098/rspa.1925.0061

164 Wang, A., Li, J. & Zhang, T. Heterogeneous single-atom catalysis. *Nat. Rev. Chem.* **2**, 65-81 (2018). https://doi.org/10.1038/s41570-018-0010-1

165 Zhang, H. *et al.* Direct probing of atomically dispersed Ru species over multi-edged TiO2 for highly efficient photocatalytic hydrogen evolution. *Sci. Adv.* **6**, eabb9823 (2020). https://doi.org/10.1126/sciadv.abb9823

166 Shen, R. *et al.* High-Concentration Single Atomic Pt Sites on Hollow CuSx for Selective O2 Reduction to H2O2 in Acid Solution. *Chem* **5**, 2099-2110 (2019). https://doi.org/10.1016/j.chempr.2019.04.024

167 Ji, D. *et al.* Atomically Transition Metals on Self-Supported Porous Carbon Flake Arrays as Binder-Free Air Cathode for Wearable Zinc−Air Batteries. *Adv. Mater.* **31**, 1808267 (2019). https://doi.org/10.1002/adma.201808267

168 Gao, C. *et al.* Heterogeneous Single-Atom Catalyst for Visible-Light-Driven High-Turnover CO2 Reduction: The Role of Electron Transfer. *Adv. Mater.* **30**, 1704624 (2018). https://doi.org/10.1002/adma.201704624

169 Nørskov, J. K. *et al.* The nature of the active site in heterogeneous metal catalysis. *Chem. Soc. Rev.* **37**, 2163-2171 (2008). http://dx.doi.org/10.1039/B800260F

170 Vogt, C. & Weckhuysen, B. M. The concept of active site in heterogeneous catalysis. *Nat. Rev. Chem.* **6**, 89-111 (2022). https://doi.org/10.1038/s41570-021-00340-y

171 Dickens, C. F. & Nørskov, J. K. A Theoretical Investigation into the Role of Surface Defects for Oxygen Evolution on RuO2. *J. Phys. Chem. C* **121**, 18516-18524 (2017). https://doi.org/10.1021/acs.jpcc.7b03481

172 Stoerzinger, K. A., Qiao, L., Biegalski, M. D. & Shao-Horn, Y. Orientation-Dependent Oxygen Evolution Activities of Rutile IrO2 and RuO2. *J. Phys. Chem. Lett.* **5**, 1636-1641 (2014). https://doi.org/10.1021/jz500610u

173 Trasatti, E. G. a. S. Recent Developments in Understanding Factors of Electrocatalysis. *Russ. J. Electrochem.* **42**, 1017-1025 (2006).

174 Consonni, V., Trasatti, S., Pollak, F. & O'Grady, W. E. Mechanism of chlorine evolution on oxide anodes study of pH effects. *J. Electroanal. Chem.* **228**, 393-406 (1987). https://doi.org/10.1016/0022-0728(87)80119-5

175 Rao, R. R. *et al.* Surface Orientation Dependent Water Dissociation on Rutile Ruthenium Dioxide. *J. Phys. Chem. C* **122**, 17802-17811 (2018). https://doi.org/10.1021/acs.jpcc.8b04284
176 Adiga, P. *et al.* Breaking OER and CER scaling relations via strain and its relaxation in RuO2 (101). *Mater. Today Energy* **28**, 101087 (2022).
177 Exner, K. S., Anton, J., Jacob, T. & Over, H. Ligand Effects and Their Impact on Electrocatalytic Processes Exemplified with the Oxygen Evolution Reaction (OER) on RuO2(110). *ChemElectroChem* **2**, 707-713 (2015). https://doi.org/10.1002/celc.201402430
178 Exner, K. S., Anton, J., Jacob, T. & Over, H. Controlling Selectivity in the Chlorine Evolution Reaction over RuO2-Based Catalysts. *Angew. Chem. Int. Ed.* **53**, 11032-11035 (2014). https://doi.org/10.1002/anie.201406112
179 Karlsson, R. K. B. & Cornell, A. Selectivity between Oxygen and Chlorine Evolution in the Chlor-Alkali and Chlorate Processes. *Chem. Rev.* **116**, 2982-3028 (2016). https://doi.org/10.1021/acs.chemrev.5b00389
180 Näslund, L.-Å. *et al.* The Role of TiO2 Doping on RuO2-Coated Electrodes for the Water Oxidation Reaction. *J. Phys. Chem. C* **117**, 6126-6135 (2013). https://doi.org/10.1021/jp308941g
181 Tilak, B. V., Birss, V. I., Wang, J., Chen, C. P. & Rangarajan, S. K. Deactivation of Thermally Formed Ru/Ti Oxide Electrodes: An AC Impedance Characterization Study. *J. Electrochem. Soc.* **148**, D112 (2001). https://dx.doi.org/10.1149/1.1388630
182 Macounová, K. M., Pittkowski, R. K., Nebel, R., Zitolo, A. & Krtil, P. Selectivity of Ru-rich Ru-Ti-O oxide surfaces in parallel oxygen and chlorine evolution reactions. *Electrochim. Acta* **427**, 140878 (2022). https://doi.org/10.1016/j.electacta.2022.140878
183 Astudillo, C. *et al.* Ru rich Ru-Mn-O phases for selective suppression of chlorine evolution in sea water electrolysis. *Electrochim. Acta* **470**, 143295 (2023). https://doi.org/10.1016/j.electacta.2023.143295
184 Divanis, S., Frandsen, A. M., Kutlusoy, T. & Rossmeisl, J. Lifting the discrepancy between experimental results and the theoretical predictions for the catalytic activity of RuO2(110) towards oxygen evolution reaction. *Phys. Chem. Chem. Phys.* **23**, 19141-19145 (2021). http://dx.doi.org/10.1039/D1CP02999A
185 Petrykin, V., Macounova, K., Shlyakhtin, O. A. & Krtil, P. Tailoring the Selectivity for Electrocatalytic Oxygen Evolution on Ruthenium Oxides by Zinc Substitution. *Angew. Chem. Int. Ed.* **49**, 4813-4815 (2010). https://doi.org/10.1002/anie.200907128
186 Wu, Z.-Y. *et al.* Non-iridium-based electrocatalyst for durable acidic oxygen evolution reaction in proton exchange membrane water electrolysis. *Nat. Mater.* **22**, 100-108 (2023). https://doi.org/10.1038/s41563-022-01380-5
187 Zhao, Z. L. *et al.* Boosting the oxygen evolution reaction using defect-rich ultra-thin ruthenium oxide nanosheets in acidic media. *Energy Environ. Sci.* **13**, 5143-5151 (2020). http://dx.doi.org/10.1039/D0EE01960G
188 Zagalskaya, A. & Alexandrov, V. Role of Defects in the Interplay between Adsorbate Evolving and Lattice Oxygen Mechanisms of the Oxygen Evolution

Reaction in RuO2 and IrO2. *ACS Catal.* **10**, 3650-3657 (2020). https://doi.org/10.1021/acscatal.9b05544

189 Gayen, P., Saha, S., Bhattacharyya, K. & Ramani, V. K. Oxidation State and Oxygen-Vacancy-Induced Work Function Controls Bifunctional Oxygen Electrocatalytic Activity. *ACS Catal.* **10**, 7734-7746 (2020). https://doi.org/10.1021/acscatal.0c01541

190 Gayen, P., Saha, S. & Ramani, V. Pyrochlores for Advanced Oxygen Electrocatalysis. *Acc. Chem. Res.* **55**, 2191-2200 (2022). https://doi.org/10.1021/acs.accounts.2c00049

191 Gayen, P., Saha, S. & Ramani, V. Selective Seawater Splitting Using Pyrochlore Electrocatalyst. *ACS Appl. Energy Mater.* **3**, 3978-3983 (2020). https://doi.org/10.1021/acsaem.0c00383

192 Subramanian, M. A., Aravamudan, G. & Subba Rao, G. V. Oxide pyrochlores — A review. *Prog. Solid State Chem.* **15**, 55-143 (1983). https://doi.org/10.1016/0079-6786(83)90001-8

193 Fuentes, A. F. *et al.* A Critical Review of Existing Criteria for the Prediction of Pyrochlore Formation and Stability. *Inorg. Chem.* **57**, 12093-12105 (2018). https://doi.org/10.1021/acs.inorgchem.8b01665

194 Hubert, M. A. *et al.* Acidic Oxygen Evolution Reaction Activity–Stability Relationships in Ru-Based Pyrochlores. *ACS Catal.* **10**, 12182-12196 (2020). https://doi.org/10.1021/acscatal.0c02252

195 Nong, H. N. *et al.* A unique oxygen ligand environment facilitates water oxidation in hole-doped IrNiOx core–shell electrocatalysts. *Nat. Catal.* **1**, 841-851 (2018). https://doi.org/10.1038/s41929-018-0153-y

196 Lu, B., Liu, Q. & Chen, S. Electrocatalysis of Single-Atom Sites: Impacts of Atomic Coordination. *ACS Catal.* **10**, 7584-7618 (2020). https://doi.org/10.1021/acscatal.0c01950

197 Ji, J. *et al.* Ruthenium Oxide Clusters Immobilized in Cationic Vacancies of 2D Titanium Oxide for Chlorine Evolution Reaction. *Small Struct.* **In Press**, 2300240 https://doi.org/10.1002/sstr.202300240

198 Shan, J. *et al.* Metal-metal interactions in correlated single-atom catalysts. *Sci. Adv.* **8**, eabo0762 (2022). https://doi.org/10.1126/sciadv.abo0762

199 Cho, J. *et al.* Importance of broken geometric symmetry of single-atom Pt sites for efficient electrocatalysis. *Nat. Commun.* **14**, 3233 (2023). https://doi.org/10.1038/s41467-023-38964-x

200 Lim, T. *et al.* Atomically dispersed Pt–N4 sites as efficient and selective electrocatalysts for the chlorine evolution reaction. *Nat. Commun.* **11**, 412 (2020). https://doi.org/10.1038/s41467-019-14272-1

201 Shan, J. *et al.* Short-Range Ordered Iridium Single Atoms Integrated into Cobalt Oxide Spinel Structure for Highly Efficient Electrocatalytic Water Oxidation. *J. Am. Chem. Soc.* **143**, 5201-5211 (2021). https://doi.org/10.1021/jacs.1c01525

202 Souza Junior, J. B. *et al.* Pair Distribution Function Obtained from Electron Diffraction: An Advanced Real-Space Structural Characterization Tool. *Matter* **4**, 441-460 (2021). https://doi.org/10.1016/j.matt.2020.10.025

203 Antolini, E. Iridium As Catalyst and Cocatalyst for Oxygen Evolution/Reduction in Acidic Polymer Electrolyte Membrane Electrolyzers and Fuel Cells. *ACS Catal.* **4**, 1426-1440 (2014). https://doi.org/10.1021/cs4011875

204 Liang, X. *et al.* Activating Inert, Nonprecious Perovskites with Iridium Dopants for Efficient Oxygen Evolution Reaction under Acidic Conditions. *Angew. Chem. Int. Ed.* **58**, 7631-7635 (2019). https://doi.org/10.1002/anie.201900796

205 Liu, Y. *et al.* Electrosynthesis of chlorine from seawater-like solution through single-atom catalysts. *Nat. Commun.* **14**, 2475 (2023). https://doi.org/10.1038/s41467-023-38129-w

206 Bennett, J. E. Electrodes for generation of hydrogen and oxygen from seawater. *Int. J. Hydrog. Energy.* **5**, 401-408 (1980). https://doi.org/10.1016/0360-3199(80)90021-X

207 Habazaki, H. *et al.* Nanocrystalline manganese-molybdenum-tungsten oxide anodes for oxygen evolution in seawater electrolysis. *Scr. Mater.* **44**, 1659-1662 (2001). https://doi.org/10.1016/S1359-6462(01)00876-4

208 Abdel Ghany, N. A., Kumagai, N., Meguro, S., Asami, K. & Hashimoto, K. Oxygen evolution anodes composed of anodically deposited Mn–Mo–Fe oxides for seawater electrolysis. *Electrochim. Acta* **48**, 21-28 (2002). https://doi.org/10.1016/S0013-4686(02)00539-X

209 Vos, J. G., Wezendonk, T. A., Jeremiasse, A. W. & Koper, M. T. M. MnOx/IrOx as Selective Oxygen Evolution Electrocatalyst in Acidic Chloride Solution. *J. Am. Chem. Soc.* **140**, 10270-10281 (2018). https://doi.org/10.1021/jacs.8b05382

210 Beatty, M. E. S., Chen, H., Labrador, N. Y., Lee, B. J. & Esposito, D. V. Structure–property relationships describing the buried interface between silicon oxide overlayers and electrocatalytic platinum thin films. *J. Mater. Chem. A.* **6**, 22287-22300 (2018). http://dx.doi.org/10.1039/C8TA06969G

211 Pourbaix, M. *Atlas of Electrochemical Equilibria in Aqueous Solution*. National Association of Corrosion Engineers.(1974).

212 Robinson, J. E., Labrador, N. Y., Chen, H., Sartor, B. E. & Esposito, D. V. Silicon Oxide-Encapsulated Platinum Thin Films as Highly Active Electrocatalysts for Carbon Monoxide and Methanol Oxidation. *ACS Catal.* **8**, 11423-11434 (2018). https://doi.org/10.1021/acscatal.8b03626

213 Marcus, Y. Ionic radii in aqueous solutions. *Chem. Rev.* **88**, 1475-1498 (1988). https://doi.org/10.1021/cr00090a003

214 Vos, J. G., Bhardwaj, A. A., Jeremiasse, A. W., Esposito, D. V. & Koper, M. T. M. Probing the Effects of Electrode Composition and Morphology on the Effectiveness of Silicon Oxide Overlayers to Enhance Selective Oxygen Evolution in the Presence of Chloride Ions. *J. Phys. Chem. C* **126**, 20314-20325 (2022). https://doi.org/10.1021/acs.jpcc.2c07116

215 Balaji, R. *et al.* An alternative approach to selective sea water oxidation for hydrogen production. *Electrochem. Commun.* **11**, 1700-1702 (2009). https://doi.org/10.1016/j.elecom.2009.06.022

216 Venkatkarthick, R. *et al.* Studies on polymer modified metal oxide anode for oxygen evolution reaction in saline water. *J. Electroanal. Chem.* **697**, 1-4 (2013). https://doi.org/10.1016/j.jelechem.2013.02.015

217 Jadhav, A. R. *et al.* Stable complete seawater electrolysis by using interfacial chloride ion blocking layer on catalyst surface. *J. Mater. Chem. A.* **8**, 24501-24514 (2020). http://dx.doi.org/10.1039/D0TA08543J

218 Kitiphatpiboon, N. *et al.* Highly durable FeNiSx/NiFe(OH)x electrocatalyst for selective oxygen evolution reaction in alkaline simulated seawater at high current densities. *Int. J. Hydrog. Energy.* **48**, 34255-34271 (2023). https://doi.org/10.1016/j.ijhydene.2023.05.207

219 Loomba, S. *et al.* Nitrogen-Doped Porous Nickel Molybdenum Phosphide Sheets for Efficient Seawater Splitting. *Small* **19**, 2207310 (2023). https://doi.org/10.1002/smll.202207310

220 Obata, K. & Takanabe, K. A Permselective CeOx Coating To Improve the Stability of Oxygen Evolution Electrocatalysts. *Angew. Chem. Int. Ed.* **57**, 1616-1620 (2018). https://doi.org/10.1002/anie.201712121

221 Balasubramanian, M., Melendres, C. A. & Mansour, A. N. An X-ray absorption study of the local structure of cerium in electrochemically deposited thin films. *Thin Solid Films* **347**, 178-183 (1999). https://doi.org/10.1016/S0040-6090(98)01754-4

222 Han, H. *et al.* Amorphous-Crystalline Interfaces on Hollow Nanocubes Derived from Ir-Doped Ni–Fe–Zn Prussian Blue Analog Enables High Capability of Alkaline/Acidic/Saline Water Oxidations. *Small* **19**, 2303912 (2023). https://doi.org/10.1002/smll.202303912

223 Xie, H. *et al.* A membrane-based seawater electrolyser for hydrogen generation. *Nature* **612**, 673-678 (2022). https://doi.org/10.1038/s41586-022-05379-5

224 Shi, H. *et al.* A sodium-ion-conducted asymmetric electrolyzer to lower the operation voltage for direct seawater electrolysis. *Nat. Commun.* **14**, 3934 (2023). https://doi.org/10.1038/s41467-023-39681-1

225 Yet-Ming Chiang, D. B. I., W. David Kingery. *Physical Ceramics: Principles for Ceramic Science and Engineering*. John Wiley and Sons, Inc.(1997).

226 Rousseau, R., Glezakou, V.-A. & Selloni, A. Theoretical insights into the surface physics and chemistry of redox-active oxides. *Nat. Rev. Mater.* **5**, 460-475 (2020). https://doi.org/10.1038/s41578-020-0198-9

227 Reticcioli, M. *et al.* Interplay between Adsorbates and Polarons: CO on Rutile TiO2 (110). *Phys. Rev. Lett.* **122**, 016805 (2019). https://link.aps.org/doi/10.1103/PhysRevLett.122.016805

228 Stoerzinger, K. A., Choi, W. S., Jeen, H., Lee, H. N. & Shao-Horn, Y. Role of Strain and Conductivity in Oxygen Electrocatalysis on LaCoO3 Thin Films. *J. Phys. Chem. Lett.* **6**, 487-492 (2015). https://doi.org/10.1021/jz502692a

229 Tian, Y. *et al.* A Co-Doped Nanorod-like RuO2 Electrocatalyst with Abundant Oxygen Vacancies for Acidic Water Oxidation. *iScience* **23**, 100756 (2020). https://doi.org/10.1016/j.isci.2019.100756

230 Thorarinsdottir, A. E. & Nocera, D. G. Energy catalysis needs ligands with high oxidative stability. *Chem Catal.* **1**, 32-43 (2021). https://doi.org/10.1016/j.checat.2021.05.012
231 Lux, H. “Säuren” und “Basen” im Schmelzfluss: Die Bestimmung der Sauerstoffionen-Konzentration. *Zeitschrift für Elektrochemie und angewandte physikalische Chemie* (1939).
232 Crabtree, R. H. *The Organometallic Chemistry of the Transition Metals*. John Wiley & Sons.((2014)).
233 Costentin, C. & Nocera, D. G. Self-healing catalysis in water. *Proc. Natl. Acad. Sci.* **114**, 13380-13384 (2017). https://doi.org/10.1073/pnas.1711836114
234 Huynh, M., Bediako, D. K. & Nocera, D. G. A Functionally Stable Manganese Oxide Oxygen Evolution Catalyst in Acid. *J. Am. Chem. Soc.* **136**, 6002-6010 (2014). https://doi.org/10.1021/ja413147e
235 Fleischmann, M., Thirsk, H. R. & Tordesillas, I. M. Kinetics of electrodeposition of γ-manganese dioxide. *Trans. Faraday Soc.* **58**, 1865-1877 (1962). http://dx.doi.org/10.1039/TF9625801865
236 Huynh, M., Bediako, D. K., Liu, Y. & Nocera, D. G. Nucleation and Growth Mechanisms of an Electrodeposited Manganese Oxide Oxygen Evolution Catalyst. *J. Phys. Chem. C* **118**, 17142-17152 (2014). https://doi.org/10.1021/jp501768n
237 Surendranath, Y., Dincă, M. & Nocera, D. G. Electrolyte-Dependent Electrosynthesis and Activity of Cobalt-Based Water Oxidation Catalysts. *J. Am. Chem. Soc.* **131**, 2615-2620 (2009). https://doi.org/10.1021/ja807769r
238 Keane, T. P. & Nocera, D. G. Selective Production of Oxygen from Seawater by Oxidic Metallate Catalysts. *ACS Omega.* **4**, 12860-12864 (2019). https://doi.org/10.1021/acsomega.9b01751
239 Keane, T. P., Veroneau, S. S., Hartnett, A. C. & Nocera, D. G. Generation of Pure Oxygen from Briny Water by Binary Catalysis. *J. Am. Chem. Soc.* **145**, 4989-4993 (2023). https://doi.org/10.1021/jacs.3c00176
240 Liu, Z. *et al.* Efficiency and stability of hydrogen production from seawater using solid oxide electrolysis cells. *Appl. Energy* **300**, 117439 (2021). https://www.sciencedirect.com/science/article/pii/S0306261921008308

Chapter 2

Application of Permselective Silica to Arrest Chloride Anion Transport

"L’evocation de la pensée par la ligne, l’arabesque et les moyens plastiques, voilà mon but."

-Gustave Moreau

II.1 Introduction

The presence of the chlorine ion in seawater at concentrations nearing 3.5 wt. % impedes the selectivity for the oxygen evolution reaction at the anode, decreasing the faradaic current efficiencies of the water splitting electrolysers through the generation of chlorine gas. This toxic parasitic side product not only contributes to reduction of the ozone layer and global warming, though also can undergo reduction at the cathode and corrode the electrode. Chlorine gas can also evolve hypochlorous acid, which can further disproportionate into hypochlorite and contribute to the corrosion of the cathode and the degradation of the electrolyser unit[1]. The chloride ion itself can moreover corrode the anode by replacing the oxygens along the passivated surface and poison the catalysts at the anode and cathode by affecting their functionality and promoting dissolution. Evading the mass transport of the chloride ion towards the catalysts thus requires a mechanism to impede the permeation of chloride and the evolution of chlorine.

II.1.1 General Transport Phenomena within Electrolytic Solutions

Within an electrolyser, the constituents in the electrolyte are subjected to the presence of the electric field, thus the mass transfer of these constituents, their movement within a solution, can be affected by not only a chemical potential difference and the difference in mechanical forces acting within the solution, though also by an electrical potential. Fick's Law describing movement via diffusion must thus be expanded to the Nernst-Plank Equation, which further considers transport by migration (the second term of *Equation 1a*) and convection (the third term of *Equation 1a*)[2].

$$\boldsymbol{J}_j = -D_j \boldsymbol{\nabla} C_j - \frac{z_j F}{RT} D_j C_j \boldsymbol{\nabla} \phi + C_j \mathbf{v} \qquad (1a)$$

Where,

$$\boldsymbol{\nabla} = \frac{\partial}{\partial r}\hat{r} + \frac{1}{r}\frac{\partial}{\partial \theta}\hat{\theta} + \frac{1}{r \sin\theta}\frac{\partial}{\partial \phi}\hat{\phi} \qquad (1b)$$

And,

$$\mathbf{v} = v_r \hat{r} + v_\theta \hat{\theta} + v_\phi \hat{\phi} \qquad (1c)$$

The flex vector ($\boldsymbol{J}_j$) of each chemical constituent in solution is thus dependent on the characteristic diffusion of the species (*j)* with a diffusion coefficient D_j and a concentration (C_j); its migration where ϕ is the potential, z_j is the charge of the species, *F* is the Faraday constant, *R* is the standard gas constant, and *T* is the temperature; and its convection described by the velocity vector of *Equation 1c* multiplied by its concentration. The evolution of the species concentration (C_j) with respect to time is given by Fick's Second Law, which can be derived by taking the divergence of the *Equation 1* vector to result in a scalar function,

$$\frac{\partial C_i}{\partial t} = -\nabla \cdot \boldsymbol{J}_j \tag{2}$$

Thus,

$$\frac{\partial C_i}{\partial t} = D_j \nabla^2 C_j + \frac{z_j F}{RT} D_j C_j \nabla^2 \phi + \frac{z_j F}{RT} D_j \nabla C_j \nabla \phi - \nabla C_j \cdot \mathbf{v} \tag{3}$$

In a hemispherical symmetric space with a spacial coordinate, *r*, the Laplacian operator in a spherical geometric form may be used, in which only radial transport is assumed[3],

$$\frac{\partial C_i}{\partial t} = D_j \frac{\partial^2 C_j}{\partial r^2} + D_j \frac{2}{r} \frac{\partial C_j}{\partial r} + \left(\frac{z_j F D_j}{RT}\right) \frac{\partial^2 \phi_j}{\partial r^2} + \left(\frac{z_j F D_j}{RT}\right) \frac{2}{r} \frac{\partial \phi_j}{\partial r} + \left(\frac{z_j F D_j}{RT}\right) \frac{\partial C_j}{\partial r} \frac{\partial \phi_j}{\partial r} + \frac{\partial C_j}{\partial r} v_r \tag{4}$$

Moreover, the charged species in solution must also satisfy the Poisson Equation[3],

$$\nabla^2 \phi = -\frac{\rho}{\epsilon_s \epsilon_0} \tag{5a}$$

where,

$$\rho = F \sum_i z_i C_i \tag{5b}$$

represents the local charge density, and ϵ_s and ϵ_0 are the dielectric constant of the solvent medium and the permittivity of free space. Thus,

$$\frac{\partial^2 \phi_j}{\partial r^2} + \frac{2}{r} \frac{\partial \phi_j}{\partial r} = \frac{F}{\epsilon_s \epsilon_0} \sum_i z_i C_i \tag{6}$$

The set of coupled partial differential equations of *Equation 4* and *Equation 6* are known as the Nernst-Planck-Poisson equations[3]. The local charge density may be preferentially distributed away from the electroactive species by the addition of an excess of nonelectroactive ions, which enables the majority of the current within the system to be carried by this supporting electrolyte, homogenizing the electric field and preventing electric field perturbation by oxidation or reduction of the electroactive species[2]. Thus, with the addition of a supporting electrolyte, the migration contribution to mass transfer of the electroactive species shown in *Equation 1* may be diminished and the transport phenomena of these electroactive species can be described by considering their respective diffusion and convection.

II.1.2 Affecting Mass Transport of the Electroactive Species

The preferential movement of these electroactive constituents in the electrolyte may further be affected through the placement of a membrane, which introduces an interface between two bulk phases to achieve a preferential separation of constituents by controlling their respective rates of permeation[4]. Membranes can be characteristically neutral or charged, porous or non-porous by design to create a permselective barrier that selectively impedes the mass transport of the electroactive species. Both water and chloride ions are subjected to the random walk of diffusion, thus although their average displacement from a starting point can be calculated for a period of time, no net direction of movement may be inferred. Establishing a concentration gradient in a membrane medium through adjacent placement of two volume elements of different component i concentrations creates a driving force that enables a net transport of matter from regions of high concentration to regions of low concentration[4]. The nature of this driving force (ΔC_i) on component i thus utilizes adsorption coefficients (K_i) and diffusion coefficients (D_i) to describe the thermodynamic partitioning and kinetic mobilities that dictate the control of the molecular separation[5]. The flux ($\mathcal{F}_i$) of the component i through the selective membrane layer of thickness δ under steady-state permeation can be evaluated by integration from the upstream concentration (C_o) at (x = 0) to the downstream concentration (C_δ) at (x= δ)[6].

$$\mathcal{F}_i = \frac{1}{\delta}\int_{C_\delta}^{C_o} P_i dc = \frac{P}{\delta}\Delta C_i \qquad (7a)$$

Where (P_i) denotes the permeability of component i, a measure of the productivity of the membrane,

$$P_i = K_i D_i \qquad (7b)$$

And $P = P_i$ only for ideal systems in which there is a lack of interactions among solutes and a constant interaction between the component i and the membrane matrix, enabling,

$$\bar{P} = \frac{P}{\delta} = \frac{K_i D_i}{\delta} \qquad (7c)$$

Otherwise $\bar{P}$ is the mean value of P_i in the range $c_\delta \leq c \leq c_o$. $\bar{P}$ is also shown to be inversely proportional to the thickness of the membrane[7]. Indeed, to diffuse through a membrane, the permeant (component i) must break successive bonds with neighboring molecules in the host membrane medium to advance towards the next coordinate in the medium and form a stabilizing bond[8]. Thus each transition to a new coordinate may be considered an elementary reaction, requiring an molecular rearrangement with a transition state of high-potential energy to establish the new bonding arrangement. This transition state is associated with an activation energy that limits transport to permeants possessing sufficient energy to overcome the barrier. This Transition State Theory, or the theory of absolute reaction rates, was initially

proposed by Eyring, who assumed that an elementary rate process such as a chemical reaction or molecular diffusion can be modeled by characterizing the change in the reactants along their reaction coordinate[9]. The concentration of the molecular transition state, which was moreover thought to be in equilibrium with the reactants, and the rate at which it decomposed into the product molecules could be evaluated using statistical mechanics or thermodynamics[8]. A molecular level interpretation of the experimental activation energy and preexponential factor proposed by Arrhenius could be thus formulated as shown in the Erying Equation for the specific rate constant of a reaction (k_i),

$$k_i = \kappa \frac{k_b T}{h} e^{-\Delta G^{\ddagger}/RT} \tag{8}$$

Where $\Delta G^{\ddagger}$ is the free energy of activation between the transition state and the reactant state and κ is the transmission coefficient, the ratio of the reagent species crossing the barrier to those reaching the barrier, which is often assumed to be one, k_b is the Boltzmann constant, T is the temperature, and h is the Plank constant[7,9]. This rate constant can furthermore govern the transport through the condensed phases, which can be treated as jumps of the permeant in between the molecular coordinates as indicated in *Figure 1*[7].

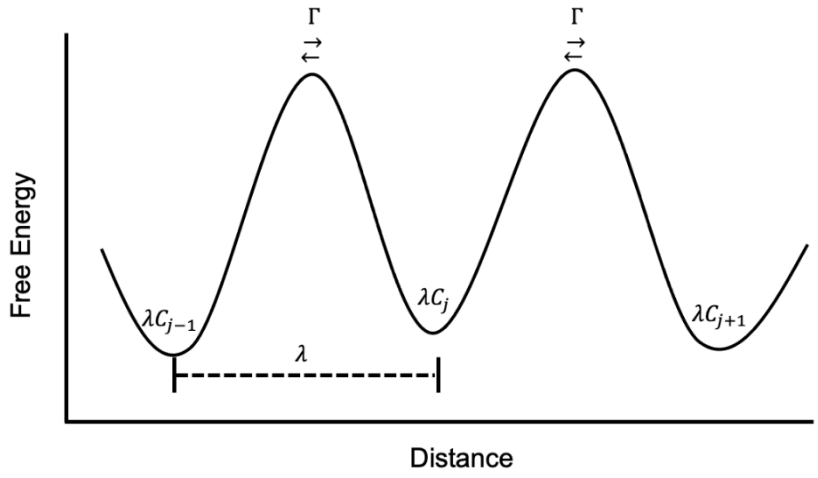

Figure 1: Representation of potential energy profile through coordinates of a membrane.

Here C_j is the concentration per cubic centimeter at j^{th} position. The amount of component (i) in a square centimeter across a length (λ), which is the distance between equilibrium minima in Figure *1*, is λC_j. If Γ is the number of jumps per second that a molecule attempts, then the net flux ($\mathcal{F}_i$) of the amount of component (i) passing through a square centimeter of surface at steady state is given by,

$$\mathcal{F}_i = \Gamma \lambda C_j - \Gamma \lambda C_{j+1} \tag{9}$$

The flux may also be determined at the various maxima ($\mathcal{F}_m$) of *Figure 1* by considering that the specific rate constant defined above (k_i) is a product of the rate at which the transition state is transversed multiplied by the probability of the system being located in the transition state[7,10]. The specific rate constant in the forward direction for C_j can be defined as k_j^+ and the specific rate of the reverse direction from the equilibrium position C_j can be defined as k_j^-. Thus the net flux at the various transition state maxima within the transversed path of a component may be determined, assuming the distance λ between each minima are equal[7],

$$\mathcal{F}_m = \mathrm{k}_0^+ \lambda C_0 - k_1^- \lambda C_1 \tag{10a}$$

$$\mathcal{F}_m = \mathrm{k}_1^+ \lambda C_1 - k_2^- \lambda C_2 \tag{10b}$$

$$\ldots \mathcal{F}_m = \mathrm{k}_n^+ \lambda C_n - k_{n+1}^- \lambda C_{n+1} \tag{10c}$$

The net flux may thus be solved, arriving at the expression,

$$\mathcal{F}_m = \frac{\mathrm{k}_0^+ \lambda C_0 - \prod_{i=1}^{n} \left(\frac{k_i'}{k_i}\right) k_{n+1}^- \lambda C_{n+1}}{1 + \sum_{r=1}^{n} \prod_{i=1}^{r} \left(\frac{k_j^-}{k_j}\right)} \tag{11}$$

The diffusing system may be further defined with varying four rate constants: the constant for diffusion in solution, k_s, the rate constant for diffusion in a membrane, k_m, the rate constant for the diffusion through the solution-membrane interface, k_{sm}, and the rate constant for the diffusion through the membrane solution interface, k_{ms}. The number of jumps from the bulk solution towards the membrane may be defined as (s^+); the number of jumps from the membrane towards the bulk solution (s^-) ; and the number of jumps in the membrane itself can be defined as m[7]. With the total number of jumps along the permeant flow coordinate (n+1) being equivalent to s^+ + m + s^- + 2 and considering that the remaining rate constants within the flow pathway to be equivalent, the terms in the numerator and denominator of *Equation 11* may be evaluated[7].

$$\prod_{i=1}^{n} \left(\frac{k_i^-}{k_i^+}\right) = 1 \tag{12a}$$

And in the denominator,

$$1 + \sum_{r=1}^{n} \prod_{i=1}^{r} \left(\frac{k_i^-}{k_i^+}\right) = s^+ + m\frac{k_s k_{ms}}{k_{sm} k_m} + s^- + 2\frac{k_s}{k_{sm}} \tag{12b}$$

Enabling,

$$\mathcal{F}_m = \frac{k_s\lambda(C_0 - C_{n+1})}{s^+ + s^- + 2\frac{k_s}{k_{sm}} + m\frac{k_s k_{ms}}{k_{sm}k_m}} \tag{13}$$

The permeability constant ($\bar{P}$) may further be defined,

$$\bar{P} = \frac{k_s\lambda}{s^+ + s^- + 2\frac{k_s}{k_{sm}} + m\frac{k_s k_{ms}}{k_{sm}k_m}} \tag{13a}$$

And with a partition coefficient (K_i),

$$K_i = \frac{k_{sm}}{k_{ms}} \tag{13b}$$

And the thickness of the membrane (δ),

$$\delta \cong \lambda m \tag{13c}$$

And by further considering the rate determining step to be diffusion in the membrane, the permeability constant may be expressed below, as initially shown in *Equation 7c*,

$$\bar{P} = \frac{K_i D_i}{\delta} \tag{14a}$$

Where,

$$D_i = k_i\lambda^2 \tag{14b}$$

Substitution of the Erying *Equation 8* into *Equation 14b*, the permeant permeability constant may be described as,

$$\bar{P} = \frac{K_i D_i}{\delta} = \frac{K\lambda^2}{\delta}\frac{k_b T}{h}e^{\left(\frac{-\Delta G^{\ddagger}}{RT}\right)} \tag{14c}$$

The Gibbs-Helmholtz equation may be further applied,

$$\bar{P} = \frac{K_i D_i}{\delta} = \frac{K\lambda^2}{\delta}\frac{k_b T}{h}e^{\left(\frac{-\Delta H^{\ddagger}}{RT}\right)}e^{\left(\frac{\Delta S^{\ddagger}}{R}\right)} \tag{14d}$$

Where ($\Delta H^{\ddagger}$) is the difference in enthalpies between the transition state and the reactant state ($\Delta S^{\ddagger}$) is the difference in entropies between the transition state and the reactant state. The separation efficiency of a membrane (α) may be defined as the ratio of the respective permeabilities of each component,

$$\alpha_{H_2O/Cl^-} = \frac{\bar{P}_{H_2O}}{\bar{P}_{Cl^-}} = \left(\frac{K_{H_2O}}{K_{Cl^-}}\right)\left(\frac{D_{H_2O}}{D_{Cl^-}}\right) = \left(\frac{K_{H_2O}}{K_{Cl^-}}\right)\left(\frac{\lambda^2_{H_2O}}{\lambda^2_{Cl^-}}\right) exp\left(\frac{-\Delta H^{\dagger}_{H_2O/Cl^-}}{RT}\right) exp\left(\frac{\Delta S^{\dagger}_{H_2O/Cl^-}}{R}\right) \quad (15)$$

Here ($-\Delta H^{\dagger}_{H_2O/Cl^-}$) is the difference in the enthalpies between the transition state and the reactant state determined for water and that determined for the chloride ion. The ($\Delta S^{\dagger}_{H_2O/Cl^-}$) is the difference in the entropies between the transition state and the reactant state determined for water and that determined for the chloride ion. Thus the separation efficiency of the membrane may be modulated through the sorption selectivity and the diffusion selectivity. Achieving sorption selectivity by increasing the affinity of a membrane for a single component has shown modest success[5]. The diffusion selectivity may be modulated by the jump lengths, by the enthalpic energies of the transition states evolved between molecular coordinates in the membrane, and by the entropic translational and rotational modes of the permeant within the transition state[5].

II.1.3 The Upper Bound

Commercialization of polymeric membranes for gaseous molecule separation in the late 1970s propelled studies of permeation with various membrane materials. In compiling the data, Robeson noted that a relationship between the logarithm of the separation factor versus the logarithm of the gaseous molecule of higher permeability yielded a linear correlation that limited the achievable selectivity of the gaseous molecule for a given permeability[11]. This upper bound relationship may be expressed,

$$\bar{P}_i = k_H \alpha_{ij}^n \quad (16)$$

here, ($\bar{P}_i$) is the permeability of the more permeable gas, (α) is the separation factor, (k_H) is Henry's Law constant, and (n) is the slope within the log-log limit[12]. Though originally applied to homogenous polymeric membranes, this relationship has shown to uphold for virtually all synthetic polymeric membranes and is a common means of gauging the performance of a membrane materials, including those utilized for water desalination[13]. Shown below in *Figure 2* is a correlation between water/NaCl permeability selectivity indicating the presence of an upper bound beyond which there are few polymeric membrane materials capable of achieving a greater permeability and selectivity for the desired water permeant[14]. Geise et. al. also indicated that it is the diffusivity selectivity that was the greatest determining contribution towards high water selectivity permeability[14].

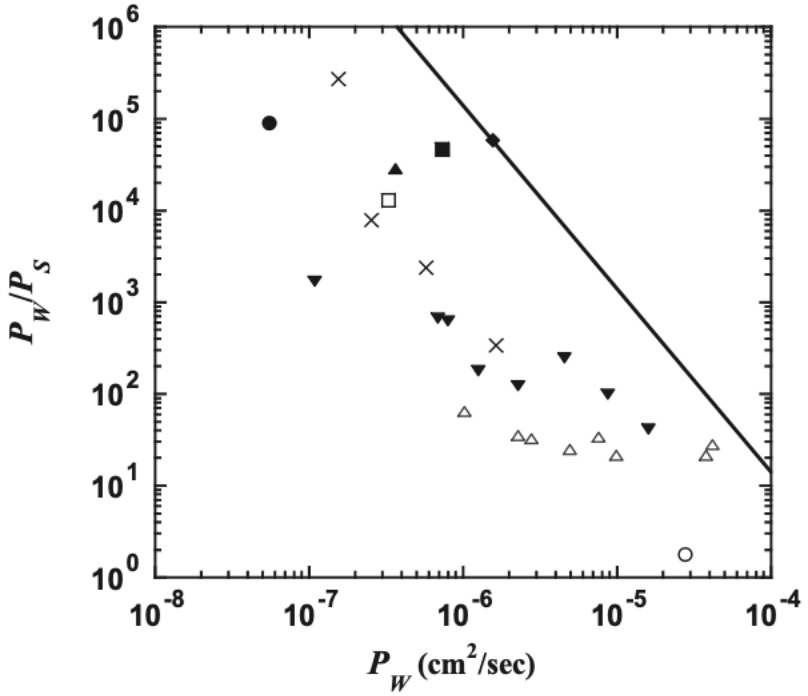

Figure 2: The logarithm of the water/ NaCl selectivity against the logarithm of the permeability of water for various polymeric membranes including polyamide (•), aromatic polyamide (□), polybenzimidazolepyrrolone (♦), polyamide-hydrazide (▲), cellulose acetate (x), aromatic polyamide 2 (■), sulfonated poly(arylene ether sulfone) (▼), PEG (△), and water (○). Figure of Geise et. al.[14]

II.1.4 Affecting Permeant Mass Transport with Permselective Membranes

Being economically advantageous and possessing a high processibility, the utilization of polymeric membranes to desalinate water is widespread. The gold standard in nanofiltration (NF), forward osmosis (FO), and reverse osmosis (RO) desalination processes is the application of a thin-film composite polyamide membrane (TFCPA)[15]. The membrane consists of a non-porous, highly crosslinked selective polyamide layer that adheres through physical interactions to a porous, polysulfone support[15-17]. For (RO) membranes, the polysulfone support is initially immersed in m-phenylenediamine and then brought into contact with a triacyl chloride initiator; the diffusion of the monomers towards the water/organic interface initiates the interfacial polymerization. Subsequent hydrolysis of the remaining acyl chloride groups forms carboxyl groups, creating a net negative charge along the membrane surface.

Permeation through these non-porous, dense membranes can be described by transition state theory previously discussed. The jump lengths within the membrane are similar for similar sizes solutes, though the imprecisely controlled motions within the zone of activations of the polymer segments create transient gaps that limit the ability to control the entropic selectivity of the membrane as shown in *Figure 3*a[5]. Thus diffusional selectivity is achieved enthalpically by the exponential difference in

activation energies of the molecular rearranging transition states that evolve between the coordinates as the permeant diffuses within the membrane. Furthermore, it has been shown that the most cost-effective optimization of water desalination processes would be to increase the selectivity of membrane[15]. Though salt-rejections of RO membranes are reaching 99.5% salt rejection, multiple passes through the membrane are still needed for high purity usages[18].

Molecular sieving materials such as crystalline zeolites and metal-organic frameworks (MOFs) and amorphous carbon molecular sieves and ceramics compositions such as silica represent another class of membranes with characteristically rigid pores that enable differences in both the enthalpies and the entropies of the transition states to contribute to the diffusional selectivity of the membrane, enabling potential improvement above the upper bound evidenced for polymeric materials[5,19]. The motion of the transition state of the larger solute can be hindered within the window of a rigid pore, suppressing rotation and vibrational degrees or freedom, exponentially favoring the passage of the smaller permeant (*Figure 3*b)[5].

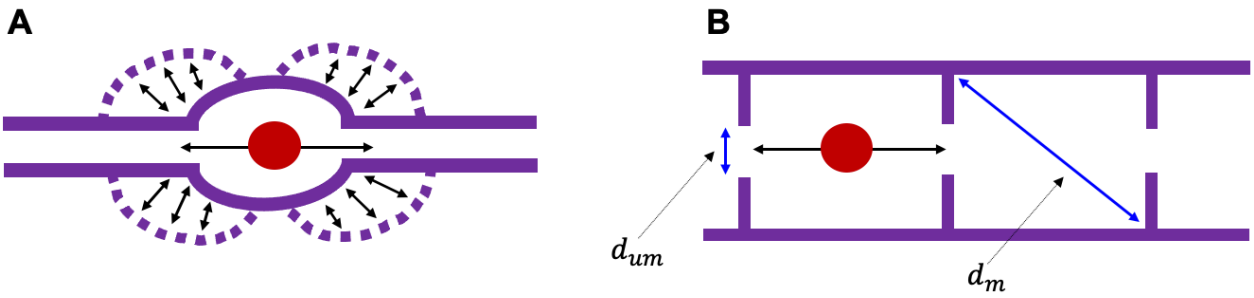

Figure 3: (A) Schematic of a flexible polymer with transient segmental motion. (B) Molecular sieve with a characteristic pore size (d_{um}) with a window dimension (d_m) connecting adjacent pores. Figure adapted from Koros and Zhang[5].

II.1.5 Silica as a Molecular Sieve Membrane

Developing a permselective molecular sieve membrane such as silica can enable the upper bound to be surpassed and provide an improved diffusion selectivity that is crucial prerequisite for a membrane encompassing catalytically active sites for the OER to impede the mass transport of the chloride ion[20]. Previous attempts to arrest the transport of chloride ions to the overlayer-catalyst interface include overlayer depositions of manganese-oxide and Nafion in acidic electrolyte solutions; silica in acidic and in neutral solutions; and manganese-molybdenum oxide, graphene, nickel-iron hydroxide, polystyrene, and cerium oxide in alkaline electrolytes[20-26]. An overlayer coating with an oxide such as silica, which is thermally and thermodynamically stable across a wide range of potentials in acidic and pH neutral conditions, can improve the durability and moreover reduce the degradation of the electrocatalytic material[27,28]. This inert material prevents side reactions at its surface, can concentrate reactants at the buried interface, prevent dissolution of the catalytically active species, and create confinement effects that can be selectively tuned to improve the selectivity and activity of the catalytic active sites[27,29]. It has also

shown to be an effective nanomembrane that selects for CO_2 and participates in a bifunctional mechanism, with a platinum substrate providing the initial adsorption sites, by supplying an oxyphilic species that can oxidize the carbonaceous intermediates to CO_2, relieving the active sites from potential CO_2 poisoning[30,31].

The mechanism utilized by silica to control the rate of permeation of the electroactive species have further been considered and include electrostatic interactions between a silica membrane and the electroactive species as shown in *Figure 4*a; the point of zero charge of silica is between 1 and 3 pH units, below which the overlayer is expected to be positively charged[8,20]. There may also be steric size exclusion in which the size of the electroactive species equals or exceeds the size of the rigid pores or free volume elements within the silica overlayer as shown in *Figure 4*b[8]. However, in contrast to rigid pores, free volume elements are small spaces between matter caused by thermal motion that appear and disappear on a time scale similar to the motion of the permeants traveling through the membrane[4]. Their presence would thus be expected to diminish the entropic selectivity of the membrane. The transition range of characterizing pores as permanent or transient is further considered to be 5-10 Å[4].

Bhardwaj et. al. conjectured that a mechanism related to the dielectric effect of water solvation differentiated the rate of permeation of chloride ions through an SiO_x overlayer deposited onto a Pt thin film, as indicated in *Figure 4*c. The membrane was produced by spin coating a dimethylsiloxane precursor onto the thin film that was subsequently exposed to UV-generated ozone; the procedure produced free volume elements with dimensions of 4.8 Å in their 4.8nm SiO_x overlayers, cured for 120 min, which are smaller than the 6.5 Å hydrated diameter of chloride. Permeating through the pores required an additional activation energy to shed the hydration sphere surrounding a negatively charged ion that was proposed to impede the species transport of the chloride ion[20,32]. The polar bonds in silica have moreover been proposed to form favorable interactions that displace the water-ions interactions and compensate for the loss of the hydration shell, reducing the energy barrier for partitioning[33,34]. The overlayer medium interactions with uncharged solutes can be also ascribed to Van der Waals type forces depicted in *Figure 4d*, where the energy barrier for partitioning from the bulk solution into the pore or diffusion inside the membrane is ascribed to the energetic cost of breaking the interactions with other solvent water molecules to stabilize the permeant water molecules within the overlayer medium[8]. Thus, multiple mechanisms of permeation may account for the achieved selectivity of a silica overlayer for the water permeant and crucially depend on the characteristic size of the pores and their rigid or transient nature.

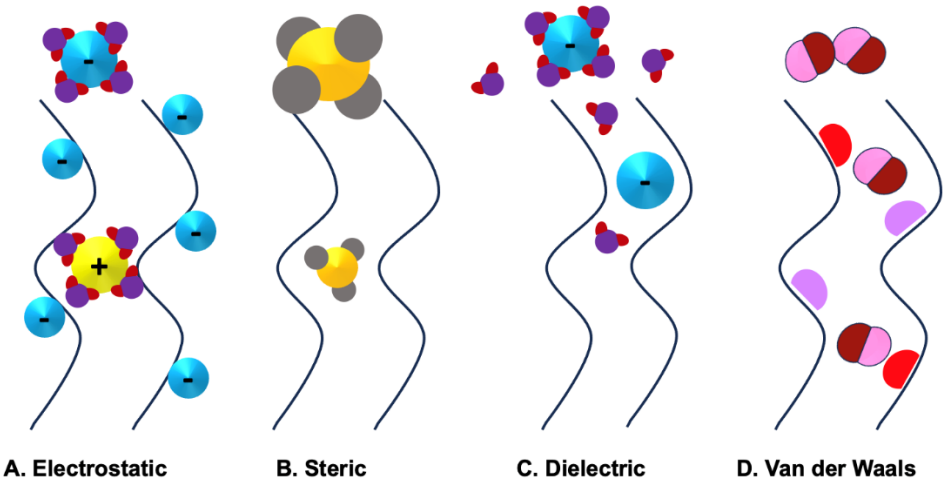

Figure 4: Rate determining mechanisms affecting the permeation of solutes through a molecular-sieving membrane.

II.1.6 Encapsulated Catalytic Target for Selective OER Activity

An approach that differentiates the permeabilities of the water molecules and the chloride ions was considered by designing the deposition of an overlayer with a method for monitoring the thickness. A strategic target was thus conceived that endeavors to promote heterogenous electrocatalysis of the oxygen evolution reaction while preventing the chlorine evolution reaction at the anode. Aspiring to conduct a pragmatic one-pot, sol-gel synthesis of a silica overlayer[35] conducive to this three dimensional system, the encapsulated electrocatalyst is imparted with improved stability in harshly acidic conditions and a deposited coating that has been shown to arrest the species transport of the chloride ion while permitting the oxygen evolution reaction. The overlayer material further consists of a tunable porosity through the versatility of the templating agent. The layer is deposited onto a carbonaceous support of high surface area that prevents aggregation while promoting conduction between the interdispersed iridium nanoparticles of high catalytic surface area. The design is illustrated below in *Figure 5.*

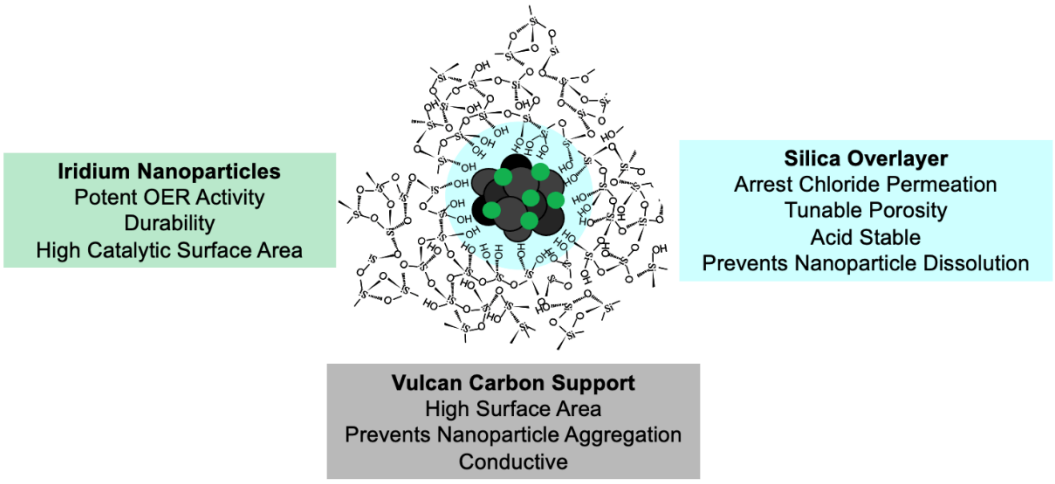

Figure 5: Schematic depiction of the encapsulated nanocatalyst.

Encapsulation of iridium nanoparticles, interdispersed on a conductive carbonaceous support of high surface area to prevent aggregation, is further proposed to hinder dissolution of the iridium nanoclusters, which is known to occur during catalysis of the oxygen evolution reaction[27,36]. Indeed, during anodic polarization, metallic Ir can be oxidized to IrO_2 and enter into the OER reaction or be dissolved into soluble Ir, as discussed previously[36]. This dissolution to Ir^{+3} is thought to be kinetically faster than oxidation to IrO_2 and may degrade the stability of the nanoclusters over the long term[37]. Thus direct formation of an oxide layer at a buried interface between the metal and an overlayer, evidenced to occur on a platinum substrate protected with a silica overlayer, may improve the stability and long-term activity of the iridium catalytic nanoclusters[38].

II.2 Results and Discussion

II.2.1 Morphological Characterization of the Silica Overlayer

II.2.1.1 Optimization of Silica Shell Synthesis with a Vulcan Carbon Core

The silica overlayers investigated herein were deposited through a sol-gel synthesis beginning with the hydrolysis of a precursor silica source, tetraethyl orthosilicate (TEOS), templated with cetyl-trimethylammonium bromide (CTAB); an ammonium hydroxide catalysis was added to promote the hydrolysis. The hydrolyzed precursor was then condensed onto conductive Vulcan Carbon (VC) in this one-pot synthesis shown below in Figure 6. Samples were then subjected to an 80°C ethanolic reflux with 10g/L ammonium nitrate overnight to extract the CTAB.

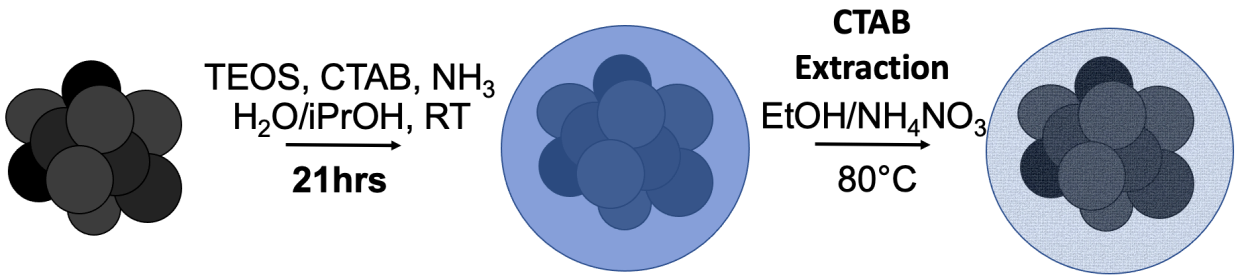

Figure 6: Synthesis scheme of the silica encapsulation of VC.

Syntheses with molar equivalence ratios of the reagents shown below in Table 1 were performed to investigate a range of formulations that would enable the crystallographic organization of the silica overlayer and the structural conformation of the composite material to be probed through transmission electron microscopy (TEM). Samples were isolated after 21 h of reaction.

Table 1: Reagent equivalence ratios utilized to characterize the morphology of the composite material.

Morphological Characteristic	Vulcan Carbon (molar eq.)	TEOS (molar eq.)	CTAB (molar eq.)
Shell Organization	1	5	1.32
	1	5	5
	1	5	10
Composite Structure	1	0.5	1.32
	1	1	1.32
	1	5	1.32
	1	10	1.32
	1	50	1.32

Both the TEM and its Fast Fourier Transform (FFT) image of each reagent equivalence ratio were probed to analyze the composite structure and the organization the silica shell as shown below in *Figure 7.* Firstly, the influence of the TEOS/CTAB ratio on the catalyst shell morphology was studied. High resolution observations (HR-TEM) performed from 125,000x to 840,000x magnification and the FFT images enabled a depiction of the crystallographic organization of the silica shell. *Figure 7a* and *Figure 7b* represent reagent equivalence ratios that probed for silica shell crystallographic organization through changes in the TEOS/CTAB ratio. The lack of a Fourier pattern corresponding to crystalline silica in the FFTs indicated that the silica shell is amorphous. *Figure 7 (c-f)* represent images of reagent equivalence ratios probed through changes in the VC/TEOS ratio for the morphological structure of the composite material and indicated the extent of silica coverage on the carbon supported catalytic nanoparticles. The TEM and FFT images of the 1:5:1.32 VC/TEOS/CTAB reagent equivalence ratio are shown below in *Figure 8.*

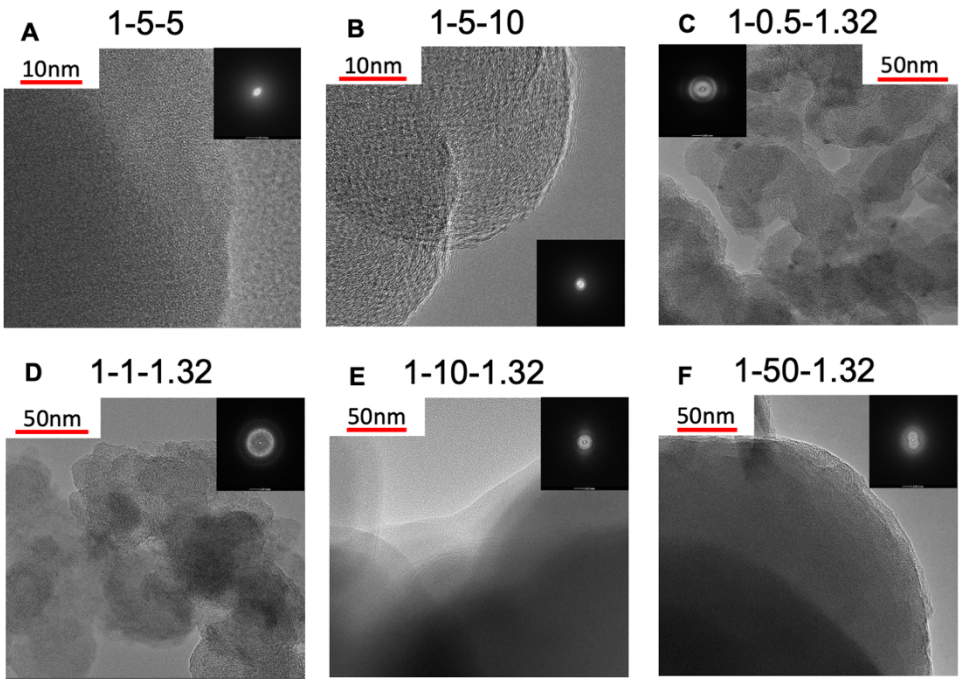

Figure 7: TEM images of the reagent equivalence ratios probing for shell crystallographic organization (a-b) and composite structure (c-f) with the FFT image indicated to probe the crystallographic organization of the silica shell.

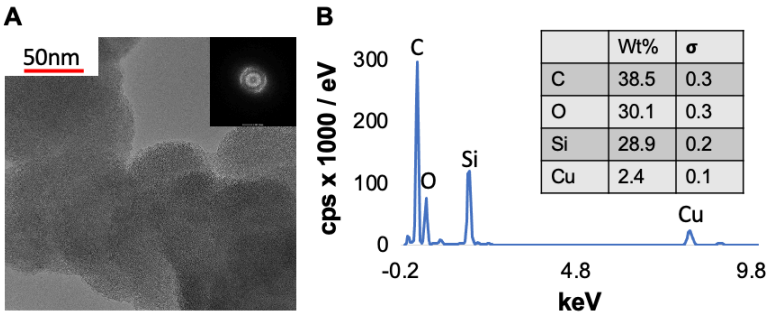

Figure 8: A) TEM image of the 1:5:1.32 reagent equivalence ratio with the FFT of the image shown in the inset. (B) Energy Dispersive X-Ray spectrum confirming the presence of silica.

Figure 8a shows homogeneous coverage of the precursor material at 21 h, and moreover the FFT inset reveals the crystallographic d-spacings of the graphitic carbon. *Figure 8b* depicts the Energy Dispersive X-Ray spectrum (EDS) with peaks pertaining to Silicon, Oxygen, and Carbon. The 1:5:1.32 VC/TEOS/CTAB reagent equivalence ratio was thus chosen for subsequent syntheses and analyses with the catalytic nanoparticle materials as it showed homogeneous coverage of the VC precursor in the TEM imaging with the least quantities of required reagents.

The silica shell appears amorphous in the Fast Fourier Transform imaging depicted in *Figure 7* and *Figure* 8. Subsequent analysis with X-Ray Diffraction (XRD) at low diffraction angles shown below in *Figure 9* indicated a silica cluster width of 71

Å within a pure silica sample synthesized with the 5:1.32 TEOS/CTAB reagent equivalence ratio. Moreover, the VC@21hrSiO_2 measured a cluster width of 44 Å at low angles. The presence of silica in the composite structure further appeared to shift the spectra towards smaller angles; the underlying explanation is considered elusive at present.

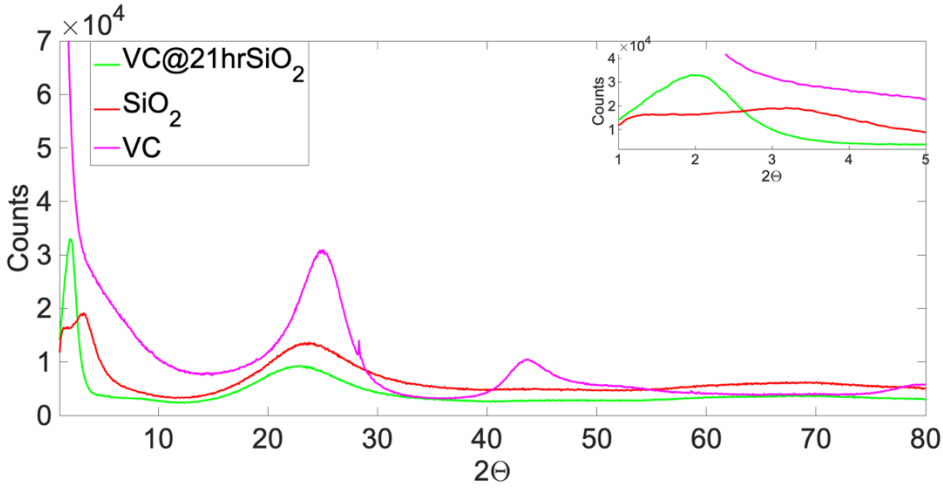

Figure 9: X-Ray diffraction spectra of the VC@21hrSiO_2, a pure silica sample synthesized with the 1:5:1.32 Carbon/TEOS/CTAB reagent equivalence ratio, and the VC. The inset reveals the low angle region of the spectrum.

II.2.1.2 Growth of the Silica Overlayer with the Optimized Ratio 1:5:1.32

The presence of silica is further confirmed through Fourier Transform Infrared Spectroscopy (FTIR). Indeed, the absorbance at 1086 cm^{-1} in *Figure 10a* below indicates the presence of the Si-O-Si symmetrical stretch. A kinetic analysis of the silica growth on the VC@SiO_2 was further conducted by taking aliquots of the optimized 1:5:1.32 Carbon/TEOS/CTAB reagent equivalence ratio synthesis at 15 minutes, 30 minutes, 1 hour, 3 hours, 5 hours, and 21 hours (VC@SiO_2). The total change in transmission at the 1086 cm^{-1} peak was measured for each aliquot, converted to adsorbance, and then plotted in black as shown in *Figure 10b*. The kinetic growth of the silica overlayer through a sol gel synthesis appears to follow a logarithmic trend.

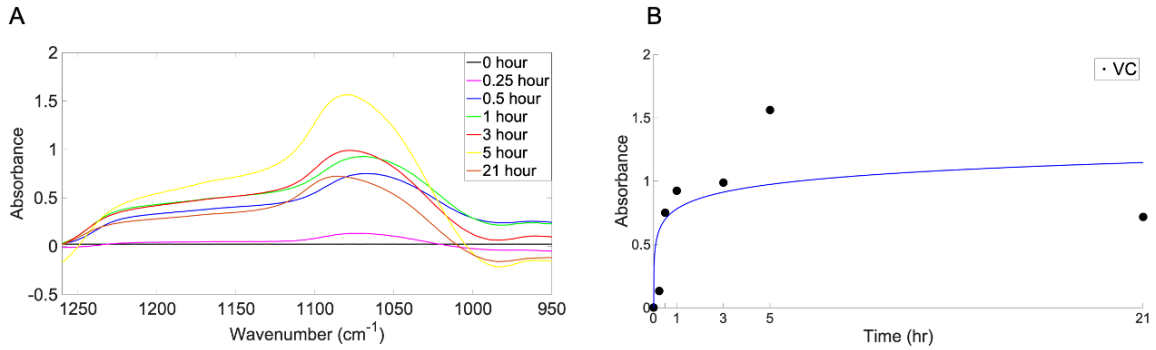

Figure 10: (A) FTIR spectra of the VC@SiO_2 synthesis with the 1:5:1.32 VC/TEOS/CTAB equivalence ratio from 30 minutes to 21 hours after reaction initiation showing an increasing absorbance of the 1086 cm^{-1} symmetric Si-O-Si stretch. (B)

Total transmission of the 1086 cm^{-1} peak was converted to absorbance and plotted as a function of time for the VC@SiO_2 in black with a fitted logarithmic curve in blue.

The conclusions of the studies encapsulating the VC core indicated that the 1:5:1.32 VC/TEOS/CTAB reagent equivalence ratio shows homogeneous coverage of the precursor material and that the silica shell is amorphous with a characteristic cluster width. The growth of the SiO_2 overlayer appears complete according the qualitative interpretation through the FTIR. Though the morphology of the composite material was undiscernible with the VC@21hrSiO_2 and prompted the synthetic encapsulation of the catalytic nanoparticles to provide a crystallographic nanocluster structure of high contrast in the transmission electron imaging to arrive at the structural morphology of the composite materials and enable the thickness of the silica overlayer to be computed.

II.2.2 Synthesis and Characterization of Encapsulated Catalytic Nanoparticles

II.2.2.1 Synthesis of Silica Shell with Ir10 and Pt10 Core Materials

The silica encapsulation was similarly conducted as shown in the synthesis scheme of *Figure 11* below, the green dots represent the iridium catalytic nanoparticles.

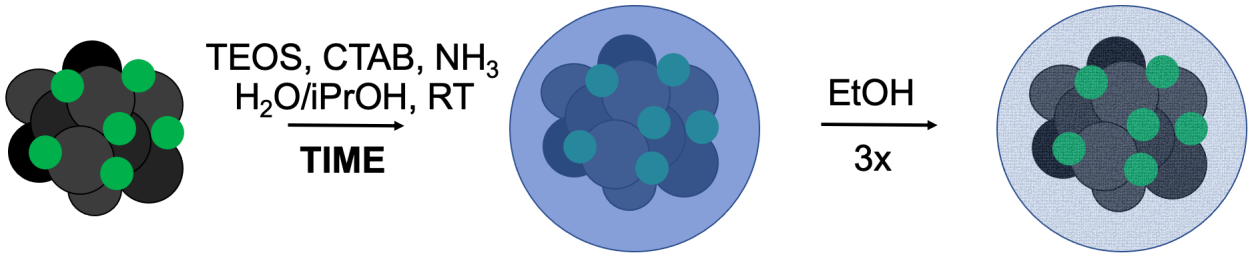

Figure 11: Synthesis scheme of silica encapsulation of Ir10 catalytic nanoclusters.

II.2.2.2 TEM, FTIR, and XRD Characterization of Encapsulated Ir10 and Pt10

Aliquots of the encapsulation at 15 min, 30 min, 1 h, 3 h, 5 h, and 21 h were taken during the syntheses with the Ir10 and Pt10 catalytic precursors; TEM images of the 3 h, 5 h, and 21 h aliquots of the Ir10@SiO_2 encapsulation are represented in *Figure* **12** below.

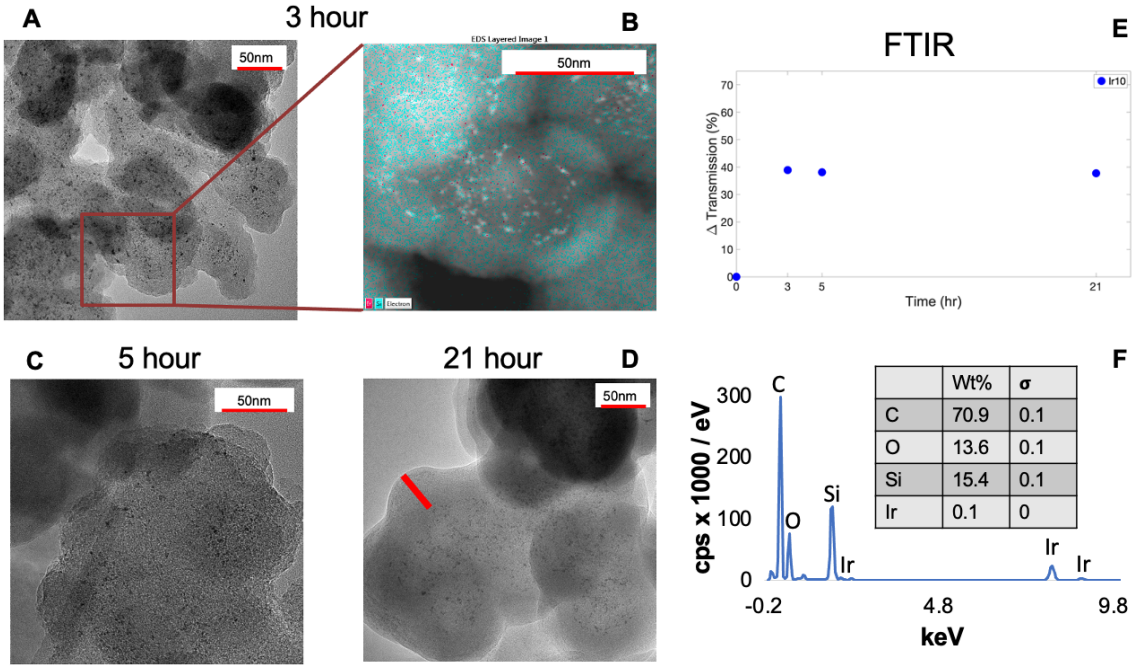

Figure 12: TEM images of aliquots of the Ir10 encapsulation synthesis taken (a) 3 h, (c) 5 h, and (d) 21 h after the commencement of the synthesis; the red line is a representative measurement of the shell thickness. A scanning electron transmission image of the 3 h aliquot is shown in (b) with the iridium indicated in red and the silicon in light blue. A kinetic analysis of the silica growth using FTIR spectroscopy is represented in (e), and the Energy Dispersive X-Ray spectrum confirms the presence of silica, iridium, and carbon as shown in (f).

A scanning transmission electron microscopy image of the Ir10@3hSiO_2 in Figure 12b confirms the presence of silicon, as shown in light blue. The sol gel synthesis of the silica overlayer appears complete at 5 h. Figure 12e represents the kinetic analysis of the silica growth using FTIR spectroscopy; the total change in transmission at the 1086 cm^{-1} peak was measured for the 3h, 5h, and 21h aliquots for the Ir10@SiO_2 and then plotted as shown in blue. It is apparent that the growth of the silica layer approaches saturation at a greater rate for those syntheses conducted with the Ir10 and Pt10 (to be subsequently shown) materials than with the VC precursor material.

Figure 13 represents the native Pt10, the 3 h, the 5 h, and the 21 h aliquots of the Pt10@SiO_2 synthesis. *Figure 13f* represents the kinetic analysis of the silica growth; the total change in transmission at the 1086 cm^{-1} peak was measured for the 3h, 5h, and 21h aliquots for the Pt10@SiO_2 and then plotted as shown in magenta. The sol-gel synthesis reaction appears complete at 5 h.

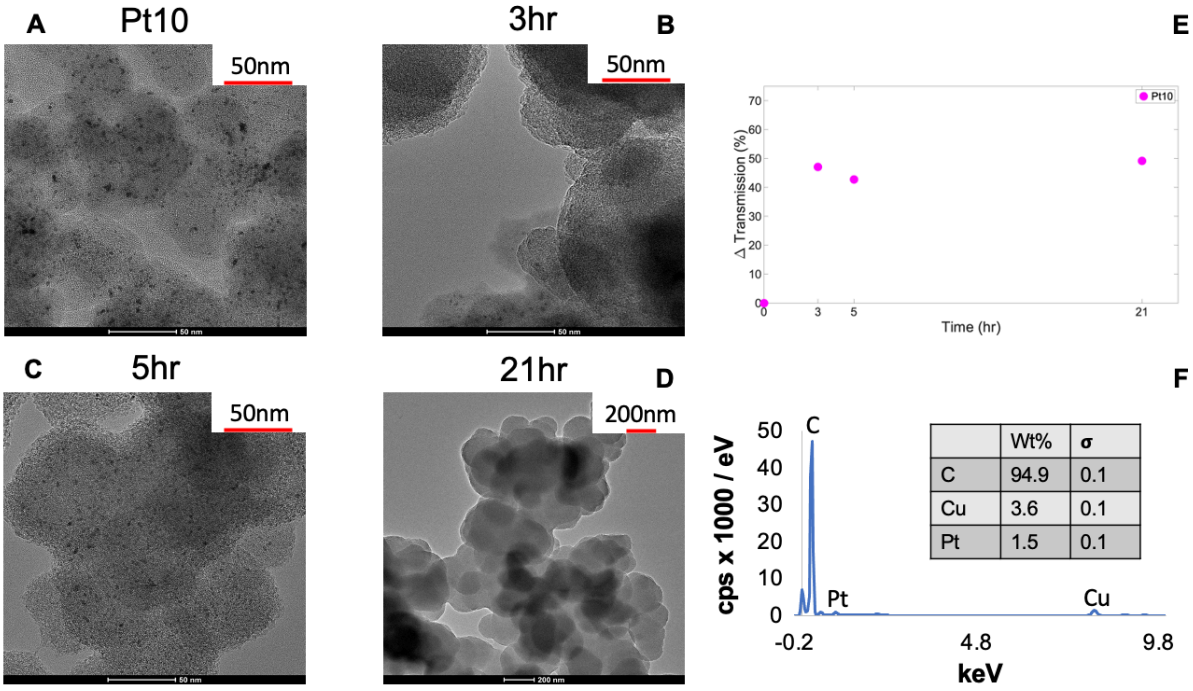

Figure 13: Transmission Electron Microscopy images of the native Pt10 (a) and aliquots of the material taken 3 h (b), 5 h (c), and 21 h (d) after the commencement of the encapsulation synthesis.

3D reconstruction with Electron Tomography of the Ir10@21hrSiO_2 (data not shown) further rendered the interdispersed nanoparticles surrounded by the silica shell, indicating a core-shell morphological structure.

The presence of iridium seems to affect the cluster width within the Ir10@SiO_2 shell according to the X-Ray Diffraction spectra (data not shown); cluster width measurements of 87 Å were computed. Interestingly, these dimensions are expected to create porous elements within the amorphous silica overlayer well above the size of the primary solvating shell of the hydronium ion (diameter 2.82 Å) and the chloride ion (diameter 6.36 Å); thus, these molecules aren't expected to encounter a sieving effect that could hinder transport through the overlayer[32,39,40]. Moreover, this dimensional difference between the cluster width and the hydrated ions indicates that these molecules aren't expected to be subjected to the energy barrier of dehydration that could hinder species transport[8].

II.2.2.3 X-Ray Photoelectron Spectroscopy (XPS) Characterization of Ir10@SiO_2

Elucidating a mechanistic interpretation for the electrocatalytic activity of the encapsulated catalysts towards the oxygen evolution reaction may be revealed by dissecting the oxidation states of the iridium catalysis in the presence of a silica overlayer, which could indicate a potential interaction that may affect the catalytic activity of the nanoparticles. This potential interaction between the silicate overlayer and the iridium catalyst can be analyzed through XPS. Samples of each aliquot were deposited on gold coated silicon wafers and subjected to selected photon irradiation

from an MgKα source, which interacted directly with the electrons of Ir4f orbitals and the Si2p orbitals to measure the characteristic binding energies of these core electrons, as shown in *Figure 14* below.

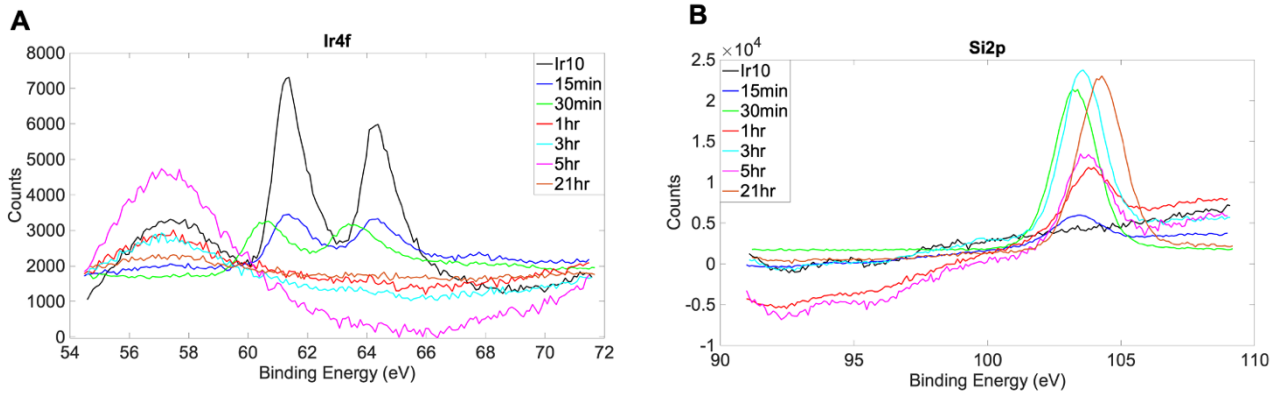

Figure 14: X-ray photoelectron spectra of the Ir10 encapsulated samples indicating the binding energies of the (a) Ir4f electrons and (b) the Si2p electrons throughout the growth of the silica overlayer.

However, the attenuation length of the emitted photoelectrons from the samples is quite low[41], and thus evolution of the binding energies of the Ir4f electrons may be obscured as the silica layer grows, which is apparent; the Ir4f signals decreases quite quickly as the growth of an insulating silica layer begins.

II.2.3 Shell Thickness Estimation

II.2.3.1 Quantification of Ir10@SiO_2 shell thickness

Considering that the encapsulated Ir10@SiO_2 may be represented by a core-shell morphology, localizing the position of the catalytic nanoparticles to delineate the core in the TEM images enabled an estimation thickness of the silica shell encapsulating the Ir10@SiO_2. The theoretical thickness may also be quantified and is calculated according to *Equation 16*; the amount of TEOS added to the reaction is assumed to be completely converted to silica. S^* represents the absolute surface area of the precursor material and m_{SiO_2} represents the calculated mass of silica. The density of silica is represented by ρ_{SiO2} and $m_{c\bullet m}$ is the precursor material mass.

$$\text{Theoretical Thickness} = \frac{m_{SiO_2}}{\rho_{SiO_2} m_{c\bullet m} S^*} \tag{16}$$

The theoretical thickness was calculated to be 34 nm. Experimentally, m_{SiO_2} was determined through Thermogravimetric Analysis (TGA) to compute the silica shell thickness of Ir10@SiO_2 with *Equation 12*. Indeed, the experimentally measured masses of silica remaining in the Ir10@SiO_2 after combustion with TGA were calculated for each aliquot; moreover, considering that the pure Vulcan carbon began to decompose at 600°C (data not shown) and that decomposition of silica begins above the experimental 1100°C temperature limit at positive O_2 partial pressures, deconvolution of the composite mass through calculation of the mass

losses rendered through TGA is expected to resolve the residual mass of silica and Iridium[42]. Iridium was further subtracted from this residual mass by considering that it comprised 10% by weight of the precursor carbon supported material. The corresponding thickness for the 1 h, 3 h, 5 h, and 21 h aliquots of the Ir10@SiO_2 were computed and plotted below in Figure *15* in blue; these values can be compared to the values shown in red of Figure 15 computed from the TEM images of Figure 12 which were calculated through the average of 50 measurements in Image J.

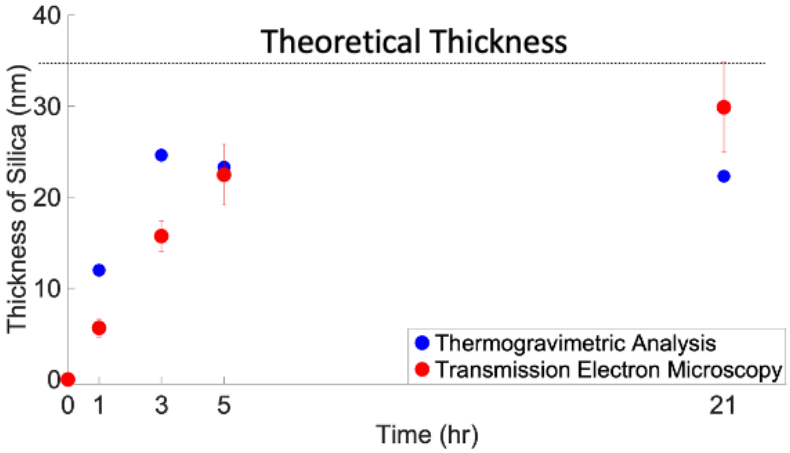

Figure 15: Thickness of the silica overlayer determined by TGA in blue and TEM in red for each time aliquot of the Ir10@SiO_2 synthesis with the dotted line indicating the theoretical thickness value of 34 nm. The difference between the thicknesses calculated by TGA and those calculated by TEM may be attributed to the presence of a separate population of SiO_2 particles in the aliquot samples.

The thickness value measured with TEM of the Ir10@21hSiO_2 aliquot approaches the theoretical value of 34 nm and the thickness of the Ir10@21hSiO_2 measured with TGA approaches values just below of 22 nm.

II.2.4 Electrochemical Characterization

II.2.4.1 Electrocatalytic Activity Evaluation of Ir10@21hSiO_2 towards the OER

The electrochemical characteristics of the encapsulated catalytic materials were evaluated for activity towards the OER by performing linear sweep voltammetry (LSV). Films of the Ir@21hSiO_2 and the Pt10@21hSiO_2 were prepared as described in the Appendix. A film schematic on the working electrode is depicted in *Figure 16* below. The homogenized solution is drop casted onto the working electrode, a rotating disk electrode that enables steady state conditions to be attained for mass transport limited reactions and electron transfer kinetics to be studied. All potential ranges are compared to the reversible hydrogen electrode (RHE).

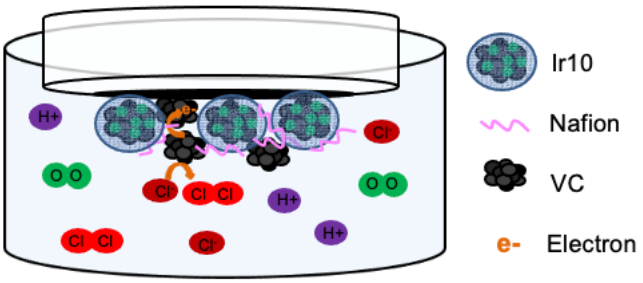

Figure 16: Schematic of a typical film on the working electrode with Ir10@21hSiO_2 depicted. The VC, Nafion, and chlorine evolution reaction are shown in an acidic, salinated solution.

The rotating disk electrode was arranged in a three-electrode set-up in a 0.1 N H_2SO_4 supporting electrolyte (pH 1.3) at 25°C with a silver/silver chloride reference electrode that allows the potential applied to the working electrode to be measured, and with a platinum counter electrode to supply electrons for the reaction at the working electrode. A scan rate of 10 mV/sec was first applied and the potential was positively swept to measure the oxidation current and then reversed at the positive vertex. The film was then subjected to 10 conditioning cycles between 0.680 V and 0.180 V vs. RHE at 200 mV/s followed by a scan recorded at 10 mV/sec; this sequence was repeated until a stabilized forward scan was obtained. Trials were conducted in 0.1 N H_2SO_4 and also in 0.1 N H_2SO_4 with a 0.5 M NaCl concentration to mimic the chloride concentration in seawater. The reduction current was also studied in 0.1 N H_2SO_4 supporting electrolyte to maximize the proton conduction by applying a negative potential sweep and then reversing the potential at the negative vertex; each scan was also followed with conditioning cycles performed at a 200mV/sec scanning rate until stable current reading at the vertex was obtained (not shown). The current metric of 10 mA/cm^2 was used to determine the potential range that was scanned as this value is a generally accepted metric within the literature.

The voltammograms of *Figure 17* below represent a comparison of the potentials required to approach oxidative current densities of 10 mA/cm^2 for Ir10, Ir10@21hSiO_2, and VC; the solid curves represent measurements in the acidic supporting electrolyte and the dotted curves represent the measurements in the acidic supporting electrolyte with 0.5 M NaCl concentration.

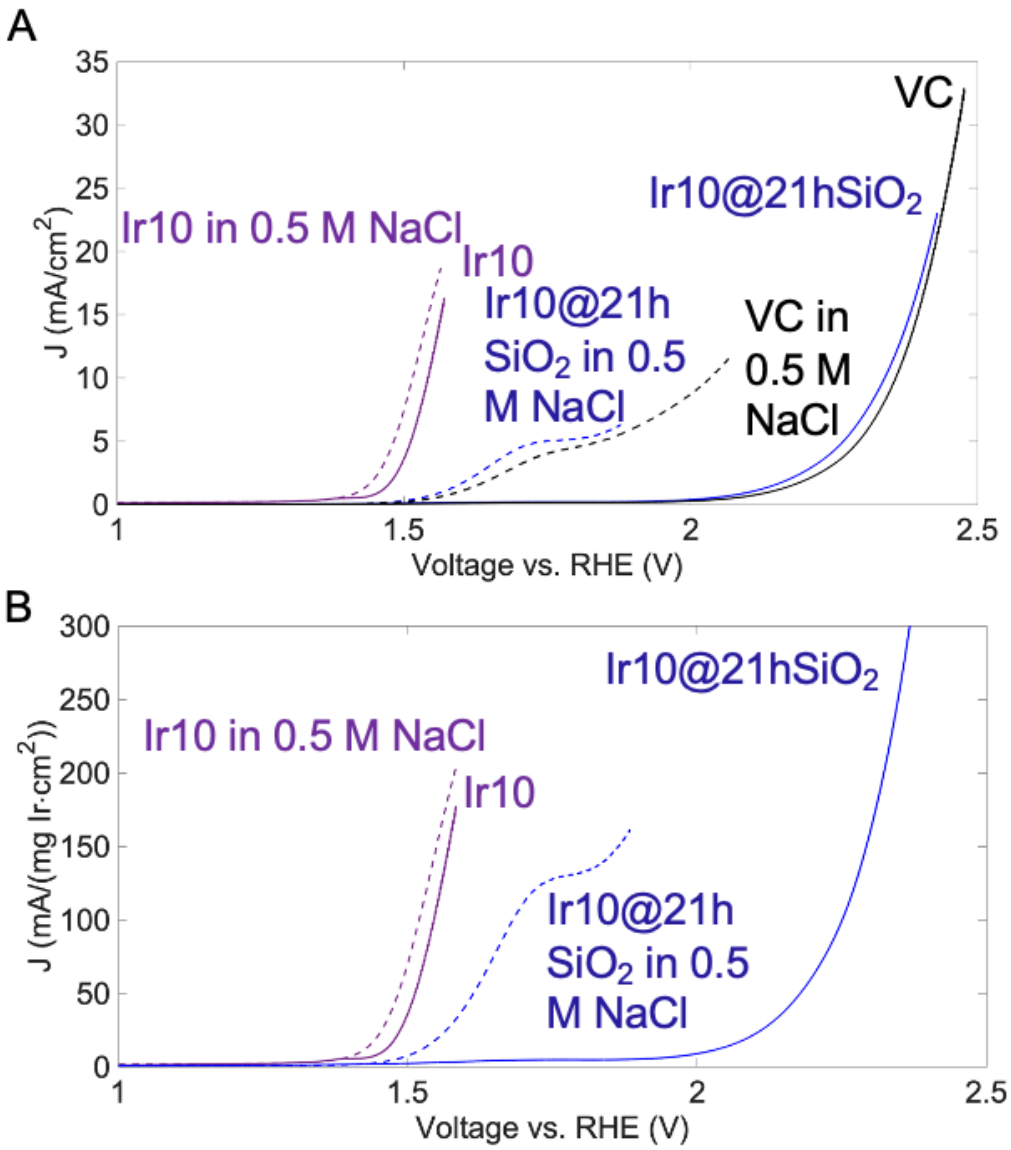

Figure 17: (A) Voltammograms of the precursor Ir10 in purple and the Ir10@21hSiO$_2$ in blue trialed at pH 1.3 supporting electrolyte in the solid curves and at pH 1.3 with a 0.5 M NaCl solution along the dotted curves. Voltammograms of pure VC are shown in black. (B) Native Ir10 and Ir10@21hSiO$_2$ voltammograms normalized by the mass of iridium deduced from the TGA analysis.

The film of Ir10 on the working electrode shown in purple in *Figure 17* is swept towards positive potentials and oxidative currents of 10 mA/cm^2 are reached around 1.51 V vs. RHE in the acidic supporting electrolyte, demonstrating an overpotential for OER of about 300 mV. The overpotential decreases by about 30 mV to 1.47 V vs. RHE in the acidic supporting electrolyte with 0.5 M NaCl, as shown in the purple dotted line. This observed decrease in potential in saline solutions to reach the metric of 10 mA/cm^2 is indicative of chloride being oxidized to chlorine in the chlorine evolution reaction with the Ir10 catalyst[43]. Indeed, the characteristic odor of chlorine gas was

detectable; quantification of the evolved chlorine gas may be conducted with the use of a rotating ring-disk electrode and a bipotentiostat, which at the time of the analysis was not available[21]. Moreover, Vos et. al. observed the same phenomenon in the current voltage characteristics of a glassy carbon working electrode electroflocculated with IrO_2 nanoparticles upon the addition of hydrochloric acid to a supporting electrolyte solution of 0.5 M $HClO_4$, and moreover found the presence of the chloride ion to decrease the activity of the OER, which was found, as discussed previously, to be caused by competitive absorption that blocks active sites and retards the OER, noting that the selectivity of the OER sharply decreases upon the addition of the chloride ion[43,44].

The potentials increase more positively as the overpotential increases by about 1 V to 2.25 V in 0.1 N H_2SO_4 supporting electrolyte for the Ir10@21hSiO_2 material as shown in the solid blue curve of *Figure 17*. Interestingly, the current voltage characteristic of the Ir10@21hSiO_2 depicts only a slightly greater overpotential than the Ir10 material in the acidic, saline supporting electrolyte. Moreover, similar current densities in the acidic supporting electrolyte and the acidic saline supporting electrolyte were achieved for scans with drop casts of pure Vulcan carbon on the working glassy carbon electrode as shown in the black solid and dotted lines of *Figure 17,* respectively. Observing that both the Ir10@21hSiO_2 and the VC materials achieve similar current density characteristics indicates that encapsulating the material with an SiO_2 overlayer approaching a thickness of 34 nm effectively arrests the oxidizing species from transporting towards the catalytic nanoclusters and/or prevents the electrons from conducting away from the Vulcan carbon that surrounds the iridium catalytic centers of the core Ir10 material[45]. Indeed, Fujii et. al. proposed the electron conduction pathway of a similar carbon black composite material encapsulated by silica layers to be through the exposed carbon black surfaces and found those particles with a 5nm SiO_2 coverage to have a lower electrochemical surface area[46]. The observed current densities at lower overpotentials in the dotted lines of *Figure 17* can thus be the result of chloride ions diffusing directly through the film and reaching the glassy carbon electrode where oxidation can occur directly; linear sweep voltammetry of pure Nafion films showed similar current densities in saline acidic supporting electrolyte indicating that this oxidation can indeed occur directly on glassy carbon[47]. The chloride ions can also become oxidized on the Vulcan carbon and initiate electron conduction through the movement of holes within the graphitic domains of the VC additive in the film; these aggregates of carbon nanoparticles allow for electron tunneling across the particle-particle contacts to the glassy carbon electrode[48].

Furthermore, the large overpotentials observed in the current-voltage characteristics of the Ir10@21hSiO_2 and VC were similarly observed by Yi, Y et. al. on a pure glassy carbon electrode within an acidic supporting electrolyte following scans at anodic potentials, implying that water may diffuse directly through the film and become oxidized at the glassy carbon electrode[49]. Smaller overpotential measurements were observed for an Ir10@3hSiO_2 material in the acidic, saline supporting electrolyte though TEM images indicated that complete coverage of the material hadn't been achieved.

II.2.4.2 Electrocatalytic Activity Evaluation of Pt10@21hSiO$_2$ towards the OER

The current-voltage characteristics of the Pt10@21hSiO$_2$ were also acquired and are shown in *Figure 18*. The precursor Pt10 and the Pt10@21hSiO$_2$ were each weighted into a film and drop casted on the glassy carbon working electrode with the same procedure that was conducted for the Ir10@21hSiO$_2$.

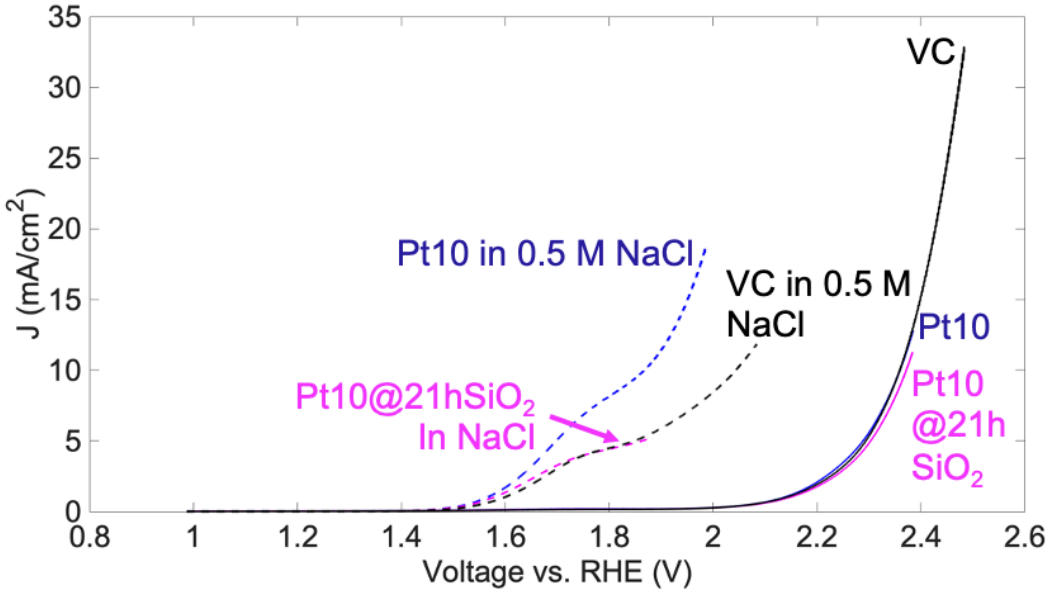

Figure 18: Voltammograms of the precursor Pt10 in purple and the encapsulated Pt10@21hSiO$_2$ in blue trialed at pH 1.3 supporting electrolyte in the solid curves and at pH 1.3 with a 0.5M NaCl along the dotted curves. The VC is shown in black trialed in acidic supporting electrolyte (solid line) and acidic, salinated supporting electrolyte (dotted line).

The solid curves of *Figure 18* represent the scans in 0.1 N H_2SO_4 supporting electrolyte and the dotted curves represent the scans taken in 0.1 N H_2SO_4 with 0.5 M NaCl. It is apparent that the precursor Pt10 reaches an oxidative current density of 10 mA/cm^2 at a large overpotential of about 2.30 V, indicating a fable activity towards catalyzing the OER reaction. Similar results have been demonstrated by Reier et. al. who found Pt nanoparticles to display low OER activity and were completely deactivated during an OER stability protocol; the increased oxophilicity of Pt nanoparticles was thought to promote oxidation of the nanoparticles, leading to a growth of an insulating oxide layer that inhibits electron conduction[50]. These results suggest that the observed current density similarly arises from the electron conduction through the Vulcan carbon and from the direct oxidation of water at the glassy carbon electrode[48,49]. The lower overpotentials displayed in the current voltage characteristics of the Pt10 and Pt10@21hrSiO$_2$ in the acidic saline supporting electrolyte indicate a similar conduction pathway as the iridium materials above in which the chloride either diffuses or migrates toward the glassy carbon electrode to be oxidized and initiates electron conduction through oxidation on the Vulcan carbon in the film.

Selectivity for the oxygen evolution reaction had been reported by Bhardwaj et. al. who had used a photochemical process in which the precursor dimethylsiloxane

was spin coated onto a Pt thin film and subjected to UV-generated ozone to generate silica layers that decreased the chloride concentration at the buried interface from the bulk solution by two orders of magnitude[20]. Moreover, silica layer thicknesses of 1.2, 2.9, 4.8, 5.4, and 8.7 nm were compared and a decrease in the OER activity was found upon increasing the shell thickness; current-voltage characteristics are displayed below in *Figure 19*[20].

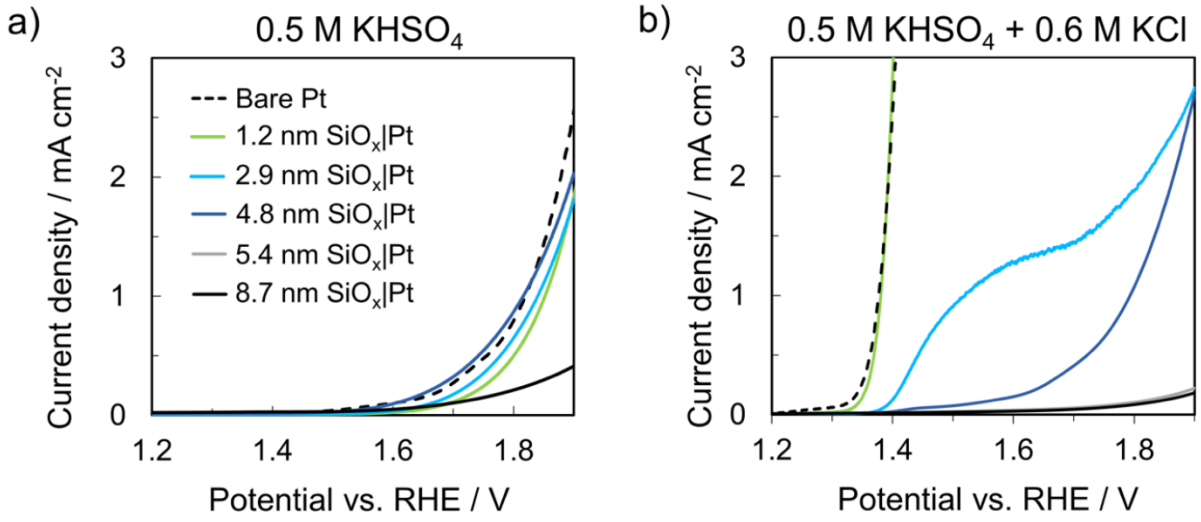

Figure 19: Taken from Bhardwaj et. al. supporting information. "LSV measurements for SiO_x/Pt electrodes with varying overlayer thickness and bare Pt in a) 0.5 M $KHSO_4$ and b) 0.5 M $KHSO_4$ + 0.6 M KCl. All measurements were performed at 20 mV/sec in deaerated electrolytes at pH 0.8 and 25°C. The legend in a) applies to the LSV curves in both a) and b)."

These SiO_2 overlayers were demonstrated to effectively impede the transport of the chloride ion, which was proposed to be caused by an energy barrier to dehydration in which the bonds between the water molecules and the ion must be rearranged or removed in order to transverse the disordered, sub-nanometer-sized free volume elements of the silica overlayer, as introduced in the introduction[8,20]. However, as demonstrated in *Figure 19*, as the shell thickness increases above 4.8 nm, the oxygen evolution reaction current density also begins to decrease, and thus the shell may be too thick to enable adequate diffusion of the water species at the scan rates utilized. Considering that the shell thickness of the Pt10@21hSiO_2 in our study measured by TEM approaches a value of 30 nm upon encapsulation, similar to the shell thickness measured for the encapsulated Ir10@21hSiO_2, this cited study indicates that the Pt10@21hSiO_2 wouldn't be expected to produce high OER current densities.

Moreover, considering that the catalytic nanoclusters aren't in direct contact with the electrode as was the platinum thin film in the Bhardwaj study, the shell thickness is expected to be a crucial parameter to selectively arrest the permeability of the chloride ion; these two parameters were derived in the introduction to have an inversely proportional relationship. Though, it also must be optimized to selectively permit OER reactant and product diffusion and crucially electron transport toward and

from the electrocatalytic material. Indeed, Szunerits et. al. were able to perform cyclic voltammetry on silica layer film thicknesses only smaller than 9 nm and further found the interface capacitance to be dependent on the thickness of the silica layer[51].

II.2.5 Modifying the Surface Charge of the Silica Overlayer

The species transport through the overlayer may moreover be modulated by the mechanism of electrostatic interactions discussed in the introduction[52-54]. Indeed, the presence of silanol moieties on the surface of the silica overlayer creates an electrostatic leverage that can affect the species transport of the chloride ion. The locas of ions with high chemical affinity for the surface silanol groups, such as the protons in solution, is within the inner Helmholtz plane of the electrical double layer. The calculated point of zero charge (PZC) of these silanol groups is known to lie between 1 and 3 pH units[55,56]. Indeed, comparison of the current evolved in the voltammogram at pH 0 of Ir10 in *Figure 20a* with that of Ir10@21hSiO$_2$ in *Figure 20b* indicates that the positively charged silica overlayer may be affecting the species transport of the protons, encumbering the electrocatalytic evolution of oxygen by the iridium nanoclusters.

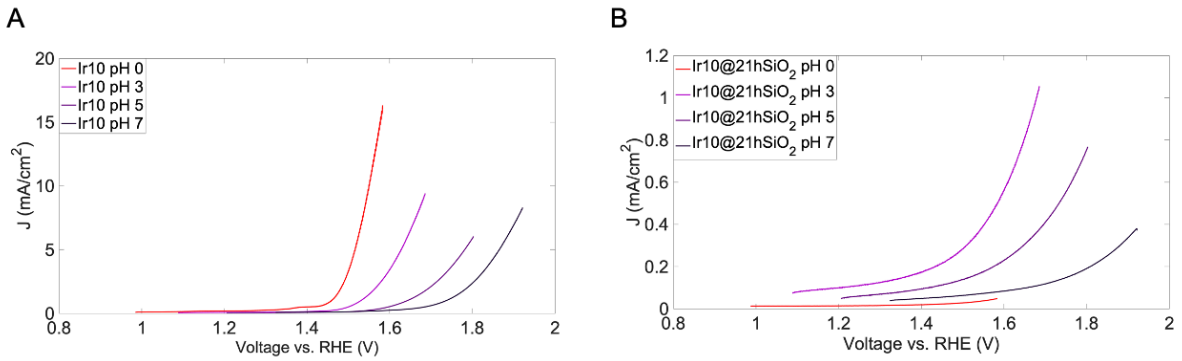

Figure 20: Linear scanning voltammograms of an (A) Ir10 electrocatalytic film and an (B) Ir10@21hSiO$_2$ electrocatalytic film at different pH values. The pH 0 solution and the pH 3 solution were prepared utilizing sulfuric acid while correcting for the ionic strength, and the pH 5 and pH 7 solutions were prepared with a phosphate buffer system.

The PZC can differ from the isoelectric point, which indicates the pH at which the zeta potential equals zero[57]. This potential refers to the potential at the slip plane just outside the outer Helmholtz layer with respect to the bulk solution. Nonetheless, the Zeta potentials of the Ir10 precursor and the Ir10@21hSiO$_2$ were taken at pH 0, 3, 5, and 7 and plotted in *Figure 21*.

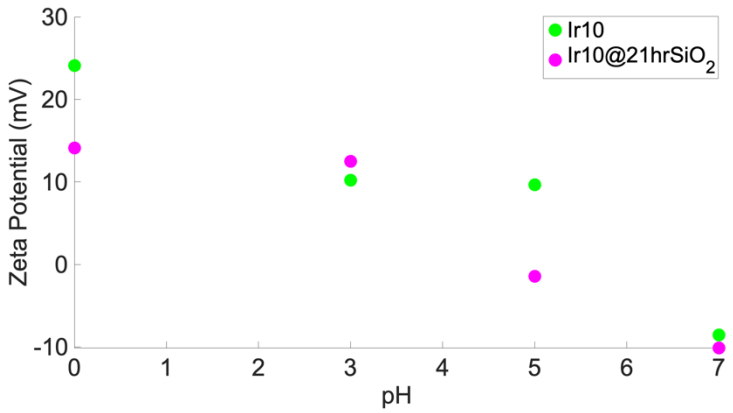

Figure 21: Zeta potential of the native Ir10 material in green and the Ir10@SiO_2 in magenta as a function of increasing pH.

The zeta potential values of both the Ir10 and Ir10@21hSiO_2 appear positive in highly acidic pH conditions. The measured negative zeta potential of Ir10@21hSiO_2 at pH 5 suggests that the potential between the slip plane lying just outside the outer Helmholtz layer and the bulk solution has a net negative charge. The isoelectric point appears to be about 4.7 pH units. Thus, Cl^- ions are expected to be more permeable at low pH values. The zeta potential of the native Ir10 becomes negative at pH 7 suggesting the presence of basic functionalities on the surface of the VC supporting material. Considering that the fixed charges within the core and overlayer may attract or repel solutes to varying degrees, permeability through the overlayer is thus shown to be affected by the species charge state. Therefore, a strategy could be implemented towards the design of a permselective overlayer that mitigates charge repulsion at acidic pH values through silane coupling chemistry to permit the passage of predominate water species while inhibiting the passage of the chloride ion[58].

II.3 Conclusion

Realizing the urgency of a needed energy alternative that is sustainable for our globally increscent societies elicits the utilization of seawater for the production of the hydrogen energy vector, representing a potent initiative, though with challenges that remain to be overcome. The catalytic design at the anode is surfacing to be of paramount importance as the sluggish rate of the OER continues to impede the overall electrolytic rate of water splitting. Splitting seawater is moreover shown to further complicate this catalysis; in particular, its ionic constituents can compete with water at the anodic catalytic sites and cause unwanted side reactions that further impede the catalytic decomposition. This work has engendered to synthesize a protective overlayer composed of silica proposed to hinder the species transport of the chloride ion. Synthesis formulations were optimized through TEM analysis to promote homogenous surface coverage of the precursor carbon supported catalytic nanoparticles with minimal reagent quantities. The kinetic growth of the overlayer was accessed through FTIR spectroscopy and the thickness of the silica layer encasing the composite material was further determined through TEM and TGA analysis. XRD results indicated a cluster width of 87 Å within the silica overlayer encompassing the

iridium catalyst. This width is expected to render pores between the clusters that are greater than the hydrated diameter of both the chloride ion and water molecule and may relegate the diffusion selectivity of the membrane to that which is enthalpically achievable. An analysis of the potential interactions between the iridium catalyst and the silica overlayer was attempted through X-Ray Photoelectron Spectroscopy; analysis of the Tougaard background of the XPS spectra could give another indication of the thickness of the silica layer. The electrocatalytic activity of the encased material towards the selective evolution of oxygen was moreover accessed through the preparation of a catalytic film drop-casted onto a glassy carbon electrode evaluated with linear sweep voltammetry. Results and comparisons with the literature indicate that the integration of the encapsulated composite material into a catalytic film is underscored by the importance of electronic conductivity in the design of a film homogenized with catalytic nanoparticles. The experimentally determined thickness approached the theoretically value of 34 nm according to the HR-TEM and Electron Tomography, well above referenced literature values; thus, the thickness of the overlayer may indeed be crucial to promote electron transfer through the overlayer and towards the electrode surface. Further studies are proposed to modify the composition of the overlayer material to promote electron transfer while selectively impeding the species transport of the chloride ion. Mitigation of its diffusion by addressing the enthalpic and entropic selectivity of the overlayer may indeed further this potent initiative to go beyond the upper bound and realize a potent solution.

II.4 References

1 Harvey, C. *Dissertation Chapter 1: Figure 4* PhD thesis, Ecole Polytechnique, (2024).

2 Bard, A. J. F., Larry R., White, Henry S. *Electrochemical Methods: Fundamentals and Applications*. 3rd edn. John Wiley & Sons.(2022).

3 Dickinson, E. J. F., Limon-Petersen, J. G., Rees, N. V. & Compton, R. G. How Much Supporting Electrolyte Is Required to Make a Cyclic Voltammetry Experiment Quantitatively "Diffusional"? A Theoretical and Experimental Investigation. *J. Phys. Chem. C* **113**, 11157-11171 (2009). https://doi.org/10.1021/jp901628h

4 Baker, R. W. *Membrane Technology and Applications*. 15-27. John Wiley & Sons, Ltd.(2012).

5 Koros, W. J. & Zhang, C. Materials for next-generation molecularly selective synthetic membranes. *Nat. Mater.* **16**, 289-297 (2017). https://doi.org/10.1038/nmat4805

6 Petropoulos, J. H. Some fundamental approaches to membrane gas permeability and permselectivity. *J. Membr. Sci.* **53**, 229-258 (1990). https://doi.org/10.1016/0376-7388(90)80017-G

7 Zwolinski, B. J., Eyring, H. & Reese, C. E. Diffusion and Membrane Permeability. *J. Phys. Colloid Chem.* **53**, 1426-1453 (1949). https://doi.org/10.1021/j150474a012

8 Epsztein, R., DuChanois, R. M., Ritt, C. L., Noy, A. & Elimelech, M. Towards single-species selectivity of membranes with subnanometre pores. *Nat. Nanotechnol.* **15**, 426-436 (2020). https://doi.org/10.1038/s41565-020-0713-6

9 Eyring, H. The theory of absolute reaction rates. *Trans. Faraday Soc.* **34**, 41-48 (1938). http://dx.doi.org/10.1039/TF9383400041

10 B. Hammer, J. K. N. Theoretical Surface Science and Catalysis - Calculations and Concepts. *Adv. Catal.* **45**, 71 (2000). https://doi.org/10.1016/S0360-0564(02)45013-4

11 Robeson, L. M. Correlation of separation factor versus permeability for polymeric membranes. *J. Membr. Sci.* **62**, 165-185 (1991). https://doi.org/10.1016/0376-7388(91)80060-J

12 Robeson, L. M. The upper bound revisited. *J. Membr. Sci.* **320**, 390-400 (2008). https://doi.org/10.1016/j.memsci.2008.04.030

13 Park, H. B., Kamcev, J., Robeson, L. M., Elimelech, M. & Freeman, B. D. Maximizing the right stuff: The trade-off between membrane permeability and selectivity. *Science* **356**, eaab0530 (2017). https://doi.org/10.1126/science.aab0530

14 Geise, G. M., Park, H. B., Sagle, A. C., Freeman, B. D. & McGrath, J. E. Water permeability and water/salt selectivity tradeoff in polymers for desalination. *J. Membr. Sci.* **369**, 130-138 (2011). https://doi.org/10.1016/j.memsci.2010.11.054

15 Werber, J. R., Osuji, C. O. & Elimelech, M. Materials for next-generation desalination and water purification membranes. *Nat. Rev. Mater.* **1**, 16018 (2016). https://doi.org/10.1038/natrevmats.2016.18

16 Yang, Z., Guo, H. & Tang, C. Y. The upper bound of thin-film composite (TFC) polyamide membranes for desalination. *J. Membr. Sci.* **590**, 117297 (2019). https://doi.org/10.1016/j.memsci.2019.117297

17 Yang, Z. *et al.* A Critical Review on Thin-Film Nanocomposite Membranes with Interlayered Structure: Mechanisms, Recent Developments, and Environmental Applications. *Environ. Sci. Technol.* **54**, 15563-15583 (2020). https://doi.org/10.1021/acs.est.0c05377

18 Singh, R. Production of high-purity water by membrane processes. *Desalination and Water Treatment* **3**, 99-110 (2009). https://doi.org/10.5004/dwt.2009.443

19 Gin, D. L. & Noble, R. D. Designing the Next Generation of Chemical Separation Membranes. *Science* **332**, 674-676 (2011). https://doi.org/10.1126/science.1203771

20 Bhardwaj, A. A. *et al.* Ultrathin Silicon Oxide Overlayers Enable Selective Oxygen Evolution from Acidic and Unbuffered pH-Neutral Seawater. *ACS Catal.* **11**, 1316-1330 (2021). https://doi.org/10.1021/acscatal.0c04343

21 Vos, J. G., Wezendonk, T. A., Jeremiasse, A. W. & Koper, M. T. M. MnOx/IrOx as Selective Oxygen Evolution Electrocatalyst in Acidic Chloride Solution. *J. Am. Chem. Soc.* **140**, 10270-10281 (2018). https://doi.org/10.1021/jacs.8b05382

22 Fujimura, K. *et al.* Anodically deposited manganese-molybdenum oxide anodes with high selectivity for evolving oxygen in electrolysis of seawater. *J. Appl. Electrochem.* **29**, 769-775 (1999). https://doi.org/10.1023/A:1003492009263

23 Jiang, S., Liu, Y., Qiu, H., Su, C. & Shao, Z. High Selectivity Electrocatalysts for Oxygen Evolution Reaction and Anti-Chlorine Corrosion Strategies in Seawater Splitting. *Catalysts* **12** (2022). <https://doi.org/10.3390/catal12030261>.

24 Balaji, R. *et al.* An alternative approach to selective sea water oxidation for hydrogen production. *Electrochem. Commun.* **11**, 1700-1702 (2009). https://doi.org/10.1016/j.elecom.2009.06.022

25 Venkatkarthick, R. *et al.* Studies on polymer modified metal oxide anode for oxygen evolution reaction in saline water. *J. Electroanal. Chem.* **697**, 1-4 (2013). https://doi.org/10.1016/j.jelechem.2013.02.015

26 Obata, K. & Takanabe, K. A Permselective CeOx Coating To Improve the Stability of Oxygen Evolution Electrocatalysts. *Angew. Chem. Int. Ed.* **57**, 1616-1620 (2018). https://doi.org/10.1002/anie.201712121

27 Liu, Q., Ranocchiari, M. & van Bokhoven, J. A. Catalyst overcoating engineering towards high-performance electrocatalysis. *Chem. Soc. Rev.* **51**, 188-236 (2022). http://dx.doi.org/10.1039/D1CS00270H

28 Pourbaix, M. *Atlas of Electrochemical Equilibria in Aqueous Solutions*. National Association of Corrosion Engineers.(1974).

29 Beatty, M. E. S., Gillette, E. I., Haley, A. T. & Esposito, D. V. Controlling the Relative Fluxes of Protons and Oxygen to Electrocatalytic Buried Interfaces with Tunable Silicon Oxide Overlayers. *ACS Appl. Energy Mater.* **3**, 12338-12350 (2020). https://doi.org/10.1021/acsaem.0c02359

30 Robinson, J. E., Labrador, N. Y., Chen, H., Sartor, B. E. & Esposito, D. V. Silicon Oxide-Encapsulated Platinum Thin Films as Highly Active Electrocatalysts for Carbon Monoxide and Methanol Oxidation. *ACS Catal.* **8**, 11423-11434 (2018). https://doi.org/10.1021/acscatal.8b03626

31 Ouyang, M., Muisener, R. J., Boulares, A. & Koberstein, J. T. UV–ozone induced growth of a SiOx surface layer on a cross-linked polysiloxane film: characterization and gas separation properties. *J. Membr. Sci.* **177**, 177-187 (2000). https://doi.org/10.1016/S0376-7388(00)00471-3

32 Marcus, Y. Ionic radii in aqueous solutions. *Chem. Rev.* **88**, 1475-1498 (1988). https://doi.org/10.1021/cr00090a003

33 Sun, P. *et al.* Selective Trans-Membrane Transport of Alkali and Alkaline Earth Cations through Graphene Oxide Membranes Based on Cation−π Interactions. *ACS Nano.* **8**, 850-859 (2014). https://doi.org/10.1021/nn4055682

34 Zhang, H. *et al.* Ultrafast selective transport of alkali metal ions in metal organic frameworks with subnanometer pores. *Sci. Adv.* **4**, eaaq0066 (2018). https://doi.org/10.1126/sciadv.aaq0066

35 Daoura, O. *et al.* One-pot prepared mesoporous silica SBA-15-like monoliths with embedded Ni particles as selective and stable catalysts for methane dry reforming. *Applied Catalysis B: Environmental* **280**, 119417 (2021). https://doi.org/10.1016/j.apcatb.2020.119417

36 Kasian, O., Grote, J.-P., Geiger, S., Cherevko, S. & Mayrhofer, K. J. J. The Common Intermediates of Oxygen Evolution and Dissolution Reactions during Water Electrolysis on Iridium. *Angew. Chem. Int. Ed.* **57**, 2488-2491 (2018). https://doi.org/10.1002/anie.201709652

37 Lončar, A., Escalera-López, D., Cherevko, S. & Hodnik, N. Inter-relationships between Oxygen Evolution and Iridium Dissolution Mechanisms. *Angew. Chem. Int. Ed.* **61**, e202114437 (2022). https://doi.org/10.1002/anie.202114437

38 Beatty, M. E. S., Chen, H., Labrador, N. Y., Lee, B. J. & Esposito, D. V. Structure–property relationships describing the buried interface between silicon oxide overlayers and electrocatalytic platinum thin films. *J. Mater. Chem. A.* **6**, 22287-22300 (2018). http://dx.doi.org/10.1039/C8TA06969G

39 Madauß, L. *et al.* Selective Proton Transport for Hydrogen Production Using Graphene Oxide Membranes. *J. Phys. Chem. Lett.* **11**, 9415-9420 (2020). https://doi.org/10.1021/acs.jpclett.0c02481

40 Mi, B. Graphene Oxide Membranes for Ionic and Molecular Sieving. *Science* **343**, 740-742 (2014). https://doi.org/10.1126/science.1250247

41 Hofmann, S. *Auger- and X-Ray Photoelectron Spectroscopy in Materials Science*. 2013).

42 Heuer, A. H. & Lou, V. L. K. Volatility Diagrams for Silica, Silicon Nitride, and Silicon Carbide and Their Application to High-Temperature Decomposition and Oxidation. *J. Am. Ceram. Soc.* **73**, 2789-2803 (1990). https://doi.org/10.1111/j.1151-2916.1990.tb06677.x

43 Vos, J. G., Venugopal, A., Smith, W. A. & Koper, M. T. M. Competition and selectivity during parallel evolution of bromine, chlorine and oxygen on IrOx

electrodes. *J. Catal.* **389**, 99-110 (2020). https://doi.org/10.1016/j.jcat.2020.05.024

44 Vos, J. G. & Koper, M. T. M. Measurement of competition between oxygen evolution and chlorine evolution using rotating ring-disk electrode voltammetry. *J. Electroanal. Chem.* **819**, 260-268 (2018). https://doi.org/10.1016/j.jelechem.2017.10.058

45 Muller, D. A. *et al.* The electronic structure at the atomic scale of ultrathin gate oxides. *Nature* **399**, 758-761 (1999). https://doi.org/10.1038/21602

46 Fujii, K., Ito, M., Sato, Y., Takenaka, S. & Kishida, M. Performance and durability of carbon black-supported Pd catalyst covered with silica layers in membrane-electrode assemblies of proton exchange membrane fuel cells. *J. Power Sources* **279**, 100-106 (2015). https://doi.org/10.1016/j.jpowsour.2014.12.144

47 Tilak, B. V. Kinetics of Chlorine Evolution—A Comparative Study. *J. Electrochem. Soc.* **126**, 1343 (1979). https://dx.doi.org/10.1149/1.2129274

48 Khodabakhshi, S., Fulvio, P. F. & Andreoli, E. Carbon black reborn: Structure and chemistry for renewable energy harnessing. *Carbon* **162**, 604-649 (2020). https://doi.org/10.1016/j.carbon.2020.02.058

49 Yi, Y. *et al.* Electrochemical corrosion of a glassy carbon electrode. *Catal. Today* **295**, 32-40 (2017). https://doi.org/10.1016/j.cattod.2017.07.013

50 Reier, T., Oezaslan, M. & Strasser, P. Electrocatalytic Oxygen Evolution Reaction (OER) on Ru, Ir, and Pt Catalysts: A Comparative Study of Nanoparticles and Bulk Materials. *ACS Catal.* **2**, 1765-1772 (2012). https://doi.org/10.1021/cs3003098

51 Szunerits, S., Kirchner, C. N., Wittstock, G., Boukherroub, R. & Gondran, C. Electrochemical investigation of the influence of thin SiOx films deposited on gold on charge transfer characteristics. *Electrochim. Acta* **53**, 7908-7914 (2008). https://doi.org/10.1016/j.electacta.2008.05.070

52 O'Hern, S. C. *et al.* Selective Ionic Transport through Tunable Subnanometer Pores in Single-Layer Graphene Membranes. *Nano Letters* **14**, 1234-1241 (2014). https://doi.org/10.1021/nl404118f

53 Wang, G., Zhang, B., Wayment, J. R., Harris, J. M. & White, H. S. Electrostatic-Gated Transport in Chemically Modified Glass Nanopore Electrodes. *J. Am. Chem. Soc.* **128**, 7679-7686 (2006). https://doi.org/10.1021/ja061357r

54 Epsztein, R., Shaulsky, E., Dizge, N., Warsinger, D. M. & Elimelech, M. Role of Ionic Charge Density in Donnan Exclusion of Monovalent Anions by Nanofiltration. *Environ. Sci. Technol.* **52**, 4108-4116 (2018). https://doi.org/10.1021/acs.est.7b06400

55 Ishii, Y. *et al.* Fabrication of silica/platinum core-shell particles by electroless metal plating. *Adv. Powder Technol.* **30**, 829-834 (2019). https://www.sciencedirect.com/science/article/pii/S0921883119300159

56 Cloarec, J.-P. *et al.* pH driven addressing of silicon nanowires onto Si3N4/SiO2 micro-patterned surfaces. *Nanotechnology* **27**, 295602 (2016). https://dx.doi.org/10.1088/0957-4484/27/29/295602

57 Adamson, A. W. & Gast, A. P. *Physical Chemistry of Surfaces*. 6th edn. John Wiley & Sons.(1997).

58 Fattakhova-Rohlfing, D., Wark, M. & Rathousky, J. Electrode layers for electrochemical applications based on functionalized mesoporous silica films. *Sensors and Actuators B: Chemical* **126**, 78-81 (2007). https://doi.org/10.1016/j.snb.2006.10.043

Chapter 3

Application of a Permselective MOF (ZIF-8) to Arrest Chloride Anion Transport

“Ayez l'imagination de la couleur.”

-Gustave Moreau

III.1 Dilemma

Going beyond the upper bound evidenced in the application of polymeric membranes for the desalination of water requires an improvement in the entropic selectivity of the membrane. The characteristic rigidity of a molecular sieve membrane has the potential to indeed go beyond the upper bound through the delicate refinement of the ultramicropores (d_{um}) and their microporous windows (d_m) as shown in *Figure 1b* below[1].

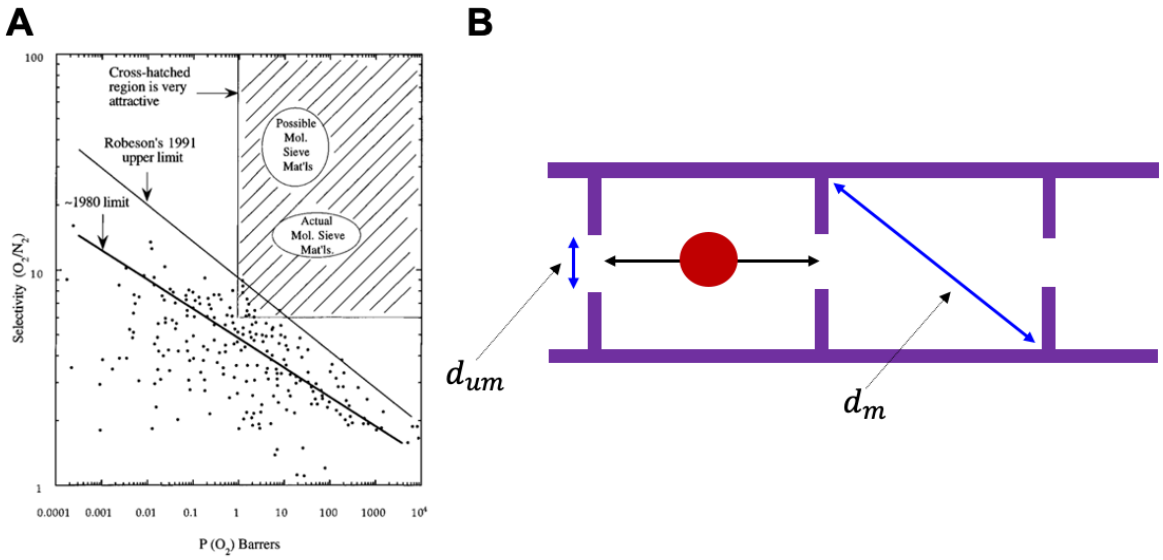

Figure 1: (A) Upper bound of oxygen gas permeability and oxygen/nitrogen selectivity indicating the attractive region achievable with molecular sieve membranes, figure of Singh and Koros[2]. (B) Molecular sieve membrane with a characteristic pore size (d_{um}) and a window dimension (d_m) connecting adjacent pores, figure adapted from Koros and Zhang[1].

Leveraging the characteristic porosity of these molecular sieve materials to improve the diffusional entropic selectivity of the membrane is the essence of this strategy and requires a precise means of controlling the pore size during the synthesis of the membrane. Silica is a thermodynamically robust material under neutral and the harsh acidic conditions of PEM technology. Though growth of the overlayer encapsulating the iridium catalyst through a sol-gel synthesis was shown to produce amorphous silica with cluster widths of 87 Å. Imbued with a characteristic rigidity lacking in polymeric membranes devoid of significant cross linkages, the pores within the material are however uncharacterizable and could well exceed the hydrodynamic diameters of both the chloride ion and the water molecule, which may relegate the diffusion selectivity of a sol-gel synthesized silica overlayer to that which can be achieved enthalpically. The thickness is also a crucial parameter of the OER reagent water permeability, though attempting to arrest the growth of the overlayer before the estimated thickness of 34 nm by TEM and TGA was shown to produce incomplete coverage of the catalyst. Thus, a method that finely controls the porosity and the

thickness of the overlayer is exigent. Placing the catalyst within a nanoparticle homogenized within a film subsequently drop casted onto working electrode also requires the overlayer that promotes significant electronic conduction between this 3D electrocatalytic nanosystem towards the electrode.

III.2 Metal-Organic Frameworks as Molecular Sieve Membranes

Traditional synthetic methods create a product from a starting entity that may or may not retain its structure during the reactional transformation. This general lack of control encumbers the ability to design solid state materials with a well-defined and tunable porosity. The concept of a secondary, rigid molecular building block such as an imidazolate functionality that can maintain its structural integrity while chelating and latching a metal ion into a rigid and thus directional cluster can be used to direct an ordered framework assembly. This reactional approach is referred to as reticular synthesis and has yielded materials known as metal-organic frameworks (MOFs) that can be designed with predetermined structures, properties, and compositions[3-5]. The characteristic porosity, stabilized by metal-nitrogen bonds with additional nonbonding interactions between the organic moieties of the functional linker, yields unprecedented surface areas with pore densities that can be utilized for the unique demands of separations, storage, and catalysis[6]. Indeed, achieving selectivity within a membrane requires a uniform pore size, if there is a pore size distribution, the molecules will pass through the largest pore with the least resistance, which decreases the diffusional selectivity of the membrane[7]. The tunability of MOF materials facilitates the design of pores that can achieve ion size exclusion and solute specific chemical interactions, and moreover furthers the prospect of realizing a synthetic membrane that mimics the selectivity of the revered aquaporin channels, with an hourglass interior morphology and matched ionic interactions that selectively permit the passage of water molecules[8,9].

III.2.1 Zeolitic Imidazolate Framework-8 (ZIF-8)

The zeolitic imidazolate framework-8 (ZIF-8) with a d_{um} of 3.4 Å in its cubic phase, between the hydrated diameter of the chloride ion (6.64 Å) and the water molecule (2.76 Å), is an attractive target to improve the diffusional selectivity of the membrane; its diffusional selectivity is indeed known to be an order of magnitude greater than state-of-the-art flexible polymers[1]. The Lewis acid Zn metal atom centers accept electrons from the Lewis base N atom donors of ditopic imidazolate (IM) to form coordination bonds with Zn-Im-Zn bond angles of 145°; this metal-ligand-metal bond angle is identical to the Si-O-Si bond angle within zeolite structures and enable the open-framework sodalite cage to be formed. The framework is neutral and surrounded by ZnN_4 tetrahedral clusters[10] with characteristic pore diameters (d_m) of 11.6 Å that are connected by the small 3.4 Å apertures (d_{um}) as shown in *Figure 2*[10].

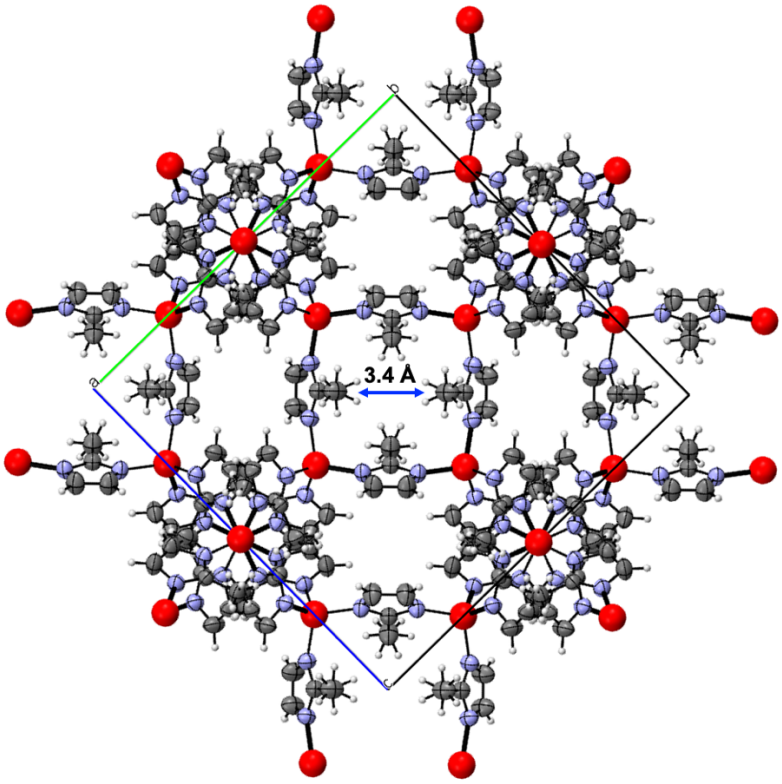

Figure 2: Single X-Ray crystal structure of ZIF-8 in the cubic phase with the d_{um} pore aperture of 3.4 Å indicated. Zinc atoms are in red, nitrogen atoms are in light blue, carbon atoms are in dark grey, and hydrogen atoms are in depicted in white.

When dissolved in dimethylformamide, the nitrogens in the 1,3-positions of the azolate ligand 2-methylimidazole become deprotonated when forming the coordination bond with a Zn (II) tetrahedral center leading to exceptional thermal and chemical stabilities[11]. Indeed, the strength of this bonding was proposed to impart impressive resistance towards hydrolysis when subjected to boiling benzene, methanol, boiling water, and aqueous sodium hydroxide[11,12] ZIF-8 MOF materials have been further implemented under the harsh acidic conditions of PEMWE[13,14]. Moreover, the crystallization kinetics and the reactivity of the azolate ligand is determined by the deprotonation step and may be thus tuned through adjustments to the pKas through modification of the azolate structure, the pH of the solution, and the reaction temperature[15]. The azolate ligand may not only act as a linker between metal nodes in its deprotonated form, though may also terminate crystal growth and stabilize the positively charged crystals in its neutral form[16].

The impressive molecular sieving properties of these materials were further found to be dominated by nonelectrostatic energies[17]. Though the crystallographic pore aperture of ZIF-8 is 3.4 Å in the cubic phase, the rotatable motion of the azolate linker induces a flexibility that enables C_3H_6 (~4.0 Å) to be separated quite effectively from C_3H_8 (~4.2 Å)[15]. The rotatable motion of the azolate ligand may furthermore be stiffen when the ZIF-8 is made to form in the monoclinic crystalline system, which was shown to improve C_3H_6/C_3H_8 separations[18]. Moreover, manipulating the carbonization temperature enabled Qiao et. al. to tune the specific surface area and the pore size of

ZIF-8 derived nanoporous carbon for selective separation of chloride ions[19] and Hu et. al. conducted a molecular simulation study of a ZIF-8 membrane for water desalination and reported a high salt rejection, though a lower water permeability than that of carbon nanotubes and boron nitride nanotubes even with a higher pore density[20].

III.2.2 The Aspect Ratio of the Membrane

Enabling the growth of a crystal in just two dimensions to create a highly anisotropic material with one dimension approaching a monolayer can conceive distinct mechanical and electronic properties. Through selection of the appropriate crystalline structure, the monolayer thickness may be tailored to permit selective water permeation. Indeed, the basic principle of a two-dimensional material is to leverage the strong interactions within the 2D plane and the weaker interactions between the plane layers to dissociate adjacent planer layers and reach the desired thickness. Luo et. al. demonstrated that the presence of the surfactant sodium dodecyl sulfate (SDS) affected the Van der waals forces between adjacent ZIF-8 layers; addition of this surfactant thus created ZIF-8 nanosheets with characteristic thicknesses of 10 to 20 nm[21]. Indeed, reports of synthesized ZIF-8 nanosheets primarily consist of bottom-up approaches as indicated in *Figure 3*.

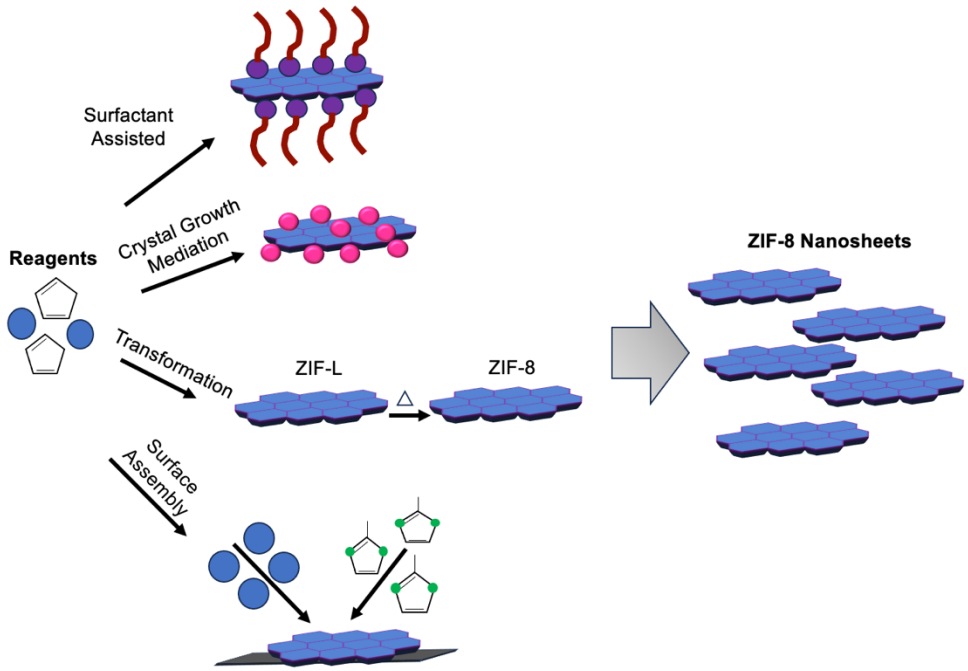

Figure 3: Reported bottom-up strategies for synthesizing ZIF-8 nanosheets. Figure adapted from Ashworth and Foster[22].

Top-down approaches such as exfoliation of the 3D crystal may subject the resultant nanosheets to a broad distribution of thicknesses and an increased number of mechanical defects[23,24]. Wang et. al. was however able to leverage the greater degree of hydrogen bonding occurring amongst the imidazole linkers within the ZIF-L structure, an analog of the ZIF-8 MOF with a smaller degree of Zn-coordination, to

obtain ZIF-L nanosheets from an oriented ZIF-L nanocrystal with thicknesses of 5 nm[25]. Subsequent thermal treatment was utilized to create ZIF-8 nanosheets. Bottom-up approaches may moreover provide a greater degree of morphological control of the nanosheet. The vertical growth of the nanosheet can be indeed inhibited by the use of surfactants, Sasaki utilized a two-dimensional reactor in amphiphilic phases (TRAP) method to grow ZIF-8 nanosheets of a few nanometers within the hydrophilic bilayer[26]. However, subsequent removal of the surfactant may pose a challenge[23]. With a rigid amphiphilic bola-like surfactant as a template, Wei et. al. formed a lamellar structure of ZIF-8 nanosheets[27]. TEM imaging indicated defined thicknesses of 36 nm with 3.6 nm spacings between the ZIF-8 lamella, though extraction of the surfactant wasn't confirmed. Epitaxial growth may exert the greatest control over the aperture size distribution and degree of crystalline defects. Chen et. al. constructed ZIF-8 sheets within the triple phase interface on hydrophobic substrates through electrophoretic deposition, which enabled the capillary-assisted peeling to produce free standing sheets[28]. Interestingly, a 1:70:1238 molar ratio of Zn(II) : 2-methylimidazole : water formed the cubic phase of the ZIF-8[12], while the 1:11:4545 molar ratio of Zn(II) : 2-methylimidazole : water utilized by Jiang et.al. formed a ZIF-8 nanosheet with a pore size of 4.74 Å in the monoclinic crystal system shown below in *Figure 4*[29]. The polarity of the water molecule and the high organic linker concentration may act as the mediators affecting the Van der Waals forces between the layers and enable anisotropic growth of the crystal. This anisotropic character may furthermore be less prone to aggregation than the isotropic particle-like counterpart morphologies.[29] This effective pore size of this ZIF-8 nanosheet is moreover larger than that of the water molecule though smaller than that of many inorganic ions found in seawater and thus could be applied towards water purification technologies[15,20,30].

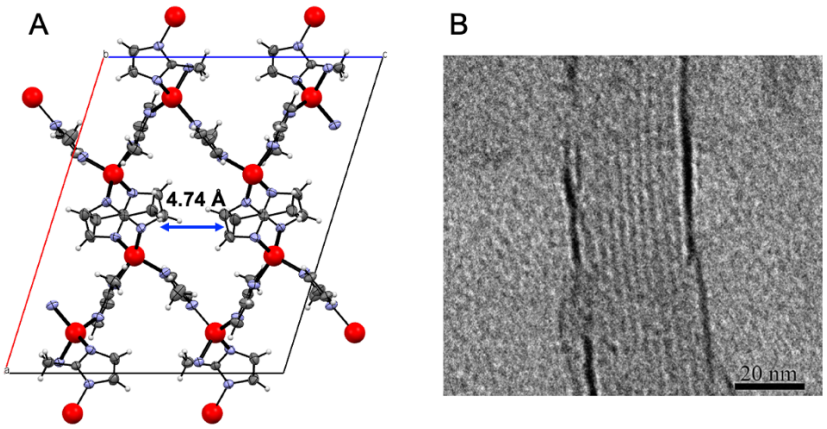

Figure 4: (A) X-Ray crystallographic structure of ZIF-8 in the monoclinic phase with the characteristic pore width indicated; zinc atoms are in red, nitrogen atoms are in light blue, carbon atoms are in dark grey, and hydrogen atoms are in depicted in white. (B) TEM image of ZIF-8 nanosheets revealing a lamellar structure of eleven crystalline layers formed with the rigid amphiphilic bola-like surfactant, figure of Wei et. al.[27]

Nanosheet morphologies with large lateral dimensions also create longer and more tortuous paths for the larger molecule impermeable to the pores and thus can further increase the selectivity of the membrane for the smaller solute. Simultaneously, their nanoscopic thickness also improves the permeation of the smaller molecule, and the interlayer space between adjacent nanosheets may be moreover leveraged to act as a selective nanochannel for ion sieving, as shown in *Figure 5* below[31,32].

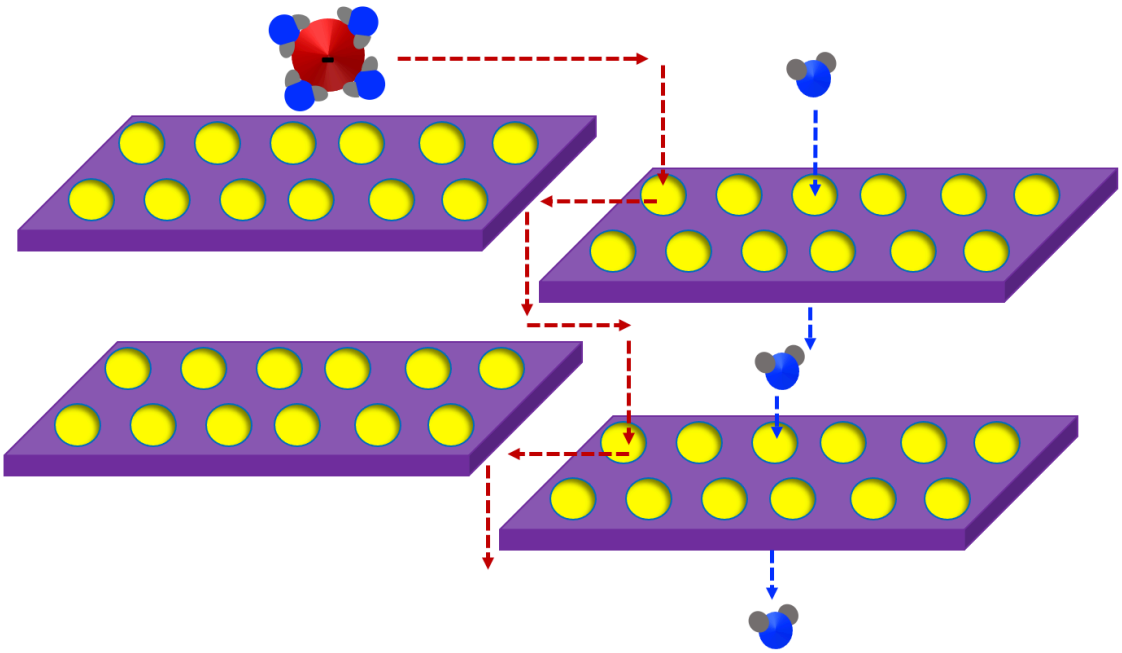

Figure 5: Increasing diffusion path length for a solute with a greater dimension than that of the pore diameter with the use of finely tuned nanosheets. Figure adapted from Kim et. al.[32]

Thus, it is hypothesized that high separation performance with a low loading can be achieved through the utilization of nanosheets[32,33]. Peng et. al. indicated improvement in both the permeability and selectivity for the gaseous separation of H_2 and CO_2 through the preparation of a molecular sieve membrane consisting of one nanometer thick nanosheets of poly[Zn_2(benzimidazole)$_4$], which achieved a high hydrogen gas permeance and an H_2/CO_2 selectivity surpassing 200[33]. In furthering the application to water desalination, Jian et. al. was able to exfoliate a two-dimensional monolayer aluminum tetra-(4-carboxyphenyl) porphyrin framework to create the building blocks for a membrane that achieved a salt rejection of nearly 100% while maintaining water fluxes reaching 2.2 mol/(m^2hour•bar) for over 750 h[34].

III.2.3 Inducing Conductivity through Confinement

Electrochemical analysis of the silica encapsulated electrocatalytic nanoparticles indicated that charge transport may be impeded with an insulating shell material. The charge transport mechanisms of MOFs include through space-charge transport that can occur by the orbital arrangements such as π stacking; charge can also transport through covalent bonding; extended conjugated pathways; guest promoted pathways; or by a hopping mechanism governed by Marcus theory in which

electrons make discrete hops between structural units[35,36]. Knowing that hopping transport is dependent on charges being transferred between the metal centers via the organic ligand, Butler et. al. performed quantum chemical calculations of the ligands within ZIF-8 to dissect the spacial resolution of the ligand wavefunctions and indicate the overlap with the d-orbitals of the metal, charge transport was proposed to be mediated by the hopping mechanism[37,38]. With a measured conductivity of 1.3-2.6 x 10^{-9} S/cm, augmenting charge transport within a ZIF-8 material requires optimizing the overlap of the frontier orbitals of the organic linker and the metal center, and incorporating metals with variable oxidation states[37]. Indeed, modulating the orbital interaction with different organic linkers can tune the conductivity of the material[39]. Adjusting the metal center can also improve the conductivity. A Co^{+2} based zeolitic imidazolate framework (ZIF-67), with a d^7 electron configuration and empty d-states within a tetrahedral environment that can hybridize with the lowest unoccupied molecular orbital (LUMO) of the organic linker through crystal field splitting, was shown to have a conductivity of ~1000 times greater, 0.6-1.2 x 10^{-6} S/cm[37]. The electronic density of states was plotted showing the degree of metal contribution to the electronic states, the Co^{+2} metal centers indeed showed a greater degree of band edges within the Fermi level as depicted in *Figure 6b*, indicating that populating the Fermi level can improve the conductivity of ZIF materials[37]. Xu et. al. further showed that dimensionally confining Ni_3N to a nanosheet increased the density of states within the Fermi level when compared to the bulk material, impedance measurements further confirmed an increase in electrical conductivity when the Ni_3N bulk material was confined to a nanosheet, as shown in *Figure 6d*[40,41].

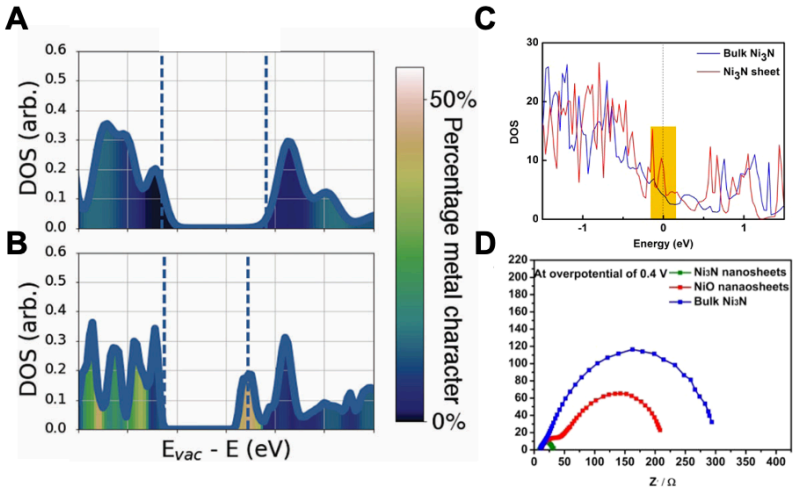

Figure 6: (A) Calculated electronic density of states for ZIF-8 and (B) ZIF-67 with the valence and conduction band edges indicated with dashed blue lines, Figure of Butler et. al.[37] (C) Calculated electronic density of states for the Ni_3N nanosheet and the bulk Ni_3N where the Fermi level depicted at 0 eV and (D) A Nyquist plot of the Ni_3N nanosheets, NiO nanosheets, and bulk Ni_3N, Z'' is the imaginary impedance and Z' is the real impedance, Figure of Xu et. al[40].

Engineering two dimensional structuration has further been suggested to increase the number of charge carriers within the material[42]. Thus, it is proposed that inducing

dimensional confinement through the construction of a nanosheet morphology can be utilized to increase the density of states at the Fermi level and improve the electrical conductivity of ZIF-8.

III.2.4 Design of the Catalytic Architectures

Concerned that a core-shell morphology, with the electrocatalytic nanoclusters surrounded by a permselective ZIF-8 overlayer, may affect electron conduction and may further prove to be synthetically complicated to control the thickness thus prompted the utilization of ZIF-8 nanosheets. With characteristic pore sizes of 4.74 Å, these nanosheets are hypothesized to selectively promote the passage of water while rejecting the species transport of the chloride ion.[43] Herein, two different architectures are proposed in which an electrocatalytic film of iridium nanoparticles is prepared and then spin coated with a layer of permselective ZIF-8 nanosheets (*Figure 7a*); the second architecture prepares the electrocatalytic ink with permselective ZIF-8 2D nanosheets that is then drop casted onto a glassy carbon working electrode (*Figure 7b*); the final design prepares a ZIF-8 overlayer in-situ through a hydrothermal synthesis (*Figure 7c*).

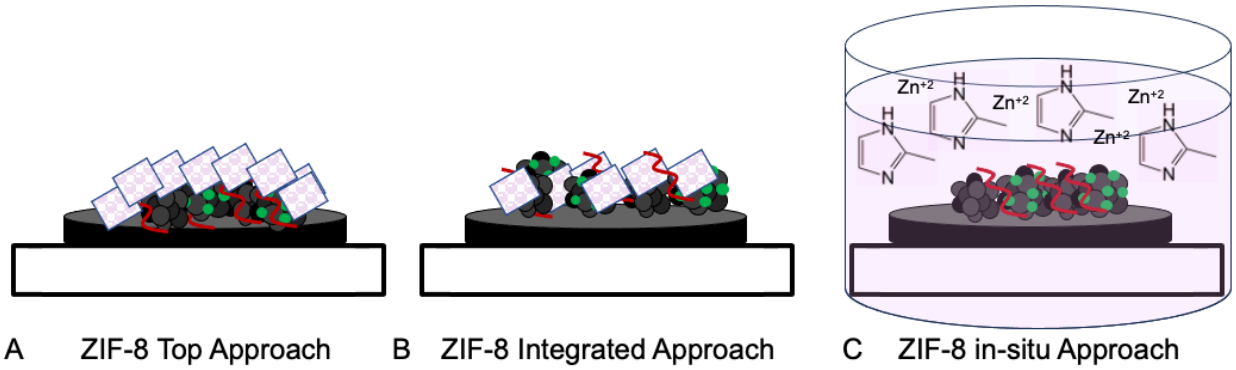

Figure 7: Schematic indicating the three different approaches taken towards incorporating a ZIF-8 layer with the electrocatalytic film to selectively arrest the species transport of the chloride ion. (A) shows a representation of the Top Approach and (B) delineates a representation of the Integrated Approach. In (C), the major chemical species are shown dissolved in methanol in a Teflon chamber with a preprepared film placed inside, the vessel is subsequently incubated in the oven and an overlayer is formed through a hydrothermal synthesis.

The designs are proposed to render an electrocatalytic film capable of both chloride ion sieving and selectively evolving oxygen, a hypothesis that is shown in the following Results and Discussion section to be evaluated through analysis of the films on rotating disk and rotating ring disk electrodes subjected to linear sweep voltammetry.

III.3 Results and Discussion

III.3.1 ZIF-8 MOF Nanosheet Synthesis

Initial synthesis refers to the work of Jiang et. al.[29] Zinc nitrate hexahydrate and 2-methylimidazole were each dissolved in water and then mixed and allowed to stir

for 24 h at room temperature as shown in *Figure 8* below. After subsequent methanolic washes, the white deposits were dried overnight at 80°C and then collected for analysis.

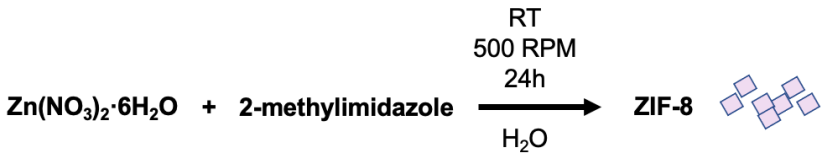

Figure 8: Protocol of the ZIF-8 nanosheet synthesis indicating the reaction conditions subjected to the metallic and organic precursors.

The X-Ray diffraction pattern of the nanosheets was processed as shown in *Figure 9a* below and indicated the monoclinic phase to be the major crystallographic system that was formed. The CIF file of the crystal system was modeled, and a rendering is presented in *Figure 9b*; a pore width of 4.74 Å nm was measured.

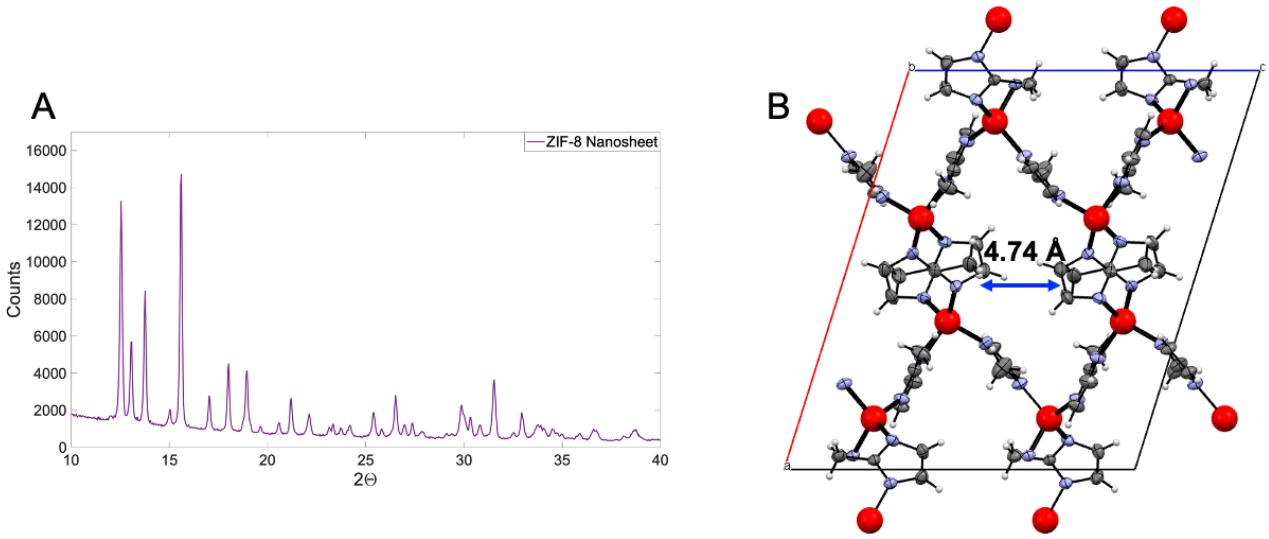

Figure 9: (A) X-Ray diffraction spectrum of the ZIF-8 nanosheets taken with an automatic anti-scatter screen to reduce the diffusion signal at very low angles. The monoclinic phase was found to be the major crystallographic system and modeled as shown in (B) with the pore width indicated; zinc atoms are in red, nitrogen atoms are in light blue, carbon atoms are in dark grey, and hydrogen atoms are in depicted in white.

The morphology of the resulting deposits was characterized through Scanning Electron Microscopy (SEM) as shown below in *Figure 10a-c*. The renderings also enabled a determination of the thickness of the nanosheet. Eighty measurements of the nanoparticle thicknesses were made with *Figure 10b* and *Figure 10c* utilizing the Image J software; the measurements are delineated in the histogram shown in *Figure 10d* and reveal a thickness range of 8 nm to 209 nm with highly populated bins that encompass thicknesses of 20 nm and thicknesses of 65 nm.

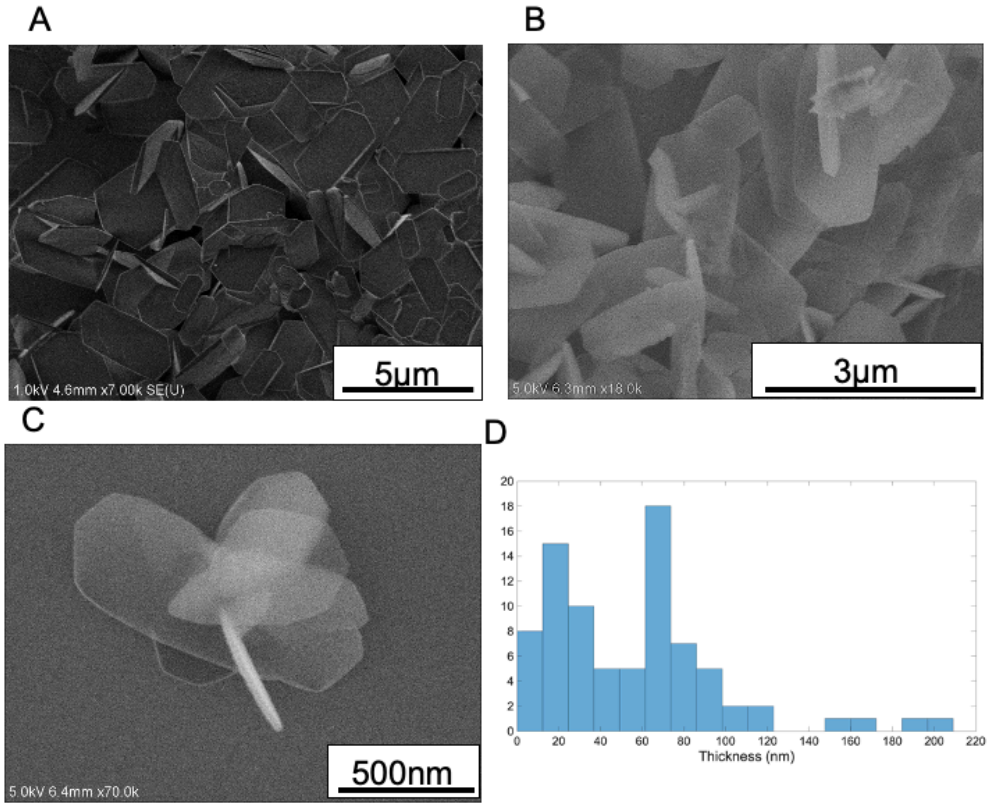

Figure 10: The (A)-(B) panels are SEM images taken on a silicon wafer that rendered depictions of the synthesized nanosheets and enable a morphological interpretation of the degree of homogeneity. The (B) and (C) images were taken after an 8 mg/mL dilution in methanol that enabled measurements of the nanosheet thickness. The resulting 17-bin histogram of (D) consists of 80 measurements of those thicknesses.

High Resolution Transmission Electron Micrography (HR-TEM) further confirmed the homogeneity of the nanosheets as shown in *Figure 11a* and *Figure 11b* below. Imaging further confirmed an average nanosheet width of approximately 500 nm. The lack of crystallinity observed in the Fast Fourier Transform of the images was attributed to the carbonization of the material under the electron beam, which is often observed for inorganic-organic hybrid materials such as MOFs.

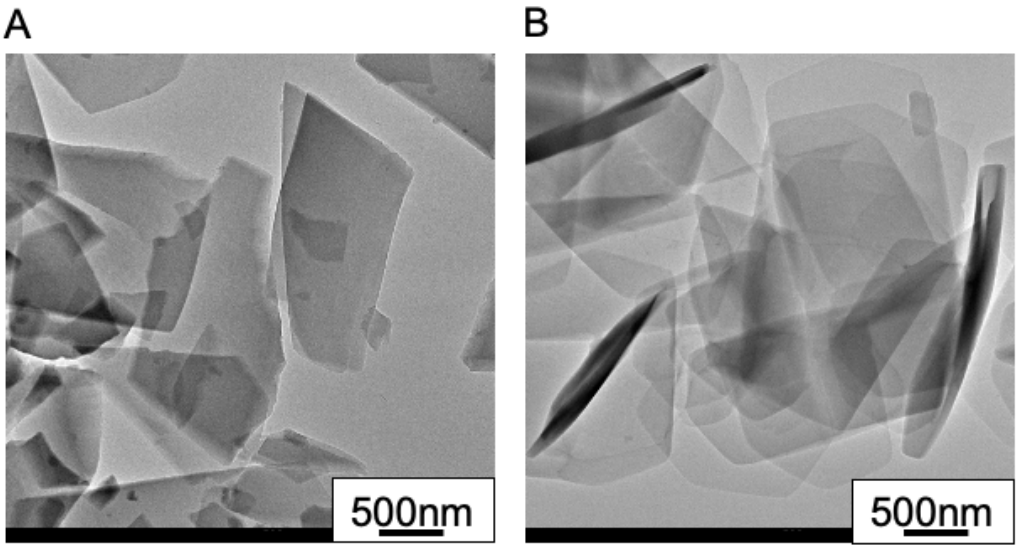

Figure 11: (A) and (B) are high resolution transmission electron microscope renderings of the ZIF-8 nanosheet, each image represents a different synthesis.

Energy Dispersive X-Ray Spectroscopy enabled the weight percent of the major elements to be detected and are tabulated in the *Table 1* below, which enabled confirmation of the presence of zinc.

Table 1: Elemental Composition from Energy Dispersive X-Ray spectroscopy confirming the weight % of the major elements in the nanosheets.

Element	**C**	**Zn**	**Cu**	**O**	**Si**
Weight %	83.2	9.2	5.8	1.4	0.4

The zeta potential of the ZIF-8 nanosheets was recorded in methanol as good dispersion was observed in this solvent. The value was approximately zero, indicating that the charge of the surface along the slip plane bounding the diffuse layer just outside the outer Helmholtz layer of the material is approximately zero with respect to the potential in the bulk solution[44].

III.3.2 Elaboration of the Catalytic Architectures

Two architectures with the ZIF-8 nanosheets were targeted for the electrocatalytic film, an integrated approach and a top approach.

III.3.2.1 Spin-Coated ZIF-8 Nanosheet Overlayer

In order to obtain the “top design”, the architecture of the electrocatalyst was prepared in two steps. First, the Ir10 film is deposited on the electrode, and then in the second step, the film is covered with the ZIF-8 nanosheets. To achieve this design, iridium nanoparticles deposited on Vulcan carbon in a 10/90 % (w/w) (Ir10) ratio and additional Vulcan carbon were homogenized in a 50/50 percent solution of water and Nafion (5% w/w in water and isopropanol), which was added volumetrically with respect to the mass of the iridium weighted (500 µL of solution to 1 mg Ir10). These

electrocatalytic inks will be subsequently referred to as Ir10ink. 8 µL of the Ir10ink was then drop casted onto a glassy carbon working electrode of 5 mm diameter, air-dried for 30 min, and then heated at 60°C in the oven for 30 min. 8 µL of a methanolic solution of ZIF-8 MOF nanosheets was then drop-casted onto the film and spin-coated at a rotation rate of 2000 RPM for 20 sec before the resulting film was allowed to dry overnight in ambient conditions. The methanolic ZIF-8 MOF solutions drop casted onto the film were prepared to afford overlayer thicknesses of 4 nm, 40 nm, 400 nm, and 4 µm by utilizing *Equation 1* shown below with t_{ZIF-8} being the desired thickness, ρ_{ZIF-8} denoting the density, and πr^2 being equal to the area of the glassy carbon electrode.

$$m_{ZIF-8} = t_{ZIF-8}\, x\, \rho_{ZIF-8}\, x\, \pi r^2 \quad (1)$$

The 400 nm thickness film will be referred to as ZIFtopfilm400 and the schematic of *Figure 12* below summarizes the preparation protocol.

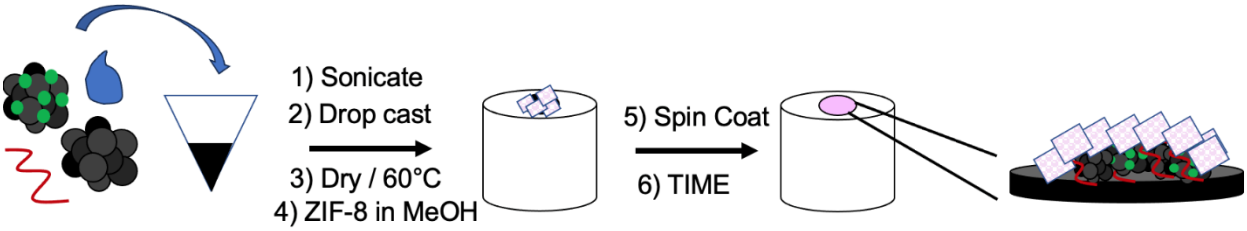

Figure 12: Schematic of the preparation procedure for the ZIFtopfilm. The required concentration of ZIF-8 nanosheets in the methanolic solution was determined through Equation 1 with a predefined thickness.

III.3.2.1 Homogeneous Integration of ZIF-8 Nanosheets

In order to obtain the "integrated design", Ir10 and ZIF-8 were mixed and the electrocatalytic ink was prepared in a one-step deposit. Electrocatalytic inks composed of iridium nanoparticles deposited on carbon in a 10/90 % (w/w) (Ir10) and Vulcan carbon were homogenized in a 50/50 percent solution of water and Nafion (5% w/w in water and isopropanol), which was added volumetrically with respect to the mass of Ir10 weighted (500 µL solution to 1 mg Ir10). In a 1:1 volumetric ratio with respect to the water/Nafion solution, a methanolic ZIF-8 MOF solution was also pipetted into the mixture before subsequent homogenization. The *Equation 1* above was also used to prepare the requisite concentration of the ZIF-8 MOF nanosheets within the methanolic solution that arrived at a mass of nanosheets integrated into the ink equivalent to the mass of nanosheets spin coated in the overlayer previously described above. Calculated Zn/ Ir ratios of 4, 0.4, and 0.04 were probed, these ink compositions will be referred to as ZIFIr10ink4, ZIFIr10ink0.4, and ZIFIr10ink0.04, respectively. Thus 16 µL of the homogenized ZIFIr10ink was drop casted onto the glassy carbon working electrode before being air-dried and subjected to a 30-min solvent evaporation cycle at 60°C to create a film. These films will be referred to as

ZIFintfilm4, ZIFintfilm0.4, ZIFintfilm0.04, respectively with the preparation procedure summarized in *Figure 13* below.

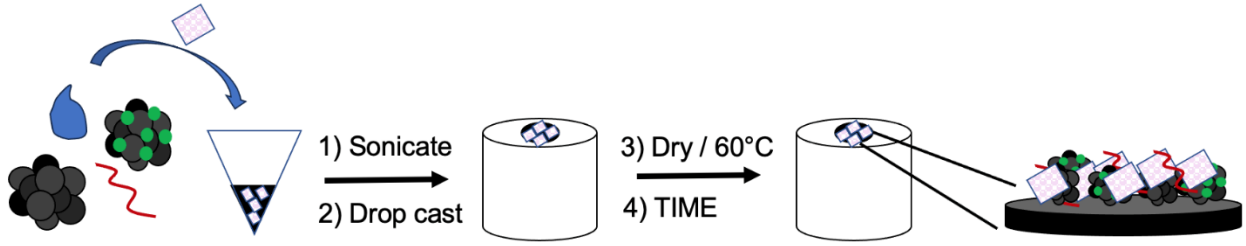

Figure 13: Schematic of the preparation procedure for the ZIFintfilm. The required concentration of ZIF-8 nanosheets in the methanolic solution was determined through *Equation 1* with a predefined thickness and converted to a molar ratio of Zn/Ir.

III.3.2.2.1 Characterization of the ZIFIr10ink4

Initial investigations were conducted with SEM to reveal the orientation of the ZIF-8 nanosheets with respect to the iridium nanoparticle catalysts in ink. A ZIFIr10ink4 was prepared and drop casted on a silicon wafer; an Ir10ink was also prepared and drop casted onto another silicon wafer. The inks were allowed to dry and subsequently imaged as shown in *Figure 14a* and *Figure 14b*. Energy Dispersive X-Ray Spectrometry (EDS) elemental analysis of both inks at 15 kV electron acceleration voltage is shown in *Figure 14c*, which enabled the calculated Zn/Ir molar ratio to be compared with an experimental value; the results indicated a ratio of 5.6 with a standard deviation of 2.1.

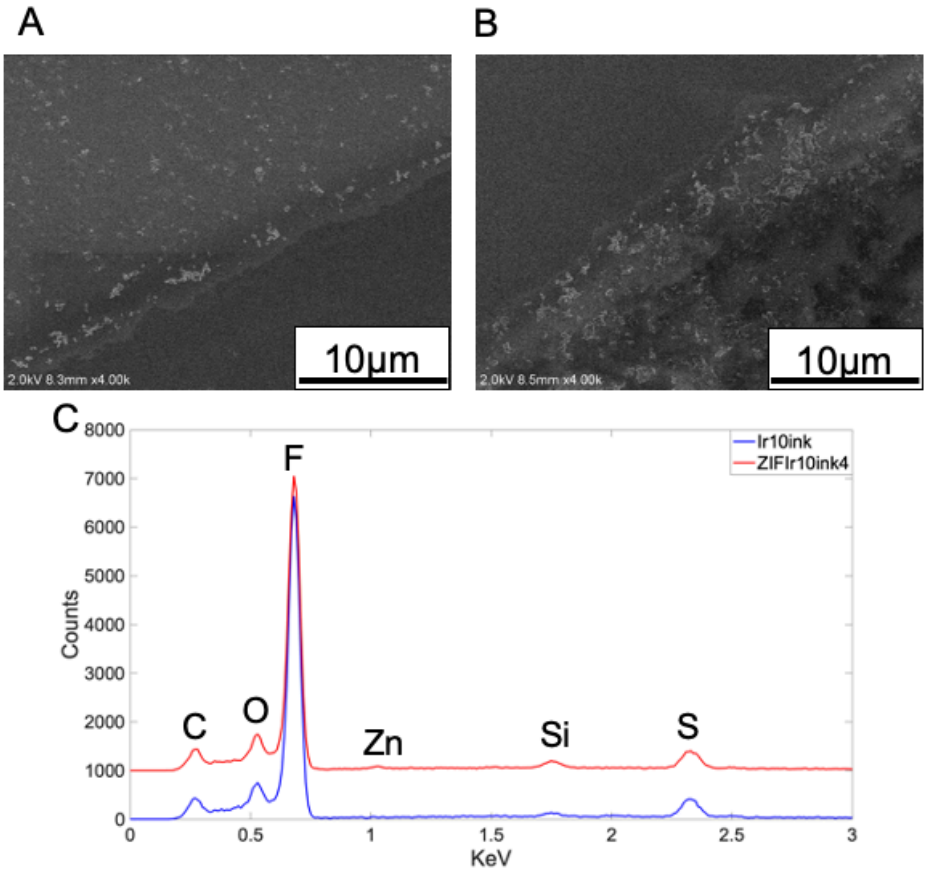

Figure 14: (A) shows an SEM image of an Ir10ink after being drop casted on a silicon wafer and dried under ambient conditions. (B) images an SEM micrograph of an ZIFIr10ink4 that was homogenized and drop casted onto a silicon wafer and allowed to dry at room temperature. The Energy Dispersive X-Ray spectrum obtained with a 15 kV acceleration voltage in the scanning electron microscope shown in (C) indicates the major elements recorded and the quantity of zinc in the ZIFIr10ink4, enabling an experimental Zn/Ir molar ratio to be compared to the calculated value.

III.3.3 Rotating Disk Voltammetric Evaluation of MOF Incorporated Films

III.3.3.1 The Fluid Velocity Profile at a Rotating Disk Electrode

Probing an electrochemical system utilizing a rotating disk working electrode enables the flux of the reactants towards the disk to be hydrodynamically controlled. Spinning the disk within a solution forces the fluid to be expelled by the centrifugal force outward in the radial direction from the center and dragged along the surface with an angular velocity (ω); the fluid is replenished by the flow normal to the surface as shown in *Figure 15*.

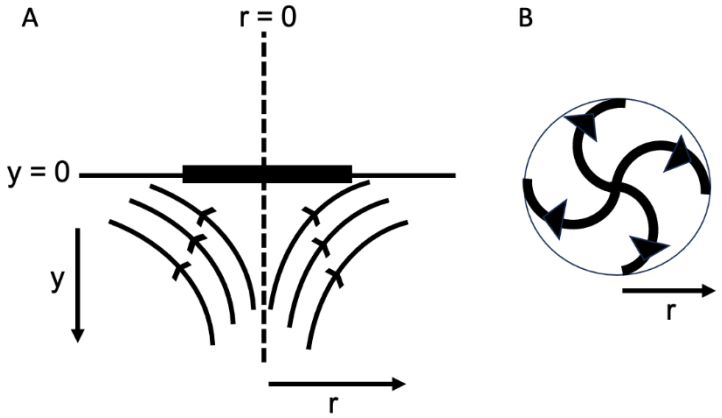

Figure 15: Resultant fluid vector streamlines (A) towards the rotating disk electrode and (B) along the surface of the disk.

The hydrodynamic vector describing this fluid velocity profile may be modeled using cylindrical coordinates with the unit vectors $\hat{\mu}_1$, $\hat{\mu}_2$, and $\hat{\mu}_3$ that indicate the directions of r, y, and φ in the positive sense,

$$\mathbf{v} = v_r\hat{\mu}_1 + v_y\hat{\mu}_2 + v_\varphi\hat{\mu}_3 \tag{2a}$$

Where the del operator may be defined,

$$\boldsymbol{\nabla} = \hat{\mu}_1\frac{\partial}{\partial r} + \hat{\mu}_2\frac{\partial}{\partial y} + \frac{\hat{\mu}_3}{r}\frac{\partial}{\partial \varphi} \tag{2b}$$

At the surface of the disk where $y = 0$: $v_r = 0$, $v_y = 0$, and $v_\varphi = \omega r$, and in the bulk of the solution where $y = \infty$: $v_r = 0$, $v_y = -V_0$, and $v_\varphi = 0$. Far from the disk, the solution flows towards the surface with a limiting velocity (V_0). Near the surface of the disk as $y \to 0$, where the solution flows with a viscosity (ν) and velocities (v_y) and (v_r),

$$v_y = -0.51\omega^{3/2}\nu^{-1/2}y^2 \tag{3}$$

$$v_r = 0.51\omega^{3/2}\nu^{-1/2}ry \tag{4}$$

III.3.3.2 Derivation of the Convective Diffusion Equation

The flux of an electroactive species (R) within the solution towards the working electrode may generally be described as previously shown,

$$\boldsymbol{J}_R = -D_R\boldsymbol{\nabla}C_R - \frac{z_jF}{RT}D_RC_R\boldsymbol{\nabla}\phi + C_R\mathbf{v} \tag{5}$$

In the presence of sufficient supporting electrolyte, the migration of the electroactive species, the second term of *Equation 5*, may be neglected and the gradient $\boldsymbol{\nabla}C_R$ can be defined as,

$$\boldsymbol{\nabla} C_R \;=\; \hat{\mu}_1 \frac{\partial C_R}{\partial r} \;+ \hat{\mu}_2 \frac{\partial C_R}{\partial y} + \frac{\hat{\mu}_3}{r} \frac{\partial C_R}{\partial \varphi} \tag{6}$$

Enabling the convective diffusion equation to be expressed as,

$$\boldsymbol{J}_R = -D_R \left[\hat{\mu}_1 \frac{\partial C_R}{\partial r} \;+ \hat{\mu}_2 \frac{\partial C_R}{\partial y} + \frac{\hat{\mu}_3}{r} \frac{\partial C_R}{\partial \varphi} \right] + C_R \left[v_r \hat{\mu}_1 + \; v_y \hat{\mu}_2 + v_\varphi \hat{\mu}_3 \right] \tag{7}$$

The variation of C_R with respect to time may be further evaluated by computing the divergence of the $\boldsymbol{J}_R$ vector field,

$$\frac{\partial C_R}{\partial t} = \; -\boldsymbol{\nabla} \cdot \boldsymbol{J}_O$$

Which may be delineated as,

$$\frac{\partial C_R}{\partial t} = -D_R \left[\frac{\partial^2 C_R}{\partial r^2} \;+ \frac{1}{r} \frac{\partial C_R}{\partial r} + \frac{\partial^2 C_R}{\partial y^2} + \frac{1}{r^2} \left(\frac{\partial^2 C_R}{\partial \varphi^2} \right) \right] + v_r \left(\frac{\partial C_R}{\partial r} \right) + v_y \left(\frac{\partial C_R}{\partial y} \right) \; + v_\phi \left(\frac{\partial C_R}{\partial \varphi} \right) \tag{8}$$

Because there is a constant flow of electroactive species towards the rotating working disk electrode upon attainment of a steady velocity profile, the concentration of the electroactive species decays not to zero at the surface of the working electrode as it would in the transient, unstirred solution of a planar electrode, though instead to a steady-state value. Thus, its concentration becomes independent of time and ${\partial C_O}/{\partial t} = 0$. Across the surface of the working electrode, *Equation 8* can be simplified,

$$-y \left(\frac{\partial C_O}{\partial y} \right) = \; \left(\frac{D_O}{0.51 \omega^{3/2} \nu^{-1/2}} \right) \frac{1}{y} \left(\frac{\partial^2 C_O}{\partial y^2} \right) \tag{9}$$

In the limiting current condition,

$$\lim_{y \to \infty} C_R = C_R^* \tag{10}$$

Thus integrating *Equation 9* from zero to C_R^* may be shown to be equal to[45],

$$C_R^* = \left(\frac{\partial C_R}{\partial y} \right)_{y=o} 0.8934 \left(\frac{D_R^{2/3} \omega^{1/2} \nu^{1/2}}{0.51} \right)^{1/3} \tag{11}$$

The measured current due to the flux of the electroactive species towards the working electrode is defined as,

$$i = nFAD_R \left(\frac{\partial C_R}{\partial y}\right)_{y=o} \quad (12)$$

where (A) is the area of the electrode and (F) is Faraday's constant. The anodic current measured under limiting, total mass-transfer control ($i_{l,a}$) at the rotating disk electrode may be deduced as initially described by Levich,

$$i_{l,a} = 0.62nFAD_R^{2/3}\omega^{1/2}\nu^{-1/6}C_R^* \quad (13)$$

Thus, this forced convection ensures that the concentration of all species remain uniformly equal to their concentrations in the bulk solution beyond a certain distance (ξ) from the electrode and further facilitates a quickly achieved steady state mass transport of the reactants towards the disk electrode. This mass transfer of reactants towards the disk electrode becomes affected only by diffusion and the measured limiting current produced by this flux is directly proportional to $\omega^{1/2}$.

III.3.3.3 Additional Nonfaradaic Processes

The total external current measured at the disk encompasses: (1) this convective-diffusion faradaic current derived by Levich; (2) the initial currents charging the double layer arising as a result of the imposed potential; (3) the oxidation and reduction of additional adsorbed species; (4) the currents generated from the oxidation and reduction of the electrode itself; and (5) any kinetically controlled currents arising from the supporting electrolyte. With an ability to control the flux of the electroactive species reaching the working electrode through adjustment of the rotation speed, studies of the faradaic, electron transfer reaction occurring at the disk may be conducted in theory by simply taking the current difference measured at two rotation speeds to reveal the net current dependent on $\omega^{1/2}$. However, the imposed hydrodynamic conditions may accelerate the alteration of these processes producing the currents within the time between two sequential experiments[46].

In particular, the current generated from charging of the double layer can be much larger than the faradaic current of the oxidation or reduction of the electroactive species, especially at low concentrations. Under a linear potential sweep with a scan rate (v), the anodic (+) or cathodic (-) current arising from the charging of the double layer with a capacitance (C_d) is deduced as,

$$i = \pm vC_d\left(1 - e^{-t/R_tC_d}\right) \quad (14)$$

Where (R_t) is the solution resistance and (t) is the time. Varying the potential linearly with respect to time at a low scanning rate (v) thus ensures that this current contribution is minimized.

III.3.3.4 The One-Electrode / Two-Solution Electroanalytical Trial Sequence

The electrocatalytic films with the ZIF-8 MOF nanosheet architectures were thus subjected to linear scanning voltammetry to probe the undesired electrocatalytic

activity of the film towards the chlorine evolution reaction and therefore evaluate its effectiveness towards arresting species transport of the chloride ion. The rotating disk working electrode was arranged in a three-electrode set-up with an Ag/AgCl reference electrode that allows the potential applied to the working electrode to be measured, and with a platinum counter electrode to supply electrons for the reaction at the working electrode. The initial supporting electrolyte solution consisted of a 0.5 M NaCl / 0.1 N H_2SO_4 (pH 1.3) at 25°C to mimic the chloride concentration in seawater. A scan rate of 10 mV/sec was first applied and the potential was positively swept to measure the oxidation current and then reversed at the positive vertex. All potential ranges are calculated and compared to the reversible hydrogen electrode (RHE). The film was then placed in an aqueous solution of 0.1 N H_2SO_4 supporting electrolyte (pH 1.3) at 25°C. A scan rate of 10 mV/sec was first applied and the potential was positively swept to measure the oxidation current and then reversed at the positive vertex. The film was then subjected to 100 conditioning cycles between 0.680 V and 0.180 V vs. RHE at 200 mV/sec followed by another scan recorded at 10 mV/sec; a delineation of the experimental protocol is depicted in *Figure 16* below. The current metric of 10 mA/cm^2 was used to determine the potential range that was scanned.

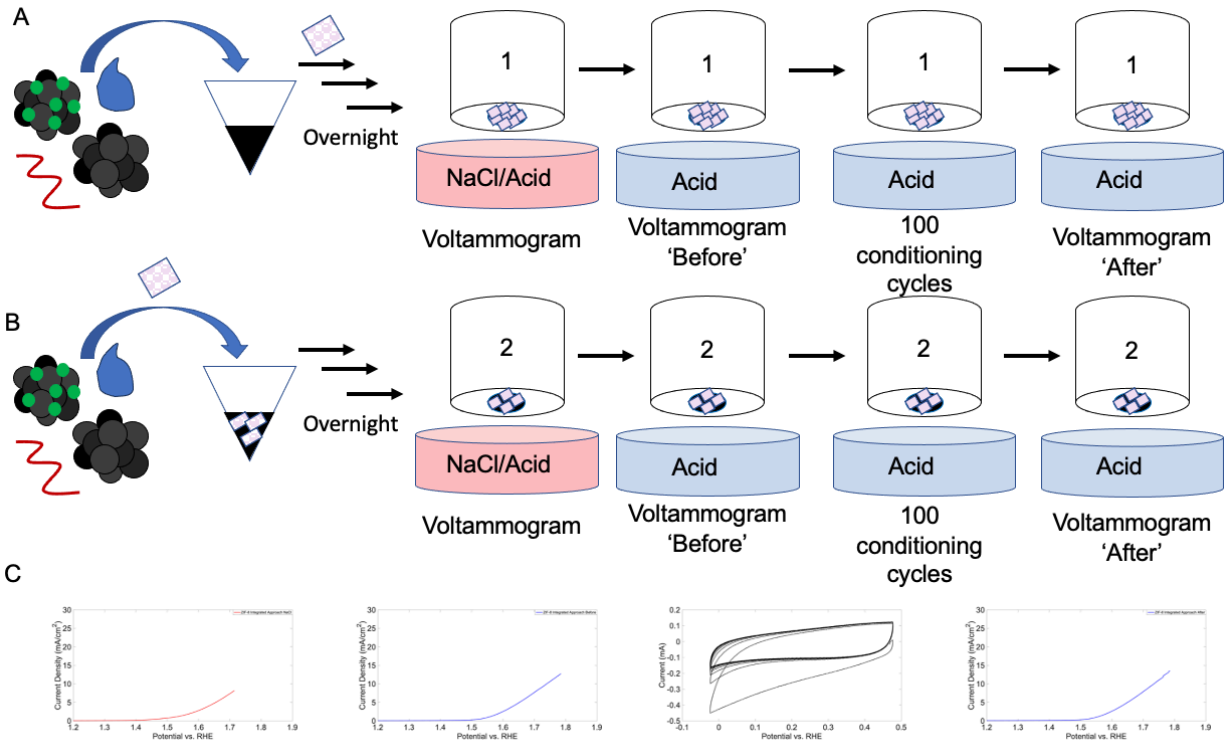

Figure 16: Schematic of the one-electrode / two-solution electroanalytical trial sequence indicating the initial supporting electrolyte to be a 0.5 M NaCl solution at pH 1.3 and the second solution to consist of an acidic supporting electrolyte at pH 1.3. The solutions were acidified with 0.1 N H_2SO_4. An ink was prepared for the (A) ZIFtopfilm and a different ink was prepared for the (B) ZIFintfilm and both films were allowed to dry overnight to promote adhesion of the ZIF-8 spin-coated top layer before

the trial sequence on each film was conducted. (C) Example voltammograms at each step of the electroanalytical protocol.

A voltammogram with recorded current densities along the potential ranges that enabled the 10 mA/cm^2 metric to be reached is shown below in *Figure 17* and compares the overpotentials of the reference Ir10film with those of the ZIFtopfilm400 and the ZIFintfilm4 obtained through the one-electrode / two-solution electroanalytical trial sequence referenced above.

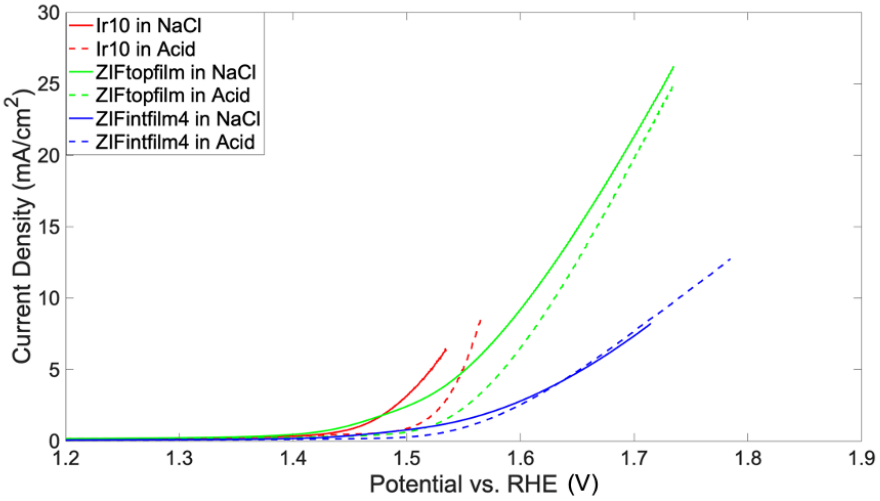

Figure 17: Voltammograms of the Ir10 in red, the ZIFtopfilm400 in green, and the ZIFintfilm4 trialed at pH 1.3 in the **dotted** curves and at pH 1.3 with 0.5 M NaCl along the **solid** curves.

These results were encouraging as it is seen that similar overpotentials for the ZIFintfilm4 in both the acidic supporting electrolyte and the acidic supporting electrolyte with 0.5 M NaCl shown in the blue dotted and solid lines, respectively, were recorded indicating that the presence of the chloride ion in the supporting electrolyte doesn't affect the recorded overpotential. This result implies that the chlorine evolution reaction (CER) is being impeded. However, the separation of the dotted curve of the acidic supporting electrolyte and solid curve of the acidic, 0.5 M NaCl supporting electrolyte solution for the ZIFtopfilm implies that this design with a 400 nm ZIF-8 nanosheet overlayer thickness doesn't impede the CER.

Furthermore, the reproducibility of the result evidenced for the ZIFintfilm4 proved to be challenging and standard deviations of greater than 50 mV were apparent when subsequent trials were compared. The wide range of error and lack of reproducibility was attributed the use of a multiple inks in the triplicate comparison, variations in the overnight drying times, and the unknown effects of consistently subjecting a film to an LSV measurement in the acidic, brine solution before taking an LSV measurement in the acidic supporting electrolyte alone. Thus, a new electroanalytical trial sequence was derived to correct for these various parameters.

III.3.3.5 The One-Electrode / One-Solution Electroanalytical Trial Sequence

The rotating disk working electrode was arranged in a three-electrode set-up with an Ag/AgCl reference electrode that allows the potential applied to the working electrode to be measured, and with a platinum counter electrode to supply electrons for the reaction at the working electrode. The supporting electrolyte solutions consisted of a 0.5 M NaCl / 0.1 N H_2SO_4 (pH 1.3) at 25°C to mimic the chloride concentration in seawater or an aqueous solution with a 0.1 N H_2SO_4 supporting electrolyte (pH 1.3) at 25°C. A scan rate of 10 mV/sec was first applied and the potential was positively swept to measure the oxidation current and then reversed at the positive vertex. All potential ranges are calculated and compared to the reversible hydrogen electrode (RHE). The film was then subjected to 50 conditioning cycles between 0.680 V and 0.180 V vs. RHE at 200 mV/s followed by another scan recorded at 10 mV/sec; a depiction of the electroanalytical trial sequence is shown in *Figure 18* below. The current metric of 5 mA/cm^2 was used to determine the potential range that was scanned to minimize the variability caused by bubble formation.

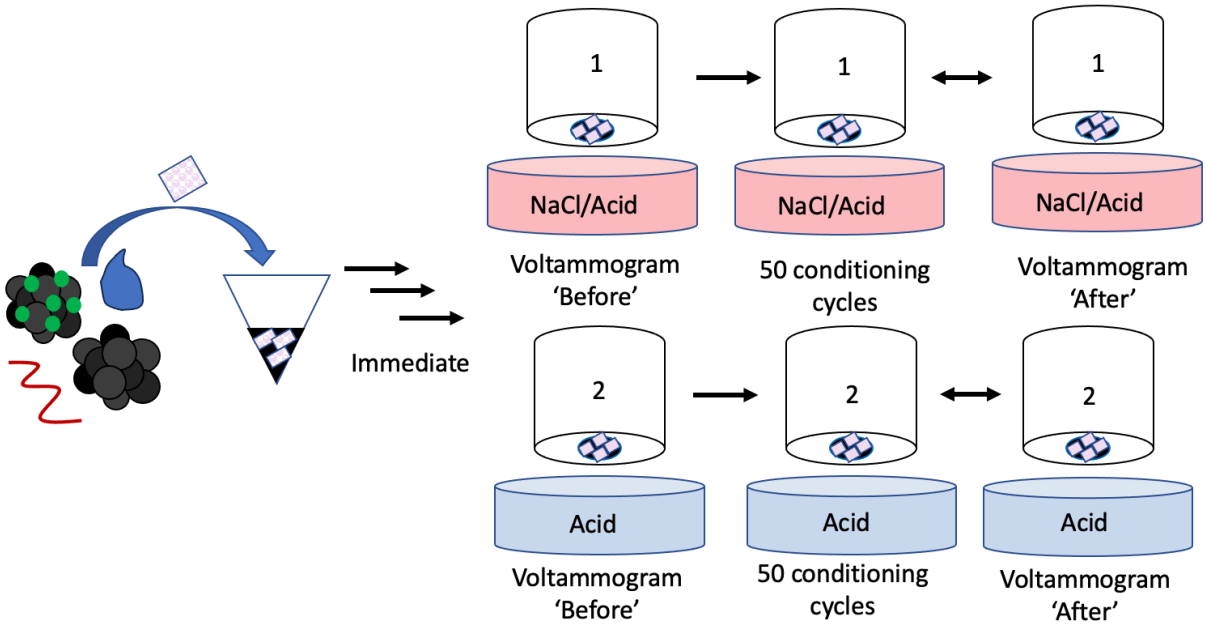

Figure 18: Schematic of the one-electrode / one-solution electroanalytical trial sequence conducted on one prepared electrocatalytic ink. Inks and drop-casted films were prepared according to the integrated approach and immediately analyzed after drying.

One ZIFIr10ink4 was made and then 16 µL was drop casted onto each rotating disk electrode, dried, and then immediately analyzed; six films were analyzed (three in each supporting electrolyte solution) within the same day to minimize any associated error associated with overnight waiting times for the prepared ink. The resultant overpotentials required to reach the 5 mA/cm^2 metric were averaged and plotted in the bar graphs of *Figure 19*. Trials with the ZIFintfilm0.4 and ZIFintfilm0.04 were also conducted.

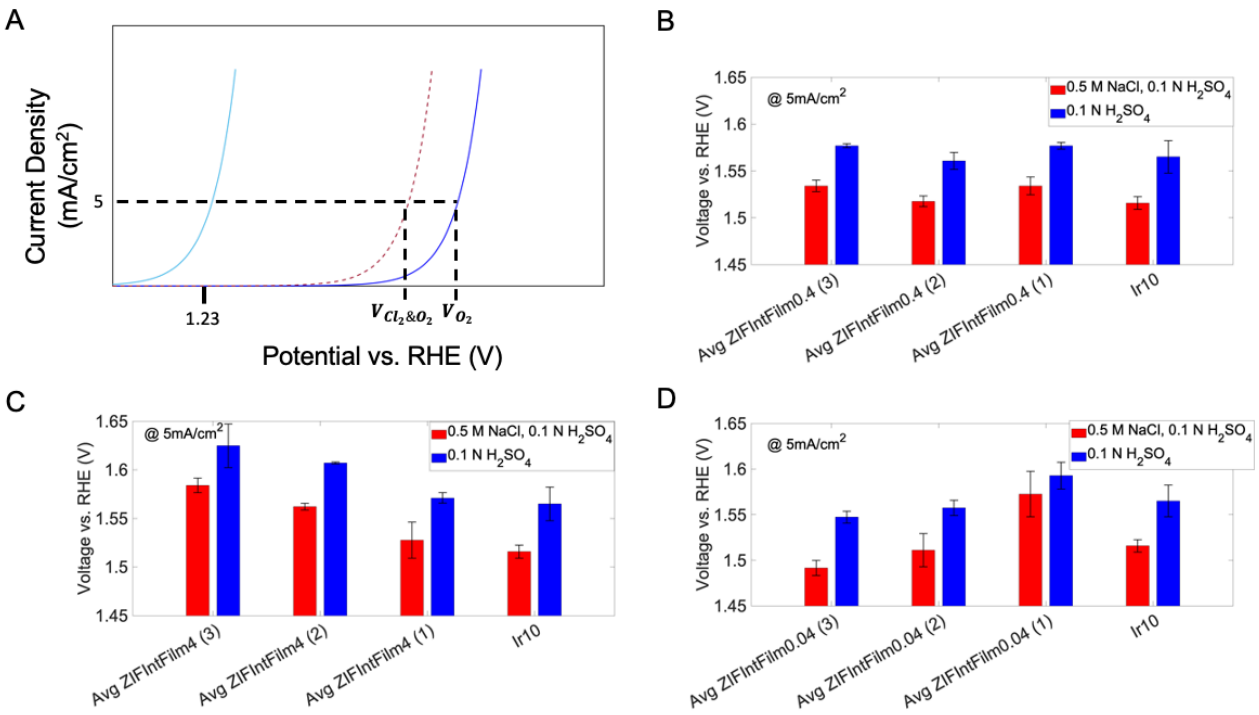

Figure 19: The schematic shown in (A) indicates a graphical representation of the potentials measured to derive the bar graph shown in (B-D). The ZIFintfilm4, ZIFintfilm0.4, and ZIFintfilm0.04 were trialed in triplicate through the one-electrode / one-solution electroanalytical trial sequence in (B), (C), and (D) with the red bars indicating potential measurements in an acidic, 0.5 M NaCl supporting electrolyte and the blue bars representing potential measurements made in the aqueous, acidic supporting electrolyte.

The standard errors of each triplicate trial with one single ink are lower than 50 mV, indicating that the one-electrode / one-solution protocol can achieve reproducible results. However, the potential values $V_{Cl_2\&O_2}$ and V_{O_2} at 5 mA/cm^2 depicted in *Figure 19a* each represented by a red bar and blue bar cluster as shown in *Figure 19b-d*, vary from one cluster to the next (each cluster representing an ink) and no evidence of the prevention of chloride ion species transport was seen as the potentials in the acidic, 0.5 M NaCl supporting electrolyte were consistently lower than the potentials recorded in the purely acidic supporting electrolyte. This variability and pattern was also evidenced for the ZIFintfilm0.4 (*Figure 19c*) and ZIFintfilm0.04 (*Figure 19d*). Although the standard deviations of the potentials in the acidic, 0.5 M NaCl supporting electrolyte showed an overlap with the standard deviations of the potentials recorded in the purely acidic supporting electrolyte for the ZIFintfilm0.04, no clear ascending or descending trend appears as greater quantities of ZIF-8 were integrated into the film. This result may be attributed to the slightly different weights of Ir10 weighted into each ink (between 0.9 to 1 mg) and/or may be caused by the direct diffusion of the chloride ion towards the glassy carbon electrode.

This consistence difference in the potentials $V_{Cl_2\&O_2}$ and V_{O_2} at 5 mA/cm^2 may be visualized in *Figure 20* below, in which the average $V_{Cl_2\&O_2}$ and the average V_{O_2}

amongst the three inks probed at the 4, 0.4, and 0.04 Zn/Ir molar ratios are plotted with respect to the Zn/Ir molar ratios. Though a slightly greater difference in the $V_{Cl_2\&O_2}$ and V_{O_2} potentials for the Ir10 blank is seen, there doesn't appear to be an evidenced relation as the Zn/Ir molar ratio is increased.

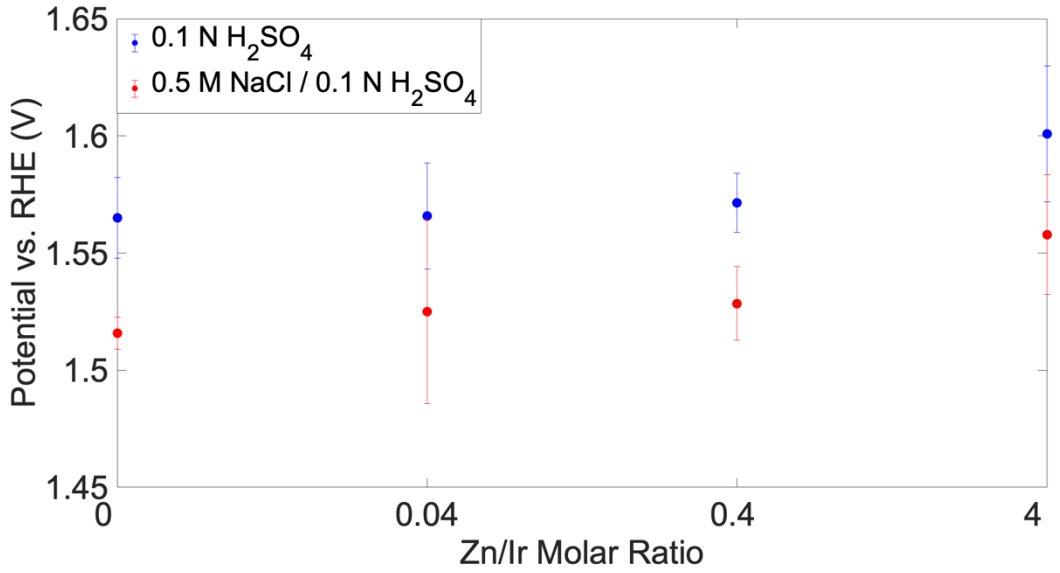

Figure 20: Plot of the average measured potentials in the presence of 0.5 M NaCl / 0.1 N H_2SO_4 (red) and pure 0.1 N H_2SO_4 with respect to the Zn/Ir molar ratio. Standard deviations are indicated.

III.3.3.5.1 A Hydrothermal Encapsulation

This second hypothesis proposing direct diffusion of the chloride ion towards the glassy carbon electrode prompted a hydrothermal synthesis of ZIF-8 overlayer according to the work by Zhu et. al.[43] Zinc chloride, 2-methylimidazole, and sodium formate were homogenized in 50 mL of methanol and then poured into a Teflon autoclave chamber. A polished rotating disk electrode prepared with an Ir10film was then placed in the autoclave and subsequently sealed, the chamber was then incubated in an oven at 85°C overnight. *Figure 21* below depicts the protocol.

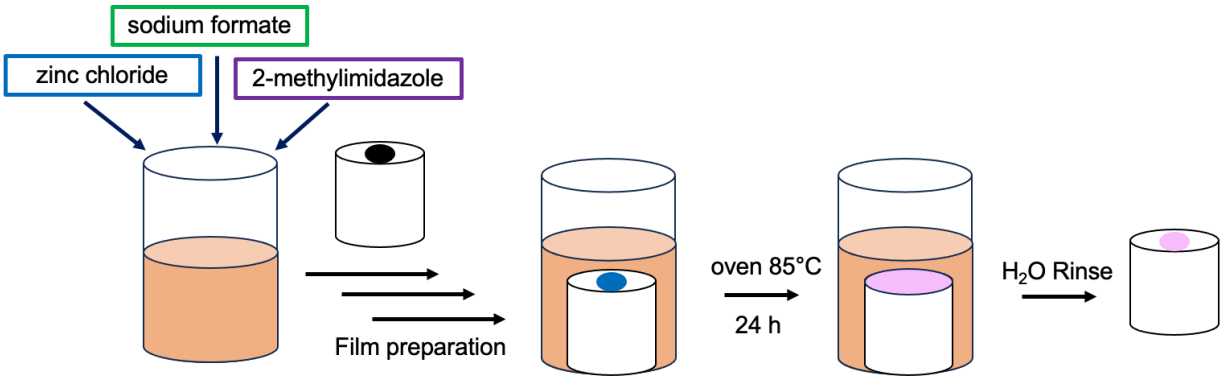

Figure 21: Hydrothermal synthesis protocol to deposit a ZIF-8 overlayer above a prepared Ir10 film. The salts were added into a methanolic solution, homogenized,

and placed in the Teflon chamber. An Ir10ink was prepared, drop casted onto an electrode, and allowed to dry; Teflon tap was wrapped along the sides to avoid salt deposition along the sides while the electrode was in the chamber. The electrode was then placed in the methanolic solution with the dissolved salts and allowed to incubate in the oven at 85°C overnight. The electrode was then removed and the top was gently rinsed with water.

The electrode was then taken from the autoclave chamber and analyzed in either the acidic, 0.5 M NaCl supporting electrolyte solution or the aqueous, acidic supporting electrolyte solution. Voltammogram results are shown below in *Figure 22*.

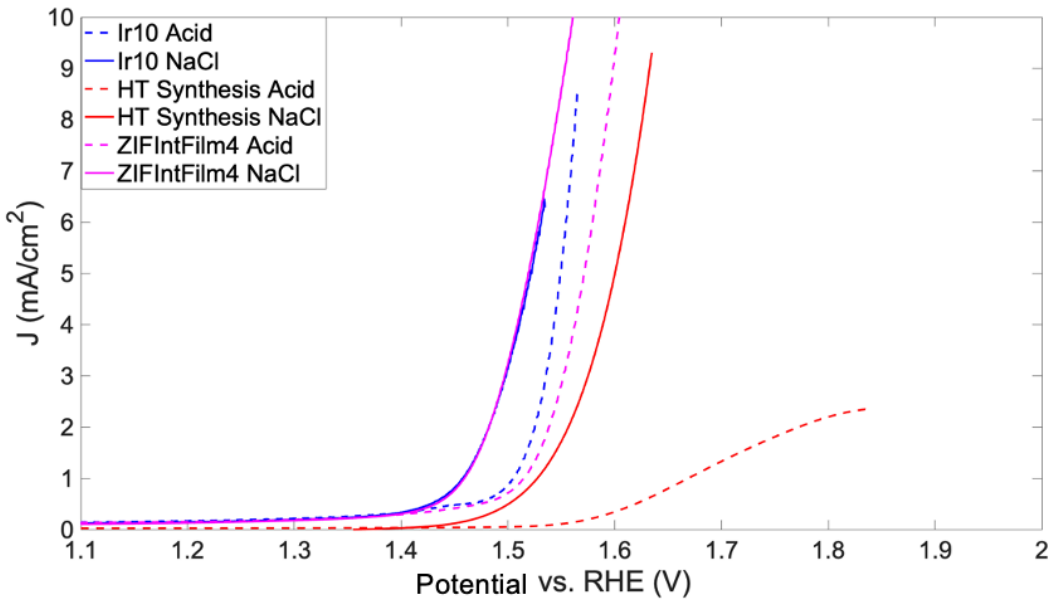

Figure 22: Voltammogram of an Ir10film with a ZIF-8 overlayer realized through a hydrothermal synthesis. Blue lines indicate a native Ir10 film, magenta lines indicate current densities recorded for a ZIFIntFilm4 trial, and the red lines are the current densities recorded for an Ir10 film modified with the ZIF-8 overlayer through the Hydrothermal synthesis. The **dotted** lines represent those measurements performed in the 0.1 N H_2SO_4 supporting electrolyte and the **solid** lines represent those measurements performed in an acidic, 0.5 M NaCl supporting electrolyte.

The ZIF-8 overlayer appears to increase the potentials recorded in both the acidic supporting electrolyte and in the acidic, 0.5 M NaCl supporting electrolyte when compared the potentials recorded for the ZIFintfilm4 and the native Ir10film. Moreover, an evidenced increase in current is still apparent upon placing the electrode in the 0.5 M NaCl / 0.1 N H_2SO_4 solution. This method may furthermore encounter difficulties in analyzing the amount of material that is dissolved over the electrocatalytic film, thus increasing the complexity of optimizing the deposition.

III.3.4 Rotating Ring Disk Voltammetric Evaluation of MOF Incorporated Films

The electrocatalytic film architecture designed through the integrated approach appeared to evolve greater quantities of current and consistently lower potentials when placed in a 0.5 M NaCl / 0.1 N H_2SO_4 solution indicating evidence for the evolution of the parasitic chlorine gas. The extent of the CER was hypothesized to be dependent on the chloride concentration. Acquisition of rotating ring disk electrodes with a bipotentiostat further enabled the current evolved from the CER to be quantitated from the current evolved from the OER with a single film. Probing solutions of varying chloride concentrations thus became feasible.

III.3.4.1 Collection Experiments

The addition of a ring electrode surrounding the disk creates a mathematical geometry that enables faradaic processes such as the oxidation of the chloride ion to molecular chlorine to be distinguished and quantified from non-faradaic processes. The electroactive species (R) may be oxidized at the disk to produce (O) and an anodic current (i_{Disk}); the generated (O) that then reaches the ring held at a selective potential becomes rapidly reduced to species (R) as a ring current (i_{Ring}) is measured, as shown in *Figure 23*.

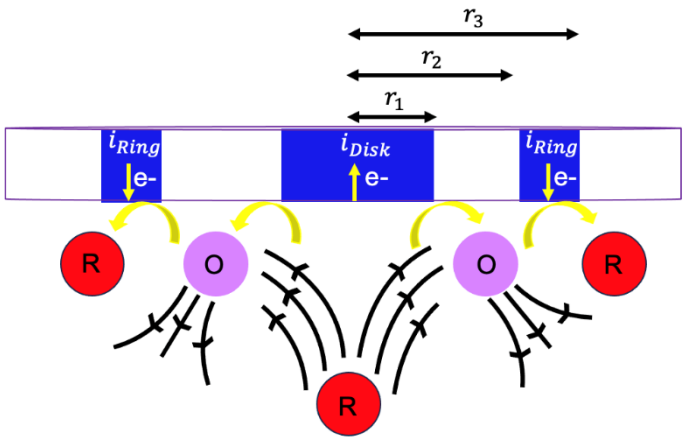

Figure 23: Rotating ring disk electrode (RRDE) geometry and flow pattern of a reduced species such as the chloride ion (R) and its oxidized counterpart (O), the chlorine molecule, produced at the disk.

A measurement of the ring collection current (i_{Ring}) can quantify the amount of (O) generated at the disk. This ring collection current may be evaluated by solving the steady-state ring convective-diffusion equation using the concentration of the electroactive species (O) generated at the disk,

$$r\left(\frac{\partial C_O}{\partial r}\right) - y\left(\frac{\partial C_O}{\partial y}\right) = \left(\frac{D_O}{0.51\omega^{3/2}\nu^{-1/2}}\right)\frac{1}{y}\left(\frac{\partial^2 C_O}{\partial y^2}\right) \qquad (15)$$

The boundary conditions required to solve this equation are more convoluted than those of a rotating disk electrode and may be stated here.

(1) The conservation of matter requires that the amount of electroactive species O generated at the disk electrode be equivalent to the amount of the initial electroactive species R arriving at the disk, and thus assuming the solubilities are equal, $-J_R(0,t) = -J_O(0,t)$ and,

$$D_O\left(\frac{\partial C_O}{\partial y}\right)_{y=0} = -D_R\left(\frac{\partial C_R}{\partial y}\right)_{y=0} \tag{16a}$$

$$\left(\frac{\partial C_O}{\partial y}\right)_{y=0} = \frac{-i_D}{nFAD_O} \tag{16b}$$

(2) There is no current flow in the insulating gap region ($r_1 \leq r < r_2$) and thus,

$$\left(\frac{\partial C_O}{\partial y}\right)_{y=0} = 0 \tag{17}$$

(3) The generated electroactive species O is absent from the bulk solution,

$$\lim_{y\to\infty} C_O = 0 \tag{18}$$

(4) Under the limiting current conditions at the ring ($r_2 \leq r < r_3$),

$$C_O(y=0) = 0 \tag{19}$$

(5) The bulk concentration of R is C_R^*,

These boundary conditions enable the ring current to be equated to,

$$i_O = nFD_O 2\pi \int_{r_2}^{r_3} \left(\frac{\partial C_O}{\partial y}\right)_{y=0} r\, dr \tag{20}$$

Further defining the dimensionless variable (w),

$$w = \left(\frac{0.51\omega^{3/2}\nu^{-1/2}}{D_O}\right)^{1/3} y \tag{21a}$$

And,

$$u = \frac{0.799\pi r_1^2 F (D_O)^{2/3} \omega^{1/2} \nu^{-1/6}}{i_R} C_O \qquad (21b)$$

Allows the collection efficiency (N) to be stated as,

$$N = -\frac{i_{ring}}{i_{disk}} = \frac{2}{r_1^2} \int_{r_2}^{r_3} \left(\frac{\partial u}{\partial w}\right)_{w=0} r dr \qquad (22)$$

Use of the Laplace transform permits the expression on the right of *Equation 22* to be given in terms of Airy functions[47,48]. Moreover, the collection efficiency turns out to only be a factor of r_1, r_2, and r_3.[45]

The collection efficiency may also be determined empirically. The oxidation and reduction of a 10 mM $K_3Fe[CN]_6$ in 0.1 M KNO_3 solution was studied through cyclic voltammetry and then linear sweep voltammetry was conducted by scanning from 0.5 V to -0.3 V vs. RHE at a rate of 0.01 V/sec at ascending rotation speeds, as shown in *Figure 24a*. The limiting ring current was then divided by the limiting disk current and a collection factor of 0.245 was obtained.

The quantity of chloride ions diffusing towards the RRDE electrode and being oxidized at the disk (i_{CER}) may thus be equated to the collection current detected at the ring divided by the collection factor,

$$i_{CER} = \left|\frac{i_{ring}}{N}\right| \qquad (23)$$

However, the analytical solution must remain sufficiently acidic to prevent the disproportionation of the molecular chlorine evolved at the disk into hypochlorous acid and hypochlorite, reactions with a pKa of 2.98 and a pKa of 7.53, respectfully[49]. The solubility of molecular chlorine at pH = 1 (0.07 mol/L) is moreover nearly 1000x greater than the solubility of molecular oxygen[50], and thus the collection current measured at the ring can be considered a quantitative indication of the molecular chlorine reaching the ring, provided that the potential imposed at the ring is within the diffusion limited current region of the chlorine reduction reaction, avoiding any significant oxygen reduction[49].

The absence of oxygen reduction occurring at the ring may be further verified by comparing the ring currents evolved when placed in a 0 mM NaCl solution (*Figure 24b*) with that evolved when placed at 500 mM NaCl *(Figure 24c*), as shown in *Figure 24d* at 1600 RPM. The current evolved at the disk contributed by the competing OER (i_{OER}) may be determined by selecting a desired current density evolved at the disk, i_{disk} (3 mA/cm^2) and ascertaining the potential at which that current density is reached, then using that potential to determine the corresponding ring current, i_{ring}. Multiplying the ring current by the collection efficiency (N), which gives the i_{CER}, and then subtracting that result from the i_{disk} gives the current produced from the OER, the i_{OER},

$$i_{OER} = i_{disk} - i_{CER} = i_{disk} - \left|\frac{i_{ring}}{N}\right| \qquad (24)$$

With the i_{CER} and the i_{OER} calculated, the faradaic selectivity for the CER can be derived (and replacement of the numerator with $^{i_{OER}}/_{4}$ can be completed to quantitate selectivity for the OER),

$$\varepsilon_{CER} = \frac{\frac{i_{CER}}{2}}{\frac{i_{OER}}{4} + \frac{i_{CER}}{2}} \tag{25}$$

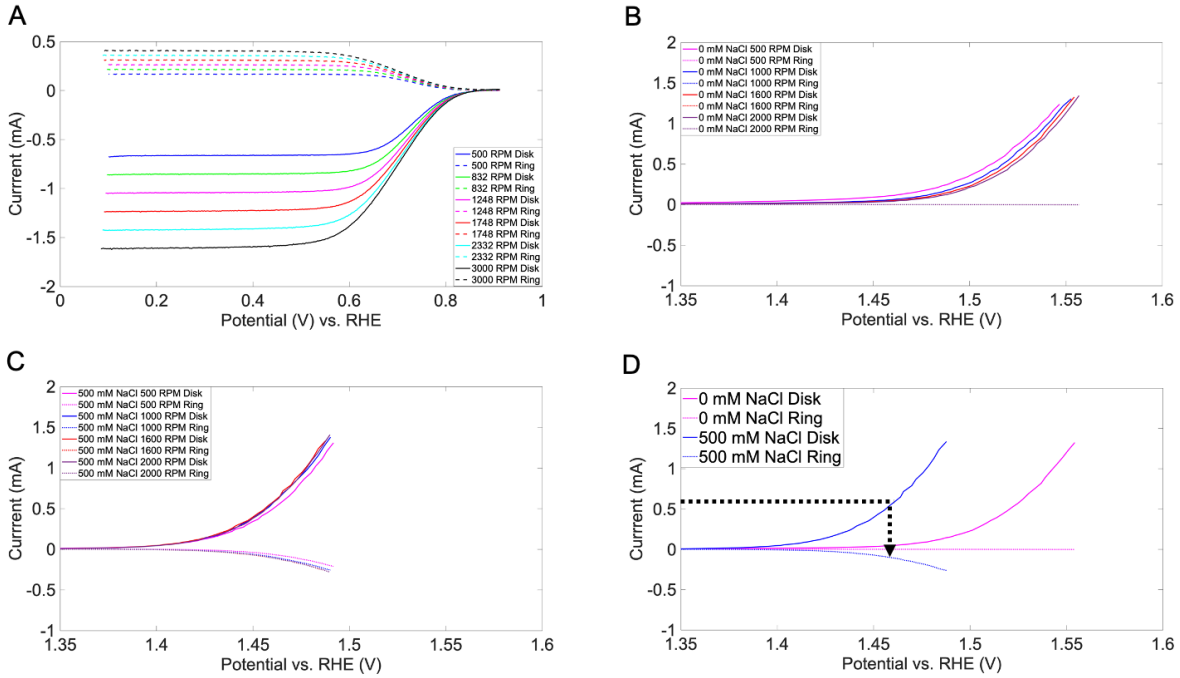

Figure 24: (A) Voltammograms of 10 mM $K_3Fe[CN]_6$ in 0.1 M KNO_3 solution analyzed at varying rotation rates for the determination of the collection efficiency. (B) Voltammograms at different rotation speeds of an Ir10 film placed in a 0.5 M perchloric acid supporting electrolyte, the lack of current recorded at the ring confirmed the absence of the ORR. (C) Voltammograms at 500 RPM, 1000 RPM, 1600 RPM, and 2000 RPM of an Ir10 film when placed in 0.5 M perchloric acid and 500 mM NaCl, showing evidence of the CRR by the current recorded along the ring. (D) Delineation of the reading of the voltammogram for the determination of the CER selectivity.

Prior to calculation of the CER selectivity, the ring currents were corrected for by subtracting the initial contribution from the resistance in the film *(Figure 25a)*, then fitting a polynomial of first order to the ring current to remove the background current *(Figure 25c),* then subtracting the Y values of the first order polynomial curve from the ring current to arrive at the corrected ring current *(Figure 25d)*. This procedure was used for all subsequent CER selectivity computations.

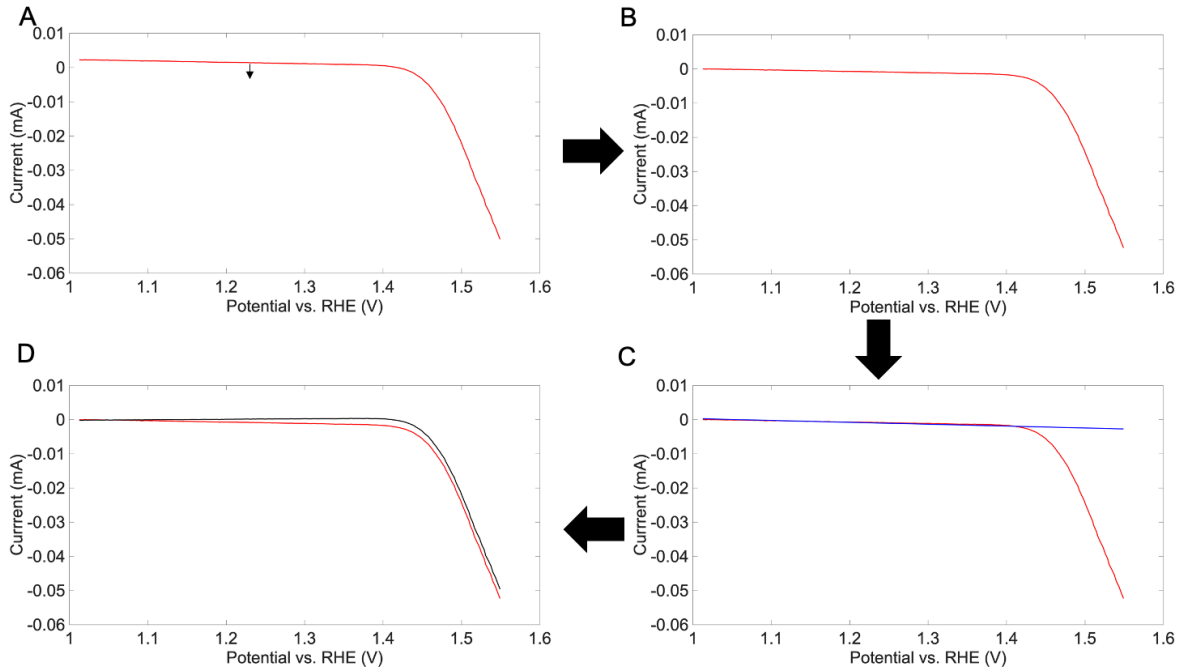

Figure 25: (A) The original ring current, the initial y value was subtracted from all y values to remove the resistance from the film and arrive at the ring current shown in (B). A polynomial of first order was then fitted to a specified index with the use of MATLAB and is displayed in (C). The y values of this polynomial were then subtracted from the y values of the ring current previously corrected for the resistance in the film to arrive at the corrected ring current shown in (D).

III.3.4.2 Development of the Electroanalytical RRDE Protocol

With reference to Vos. et. al., the electroanalytical RRDE protocol was designed with a voltammetric sequence under hydrodynamic conditions that electropolished the platinum ring, then conditioned the film, and then performed a linear sweep at four distinct rotation rates while setting the ring potential to 0.95 V vs. RHE[49]. The platinum ring was electropolished from -0.1 V to 1.7 V vs. RHE at 100 mV/sec in an acidic supporting electrolyte consisting of 0.2 N H_2SO_4 (pH = 0.88) with 500 mM KNO_3 without the presence of the chloride ion. The choice of adding a requisite amount of salt to the solution and which number of conditioning cycles to apply during the film conditioning step were probed. A single Ir10ink was prepared and then drop casted onto rotating ring disk electrodes. Eight electrodes were prepared, and the CER selectivity of each film was evaluated after being subjected to 20, 40, 60, or 80 film conditioning cycles from 0.56 V to 1.06 V vs. RHE with and without 500 mM NaCl added to the solution (*Figure 26*). A linear sweep from 1.07 V vs. RHE to a current cutoff equivalent to 5 mA/cm^2 was then conducted at 500 RPM, 1000 RPM, 1600 RPM, and 2000 RPM in 0.2 N H_2SO_4, 500 mM NaCl. The scan taken at 1600 RPM was used in the CER selectivity computation. The CER selectivity was computed by measuring the disk and ring currents at 1.46 V vs. RHE. The ring currents were corrected for the background current, while the collection delay at 1600 RPM was estimated to affect the evolved ring current by less than 10 mV and was not considered.

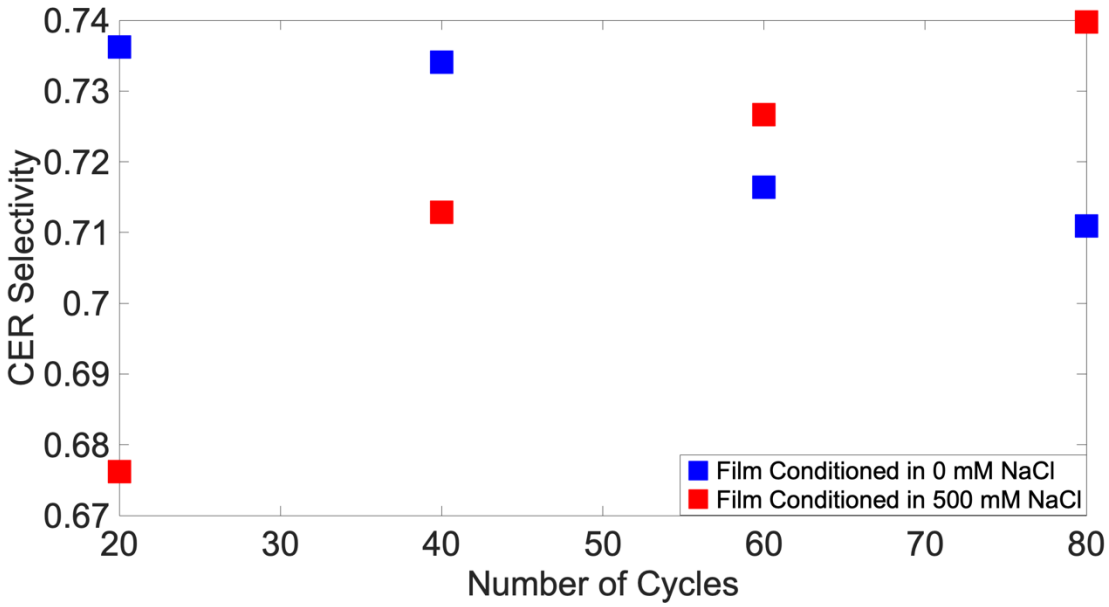

Figure 26: Effect of the number of cycles and the presence of 500 mM NaCl during the film conditioning step on the CER selectivity of an Ir10film, evaluated in a 0.2 N H_2SO_4, 500 mM NaCl supporting electrolyte. The ionic strength of both the 0 mM NaCl / 500 mM KNO_3 in 0.2 N H_2SO_4 and the 500 mM NaCl in 0.2 N H_2SO_4 analytical solutions probed during the film conditioning step were equal.

It is apparent that the number of conditioning cycles does affect the computed CER selectivity of Ir10film, increasing from 20 to 80 cycles when the conditioning is conducted in 0.2 N H_2SO_4, 500 mM NaCl, and decreasing from 20 to 80 cycles when the conditioning is conducted in 0.2 N H_2SO_4, 500 mM KNO_3. Thus 100 conditioning cycles were programmed in the film conditioning step of the electroanalytical RRDE protocol to minimize the variability in the CER selectivity computation due to the conditioning step.

III.3.4.3 Competitive Adsorption by the Acidic Supporting Electrolyte

The use of sulfuric acid as the acidifying supporting electrolyte may introduce a competitive surface adsorbate that diminishes the effects of the chloride ion on the perceived CER and OER selectivities of the electrocatalytic films[51]. Thus the electroanalytical RRDE protocol was used to probe the CER selectivity of the control Ir10film in the presence of 0 mM NaCl, 10 mM NaCl, 20 mM NaCl, 50 mM NaCl, 100 mM NaCl, 200 mM NaCl, 500 mM NaCl, and 1 M NaCl solutions acidified with either 0.2 N H_2SO_4 and KNO_3, which was added in the requisite proportion that ensured the ionic strength of each solution was equal, or 0.5 M $HClO_4$ (pH = 0). Five Ir10films from the same Ir10ink were trialed in 0.2 N H_2SO_4 / KNO_3 (dark red dots in *Figure 27*) and four Ir10films from the same Ir10ink were trialed in 0.5 M $HClO_4$ (pH = 0) (royal blue dots in *Figure 27b*) with the CER selectivity standard deviation indicated.

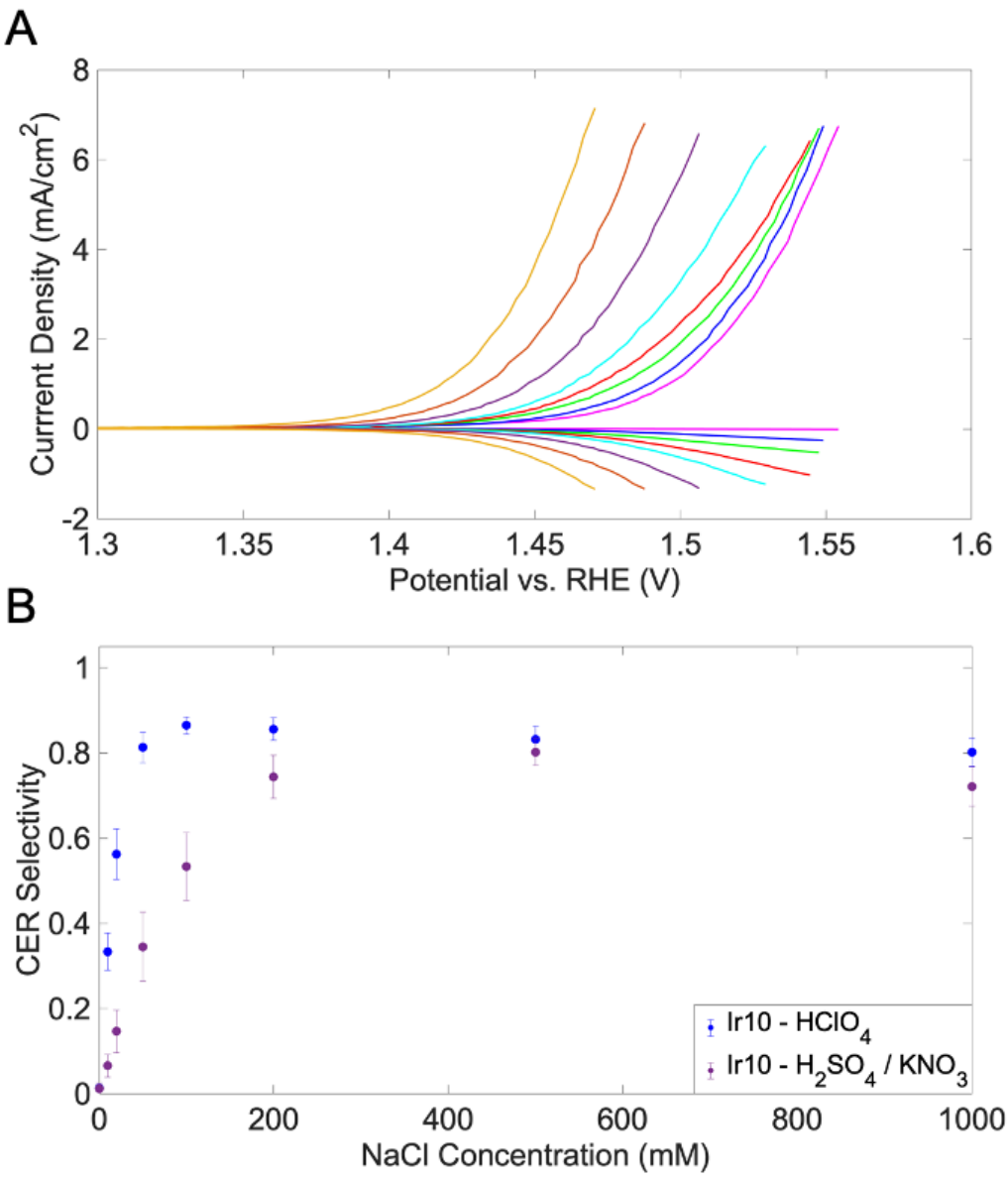

Figure 27: (A) Compiled linear sweep voltammograms for one Ir10 film in 0.5 M $HClO_4$ showing the ring and the disk currents: 0 mM NaCl (magenta), 10 mM NaCl (royal blue), 20 mM NaCl (neon green), 50 mM NaCl (red), 100 mM NaCl (cyan), 200 mM NaCl (purple), 500 mM (red), 1 M (yellow). (B) Computed CER selectivity at 3 mA/cm^2 in 0 mM NaCl, 10 mM NaCl, 20 mM NaCl, 50 mM NaCl, 100 mM NaCl, 200 mM NaCl, 500 mM NaCl, and 1 M NaCl in 0.2 N H_2SO_4/KNO_3 (pH = 0.88) or 0.5 M $HClO_4$ (pH = 0) supporting electrolyte with standard deviations calculated from five films drop-casted from the same ink and four films drop-casted from the same ink, respectively.

It is apparent that the use of perchloric acid as the acidic supporting electrolyte decreases the standard deviation amongst films drop-casted from the same ink, further enhancing the potential discrimination in the CER (and OER) selectivities between the control Ir10 films and those modified with the ZIF-8 nanosheets.

Moreover, the CER selectivity in the presence of the sulfuric acid / potassium nitrate solution appears to diminish at all probed concentrations and would render any perceived changes occurring in the presence of the ZIF-8 nanosheets quite challenging to interpret. To avoid the potential complication of an additional competitive adsorbate, perchloric acid was used to probe any perceived effect of the ZIF-8 nanosheets on the CER selectivity.

III.3.3.4 RRDE Voltammetric Evaluation of the ZIFintfilm

Electrocatalytic film architectures modified with ZIF-8 nanosheets showing a decrease in the CER selectivity can be an indication that the mass transport of the chloride ion is being impeded. With the electroanalytical RRDE protocol, the ZIFintfilm was probed at 0 mM NaCl, 10 mM NaCl, 20 mM NaCl, 50 mM NaCl, 100 mM NaCl, 200 mM NaCl, 500 mM NaCl, and 1 M NaCl solutions each in 0.5 M $HClO_4$ supporting electrolyte. The rotating ring disk electrodes are devoid of a sufficient crevice within the disk to enable 16 µL of a homogenized ZIFIr10ink with the requisite methanolic addition of ZIF-8 nanosheets to be drop-casted on the film, thus the ZIF-8 nanosheets were directly weighted into the ZIFIr10ink4 (with water as the dispersing solvent aliquot) and 8 µL was drop casted onto the disk taking care to avoid the ring. Each ink was prepared and drop-casted on multiple rotating ring disk electrodes. Each electrode was initially placed in the 0 mM NaCl, 0.5 M $HClO_4$ solution and electropolished at 1600 RPM from -0.1 V to 1.7 V vs. RHE, and then subjected to 100 film conditioning cycles at 1600 RPM from 0.56 V to 1.06 V vs. RHE, followed by a linear sweep from 1.07 V vs. RHE to a current cutoff equivalent to 5 mA/cm^2 at 500 RPM, 1000 RPM, 1600 RPM, and 2000 RPM with the ring potential set to 0.95 V vs. RHE. Then the ring was electropolished once more in the 0 mM NaCl, 0.5 M $HClO_4$ solution before subjecting the same film to a linear sweep in the presence of 10 mM NaCl, 0.5 M $HClO_4$. Between each solution of increasing NaCl molarity probed in the linear sweep, the ring was electropolished in the 0 mM NaCl, 0.5 M $HClO_4$ solution. The CER selectivity of each film at each concentration was computed for the 1600 RPM scan by measuring the disk current densities closest to 3 mA/cm^2. The ring currents were corrected for the background current, while the collection delay at 1600 RPM was estimated to affect the evolved ring current by less than 10 mV and was not considered. Four ZIFintfilm4 were trialed, and the three most similar computed CER selectivities were included in the standard deviation calculation shown within the cyan dots of *Figure 28* below, where a comparison of the CER selectivity between the four Ir10 film perchloric blank and the ZIFintfilm4 are indicated, up to 300 mM.

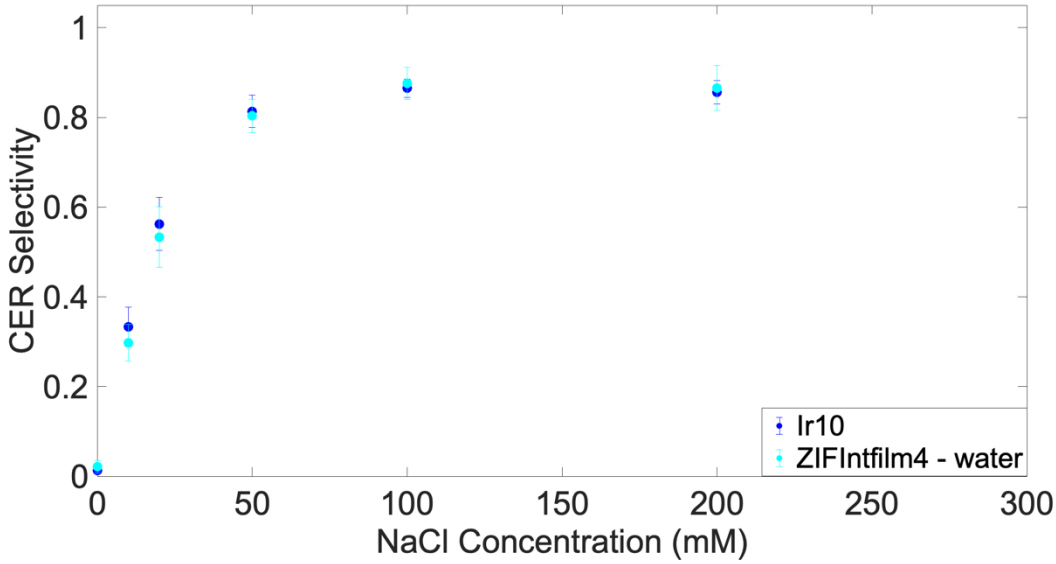

Figure 28: Comparison of the CER selectivity of four Ir10 films (royal blue dots) and three ZIFintfilm4 films with a 4 Zn/Ir molar ratio using water as the dispersing solvent aliquot.

Minimal differences between the Ir10 and a MOF-incorporated film with a 4 Zn/Ir molar ratio are evident. Thus A ZIFIr10ink40 was also prepared, which required the water aliquot of the film preparation protocol to be replaced with methanol to enhance the solubility of the nanosheets and prevent cracking of the electrocatalytic film. Five ZIFintfilm40 were probed with the two initial drop-casted films showing the most comparable CER selectivities that were thus used to compute the standard deviation, as shown in the magenta dots in *Figure 29* below.

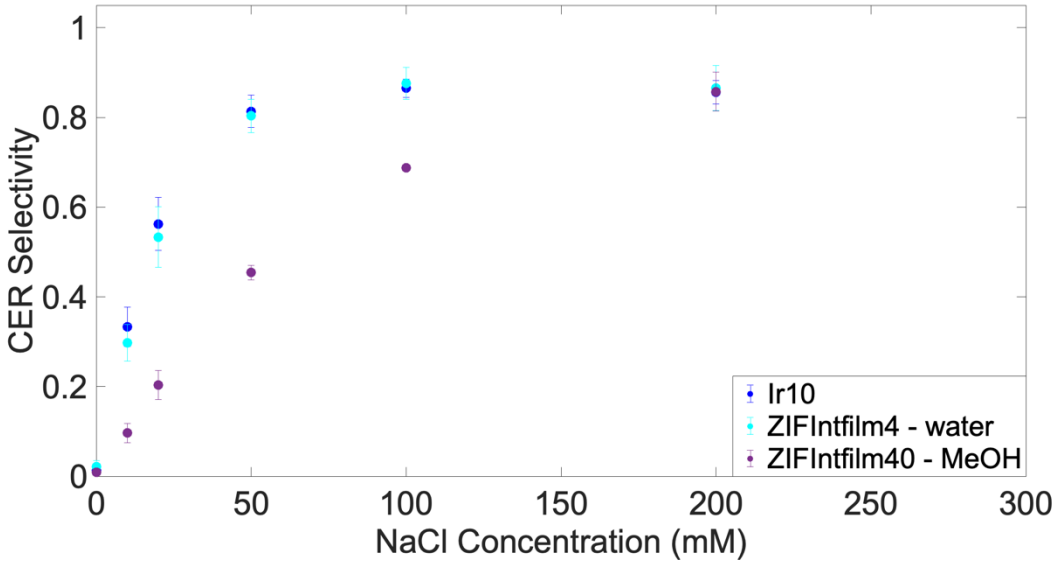

Figure 29: Comparison of the CER selectivity from 0 mM to 300 mM NaCl of four Ir10 films (royal blue), three ZIFintfilm4 constructed with water as the dispersing solvent, and two ZIFintfilm40 constructed with MeOH as the dispersing solvent.

The results indicate a near 50% decrease in the CER selectivity upon increasing the Zn/Ir molar ratio from 4/1 to 40/1 when assayed in the presence of 0.5 M $HClO_4$ supporting electrolyte, indicating that the catalytic architecture with a homogeneous integration of the ZIF-8 nanosheet may indeed arrest the mass transport of the chloride ion within the electrocatalytic film. To improve the stability of films incorporated with greater quantities of ZIF-8 nanosheets, the consistency of the dispersing solvent aliquot (previously always water) was trialed, as shown in below in Table 2.

Table 2: Ink preparation trials that varied the consistency of the solvent aliquot, the chosen solution for the solvent aliquot is highlighted.

Solvent (V/V)	Zn / Ir	Good Spot	CER	Stability
100% Water	20 / 1	Yes		Film cracked
100% MeOH	40 / 1	Yes	good (2 initial films)	ink separated
100% MeOH	80 / 1	Yes	good (2 initial films)	ink separated
50% MeOH 50% water	80 / 1	No		film cracked
75% MeOH 25% water	80 / 1	Yes	good	ink separated
50% MeOH 50% DMSO	80 / 1	Yes	bad	ink stayed together
50% MeOH 50% 1-P	80 / 1	Yes	better than DMSO	ink separated
100% 1-P	40 / 1	No		film spread
75% 1-P 25% water	40 / 1	No		film cracked
75% 1-P 25% EtOH	40 / 1	Yes	good	ink stayed together
75% MeOH 25% EtOH	40 / 1	No		film cracked

50% MeOH 50% EtOH	40 / 1	No		film cracked
75% 1-P 25% EtOH	80 / 1	Yes	good	film separated a bit
50% 1-P 50% EtOH	40 / 1	No		film cracked
65% 1-P 35% EtOH	40 / 1	No		Film not homo
75% 2-P 25% EtOH	40 / 1	No		film cracked
70% 2-P 30% MeOH	40 / 1	No		film cracked

A solvent aliquot consisting of 75% 1-propanol and 25% ethanol was chosen as it appeared to maintain the integrity of the ink while also being proposed to promote dispersion of the nanosheets. A comparison of the computed CER selectivity between Ir10film, ZIFintfilm20, ZIFintfilm40, ZIFintfilm120, and ZIFintfilm160 are indicated up to 300 mM in *Figure 30a* and indicate a decrease in CER selectivity upon increasing the Zn/Ir molar ratio within the electrocatalytic film through NaCl concentrations up to ~100 mM. This trend is further depicted in *Figure 30b* where the Zn/Ir ratio within the MOF incorporated inks prepared with the 75% 1-P and 25% EtOH solvent aliquot and an initial value of 4 to a value of 200 is plotted and the computed CER selectivity at each of these ratios is delineated. The standard deviation of the ZIFintfilm20 is of four films, the ZIFintfilm60 is of three films, the ZIFintfilm80 is of six films, the ZIFintfilm100 is of three films, the ZIFintfilm120 is of three films, ZIFintfilm160 is of three films, and the ZIFintfilm200 is of three films. It is apparent that the CER selectivity drops by ~65% upon increasing the Zn/Ir molar ratio within the MOF incorporated films from 0/1 to 160/1 at 10 mM NaCl as is depicted in the bar graphs of *Figure 30c*. Interestingly, the potential at which a current density of 3 mA/cm^2 was reached at the disk seemed only slightly vary with the Zn/Ir molar ratio, only a ~30 mV difference between the Ir10 and the ZIFintfilm160 is apparent as shown in *Figure 30d*. That difference moreover appeared to be consistent over the range of concentrations probed indicating that the electrocatalytic activity of the Ir10 remains unaffected by the presence of the nanosheets. The rate of evolution of the CER appears to increase up to about 150 mM as similarly suggested by Kuznetsova et. al. until the active sites along the catalytic surface become saturated[52]. Interestingly, the percent drop in CER selectivity through incorporation of the nanosheets is rather consistent up to this concentration.

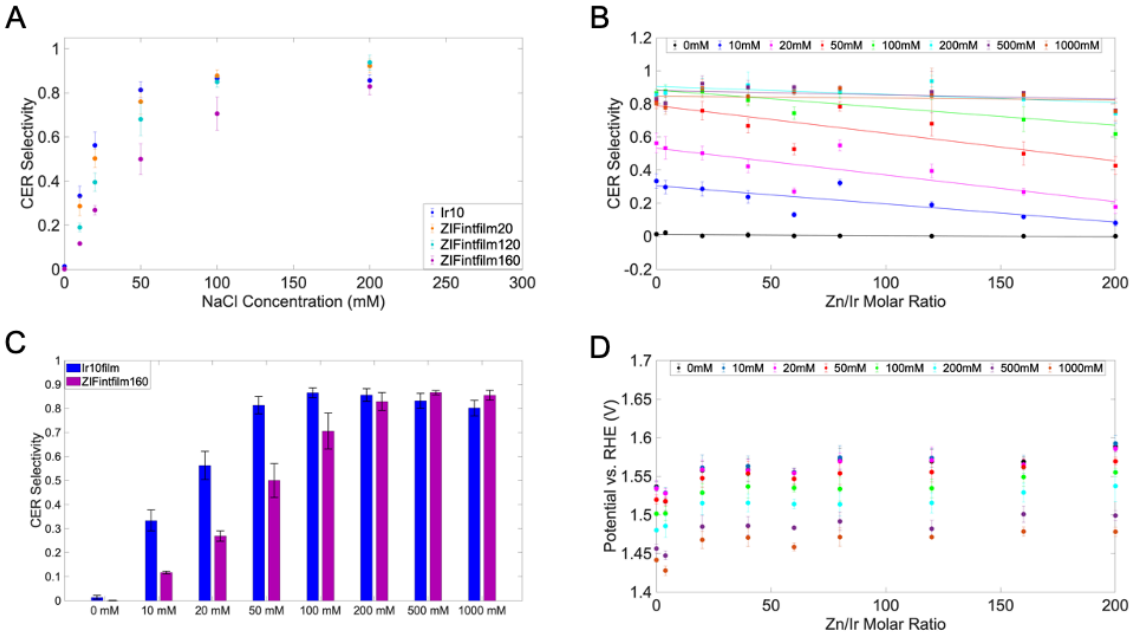

Figure 30: (A) Comparison of the CER selectivity from 0 mM to 300 mM NaCl of four Ir10 films (royal blue), three ZIFintfilm20 (orange), three ZIFintfilm120 (cyan), and three ZIFintfilm160 (magenta) with 75% 1-propanol and 25% ethanol as the dispersing solvent. The plot in (B) indicates the effect of the Zn/Ir molar ratio on the CER selectivity. (C) reveals the drop in CER selectivity especially at lower NaCl concentrations through incorporation of the nanosheets. (D) plots the potential at which the disk current reaches a current density of 3 mA/cm^2 for each Zn/Ir molar ratio at each concentration.

A consistent percent drop in CER selectivity up to ~150 mM may indeed indicate that the performance of the nanosheets isn't affected by chloride ion concentration. To confirm that the stability of the nanosheets wasn't the culprit for the evidenced increases in CER selectivity with increasing chloride ion concentration, a two-hour chronoamperometry test of the ZIFintfilm40 was conducted at 10 mM NaCl and shown in *Figure 31* and evidence for increased ring current was monitored, only modest increases were observed. A chronoamperometry measurement at 500 mM NaCl or 1000 mM NaCl would further negate the possibility that nanosheet stability is responsible for the decreased drops in CER selectivity evident as the chloride ion concentration is increased. However, it is more plausible that the coordination bond between the nitrogen and the zinc would be susceptible to degradation by the presence of the acid, though the CER selectivity of a ZIFintfilm40 for instance had been probed with six films (each film undergoing voltammetric analysis under acidic conditions for three-hour periods) drop casted from one prepared ink that maintained stability over the needed two-day period. A consistent ~25% drop in the CER selectivity as compared to the Ir10 was apparent amongst the six films probed. Thus stability of the nanosheet isn't expected to be the underlying cause of decreased drops in CER selectivity upon increase chloride ion concentrations.

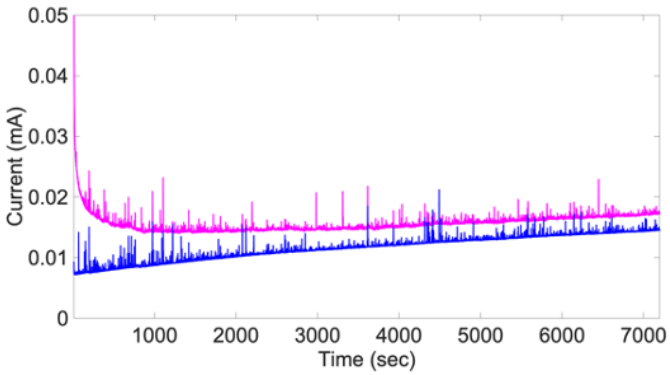

Figure 31: A two-hour chronoamperometric measurement at 10 mM chloride ion concentration of the ZIFintfilm40 drop casted from an ink prepared with the 75% 1-Propanol and 25% Ethanol solvent aliquot.

Consideration for the structure-activity relationship between the ZIF-8 nanosheets and the Ir10 electrocatalyst may enable an elucidation of the observed CER selectivity trends. Thus, the orientation of the ZIF-8 nanosheets with respect to the Ir10 electrocatalyst within the electrocatalytic film was probed through scanning electron microscopy by drop casting a ZIFintfilm60 onto a silicon wafer that had been treated through ozonolysis, to grow an oxide layer on the surface of the substrate, which prevented the spreading of the 8 µL drop. After drop casting and drying, film coated silicon wafer substrate was subsequently cut with a diamond blade and the cross section was imaged as shown in *Figure 32.*

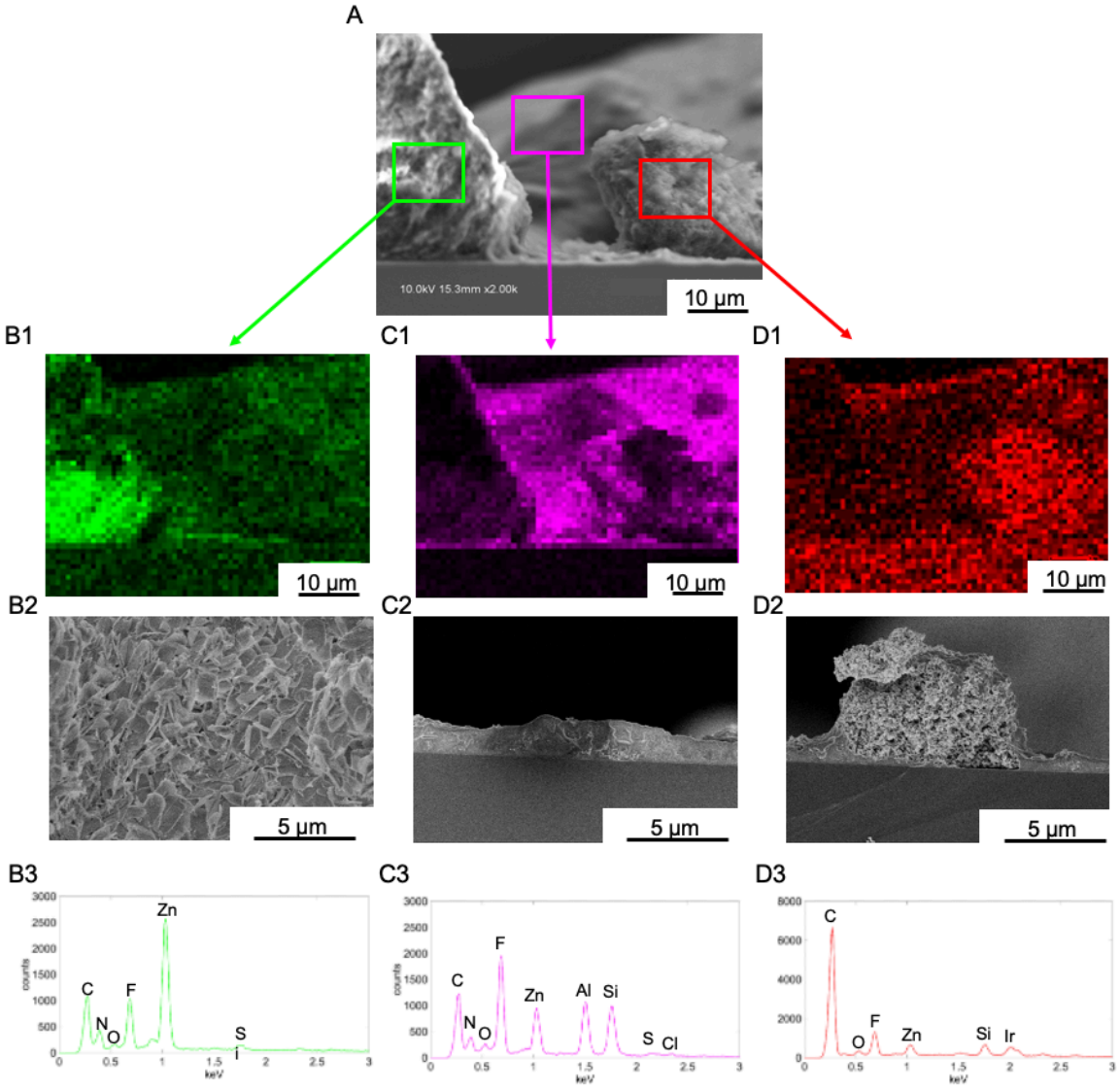

Figure 32: (A) SEM image of a cross section of an electrocatalytic film with a 60/1 Zn/Ir molar ratio highlighting three major ensembles consisting of (B1) zinc, (C1) fluorine, and (D1) iridium imaged with Scanning Electron Microscopy Energy Dispersive X-Ray Spectroscopy (SEM EDS). (B2-D2) are magnified SEM images of each elemental ensemble and (B3-D3) displays their elemental composition obtained through SEM EDS.

Three major elemental ensembles within the electrocatalytic film were found. The first shown in *Figure 32b(1-3)* is concentrated with zinc, implying a conglomeration of nanosheets. The second shown in *Figure 32c(1-3)* consists of a layer of fluorine, an element uniquely found within the Nafion of the electrocatalytic film; the layer also consisted of a large quantity of zinc, implying that the nanosheets may be interdispersed within the Nafion. Indeed, Wang et. al. indicated that the nitrogens on the organic linker within the nanosheets could form an interfacial pairs with the sulfate groups within the Nafion, promoting proton conduction within the electrocatalytic

film[53]. The third ensemble shown in *Figure 32d(1-3)* consisted of a large quantity of carbon with evidence of Ir as well as Zn. These clusters indicate that the ZIF-8 nanosheets may be within close proximity to the Ir10 electrocatalyst, though the low resolution of EDS prevented an evaluation of the element localisation. The nitrogens on the organic linker within the nanosheets are also expected to be able to interact with the iridium nanoclusters and create a positive charge on the surface metal surface, potentially promoting the electrocatalytic activity[54].

The low resolution of the SEM-EDS analysis prevents the development of a structure-activity relationship that could divulge the underlying CER selectivity trends that are being observed. However, a noticeable decrease in the applied potential required to reach the 3 mA/cm^2 at the disk shown in *Figure 30d* is apparent upon increasing the NaCl concentration. Considering that the CER selectivity is derived from the calculated OER and CER currents that sum to the overall disk current of 3 mA/cm^2 (here in terms of current density) it may be of interest to plot the calculated OER and CER currents with respect to concentration and potential, which is shown in *Figure 33(A-B)*.

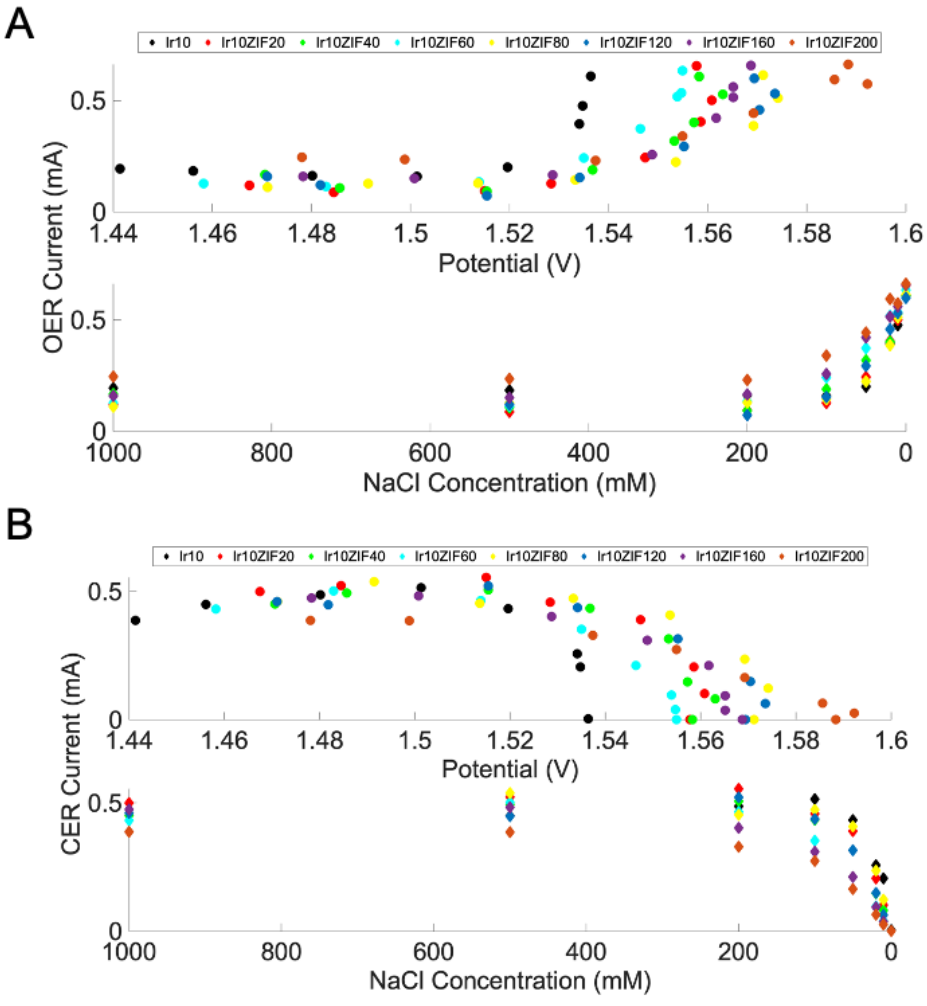

Figure 33: (A) and (B) show how the OER and CER currents are affected by the potential measured at a disk current density of 3 mA/cm^2 and the NaCl concentration.

Upon increasing the NaCl concentration, the CER current begins to increase with a simultaneous decrease in the applied potential at which the disk current density arrives at 3 mA/cm^2 as shown in *Figure 33b*. The OER current measured at the disk simultaneously begins to decrease, as shown in the bottom panel of *Figure 33a* with a concurrent decrease in the applied potential as shown in the top panel. This decrease in applied potential required to reach the 3 mA/cm^2 at the disk disfavors the formation of the OER intermediates; the driving force becomes insufficient to catalyze the OER[52]. Thus the decreased drop in CER selectivity in the presence of the nanosheets that becomes apparent at ~150 mM NaCl may indeed be at an applied potential value where the OER can no longer appreciably occur. Calculation of CER selectivity to evaluate the performance of the ZIF-8 nanosheets may thus be convoluted by the decrease in OER current that become appreciable as the chloride concentration increases and the applied potential decreases; indeed, a denominator factor is diminishing. That applied potential required to reach the 3 mA/cm^2 at the disk appears to decrease upon increasing the chloride ion concentration as the probability of permeation through any inherent defects in the material becomes promoted; it is this permeation that could enable the CER and drops the observed potential needed to reach the 3 mA/cm^2 at the disk below that which is needed for the OER. Moreover, the group of Krtil found that no oxygen could be detected at chloride concentrations above 50 mM in 0.1 M $HClO_4$ supporting electrolyte[7], though this nanosheet incorporation shows continued evidence of decreases in the CER current appear up to almost 200 mM chloride concentrations as evidenced by the decreasing regression lines plotted in *Figure 34a* below with minimal changes to the OER current observed by the regression lines of *Figure 34b.*

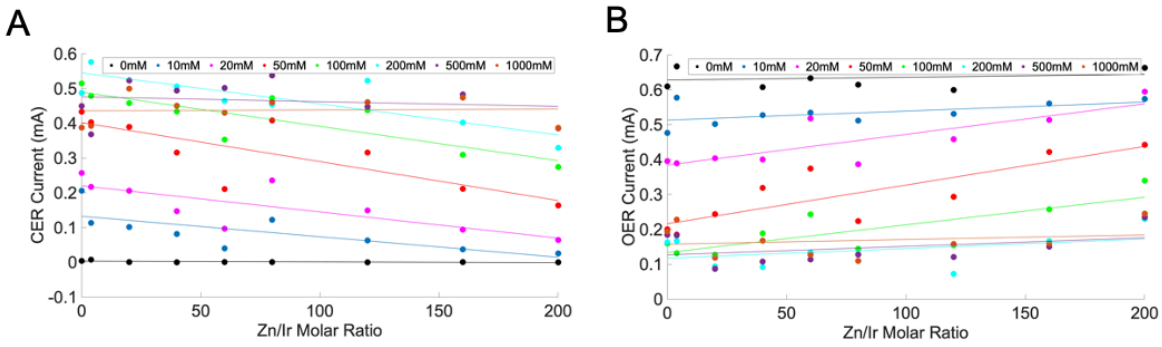

Figure 34: (A) and (B) reveals how the nanosheet quantity affects the CER and OER current calculated from a disk current density of 3 mA/cm^2.

This delay in the potential drop and concurrent decreased CER selectivity well beyond 50 mM could be due to the slight overpotential increases evidenced by the addition of the MOF as indicated previously in *Figure 30d*, though indeed these overpotential increases of 30 to 50 mV are quite modest, indicating the minimal effect of these nanosheets on the catalytic activity of the iridium nanoclusters.

Moreover, the minimal effect on the OER current with increasing nanosheet quantities indicated in *Figure 34b* suggest that the catalytic activity of the iridium nanoclusters towards the OER isn't affected by the presence of the nanosheets. This consistent OER current further indicates that the stiffen monoclinic phase doesn't

appear to decrease the water permeability even at heightened nanosheet quantities. However, the OER current appears to be affected by the presence of the chloride ion. Clarifying this potential kinetic effect would give assurance to the minimal impediment towards the mass transport of water molecules induced by the presence of the ZIF nanosheet. The observed decrease in the OER current in the presence of ascending chloride ion concentrations could begin to be understood and conceptualized. Moreover, it is evident that a decrease in the CER current is induced in the presence of the nanosheets. Verification that the CER current become under diffusion control would imply that the nanosheet indeed selectively impede the species transport of the chloride ion. Furthermore, whether chloride ion diffusion towards the glassy carbon working electrode or its nanodiffusion towards the electrocatalytic Ir nanoparticles is being impeded remains elusive; measurement of the solute diffusion coefficient within the film may reveal the arrested mode of chloride ion mass transport and indicate the most potent means of integrating the nanosheets within the film.

III.4 Conclusions

The exigent circumstance of the present-day natural resources demands a green alternative for the critical energy needs of our burgeoning society that siphons from a worldly abundant resource such as seawater. Utilization of a membrane to selectively arrest the transport of the chloride ion is an energetic efficient strategy towards tapping that unpure water source, though requires an improvement in the entropic diffusional selectivity to overcome the upper bound inherent in the state-of-the-art polymeric materials utilized in RO technology. This entropic selectivity may be achieved with the use of molecular sieve membranes with tunable apertures and pore sizes; the structural control inherent in the reticular synthesis utilized to design MOF makes these materials quite attractive towards the molecular sieve membrane applications. ZIF-8 has been indicated to have entropic selectivities over a magnitude higher than polymeric materials, and with an aperture of 3.4 Å in its cubic phase, is a potential material for the separation of the chloride ion from water for the selective evolution of oxygen at the anode for the OER. Dimensional confinement through the synthesis of ZIF-8 nanosheets with an aperture of 4.67 Å further creates additional sieving modes, extends the diffusional lengths of the impermeable chloride ion, and can improve the conductivity of the material, which was shown to be crucial when incorporated into a film dispersed with electrocatalytic nanoparticles.

Modification of iridium nanoparticle films with the ZIF-8 nanosheets to selectively arrest the species transport of the deleterious chloride ion were attempted through both a spin-coated procedure and an integrated approach. An initial promising result was seen for the Ir10 films integrated with the nanosheet, though was proven irreproducible after a thorough repetition of the electrochemical analysis, standardized through a modification of the electroanalytical trial sequence with a successful minimization of the experimental error. The hypothesis that the chloride ion may be diffusing directly toward the glassy carbon electrode was trialed through a modification to the ZIF-8 film incorporation design with a hydrothermal synthesis that deposited an overlayer encasing the Ir10 film. The promising result evidencing an increase in the overpotentials in the acidic, 0.5 M NaCl supporting electrolyte solution when compared

to the overpotentials recorded for an ZIFIntFilm4 and a control Ir10 film was however shadowed by the high increases in the overpotentials seen for the film in the acidic supporting electrolyte. This result indicates the need to decrease the precursor quantities to decrease the thickness of the film layer to improve the water permeability.

Subsequent evaluations of the decrease in the CER selectivity were conducted with a rotating ring disk working electrode, which enabled the competing faradaic oxidations occurring at the disk to be quantified at the ring. An electroanalytical protocol was developed that minimized the potential variability caused by the film conditioning on the CER selectivity. This optimized protocol was further probed with a control Ir10film at ascending concentrations of sodium chloride dissolved within sufficiently acidified aqueous solutions consisting of 0.2 N H_2SO_4 and KNO_3 or 0.5 M $HClO_4$ supporting electrolytes. Computations of the CER selectivities indicated lower standard deviations amongst the Ir10films trialed in the 0.5 M $HClO_4$ supporting electrolyte. Thus, perchloric acid was utilized to probe the CER selectivities of ZIF-integrated electrocatalytic films and the result indicated a near 65% decrease in the CER selectivity upon increasing the Zn/Ir molar ratio from 4/1 to 160/1 in 10 mM NaCl, demonstrating that the catalytic architecture with a homogeneous integration of the ZIF-8 nanosheet may indeed arrest the mass transport of the chloride ion within the electrocatalytic film. Minimal increases in the applied potential upon nanosheet integration were also evident. Morphological characterization of the proximity of the nanosheets to the electrocatalyst was attempted and improved resolution may give further insight into the proximity of the ZIF-8 nanosheets to the Ir catalytic nanoparticles.

Evaluation of the extent of kinetic or diffusional control to which the respective OER and CER currents defining the CER selectivity are subjected under the presence of the nanosheets would verify the utility of the nanosheets towards the selective arrestation of the species transport of the chloride ion. The hypothesis that the OER current decrease apparent at increased chloride ion concentrations is caused by the concurrent drop in applied potential and the creation of a kinetic impediment could moreover be verified. Molecular sieving membranes are susceptible to defects that decrease the selectivity of the membrane; these defects may indeed be the undesirable cause of continued CER selectivity calculated in the presence of the nanosheets. Thus optimization of the synthesis method may narrow the aperture distribution, enhancing the diffusional control of the CER current, and further the selectivity and permeability toward the desired water reagent. These improvements give promise to the potential of overcoming the upper bound and achieving selective OER electrocatalysis at the anode during seawater electrolysis.

III.5 References

1 Koros, W. J. & Zhang, C. Materials for next-generation molecularly selective synthetic membranes. *Nat. Mater.* **16**, 289-297 (2017). https://doi.org/10.1038/nmat4805

2 Singh, A. & Koros, W. J. Significance of Entropic Selectivity for Advanced Gas Separation Membranes. *Ind. Eng. Chem. Res.* **35**, 1231-1234 (1996). https://doi.org/10.1021/ie950559l

3 Yaghi, O. M. *et al.* Reticular synthesis and the design of new materials. *Nature* **423**, 705-714 (2003). https://doi.org/10.1038/nature01650

4 Furukawa, H., Cordova, K. E., O'Keeffe, M. & Yaghi, O. M. The Chemistry and Applications of Metal-Organic Frameworks. *Science* **341**, 1230444 (2013). https://doi.org/10.1126/science.1230444

5 Li, H., Eddaoudi, M., O'Keeffe, M. & Yaghi, O. M. Design and synthesis of an exceptionally stable and highly porous metal-organic framework. *Nature* **402**, 276-279 (1999). https://doi.org/10.1038/46248

6 Moosavi, S. M., Boyd, P. G., Sarkisov, L. & Smit, B. Improving the Mechanical Stability of Metal–Organic Frameworks Using Chemical Caryatids. *ACS Cent. Sci.* **4**, 832-839 (2018). https://doi.org/10.1021/acscentsci.8b00157

7 Gin, D. L. & Noble, R. D. Designing the Next Generation of Chemical Separation Membranes. *Science* **332**, 674-676 (2011). https://doi.org/10.1126/science.1203771

8 Dutta, S. *et al.* Metal–Organic Frameworks for Water Desalination. *Adv. Funct. Mater.* **n/a**, 2304790 (2023). https://doi.org/10.1002/adfm.202304790

9 Werber, J. R., Osuji, C. O. & Elimelech, M. Materials for next-generation desalination and water purification membranes. *Nat. Rev. Mater.* **1**, 16018 (2016). https://doi.org/10.1038/natrevmats.2016.18

10 Venna, S. R., Jasinski, J. B. & Carreon, M. A. Structural Evolution of Zeolitic Imidazolate Framework-8. *J. Am. Chem. Soc.* **132**, 18030-18033 (2010). https://doi.org/10.1021/ja109268m

11 Park, K. S. *et al.* Exceptional chemical and thermal stability of zeolitic imidazolate frameworks. *Proc. Natl. Acad. Sci.* **103**, 10186-10191 (2006). https://doi.org/10.1073/pnas.0602439103

12 Pan, Y., Liu, Y., Zeng, G., Zhao, L. & Lai, Z. Rapid synthesis of zeolitic imidazolate framework-8 (ZIF-8) nanocrystals in an aqueous system. *ChemComm* **47**, 2071-2073 (2011). http://dx.doi.org/10.1039/C0CC05002D

13 Hu, L., Xiao, R., Du, D., Zhu, C. & Lin, Y. Metal-organic framework-based electrocatalysts for acidic oxygen evolution reaction. *Trends Chem.* **5**, 324-335 (2023). https://doi.org/10.1016/j.trechm.2023.02.001

14 Qiu, L., Zheng, G., He, Y., Lei, L. & Zhang, X. Ultra-small Sn-RuO_2 nanoparticles supported on N-doped carbon polyhedra for highly active and durable oxygen evolution reaction in acidic media. *J. Chem. Eng.* **409**, 128155 (2021). https://doi.org/10.1016/j.cej.2020.128155

15 Song, Y., He, M., Zhao, J. & Jin, W. Structural manipulation of ZIF-8-based membranes for high-efficiency molecular separation. *Sep. Purif. Technol.*

270, 118722 (2021). https://www.sciencedirect.com/science/article/pii/S1383586621004342

16 Cravillon, J. *et al.* Rapid Room-Temperature Synthesis and Characterization of Nanocrystals of a Prototypical Zeolitic Imidazolate Framework. *Chem. Mater.* **21**, 1410-1412 (2009). https://doi.org/10.1021/cm900166h

17 Zhang, C. *et al.* Unexpected Molecular Sieving Properties of Zeolitic Imidazolate Framework-8. *J. Phys. Chem. Lett.* **3**, 2130-2134 (2012). https://doi.org/10.1021/jz300855a

18 Zhou, S. *et al.* Paralyzed membrane: Current-driven synthesis of a metal-organic framework with sharpened propene/propane separation. *Sci. Adv.* **4**, eaau1393 https://doi.org/10.1126/sciadv.aau1393

19 Qiao, J. *et al.* ZIF-8 derived carbon with confined sub-nanometer pores for electrochemically selective separation of chloride ions. *Sep. Purif. Technol.* **295**, 121222 (2022). https://doi.org/10.1016/j.seppur.2022.121222

20 Hu, Z., Chen, Y. & Jiang, J. Zeolitic imidazolate framework-8 as a reverse osmosis membrane for water desalination: Insight from molecular simulation. *J. Chem. Phys.* **134**, 134705 (2011). https://doi.org/10.1063/1.3573902

21 Luo, Q. *et al.* A small molecule with a big scissoring effect: sodium dodecyl sulfate working on two-dimensional metal–organic frameworks. *CrystEngComm* **23**, 1360-1365 (2021). http://dx.doi.org/10.1039/D0CE01751E

22 Ashworth, D. J. & Foster, J. A. Metal–organic framework nanosheets (MONs): a new dimension in materials chemistry. *J. Mater. Chem. A.* **6**, 16292-16307 (2018). http://dx.doi.org/10.1039/C8TA03159B

23 Wang, J., Li, N., Xu, Y. & Pang, H. Two-Dimensional MOF and COF Nanosheets: Synthesis and Applications in Electrochemistry. *Chem. Eur. J.* **26**, 6402-6422 (2020). https://doi.org/10.1002/chem.202000294

24 Liu, Y., Ban, Y. & Yang, W. Microstructural Engineering and Architectural Design of Metal–Organic Framework Membranes. *Adv. Mater.* **29**, 1606949 (2017). https://doi.org/10.1002/adma.201606949

25 Wang, S. *et al.* Oriented Zeolitic Imidazolate Framework (ZIF) Nanocrystal Films for Molecular Separation Membranes. *ACS Appl. Nano Mater.* **3**, 3839-3846 (2020). https://doi.org/10.1021/acsanm.0c00570

26 Sasaki, K. *et al.* Thin ZIF-8 nanosheets synthesized in hydrophilic TRAPs. *Dalton Trans.* **50**, 10394-10399 (2021). http://dx.doi.org/10.1039/D1DT01507A

27 Wei, X., Xu, D., Ge, K., Qi, S. & Chen, Y. Two-Dimensional Ultrathin Multilayers ZIF-8 Nanosheets with Sustained Antibacterial Efficacy for Aeromonas Hydrophila. *J. Inorg. Organomet. Polym. Mater.* **30**, 3862-3868 (2020). https://doi.org/10.1007/s10904-020-01517-6

28 Chen, Y., Zhu, Z., Jiang, X. & Jiang, L. Construction of Free-Standing MOF Sheets through Electrochemical Printing on Superhydrophobic Substrates. *ACS Mater. Lett.* **4**, 609-617 (2022). https://doi.org/10.1021/acsmaterialslett.1c00815

29 Jiang, Y. *et al.* Monoclinic ZIF-8 Nanosheet-Derived 2D Carbon Nanosheets as Sulfur Immobilizer for High-Performance Lithium Sulfur Batteries. *ACS*

Appl. Mater. Interfaces **9**, 25239-25249 (2017). https://doi.org/10.1021/acsami.7b04432

30 Wang, X.-p., Hou, J., Chen, F.-s. & Meng, X.-m. In-situ growth of metal-organic framework film on a polydopamine-modified flexible substrate for antibacterial and forward osmosis membranes. *Sep. Purif. Technol.* **236**, 116239 (2020). https://www.sciencedirect.com/science/article/pii/S1383586619322610

31 Zheng, Z., Grünker, R. & Feng, X. Synthetic Two-Dimensional Materials: A New Paradigm of Membranes for Ultimate Separation. *Adv. Mater.* **28**, 6529-6545 (2016). https://doi.org/10.1002/adma.201506237

32 Kim, W. & Nair, S. Membranes from nanoporous 1D and 2D materials: A review of opportunities, developments, and challenges. *Chemical Engineering Science* **104**, 908-924 (2013). https://doi.org/10.1016/j.ces.2013.09.047

33 Peng, Y. *et al.* Metal-organic framework nanosheets as building blocks for molecular sieving membranes. *Science* **346**, 1356-1359 (2014). https://doi.org/10.1126/science.1254227

34 Jian, M. *et al.* Ultrathin water-stable metal-organic framework membranes for ion separation. *Sci. Adv.* **6**, eaay3998 (2020). https://doi.org/10.1126/sciadv.aay3998

35 Park, S. S. *et al.* Cation-Dependent Intrinsic Electrical Conductivity in Isostructural Tetrathiafulvalene-Based Microporous Metal–Organic Frameworks. *J. Am. Chem. Soc.* **137**, 1774-1777 (2015). https://doi.org/10.1021/ja512437u

36 Thiam, A., Lopez-Ruiz, J. A., Barpaga, D. & Garcia-Segura, S. The Surge of Metal–Organic-Framework (MOFs)-Based Electrodes as Key Elements in Electrochemically Driven Processes for the Environment. *Molecules* **26** (2021). <https://doi.org/10.3390/molecules26185713>.

37 Butler, K. T. *et al.* Electronic structure design for nanoporous, electrically conductive zeolitic imidazolate frameworks. *J. Mater. Chem. C* **5**, 7726-7731 (2017). http://dx.doi.org/10.1039/C7TC03150E

38 Sun, L., Campbell, M. G. & Dincă, M. Electrically Conductive Porous Metal–Organic Frameworks. *Angew. Chem. Int. Ed.* **55**, 3566-3579 (2016). https://doi.org/10.1002/anie.201506219

39 Park, J. *et al.* Synthetic Routes for a 2D Semiconductive Copper Hexahydroxybenzene Metal–Organic Framework. *J. Am. Chem. Soc.* **140**, 14533-14537 (2018). https://doi.org/10.1021/jacs.8b06666

40 Xu, K. *et al.* Metallic Nickel Nitride Nanosheets Realizing Enhanced Electrochemical Water Oxidation. *J. Am. Chem. Soc.* **137**, 4119-4125 (2015). https://doi.org/10.1021/ja5119495

41 Liu, Y., Xiao, C., Huang, P., Cheng, M. & Xie, Y. Regulating the Charge and Spin Ordering of Two-Dimensional Ultrathin Solids for Electrocatalytic Water Splitting. *Chem* **4**, 1263-1283 (2018). https://doi.org/10.1016/j.chempr.2018.02.006

42 Duan, J., Chen, S. & Zhao, C. Ultrathin metal-organic framework array for efficient electrocatalytic water splitting. *Nat. Commun.* **8**, 15341 (2017). https://doi.org/10.1038/ncomms15341

43 Zhu, Y. *et al.* Synthesis and seawater desalination of molecular sieving zeolitic imidazolate framework membranes. *Desalination* **385**, 75-82 (2016). https://doi.org/10.1016/j.desal.2016.02.005

44 Delgado, A. V., González-Caballero, F., Hunter, R. J., Koopal, L. K. & Lyklema, J. Measurement and interpretation of electrokinetic phenomena. *J. Colloid Interface Sci.* **309**, 194-224 (2007). https://doi.org/10.1016/j.jcis.2006.12.075

45 Bard, A. J. F., Larry R., White, Henry S. *Electrochemical Methods: Fundamentals and Applications*. 3rd edn. John Wiley & Sons.(2022).

46 Bruckenstein, S. & Miller, B. Unraveling reactions with rotating electrodes. *Acc. Chem. Res.* **10**, 54-61 (1977). https://doi.org/10.1021/ar50110a004

47 Albery, W. J. Ring-disc electrodes. Part 1.—A new approach to the theory. *Trans. Faraday Soc.* **62**, 1915-1919 (1966). http://dx.doi.org/10.1039/TF9666201915

48 Albery, W. J. & Bruckenstein, S. Ring-disc electrodes. Part 2.—Theoretical and experimental collection effciencies. *Trans. Faraday Soc.* **62**, 1920-1931 (1966). http://dx.doi.org/10.1039/TF9666201920

49 Vos, J. G. & Koper, M. T. M. Measurement of competition between oxygen evolution and chlorine evolution using rotating ring-disk electrode voltammetry. *J. Electroanal. Chem.* **819**, 260-268 (2018). https://doi.org/10.1016/j.jelechem.2017.10.058

50 Alkan, M., Oktay, M., Kocakerim, M. M. & Çopur, M. Solubility of chlorine in aqueous hydrochloric acid solutions. *J. Hazard. Mater.* **119**, 13-18 (2005). https://doi.org/10.1016/j.jhazmat.2004.11.001

51 Vos, J. G., Venugopal, A., Smith, W. A. & Koper, M. T. M. Competition and selectivity during parallel evolution of bromine, chlorine and oxygen on IrOx electrodes. *J. Catal.* **389**, 99-110 (2020). https://doi.org/10.1016/j.jcat.2020.05.024

52 Kuznetsova, E., Petrykin, V., Sunde, S. & Krtil, P. Selectivity of Nanocrystalline IrO2-Based Catalysts in Parallel Chlorine and Oxygen Evolution. *Electrocatalysis* **6**, 198-210 (2015). https://doi.org/10.1007/s12678-014-0233-y

53 Wang, L. *et al.* Construction of Interpenetrating Transport Channels and Compatible Interfaces via a Zeolitic Imidazolate Framework “Bridge” for Nanofibrous Hybrid PEMs with Enhanced Proton Conduction and Methanol Resistance. *ACS Sustain. Chem. Eng.* **8**, 12976-12989 (2020). https://doi.org/10.1021/acssuschemeng.0c03833

54 Zahmakiran, M. Iridium nanoparticles stabilized by metal organic frameworks (IrNPs@ZIF-8): synthesis, structural properties and catalytic performance. *Dalton Trans.* **41**, 12690-12696 (2012). http://dx.doi.org/10.1039/C2DT31779F

Chapter 4

Interpretations and Perspectives

"Quand ce peuple pourra penser et rêver on lui donnera l'art qui fait penser et rêver."

-Gustave Moreau

IV.1 Interpretation

Tapping the naturally ubiquitous seawater reserves for water electrolysis requires the selective oxidation of water at the anode that prevents the evolution of the toxic chlorine gas and its disproportionation products from corroding the electrolyser and decreasing the faradaic efficiencies of the desired oxygen and hydrogen gases. The visionary aspiration of utilizing a molecular sieve membrane that goes beyond the selectivity permeability upper bound hampering the selectivity of state-of-the-art polymeric membranes utilized in desalination technology requires the design and development of novel materials including mixed matrix hybrids and pure molecular sieve membranes. The tunable apertures and pores of molecular sieve materials impart an additional entropic diffusional selectivity for solutes with the requisite dimensions that goes beyond the pure enthalpic diffusional selectivity of flexible polymers with characteristic transient segmental motion among the constituent polymer chains. A rigid, amorphous silica layer was synthesized around catalytic iridium nanoparticles interdispersed on carbonaceous support. The sol gel synthesis provided complete coverage of the electrocatalytic material after five hours of reaction with a 34 nm thickness determined by TGA and TEM analysis. The synthesis further produced pores around the silica clusters of 87 Å, well above the hydrated diameter of the chloride ion. These encapsulated nanoparticles were dispersed with Vulcan carbon in a 1:1 volumetric ratio of a Nafion solution and water to create an ink that was subsequently drop-casted on a working glassy carbon electrode. Electrochemical analysis with a rotating disk electrode subjected to linear sweep voltammetry showed evidence of a lack of electron transport from the silica encapsulated catalytic nanoparticles within the film towards the working electrode and a direct diffusion of the chloride ion towards the electrode and undergoing oxidation.

It became thus apparent that arresting the species transport of the chloride ion within the unique design of an electrocatalytic film requires a material that can both arrest the transport towards the electrocatalytic nanoparticle and the native glassy carbon electrode. To achieve the requisite selectivity for the sensitive analytical technique of rotating disk voltammetry, an improvement beyond the enthalpic selectivity achievable with polymeric materials is thus exigent, requiring a synthetic technique that can create precisely defined apertures and pore sizes. Reticular synthesis and the intimate control of MOF material design is another means of producing a molecular sieve membrane with the requisite aperture size that can impart an additional entropic diffusional selectivity to arrest the species transport of the chloride ion. Utilization of the ZIF-8 is shown to have an order of magnitude greater diffusional selectivity than state-of-the-art polymer membranes, and moreover possesses the requisite aperture size to selectively permit the passage of water molecules while restraining the movement of the hydrated chloride ion. Synthesis of the ZIF-8 in the form of a nanosheet forms a monoclinic phase that stiffens the rotatable motion of the azolate ligand, improving the potential separation performance. The increased aspect ratio furthers the modes of separation and provided a means of incorporating a material that could potentially arrest the species transport of the chloride ion both towards the catalyst and towards the native glassy carbon electrode, and moreover can improve the conductivity of the material through a dimensional

confinement effect. Thus architectures were designed to optimize the placement of the nanosheets to selectively arrest both transport pathways. The integrated approach showed an initially promising result, though attempts to replicate that increase in overpotential observed in the LSV curve of a 0.5 M acidified NaCl solution that indeed aligned with that of the purely acidic solution in the linear sweep voltammograms proved to be irreproducible through trials standardized through modification to the electroanalytical trial sequence. However, measurements of the decrease in the CER selectivity through the use of rotating risk disk voltammetry in sufficiently acidified perchloric acid aqueous solutions of ascending sodium chloride concentrations indicated a near ~65% drop in CER selectivity upon increasing the Zn/Ir molar ratio within the MOF incorporated films from 0/1 to 160/1 at 10 mM NaCl. This percent drop in CER selectivity through incorporation of the nanosheets is rather consistent up to 150 mM, with a concurrent decrease in the applied potential required to reach a current density of 3 mA/cm^2 at the disk within increasingly concentrated, acidified NaCl solutions. Calculation of the respective OER and CER currents contributing to that disk current indicate that the nanosheets minimally affect the evolved OER current, instead it is this decrease in the applied potential that could confound the oxygen evolution by providing an insufficient driving force to catalyze the reaction. On the other hand, the CER currents do appear to be confounded by the presence of the nanosheets, indicated by the linear decrease in CER selectivity with increasing nanosheet quantity within the electrocatalytic film up to NaCl concentrations of ~150 mM.

Elucidating the kinetic and diffusional control to which OER and CER currents may be subjected to in the presence of ZIF-8 nanosheets integrated into the electrocatalytic film would clarify this evidenced decrease in CER selectivity and instigate a mechanism by which this decreased CER selectivity may be perpetuated at higher NaCl concentrations. Separating diffusional and kinetic control may be conducted through a Koutecky-Levich analysis and electrokinetic modeling, which would enable both the verification of the hypotheses that the OER is under kinetic inhibition in the presence of the chloride ion and that the CER is indeed under diffusion control upon nanosheet integration within the electrocatalytic film. Both the Ir10 and the ZIF integrated electrocatalytic films were probed at different rotation rates under the presence of ascending NaCl concentrations, an example Ir10 film is shown in *Figure 1* below.

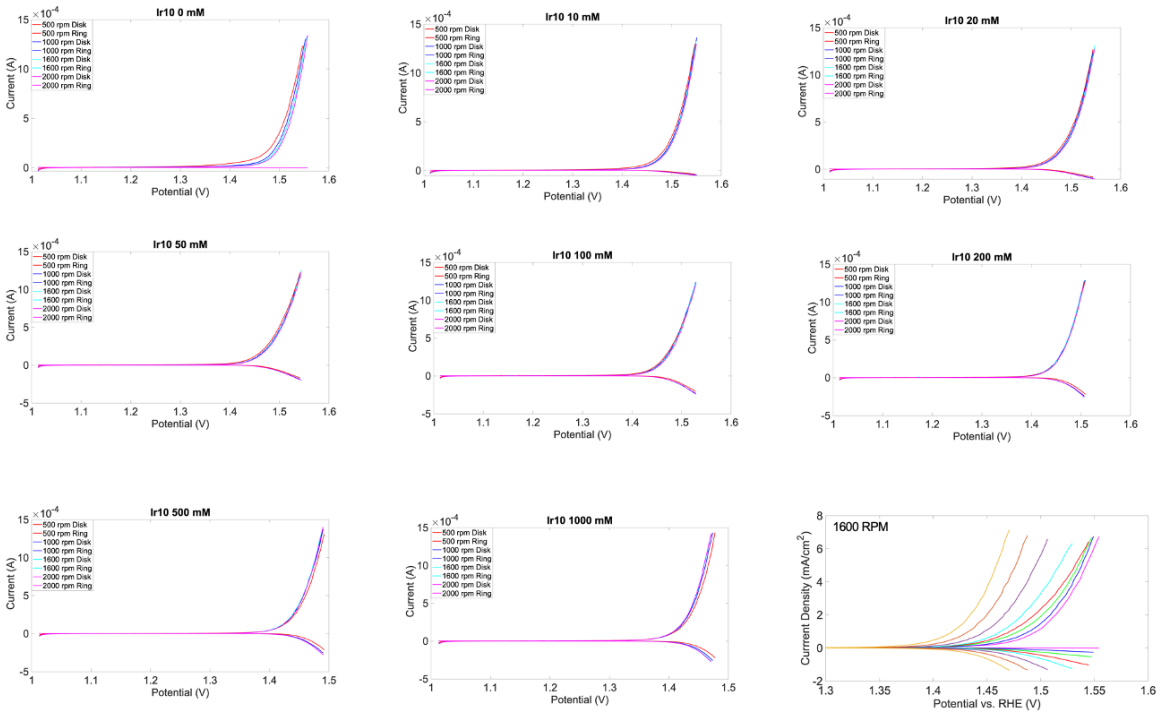

Figure 1: Linear sweep voltammetry curves of the disk and ring currents of the Ir10 electrocatalytic film under ascending NaCl concentrations at different rotation rates.

However, Bélanger et. al. began to observe negative deviations from Levich behavior beginning at 100 rpm with a metallopolymeric film of a mere 25 nm thickness that had been electrodeposited on a glassy carbon working electrode[1]. Considering that these Ir10 electrocatalytic films have a thickness of ~3 μm and higher rotation rates of 500 rpm, 1000 rpm, 1600 rpm, and 2000 rpm were probed, deviations are expected and are evident in the LSV curves of *Figure 1*. Indeed, these deviations at higher rotation rates may be caused by the excess thinning of the diffusion layer, which relegates the evolved CER current to the rate at which the chloride ion can diffuse through these electrocatalytic films. Moreover, the nafion binder and additional constituents within electrocatalytic films may subject it to unequal activities throughout the film, complicating the corrections for hindered mass transport and increased resistivity needed to extract kinetic parameters[2]. Furthermore, it is apparent in the LSV curves of *Figure 1* that the limiting current region is not reached at the reactant concentrations, though a microkinetic modeling approach may be applicable to determine the apparent catalytic rate constants for the OER and CER, enabling the extent to which these currents are under kinetic or diffusional control to be deduced[3].

Verification of the diffusional control that the ZIF nanosheets impose upon the CER current would further prompt the elucidation of the major mode of chloride ion mass transport within the film to further guide the chemical design of nanosheets and their integration with improved stability, minimized defects, and incorporated interactions that augment their localization within the electrocatalytic film.

IV.2 Perspectives

IV.2.1 Elucidating the Transport Phenomena within the Film

Designing electrocatalysts that can be interwoven within a film of conductive carbon and proton facilitating Nafion and then drop-casted onto a working electrode can improve the electrical conductivity of the working electrode surface and decrease the noble metal loading, thus unraveling the transport phenomenon within the film is crucial to realizing its practicality. Improving the OER selectivity calculated through rotating ring disk electrode voltammetry requires elucidating the evolved source of undesired current measured at the ring. Drop casting an electrocatalytic film onto the working electrode creates transport phenomena that go beyond the diffusion of the substrate towards and from the electrode surface within the solution and include the diffusive-like movement of charge throughout the film to and from the electrocatalytic nanoparticles and towards and from the electrode surface; the diffusion of the substrate towards and from the nanoparticle termed nanodiffusion; and the diffusion of the substrate within the film as depicted in below in *Figure 2*[4-7].

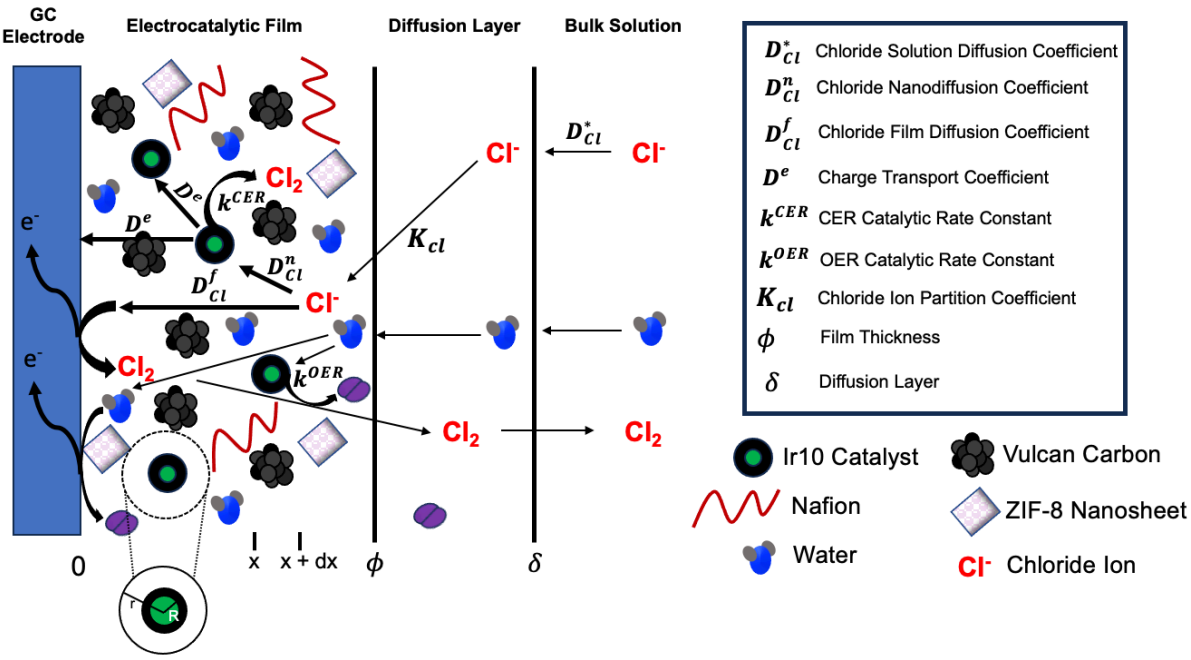

Figure 2: Schematic depiction of the major modes of transport of the chloride ion, the catalytic reactions, and the charge transport processes within an electrocatalytic film.

Moreover, Nafion, the perfluorosulfonic acid proton facilitator in the film, was also shown to effectively arrest the transport of the chloride ion towards a titanium working electrode that had been coated with IrO_2 (IrO_2/Ti) through thermal decomposition[8]. Indeed, Balaji et. al. measured the OER efficiency through conventional iodometric titration of a Nafion membrane (NM) hot pressed completely across the modified electrode (NM/IrO_2/Ti), which achieved 100% OER efficiency[8]. Applying the Nafion 117 solution "NS" (5% w/v in 2-propanol) to the IrO_2 coated Ti electrode and drying in air (NS/IrO_2/Ti) achieved only 80% efficiency, as shown *Figure*

3, which was attributed to the cracks that formed during the casting that enabled the chloride ion to permeate. Moreover, the CER selectivity (and OER selectivity) results in Chapter 3 indicated CER selectivities of almost 80% in mere 100 mM NaCl with the Ir10 electrocatalyst interwoven within the Nafion 117 solution in the drop-casted film, revealing that the chloride ion may indeed be diffusing towards the Ir10 electrocatalyst within the film.

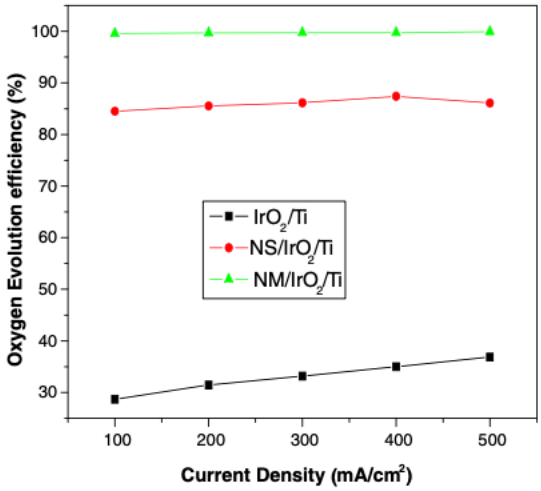

Figure 3: The dependence of the OER efficiency on the current density evaluated by subtracting the CER efficiency measured through iodometric titration by 100%. The analytical solution consisted of 0.5 M NaCl at pH 8.3. Figure of Balaji et. al.[8]

A parameter that may be convoluting a comparison of the analysis conducted with the silica and with the ZIF-8 nanosheets is the different orientations of the permselective membrane with respect to the electrocatalyst and with respect to the film; in one scenario, the nanoparticles are being encapsulated, and in another, the ZIF-8 nanosheets are being dispersed within or surrounding the film. An understanding the competing modes of chloride ion diffusion within the catalytic film would thus give insight into the proper design and orientation of a material to integrate to selectively impede the major diffusive mode of chloride ion permeation towards the electrocatalytic nanoparticles and also towards the native working electrode. The solutes are in an aqueous solution acidified with sufficient supporting electrolyte to exclude the effects of electromigration on the solute movement within the film. A means of evaluating the major competitive modes of diffusion, of evolving from a black and white scenario to defining shades of grey, can be done through the use of cyclic voltammetry and rotating ring disk voltammetry. Utilization of a potential sweep that generates a transient response such as cyclic voltammetry in addition to hydrodynamic methods that modulate the rotation rate of the working electrode can enable the chloride ion solute transport and the timescales of the transport phenomena occurring within the film to be dissected.

IV.2.1.1 Cyclic Voltammetry

To enable a calculation of these kinetic parameters, a steady state approximation in which the concentration of the chloride ion substrate within the film

(C_{Cl}^{f}) is considered constant with respect to time must be applicable, and requires that the size of the nanoparticles within the film to have a very narrow distribution, with a density (ρ), and that their radii (R) are small and of the same order of magnitude as the chloride ion diffusion layer around the nanoparticle (r), which is small in comparison to the mean distance between the nanoparticles and the film thickness (ϕ)[4]. Then, the concentrations of the chloride ion and the product chlorine gas are independent of (R) and depend only on the thickness of the film. Thus, the spherical mode of diffusion towards and from the nanoparticle and the linear modes of diffusion within the film may be coupled through equitation to the change in concentration of the chloride ion reactant and chlorine gas product with respect to time, which is equivalent to zero,

$$0 \approx \frac{\partial C_{Cl}^{f}}{\partial t} = D_{Cl}^{f} \frac{\partial^2 C_{Cl}^{f}}{\partial x^2} - 4\pi R D_{Cl}^{f} \rho [C_{Cl}^{f} - \left(C_{Cl}^{f}\right)_{r=R} \quad (1)$$

This approximation must be applicable, in addition to the approximations assuming: a) a fast-conducting film in which the charge transport proceeds through ohmic conduction or through rapid electron hopping, enabling D^{e} of Figure 2 to not be rate limiting; and b) a fast, reversible catalytic reaction (large k^{OER} and k^{CER}) occurring at the nanoparticle electrocatalyst to enable pure transport conditions to be achieved in which the current is limited only by the diffusion rate of the substrate towards the nanoparticles. With these approximations, an understanding the competition between nanodiffusion towards the catalytic nanoparticles (D_{Cl}^{n}) and chloride ion diffusion within the solution (D_{Cl}^{*}) could be elucidated, specifically by deriving a competition parameter that indicates the degree to which the diffusion of the solute is controlled by the linear diffusion within the solution or by nanodiffusion towards the nanoparticle (*Figure 4)*. Large values of the competition parameter are indicative of control by solution linear diffusion, characteristic of small scan rates, large nanoparticle densities, large nanoparticle size, fast diffusion in a thick film, and slow solution diffusion, and show a typical reversible wave. Thus by varying the scan rate and/or the nanoparticle density within the film, the system may be evolved from the reversible regime to an S-shaped wave regime indicative of nanodiffusion as depicted *Figure 4* to identify whether the system is under control by the linear diffusion of the solute within the solution or by nanodiffusion of the solute towards the electrocatalyst within the film.

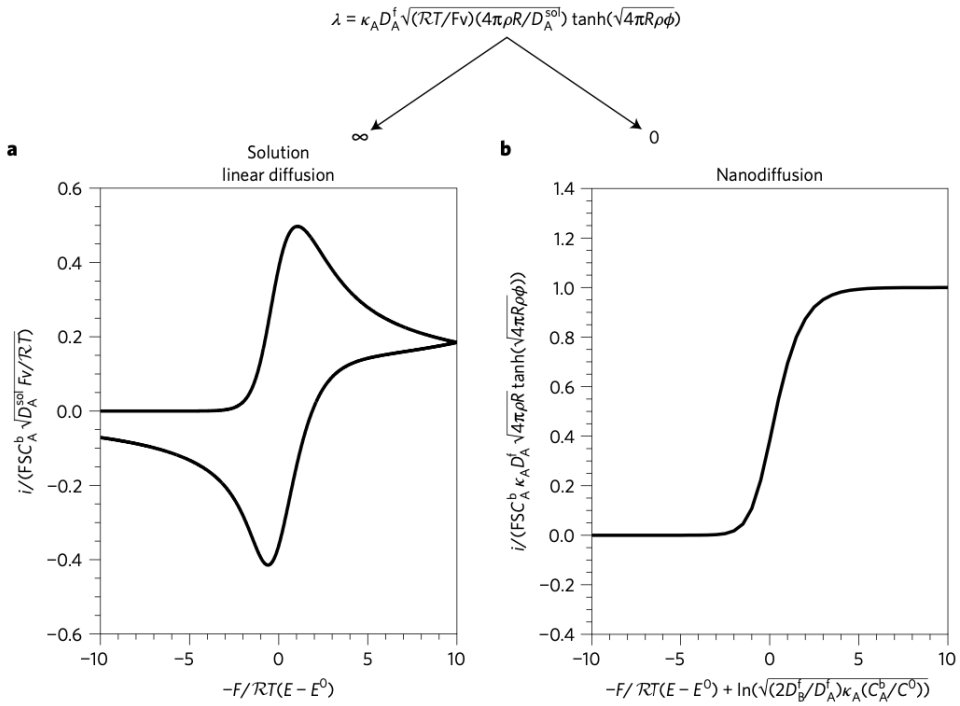

Figure 4: Cyclic voltammetry responses with respect to the derived dimensionless competition parameter. (A) is the reversible wave characteristic of control by solution linear diffusion and (B) is the CV response to control via nanodiffusion within the film. Figure of Costentin et.al.[4]

However, an assessment of chloride ion diffusion within the film (D_{Cl}^{f}) may be further required to elucidate the evidence for direct transport of the chloride ion towards the electrode surface. Its relative degree of control would indicate both the needed orientation of the nanosheets within the film and their degree of chloride ion permeability; large permeabilities would suggest that crystalline defects, such as grain boundaries, dislocations, and voids, are present within the ZIF-8 nanosheet. Measuring D_{Cl}^{f} could in theory also be conducted with cyclic voltammetry. The theory assumes that the catalyst (Q) is a molecule occupying a point in space with the measured concentration (C_P^0) defining the sum of the concentrations of the reduced (P) and oxidized forms (Q) of the electrocatalyst molecules. Assuming that the catalytic reaction is fast, the evolution of the concentration profile of the chloride ion substrate with time can be equated to zero under these steady state conditions, enabling the coupling of the chloride ion linear diffusion within the film and the rate of the second order catalytic reaction,

$$0 \approx \frac{\partial C_{Cl}^{f}}{\partial t} = D_{Cl}^{f} \frac{\partial^2 C_{Cl}^{f}}{\partial x^2} - k C_{Cl}^{f} C_Q \qquad (2)$$

Through variations of the potential scan rate (v), the film thickness (shown as d_f in *Figure 5*), and/or the concentration of the catalyst molecules (C_P^0), the kinetic regime of the system could first be diagnosed according to Costentin et. al[5]. Then the

potential scan rate needed to reach the CV response indicative of the total catalysis zone (R^{tot}) may be determined by lowering the scan rate at a constant film thickness until the peak current remains invariable with respect to the scan rate, as indicated in *Figure 5A*.

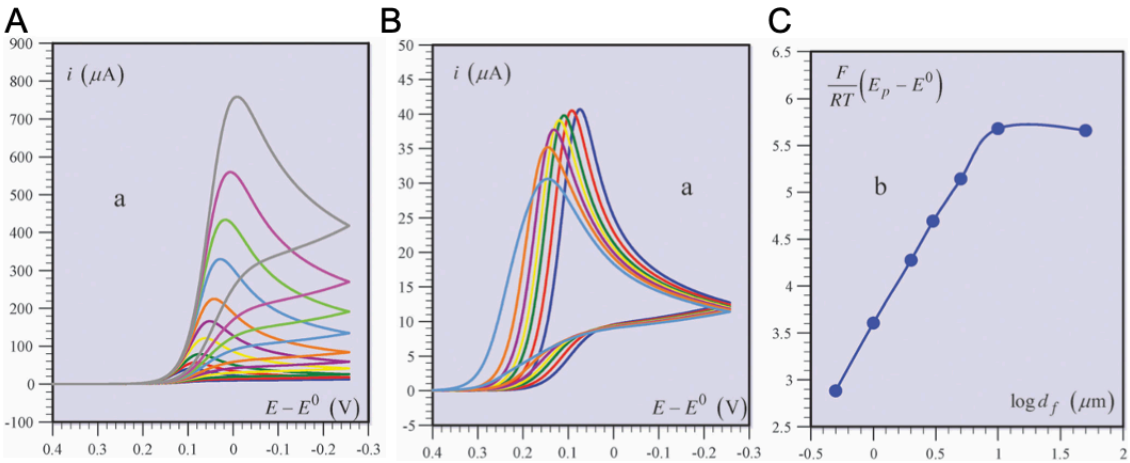

Figure 5: (A) Evolution of the scan rate from 30 V/sec in grey to 0.05 V/sec in blue at a film thickness of 1 μm to reach the total catalysis zone. (B) Evolution of the film thickness from 0.5 μm in light blue to 50 μm in blue at a scan rate of 0.05 V/sec. (C) The peak potentials obtained in (B) as a function of the film thickness. Figure adapted from Costentin et. al.[5]

Upon reaching that invariability, the peak current would give the chloride ion solution diffusion coefficient (D^*_{Cl}),

$$I_p = 0.496\, x\, FC^*_{Cl}\sqrt{D^*_{Cl}Fv/RT} \tag{3}$$

And the peak potential would indicate the product of the partition coefficient (K_{Cl}) and the rate constant of the catalytic reaction (k_{CER}),

$$E_p = E^0 - 0.78\frac{RT}{F} + \frac{RT}{F}\ln\left(\frac{\delta\kappa_{Cl}k_{CER}C^0_p}{\sqrt{D^*_{Cl}Fv/RT}}\right) \tag{4}$$

Then the thickness of the film could be adjusted at this low scan rate to reach the SR^{tot} zone, in which an invariable peak potential would give the product of the diffusion coefficient of the substrate within the film (D^f_{Cl}) and the partition coefficient (K_{Cl}),

$$E_p = E^0 - 0.86\frac{RT}{F} + \frac{RT}{F}\ln\left(\frac{K_{Cl}k_{CER}C^0_pK_{Cl}D^f_{Cl}}{\sqrt{D^*_{Cl}Fv/RT}}\right) \tag{5}$$

However, reaching the conditions in which the total catalysis wave in the R^{tot} and RS^{tot} regimes becomes invariable may be quite difficult to achieve in practice, the volume required to reach a small film thickness may be too low to completely cover

the electrode, and current values exceeding the ohmic drop limitations within the film may be reached if higher scan rates are required. Moreover, with the catalysts of the defined system of the present study being voluminous nanoparticles, the difference between the nanoparticle radii, the distance between the nanoparticles, and the required film thickness may not be great enough to assume that the concentration of the chloride ion substrate within the film is independent with time. Furthermore, the above analysis considers one electron/one step reduction. The multistep oxidation characteristic of the OER with a number of intermediates can form adducts that may become significant under this cyclic voltammetry analysis. The formation of oxide layers and leaching of the catalyst during oxidation processes may further increase the complications of acquiring reproducible results. Thus, determining a reproducible D_{Cl}^{f} value for the ZIF-8 nanosheet integrated film with cyclic voltammetry may be difficult to achieve in practice.

Though reasoned to be quite convoluted, a cyclic voltammetry analysis has been derived for the determination of D^{e} and thus could give an indication in theory of the conductivity of the film. If the catalytic reaction is fast enough or the concentration of the substrate great enough, as when the substrate is the solvent, as in the OER, the plateau current may be too large to be realistically accessible and the foot of the catalytic wave may be conducted at low scan rates and thus under pure kinetic conditions[7]. Drop-casting the films of different thicknesses could enable a determination of the optimal film thickness (ϕ^{opt}) as shown in *Figure 6* below.

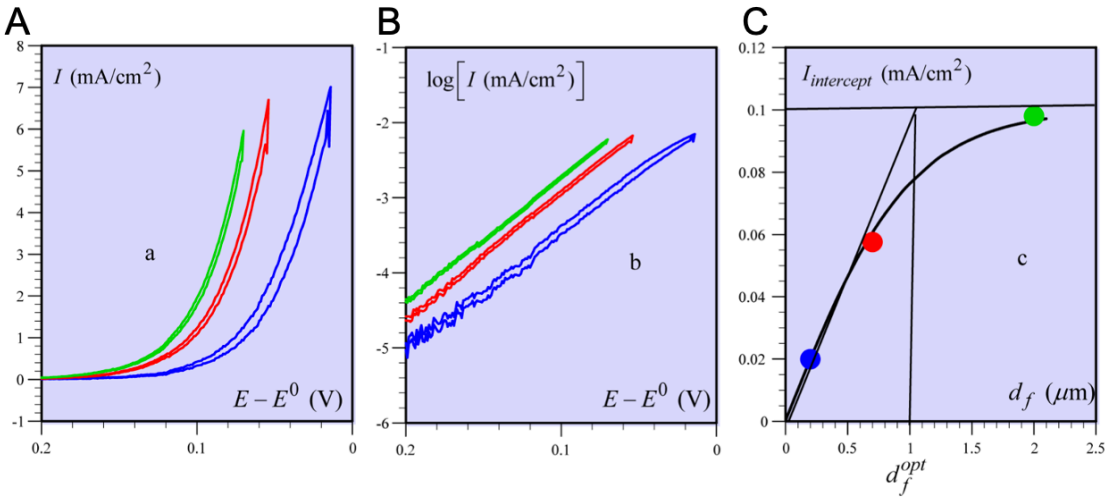

Figure 6: (A) Cyclic voltammetry simulation of the electrocatalysis of a solute also considered as the solvent within an electrocatalytic film of 0.2 (blue), 0.7 (red), and 2 (green) μm thicknesses. (B) the corresponding Tafel plots and (C) the current densities at $E = E_0$ with respect to the film thickness (d_f), where the optimal thickness is indicated at the initiation of the plateau. Figure of Costentin et. al.[7]

The optimal film thickness can then be related to D_e by,

$$\phi^{opt} = \sqrt{D_e / k_{OER} K_{H_2O} C^{*}_{H_2O}} \qquad (6)$$

IV.2.1.2 Rotating Ring Disk Voltammetry

A steady state concentration of the chloride ion may also be induced through a hydrodynamic method that invokes forced convection of the solution surrounding the electrode, most commonly by spinning the electrode, enabling the evaluation of D_{Cl}^{f}. The steady state concentration profile of the chloride ion arriving at a rotating disk electrode modified with a film across the disk is shown below in Figure 7[9,10].

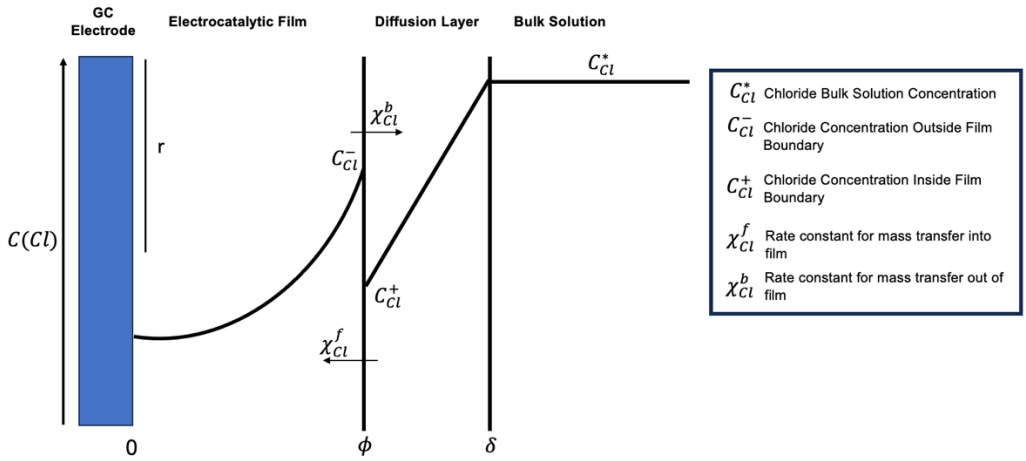

Figure 7: Steady-state concentration profiles of the chloride ion at a rotating disk electrode modified with a film.

The partition coefficient (K) relates the concentration of the solute inside and just outside the interface of the film,

$$K_{Cl} = \frac{C_{Cl}^{-}}{C_{Cl}^{+}} \tag{7}$$

Furthermore, the current measured at the disk may evolve from the OER or the CER within this electrocatalytic design.

$$i_d = i_{CER} + i_{OER} \tag{8}$$

If a ring surrounding the disk electrode is placed at a negative potential, the chlorine molecule produced from the oxidation of the chloride ion at the disk (the CER) can be reduced back to the chloride ion, evolving a current. This current can be related to the disk current as shown previously,

$$|Ni_d| = i_R = i_{CER} \tag{9}$$

Where (N) is the collection efficiency and may be determined experimentally by measuring $(-i_R/i_D)$ for a system in which a species arriving at the ring is stable. The transport phenomena of the chloride ion within the film may thus be discerned by relating the current densities measured at the disk with those measured at the ring

according to *Equation 9*. These sources of current densities measured at the disk originating from CER can thus be defined,

$$i_R^A = |Ni_D^A| = 4.98NFC_{Cl}^*(D_{Cl}^*)^{2/3}\nu^{-1/6}\omega^{1/2} \quad (10a)$$

$$i_R^f = \left|Ni_D^f\right| = NFC_{Cl}^* K_{Cl} D_{Cl}^f/\phi \quad (10b)$$

$$i_R^P = |Ni_D^P| = NFC_{Cl}^* \chi_{Cl}^f \quad (10c)$$

$$i_R^K = |Ni_D^K| = NFA\phi k^{CER} K_{Cl} C_{Cl}^* \rho \quad (10d)$$

$$i_R^e = |Ni_D^e| = NFD^e \rho/\phi \quad (10e)$$

where $A = \pi r^2$ and ν is the kinematic viscosity of the solution[10]. In the case where the electrocatalyst is removed within a fast-conducting film, where i_D^K and i_D^e are no longer rate limiting, the limiting current at the ring (i_R^l) becomes,

$$\frac{1}{i_R^l} = \frac{1}{i_R^A} + \frac{1}{i_R^P} + \frac{1}{i_R^f} \quad (11)$$

thus, a plot of $(1/i_R^l)$ vs. $(1/i_R^A)$ in a Koutecky-Levich plot, at a potential in which the rate of electron transfer is significantly slow and at different rotation rates, gives an intercept that may be equated to $((1/i_R^P) + (1/i_R^f))$.[10] The permeation current (i_D^P) expresses the rate of mass transfer across the film-solution interface, moreover, because (i_D^f) is the only contributing source of current density proportional to the thickness, the significance of i_D^P may be determined by plotting the Koutecky-Levich intercepts with respect to the film thickness. An intercept greater than zero would indicate control by the permeation current and an intercept of zero would indicate equilibrium at the interface. Equilibrium at the interface would further enable the diffusion coefficient of the chloride ion within the film D_{Cl}^f to be evaluated from the slope of the line. Comparison of D_{Cl}^f with and without the nanosheets would indicate if there may be defects increasing the degree of chloride ion permeation throughout the film or if an alternative orientation of the molecular sieve material with respect to the film is needed to arrest the species transport of the chloride ion towards the electrocatalytic active sites.

IV.2.2 Modifying the Electrocatalytic Architecture

Improving the practicality of the electrocatalytic architecture with a penchant for arresting the species transport of the chloride ion may be shown through the elucidation of the major competing modes of diffusion and give insight into the exigent orientation of the permselective membrane to mitigate the evolved current for the OER, whether that be through a membrane encapsulating only the catalytic nanoparticles, or a material interdispersed throughout the film, or an overlayer above the entire film. The encapsulation of the electrocatalytic nanoparticles with silica and

subsequent electrochemical analysis revealed that the chloride ions may be directly diffusing towards the glassy carbon working electrode, thus suggesting an orientation in which the permselective layer is dispersed within the film or deposited above the film.

IV.2.2.1 The Nanosheet Synthetic Technique

When interdispersing a material within the film, the nanosheet renders a unique aspect ratio that can increase the separation modes and moreover can be designed with a thickness that minimally impedes the transport of the desired water permeant. However, rendition of the predominant diffusive modes of chloride ion transport within the film may imply a needed modification to the synthesis of the nanosheet that minimizes the crystalline defects, the thickness distribution, and/or the stability of the material. Wang et. al. utilized a top-down approach that created extended carbon sheets after subjecting ZIF-8 nanocrystals to carbonization within an eutectic liquid; a uniform pore size distribution with the characteristic aperture size of the ZIF-8 prototype was maintained and the material showed considerable stability under acidic conditions[11]. Tuning the pulsed laser fluence with assistant solvent intercalation to break the Van der Waals forces between adjacent nanosheets represents another unprecedented top-down approach towards obtaining defect free nanosheets[12]. A sacrificial precursor made of $Zn_5(NO_3)_2(OH)_8$ could also be used as the templating agent to synthesize ZIF-8 nanoplates[13]. After acetone-assisted conversion of the template in the presence of 2-methylimidazole, gas adsorption experiments indicated that the ZIF-8 crystallites within the nanoplate were highly constrained in the matrix without grain-boundary voids[13]. The stability of the nanosheets under acidic conditions may also need to be improved. Ji et. al. integrated a polymer within ZIF-8 nanosheets that demonstrated remarkable stability against the chloride ion under a wide pH range, with a high water permeance[14]. Furthermore, Li et.al. used a similar synthetic method that was herein utilized with the mere addition of the ethyleneimine polymer; the uptake of the chloride ion by the polymer modified nanosheet was shown to be the lowest amongst the anions probed[15]. The chemical stability of the nanosheet may be further improved with the use of a covalent organic framework (COF) nanosheet, provided the aperture size can be tailored toward selective water permeation. Ying et. al. layered an anionic and cationic covalent organic nanosheets that eclipsed the apparent aperture size, the opposite charges further stabilized the stacked array with strong electrostatic interactions that created dense structures with thicknesses arriving at 41 nm[16]. Li et. al. further used an interfacial polymerization of triformylbenzene with an increased number of phenolic hydroxyl groups that modified the stacking mode from AA to AB, creating array sub-nanometer pores with thicknesses of ~2.5 nm that were stable under acid[17]. Thus, designing an efficient and robust electrochemical assessment of the major modes of solute diffusion within the film ca facilitate a nanosheet design strategy that accordingly mitigates those modes with an exigent long-term stability.

IV.2.2.2 The Integration Strategy

An electrochemical deposition of a MOF or COF material above the film may prove to be the most reproducible method to synthesize a selective membrane[18].

Electrochemical depositions would provide the opportunity to easily control deposition parameters such as the thickness of the overlayer. Wei et. al. utilized a low current density to electrochemical deposit a ZIF-8 layer of 50 nm after 20 min onto the cathode immersed in an aqueous solution[19]. The crystals were of the rhombic dodecahedra morphology with the most thermodynamically stable (110) phase exposed. Provided the proper aperture size can be constructed, the stability of a COF material may also be leveraged through an electrochemical deposition[20].

IV.3 Concluding Remarks

The heterogeneous, inner-sphere oxidation of water within an electrocatalytic film to evolve oxygen requires an optimal binding of the reactants, intermediates, and products at the electrocatalyst surface to facilitate the four-electron transfer mechanistic pathway and release the generated oxygen gas. The presence of the chloride ion introduces a competitive inhibitor of the OER, induces corrosion of the electrolyser, and promotes the evolution of toxic chlorine gas. Verification that the ZIF nanosheets indeed induce diffusional control of the CER current would compel the characterization of the major modes of diffusion of the chloride ion within the electrocatalytic film to galvanize the design strategy of a water permselective membrane that impedes the mass transport of the chloride ion at higher salt concentrations. Design of an electrocatalytic system that can decrease the OER overpotential below that of the CER would evade the increase in the electrode potential at the anode required to lower the energy of the electrons within the electrode and decrease the water oxidation activation barrier. This electrocatalyst with a selective penchant for OER catalysis would indeed circumvent the evolution of the toxic gas, though would minimally assuage the corrosion that the chloride ion can ensue. Thus, assaying the long-term stability of the nanosheets and modifying the synthesis strategy as required to ameliorate resistance to acidic conditions, such as through the implementation of a COF material with minimized intrinsic defects within the nanosheets would further the applicability. Consideration of the performance of the nanosheets in the presence of other constituents within seawater could then be encouraged. Derivation of parameters characterizing the modified system such as the solute diffusion coefficient within the film would provide additional means to evaluate its performance amongst multiple ionic constituents and facilitate the design of an impermeable layer that breaks that upper bound, with further implementations such as those providing drinkable water in water scarce regions. Engendering the design could indeed be far reaching, with a foreseen pertinence within the shadows of the rising sun.

IV.4 References

1 Bélanger, S., Stevenson, K. J., Mudakha, S. A. & Hupp, J. T. “Perfect” Electrochemical Molecular Sieving by Thin and Ultrathin Metallopolymeric Films. *Langmuir* **15**, 837-843 (1999). https://doi.org/10.1021/la980908r

2 Blanc, N., Rurainsky, C. & Tschulik, K. Implications of resistance and mass transport limitations on the common Tafel approach at composite catalyst thin-film electrodes. *J. Electroanal. Chem.* **872**, 114345 (2020). https://www.sciencedirect.com/science/article/pii/S1572665720305725

3 Thorarinsdottir, A. E., Erdosy, D. P., Costentin, C., Mason, J. A. & Nocera, D. G. Enhanced activity for the oxygen reduction reaction in microporous water. *Nat. Catal.* **6**, 425-434 (2023). https://doi.org/10.1038/s41929-023-00958-9

4 Costentin, C., Di Giovanni, C., Giraud, M., Savéant, J.-M. & Tard, C. Nanodiffusion in electrocatalytic films. *Nat. Mater.* **16**, 1016-1021 (2017). https://doi.org/10.1038/nmat4968

5 Costentin, C. & Savéant, J.-M. Cyclic voltammetry of fast conducting electrocatalytic films. *Phys. Chem. Chem. Phys.* **17**, 19350-19359 (2015). http://dx.doi.org/10.1039/C5CP02825F

6 Costentin, C. & Savéant, J.-M. Cyclic Voltammetry of Electrocatalytic Films: Fast Catalysis Regimes. *ChemElectroChem* **2**, 1774-1784 (2015). https://doi.org/10.1002/celc.201500217

7 Costentin, C. & Saveant, J.-M. Cyclic Voltammetry Analysis of Electrocatalytic Films. *J. Phys. Chem. C* **119**, 12174-12182 (2015). https://doi.org/10.1021/acs.jpcc.5b02376

8 Balaji, R. *et al.* An alternative approach to selective sea water oxidation for hydrogen production. *Electrochem. Commun.* **11**, 1700-1702 (2009). https://doi.org/10.1016/j.elecom.2009.06.022

9 Bard, A. J. F., Larry R., White, Henry S. *Electrochemical Methods: Fundamentals and Applications*. 3rd edn. John Wiley & Sons.(2022).

10 Leddy, J., Bard, A. J., Maloy, J. T. & Savéant, J. M. Kinetics of film-coated electrodes: Effect of a finite mass transfer rate of substrate across the film—solution interface at steady state. *J. Electroanal. Chem.* **187**, 205-227 (1985). https://doi.org/10.1016/0368-1874(85)85779-8

11 Wang, Y., Chen, X., Zhai, Q.-G., Guo, J. & Feng, P. Ultraporous nitrogen-rich carbon nanosheets derived from the synergy of eutectic liquid and zeolitic imidazolate for energy applications. *J. Power Sources* **434**, 126678 (2019). https://doi.org/10.1016/j.jpowsour.2019.05.084

12 Kumar, P. *et al.* Photoexfoliation Synthesis of 2D Materials. *ACS Mater. Lett.* **4**, 263-270 (2022). https://doi.org/10.1021/acsmaterialslett.1c00651

13 Kwon, O. *et al.* High–aspect ratio zeolitic imidazolate framework (ZIF) nanoplates for hydrocarbon separation membranes. *Sci. Adv.* **8**, eabl6841 (2022). https://doi.org/10.1126/sciadv.abl6841

14 Ji, Y.-L. *et al.* Roll-to-roll fabrication of large-area metal–organic framework-based membranes for high-performance aqueous separations. *Nature Water* **2**, 183-192 (2024). https://doi.org/10.1038/s44221-023-00184-4

15 Li, J. *et al.* Simultaneous removal of U(VI) and Re(VII) by highly efficient functionalized ZIF-8 nanosheets adsorbent. *J. Hazard. Mater.* **393**, 122398 (2020). https://doi.org/10.1016/j.jhazmat.2020.122398

16 Ying, Y. *et al.* Ultrathin Two-Dimensional Membranes Assembled by Ionic Covalent Organic Nanosheets with Reduced Apertures for Gas Separation. *J. Am. Chem. Soc.* **142**, 4472-4480 (2020). https://doi.org/10.1021/jacs.9b13825

17 Li, Y. *et al.* Laminated self-standing covalent organic framework membrane with uniformly distributed subnanopores for ionic and molecular sieving. *Nat. Commun.* **11**, 599 (2020). https://doi.org/10.1038/s41467-019-14056-7

18 Zhang, X. *et al.* Electrochemical deposition of metal–organic framework films and their applications. *J. Mater. Chem. A.* **8**, 7569-7587 (2020). http://dx.doi.org/10.1039/D0TA00406E

19 Wei, R. *et al.* Aqueously Cathodic Deposition of ZIF-8 Membranes for Superior Propylene/Propane Separation. *Adv. Funct. Mater.* **30**, 1907089 (2020). https://doi.org/10.1002/adfm.201907089

20 Zhao, X., Pachfule, P. & Thomas, A. Covalent organic frameworks (COFs) for electrochemical applications. *Chem. Soc. Rev.* **50**, 6871-6913 (2021). http://dx.doi.org/10.1039/D0CS01569E

General Conclusions

Implementation of electrocatalytic films at the anode within a seawater electrolyzer design under acidic conditions that selectively evolve oxygen requires a mechanism that inhibits the species transport of the chloride ion towards the catalytic iridium nanoclusters. This refined degree of selectively may be achieved by surpassing the upper bound evidenced in polymeric materials confined only to a selectivity that may be induced enthalpically. Molecular sieving materials further the prospect of achieving an additional entropic selectivity by imparting a rigidity that hinders transitional and vibrational modes of the transition state appearing as the permeant transports from one coordination state to the next within the membrane. Through a one pot synthesis, an amorphous silica layer was applied to an electrocatalyst of iridium nanoclusters interwoven within a Vulcan carbon support to create a core-shell structure with a homogenous silica layer thickness of 34 nm calculated through thermogravimetric analysis and transmission electron microscopy. The X-Ray diffraction pattern indicated that the silica shell was amorphous with cluster sizes approaching 87 Å and expected pore sizes surrounding the clusters greater than the hydrated diameter of the chloride ion. Difficulty in modulating the pore sizes of the amorphous materials rendered an imperceivable electrocatalytic performance of the encapsulated nanoparticles when dispersed within an electrocatalytic ink and subsequently drop-casted on a working glassy carbon rotating disk electrode and subjected to linear sweep voltammetry. A direct diffusion of the chloride ion towards the electrode and undergoing oxidation was evident as well as a lack of electron transport from the silica encapsulated catalytic nanoparticles within the film towards the working electrode.

Intimate control of the porosity of the molecular sieving ZIF-8 metal-organic framework was found to be achievable through the reticular synthesis of the ZIF-8 nanosheets. The X-Ray diffraction pattern confirmed an aperture diameter of 4.76 Å, just between that of the water molecule and the hydrated chloride ion. Application of a rotating ring disk electrode subjected to linear sweep voltammetry enabled an evaluation of the CER selectivity through measurement of the faradaic reduction of the undesired chlorine gas evolved at the disk. An electroanalytical protocol was optimized to enable the integration of the ZIF-8 nanosheets within the electrocatalytic film trialed to improve the dispersion of the nanosheets. This electrocatalytic film was drop casted on the rotating ring disk electrode and the CER selectivity was calculated. A drop of ~65% with a 160/1 Zn/Ir ratio within the film in a 10 mM NaCl solution acidified with a perchloric acid supporting electrolyte was evident. This drop in CER selectivity was apparent up to concentrations of ~150 mM NaCl. Minimal increases in the applied potential required to reach 3 mA/cm^2 at the disk were also evident. Assessing the degree of kinetic and diffusional control to which the OER and CER currents comprising the CER selectivity evaluation may be subjected are proposed to enable verification of the selectively diffusional control that the nanosheets impart to the CER current. Perspective studies are then discussed to elucidate the impeded modes of transport within the electrocatalytic film that the chloride ion may be susceptible in the presence of the nanosheets. Numerical development of diffusional

parameters may further enable the assessment of the performance of the nanosheets in the presence of other constituents of seawater. Modification of the synthesis strategy to improve the stability of the material under acidic conditions are also proposed to create an applicable design strategy that can further the prospect of utilizing seawater during electrolysis for the production the potent hydrogen energy carrier that can assuage our expanding energy requirements and enable our societies and the planet in which they inhabit to indeed thrive.

Appendix

Experimental

V.1 Materials

V.1.1 Precursor Catalysts and Chemicals for the Silica Encapsulation

A commercially available 10% Iridium on Vulcan XC-72 (Ir10) was purchased from Premetek. The commercially available 10% Platinum on Vulcan XC-72 (Pt10) was purchased from Thermo Fisher Scientific and Vulcan Carbon XC-72 (VC) was purchased from Cabot. Tetraethylorthosilicate (TEOS) and cetyltrimethylammonium bromide (CTAB) were supplied by Sigma Aldrich and Carlo Erba prepared the 30% w/w ammonium hydroxide and anhydrous ethanol. Isopropanol was purchased from VWR Chemicals. Infrared Spectroscopy studies were conducted with potassium bromide also purchased from Sigma Aldrich. Technical grade ethanol was used for cleaning and disinfection.

V.I.2 Precursor Chemicals for the ZIF-8 Nanosheet Preparation

A commercially available 10% Iridium on Vulcan XC-72 (Ir10) was purchased from Premetek and Vulcan Carbon XC-72 (VC) was purchased from Cabot. Zine Nitrate Hexahydrate and 2-methylimidazole were supplied from Sigma Aldrich and Janssen Chemica, respectively. Technical grade ethanol was used for cleaning and disinfection.

V.2 Synthetic Methods

V.2.1 Silica Encapsulation of the Precursor Catalysts

Beginning with 30 mg of the Vulcan carbon, 33.3 mg of Ir10, or 33.3 mg of Pt10, the compound was homogenized in 38 mL of water through sonication before being added to a round bottom mixture of 2.20 mg of CTAB that had been dissolved in 150mL of isopropanol for one hour at room temperature. The precursor mixture was added to the round bottom and allowed to stir for one hour before another 150 mL of isopropanol and 3 mL of ammonium hydroxide were added to the round bottom. The mixture was stirred for one hour at room temperature and then 2.28 mL of TEOS was added to the mixture. 30 mL aliquots were then taken at 15 min, 30 min, 1 h, 3 h, 5 h, and 21 h; each aliquot was centrifuged for 20 min at 7°C at 11 g and then sonicated with 5 mL of ethanol for 5 min. The material was then spun down under the same conditions, the supernatant was removed, and the material was allowed to dry in the oven at 60°C overnight. The sample was then grinded with a mortar and pestle and the final weight was taken.

V.2.2 ZIF-8 MOF Nanosheet Synthesis

Initial synthesis refers to the work of Jiang et. al.[21] 330 mg of $Zn(NO_3)_2.6(H_2O)$ and 985 mg of 2-methylimidazole were each dissolved in 90 mL of water. The solutions were combined and stirred at 500 rpm at room temperature for 24 hrs. The resulting while deposit was centrifuged down at 11000 rpm for 20 minutes at 7°C followed by three methanolic washes with a five-minute sonicated incubation period. The white deposit was then collected and allowed to dry at 80°C overnight.

V.2.3 Hydrothermal Synthesis

Into a beaker was placed 0.538 g of zinc chloride, 0.648 g of 2-methylimidazole, and 0.268 g of sodium formate that were dissolved in 50 ml of methanol through sonication according to the work of Zhu et. al.[35] The solution was then poured into a Teflon autoclave. An Ir10 film as prepared above was then placed into the chamber and the chamber was sealed and incubated in an oven at 85°C. The next morning, the electrode was removed and the LSV analysis was conducted.

V.3 Characterization

V.3.1 Infrared Spectroscopy of VC@SiO_2, Ir10@SiO_2, Pt10@SiO_2

KBr pellets consisting of 10% w/w of sample and 90% w/w of potassium bromide were weighted and grinded with a mortar and pestle before being pressed into a pellet. A Bruker Equinox 55 was used to record 100 scans from 600 cm^{-1} to 4000 cm^{-1} with a resolution of 4 cm^{-1}. Data was treated with the OPUS software (Toronto, ON, Canada) before being plotted in MATLAB (R2022a).

V.3.2 Thermogravimetric Analysis of VC@SiO_2, Ir10@SiO_2

The Netzsch STA 409PC with the software Proteus Analysis was utilized to determine the residual silica masses on the VC@SiO_2 and Ir10@SiO_2 materials. The samples were heated with a 0.5 mL/min flow rate of nitrogen and a 0.5 mL/min flow rate of oxygen to 1100°C at a ramp rate of 10°C/min. The residual silica amount was calculated by measuring the initial mass of the sample and then subtracting the water loss, the carbon loss, and 10% of the carbon loss to account for the iridium mass in the case of the Ir10 precursor material.

V.3.3 Zeta potential of Ir10, Ir10@SiO_2

The zeta potential was recorded in isopropanol. Three measurements of 100 scans were acquired with the Malvern Nano ZS in conjuction with the Zetasizer software.

V.3.4 Zeta potential of the ZIF-8 Nanosheets

The zeta potential was recorded in methanol. Three measurements of 100 scans were acquired with the Malvern Nano ZS in conjuction with the Zetasizer software.

V.3.5 X-Ray Diffraction of VC@SiO_2, Ir10@SiO_2, Pt10@SiO_2

X-Ray diffraction (XRD) experiments were carried out on a high-resolution q-q powder diffractometer (D8 Advance, Bruker AXS, Germany) equipped with the LynxEye XE-T detector (1D mode), dynamic beam optimization module (DBO, combining the use of variable slits, automatic anti-scatter screen position and controlled detector opening) and a Cu radiation (Kα1 = 1.5406 Å and Kα2 = 1.5445 Å). The former drastically reduced the diffusion signal at very low angles (2qCu < 10 °) and combined with a careful control of the sample height, allows reproducible

qualitative information on samples. Samples were analyzed at room temperature without rotation, 2.5° Sollers slits and a sample illumination surface fixed at 10 mm (variable slits mode) or a fixed divergence slit set to 0.5°. XRD patterns were acquired from 1 - 80° 2θ range with an anti-scatter screen position automatically optimized by the software, a full detector opening, with a step size of 0.05° and 3 or 5 s per step.

V.3.6 X-Ray Diffraction of the ZIF-8 Nanosheets

X-Ray diffraction (XRD) experiments were carried out on a high-resolution θ/θ powder diffractometer (D8 Advance, Bruker AXS, Germany) equipped with the LynxEye XE-T detector (1D mode), dynamic beam optimization module (DBO, combining the use of variable slits, automatic anti-scatter screen position and controlled detector opening) and a Cu radiation (Kα1 = 1.5406 Å and Kα2 = 1.5445 Å). The screen drastically reduced the diffusion signal at very low angles (2qCu < 10 °) and combined with a careful control of the sample height, allowed reproducible qualitative information on the sample. ZIF-8 was analyzed at room temperature without rotation, 2.5° Soller slits, and a fixed divergence slit set to 0.5°. The XRD pattern was acquired from 5 - 40° 2θ range with a step size of 0.03° and 0.5 s per step.

V.3.7 X-Ray Photoelectron Spectroscopy of Ir10@SiO_2

XPS spectra were recorded using a K-Alpha+ spectrometer from Thermofisher Scientific, fitted with a microfocused monochromatic Al Kα X-Ray source (h **nu** = 1486.6 eV; spot size = 400 µm). The pass energy was set at 150 eV and 40 eV for the survey and the narrow regions, respectively. Spectral calibration was determined by setting the main C1s (C-C, C-H) component to 285 eV.

V.3.8 SEM/X-EDS of ZIF-8 Nanosheets, Ir10ink, ZIFIr10ink4

Sample morphology was obtained by collecting the secondary electron signals using a Hitachi S4800 microscope; a thin electron beam was scanned over the surface and the quantity of low energy electrons emitted back by the surface was recorded. The acceleration voltage was between 1 to 2 kV to avoid damage and charging effects during the measurement, not being a metallized sample, such effects could not be neglected. The working distance was varied from sample to sample though was adapted to obtain good contrast and lateral resolution of the image.

Energy dispersive X-ray spectroscopy was completed with a Thermo Noran System Six X-Ray detector installed on the electron microscope to obtain the local chemical composition of the sample. The X-Ray signal was obtained with a working distance of 15 mm, a high electron beam intensity, a ‘lens cond’ of 1, and the column lower diaphragm placed at position 1; a high acceleration voltage of 15 kV was used to obtain all characteristic X-rays peaks of the elements and allow for a better quantitative estimation of the chemical composition of those samples.

V.3.9 Transmission Electron Microscopy

Transmission Electron Microscopy (TEM) was performed on a ThermoFischer Scientific™ G3 Titan Themis 300 transmission electron microscope (C-Twin objective lens: Cs = 2.7 mm, Cc = 2.7 mm, Focal length = 3.5 mm) operating at 300 kV

accelerating voltage. Prior to the observation, particles in isopropanol or water were deposited on a 200 mesh negatively glow discharged carbon film. High Resolution observations (HR-TEM) have been performed from 125,000x to 840,000x magnification for different defocus values (defocus range: −0.1 to −0.3 µm) on a ThermoFischer Scientific™ Falcon 3EC 4Kx4K Direct Detection Electron (DDE) camera. In order to best preserve samples from electron beam irradiation during image acquisition, a total low electron dose of 100 $e^{-}/Å^2$ was used for a limited exposure time of 1 sec in TEM mode. Chemical mapping was performed by EDS (Cliff-Lorimer methods) with Scanning Transmission Electron Microscopy (STEM) module in Bright Field (BF) and High Angular Annular Dark Field (HAADF) modes at 910,000x magnification (probe size 1 Å) on a "Oxford Ultim Max 80T" detector.

V.4 Electrochemical Analysis

V.4.1 Ir10 and Pt10 RDE, and Ir10 RRDE film preparation

One milligram of either Ir10 or Pt10 were weighted and combined with two milligrams of VC. The solids were homogenized through sonication for 20 min in 250 µL deionized water (0.059 $µS/cm^2$) and 250 µL of a Nafion solution (5% (w/w) dispersion in water and isopropanol, purchased from Alfa Aesar. The working RDE electrode was made of glassy carbon (Pine Instruments) and was 5 mm in diameter; the working RRDE electrode was made of glassy carbon (Metrohm) and was 5 mm in diameter encompassed by a Pt ring at a distance of 375 µm. They were carefully rotated clockwise and counterclockwise in an eight shape on a polishing machine (SmartLam 2.0), first with a course polishing pad (LamPlan 2TS3) initially sprayed with a Neodia abrasive liquid (6 µm diamond diameter) for 2 min, then rinsed with water and ethanol. The cycle was repeated with a finer polishing pad (LamPlan 2TS4) that was sprayed with a Neodia abrasive liquid (3 µm diamond diameter), and lastly with a final polishing pad (LamPlan 4FV3) sprayed with a Neodia abrasive liquid (1 µm diamond diameter). 8µL of the film solution was drop casted onto the polished working electrode RDE disk surface or on the polished working electrode RRDE disk surface and then left to dry in air for 30 minutes before being placed in the oven at 60°C for 30 minutes.

V.4.2 VC@SiO_2, Ir10@21hrSiO_2, Pt10@21hrSiO_2 RDE film preparation

One milligram of the silica encapsulated catalyst was weighted and combined with two milligrams of VC. The solids were homogenized through sonication for 20 min in 250 µL deionized water and 250 µL of the Nafion solution. 8 µL of the film solution was drop casted onto a polished working electrode RDE disk surface and then left to dry in air before being placed in the oven at 60°C for 30 minutes.

V.4.3 ZIFtopfilm400, ZIFtopfilm40, ZIFtopfilm4 RDE film preparation

One milligram of Ir10 was weighted and combined with two milligrams of VC. The solids were homogenized through sonication for 20 min in 250 µL deionized water and 250 µL of the Nafion solution. 8 µL of the film solution was drop casted onto the polished working electrode RDE disk surface and then left to dry in air for 30 minutes before being placed in the oven at 60°C for 30 minutes. 8 µL of a methanolic solution

of ZIF-8 MOF nanosheets was then drop-casted onto the film and spin-coated at a rotation rate of 2000 RPM for 20 seconds before the resulting film was allowed to dry overnight in ambient conditions. The concentrations of the ZIFtopfilm400, ZIFtopfilm40, and ZIFtopfilm4 methanolic solutions consisted of 0.932 mg ZIF-8 / 1 mL MeOH, 1.86 mg ZIF-8 / 20 mL MeOH, and 0.932 mg ZIF-8 / 100 mL MeOH, respectively.

V.4.4 ZIFintfilm4, ZIFintfilm0.4, ZIFintfilm0.04 RDE film preparation

One milligram of Ir10 was weighted and combined with two milligrams of VC. The solids were homogenized through sonication for 20 min in 250 µL deionized water and 250 µL of the Nafion solution. Taking the actual mass of Ir10 weighted and multiplying by (500 µL Nafion&water solution / 1 mg Ir10) gave the needed volume of the ZIF-8 nanosheet methanolic solutions. These solutions were prepared with (Zn/Ir) molar ratios of 4, 0.4, and 0.04, which was equivalent to 0.932 mg ZIF-8 / 1 mL MeOH, 1.86 mg ZIF-8 / 20 mL MeOH, and 0.932 mg ZIF-8 / 100 mL, respectively. The final solution was homogenized through sonication for 20 min and then 16 µL of the ZIFIr10ink solution was drop casted onto the polished working electrode RDE disk surface. After drop casting, the electrodes were left to dry in air for 30 min before being placed in the oven at 60°C for 30 min.

V.4.5 ZIFintfilm4 RRDE film preparation

The concavity of the ring-disk electrodes wasn't sufficient to enable 16 µL of the ink to be drop-casted onto the electrode. Thus, the ZIFIr10ink4 was prepared by weighting one milligram of Ir10 and combining with two milligrams of VC and 0.465 mg of ZIF-8 nanosheets; the solids were homogenized through sonication for 20 min in 250 µL deionized water and 250 µL of the Nafion solution for 20 min. 8 µL of ZIFIr10ink4 solution was drop casted onto the polished working electrode RRDE disk surface taking care to avoid the ring (and the spacer) and then left to dry in air for 30 min before being placed in the oven at 60°C for 30 min.

V.4.6 ZIFintfilm20 – ZIFintfilm200 RRDE film preparation

The concavity of the ring-disk electrodes wasn't sufficient to enable 16 µL of the ink to be drop-casted onto the electrode. Thus, the ZIFIr10ink20 - ZIFIr10ink200 were prepared by weighting one milligram of Ir10 and combining with two milligrams of VC and 2,325 mg – 23,25 mg of ZIF-8 nanosheets; the solids were homogenized through sonication for 20 min in 250 µL of 75% isopropanol and 25% ethanol (v/v) and 250 µL of the Nafion solution for 20 min. 8 µL of ZIFIr10ink solutions were drop casted onto the polished working electrode RRDE disk surface taking care to avoid the ring (and the spacer) and then left to dry in air for 30 min before being placed in the oven at 60°C for 30 min.

V.4.7 RDE Linear Sweep Voltammetry of VC@SiO_2, Ir10@SiO_2, Pt10@SiO_2

The potentiostat was an Autolab PGSTAT 12 and an ohmic drop (typically 30 ohms) was compensated for in all measurements. The counter electrode was a platinum wire and a Hach silver/silver chloride reference electrode was used for all

measurements. RDE glassy carbon working electrodes (Pine Instruments) with a 5 mm diameter were used. The experiments were carried out in air at a rotation rate of 1600 rpm. The rotating disk electrode was arranged in a three-electrode set-up in a 0.1 N H_2SO_4 supporting electrolyte (pH 1.3) at 25°C. A scan rate of 10 mV/sec was first applied and the potential was positively swept to measure the oxidation current and then reversed at the positive vertex. The film was then subjected to 10 conditioning cycles between 0.680 V and 0.180 V vs. RHE at 200 mV/s followed by a scan recorded at 10 mV/s; this sequence was repeated until a stabilized forward scan was obtained. Trials were also conducted in 0.5 M NaCl / 0.1 N H_2SO_4 (pH 1.3) at 25°C to mimic the chloride concentration in seawater. The Nova program was utilized to acquire the data and MATLAB was employed to create the codes and analyze the data.

V.4.8 RDE Linear Sweep Voltammetry of ZlFIr10film4, ZlFIr10film0.4, ZlFIr10film0.04

The potentiostat was an Autolab PGSTAT 12 and an ohmic drop (typically 30 ohms) was compensated for in all measurements. The counter electrode was a platinum wire and a Hach silver/silver chloride reference electrode was used for all measurements. Supporting electrolytes consisted of a 0.5 M NaCl / 0.1 N H_2SO_4 (pH 1.3) at 25°C and a 0.1 N H_2SO_4 supporting electrolyte (pH 1.3) at 25°C. The films were conditioned by cycling between 0.680 V and 0.180 V vs. RHE at 200 mV/s. The analysis was conducted through either the one-electrode / two-solution electroanalytical trial sequence, in which the current metric of 10 mA/cm^2 was used to determine the potential range that was scanned during the linear sweep at 10 mV/sec, or the one-electrode / one-solution electroanalytical trial sequence, which linearly swept the potential at 10 mV/sec to a current metric of 5 mA/cm^2 before the backward scan began to avoid inconsistent bubble formation and improve the reproducibility. The Nova program was utilized to acquire the data and MATLAB was employed to create the codes and analyze the data.

V.4.9 RRDE Collection Efficiency Experiment

$K_3Fe[CN]_6$ was obtained from Sigma-Aldrich and a 10 mM aqueous solution was prepared in 0.1 M KNO_3 (Alfa Aesar). The solution was studied through cyclic voltammetry by scanning from -0.1 V to 0.8 V to -0.1 V vs. RHE and then linear sweep voltammetry was conducted by scanning from 0.5 V to -0.3 V vs. RHE at a sweep rate of 10 mV/sec at ascending rotation speeds. The scanning rates were also probed. The limiting ring current was then divided by the limiting disk current and a collection factor of 0.245 was obtained. The Nova program was utilized to acquire the data and MATLAB was employed to create the codes and analyze the data.

V.4.10 RRDE Linear Sweep Voltammetry of Ir10, ZlFintfilm4 – ZlFintfilm200

The bipotentiostat was an Autolab PGSTAT 12 with the FRA32M and the BA modules. The ohmic drop (typically 8 ohms) was compensated for during ring cleaning, film conditioning, and linear sweep measurements. The counter electrode was a platinum wire, and a silver/silver chloride reference electrode (Hach) was

utilized. The electroanalytical RRDE protocol was designed with a voltammetric sequence under hydrodynamic conditions that electropolished the platinum ring, then conditioned the film without the presence of the chloride ion, and then performed a linear sweep at four distinct rotation rates in 0 mM NaCl, 10 mM NaCl, 20 mM NaCl, 50 mM NaCl, 100 mM NaCl, 200 mM NaCl, 500 mM NaCl, and 1 M NaCl solutions.

Initially, in the presence of in an acidic supporting electrolyte consisting of 0.2 N H_2SO_4 (pH = 0.88) with 500 mM KNO_3 (Alfa Aesar), the platinum ring was electropolished from -0.1 V to 1.7 V vs. RHE at 100 mV/sec. After probing the number of conditioning cycles and the effect of the chloride ion on the CER selectivity, 100 film conditioning cycles from 0.56 V to 1.06 V vs. RHE in 0.2 N H_2SO_4 (pH = 0.88) with 500 mM KNO_3 were decided upon. A linear sweep from 1.07 V vs. RHE to a current cutoff equivalent to 5 mA/cm^2 was then conducted at 500 rpm, 1000 rpm, 1600 rpm, and 2000 rpm in 0.2 N H_2SO_4, 500 mM NaCl. This electroanalytical RRDE protocol was used to probe the CER selectivity of the control Ir10film in the presence of 0 mM NaCl, 10 mM NaCl, 20 mM NaCl, 50 mM NaCl, 100 mM NaCl, 200 mM NaCl, 500 mM NaCl, and 1 M NaCl solutions each with the requisite amount of KNO_3 that summed to a 500 mM total salt concentration in 0.2 N H_2SO_4 (pH = 0.88). Five Ir10 films from the same Ir10ink were probed with this electroanalytical voltammetric protocol. In an attempt to decrease the standard deviation and the possibility of a competitive adsorbate contaminant, four Ir10 films of a different Ir10ink were probed with the same electroanalytical voltammetric protocol in 0.5 M $HClO_4$ (pH = 0) without the presence of KNO_3.

The ZIFintfilm4 – ZIFintfilm200 were trialed by placing the ring of each electrode initially in the 0 mM NaCl, 0.5 M $HClO_4$ solution and electropolishing at 1600 rpm from -0.1 V to 1.7 V vs. RHE, and then subjecting the film to 100 conditioning cycles at 1600 rpm from 0.56 V to 1.06 V vs. RHE, followed by a linear sweep from 1.07 V vs. RHE to a current cutoff equivalent to 5 mA/cm^2 at 500 rpm, 1000 rpm, 1600 rpm, and 2000 rpm with the ring potential set to 0.95 V vs. RHE. Then the ring was electropolished once more in the 0 mM NaCl, 0.5 M $HClO_4$ solution before subjecting the same film to a linear sweep in the presence of 10 mM NaCl, 0.5 M $HClO_4$. Between each solution of increasing NaCl molarity probed in the linear sweep, the ring was electropolished in the 0 mM NaCl, 0.5 M $HClO_4$ solution. The Nova program was utilized to acquire the data and MATLAB was employed to create the codes and analyze the data.

Printed and Bound in Palaiseau

at the École Polytechnique

Institut Polytechnique de Paris
91120 Palaiseau, France

ECOLE DOCTORALE

Titre : Optimisation de la sélectivité anodique de lors de l'électrolyse de l'eau de mer grâce à des nanoclusters d'iridium enrobés et supportés sur carbone

Mots clés : Électrochimie, Procédé sol-gel, Énergie

Résumé : Obtenir une sélectivité optimale à l'anode pour la production d'oxygène lors de l'électrolyse de l'eau de mer est un défi crucial afin de permettre la production d'hydrogène décarboné. Cela nécessite le développement de matériaux permsélectifs qui dépassent les limites de perméabilité et de sélectivité des membranes de dessalement classiques. En utilisant une membrane de tamisage moléculaire rigide, on obtient une meilleure capacité de sélection des molécules en comparaison avec les membranes de dessalement en polymère, qui se basent principalement sur un processus de séparation dépendant de l'énergie, dû au mouvement des chaînes polymériques constitutives. Au cours de cette thèse, une encapsulation de nanoparticules d'iridium greffées sur du carbone dans une matrice de silice a été réalisée afin de bloquer le transport des ions chlorure hydratés. L'analyse thermogravimétrique et la microscopie électronique à transmission ont confirmé un recouvrement complet du matériau électrocatalytique après cinq heures de réaction, avec une épaisseur moyenne de 34 nm. La caractérisation structurale par diffraction des rayons X a montré la présence de pores autour des agrégats de silice amorphe d'une taille d'environ 9 nm, bien supérieur au diamètre de l'ion chlorure hydraté. L'incorporation ultérieure de l'électrocatalyseur encapsulé dans une encre de carbone et de Nafion, puis déposée sur une électrode de carbone vitreux et analysée par voltammétrie à balayage linéaire, a révélé que le transport des électrons des nanoparticules électrocatalytiques encapsulées vers l'électrode de travail était une étape limitante dans ces processus. Il est aussi apparu que la diffusion directe de des ions vers l'électrode en vue d'une oxydation ultérieure était également apparente. Une autre approche exploitant la synthèse de nanofeuilles de MOF de type ZIF-8 avec un diamètre de pore contrôlé a été étudié. L'hypothèse envisagée souhaitait conférer une perméabilité sélective à l'eau par exclusion de taille afin de bloquer le transport des ions chlorures hydratés dans le film électrocatalytique, tout en améliorant la conductivité du matériau grâce aux propriétés conductrices des MOF. L'architecture des nanofeuilles a été conçue pour optimiser leur disposition afin de bloquer sélectivement les multiples voies de transport à travers le film électrocatalytique. La reproductibilité des analyses a été au cœur des expériences menées en utilisant une électrode de travail de type RRDE (rotating ring-disk electrode), et a permis la détection sélective de l'ion chlorure tout en facilitant l'approche intégrée avec un rapport Zn/Ir de 160/1 dans le film électrocatalytique. Nous avons pu démontrer une efficacité réduite de 65% dans la réaction de production de dichlore à des concentrations de 10 millimolaires en ions chlorures en présence de perchlorate comme électrolyte support. L'évaluation du degré de contrôle cinétique et de contrôle diffusionnel auquel les courants OER et CER comprenant l'évaluation de la sélectivité CER peuvent être soumis est proposée, afin de créer un matériau électrocatalytique favorisant la production sélective d'oxygène en présence d'ions chlorures en milieu acide. Ces propositions renforcent l'intérêt de l'utilisation de l'eau de mer comme électrolyte pour l'électrolyse de l'eau dans le contexte de l'utilisation de l'hydrogène comme solution durable pour répondre aux besoins critiques de nos sociétés.

Title : Achieving OER Selectivity in the Electrolysis of Seawater through Shielded Carbon-Supported Iridium Nanoclusters

Keywords : Electrochemistry, Sol-Gel Synthesis, Energy

Abstract : Achieving selectivity at the anode for oxygen evolution during the electrolysis of seawater is considered a critical challenge with a rendered exigency for the generation of permselective materials that transcend the selectivity permeability upper bound of state-of-the-art desalination membrane materials for the appreciable production of green hydrogen. Utilizing a rigid molecular sieving membrane material imparts an additional entropic diffusional selectivity devoid in polymeric desalination membranes limited to separation impartment by an enthalpic diffusional selectivity due to the inherent transient segmental motion among the constituent polymeric chains. A silica encapsulation of iridium nanoparticles interwoven on Vulcan carbon was thus achieved by means of a sol gel synthesis to arrest the species transport of the hydrated chloride ion. Thermogravimetric Analysis and Transmission Electron Microscopy confirmed complete coverage of the electrocatalytic material after five hours of reaction with a 34 nm thickness. Structural characterization with X-Ray Diffraction indicated pores around the amorphous silica clusters of 87 Å, well above the hydrated diameter of the chloride ion. Subsequent incorporation of the encapsulated electrocatalyst into an ink of Nafion and Vulcan carbon that was then drop-casted on a working glassy carbon electrode and probed through rotating disk linear scanning voltammetry showed evidence of a lack of electron transport from the silica encapsulated electrocatalytic nanoparticles within the film towards the working electrode. A direct diffusion of the chloride ion towards the electrode and for subsequent oxidation was also apparent. Another approach leveraging the intimate control of reticular synthesis to create a ZIF-8 nanosheet with a characteristic aperture diameter that imparts selective water permeability through size exclusion was thus exploited to arrest the species transport of the hydrated chloride ion within the electrocatalytic film, while moreover improving the conductivity of the material through a proposed dimensional confinement effect. Architectures of the nanosheets were designed to optimize their placement to selectively arrest the multiple transport pathways within the electrocatalytic film. The electrochemical analytical procedure was developed to increase its characteristic reproducibility of the trialed electrocatalytic films. A rotating ring disk working electrode further enabled the selective detection of the chloride ion and enabled the integrated approach with a 160/1 Zn/Ir ratio within the electrocatalytic film to show a ~65% drop in selectivity for the chlorine evolution reaction when assayed at 10 mM concentrations of the chloride ion in the presence of a perchloric acid supporting electrolyte. Assessing the degree of kinetic and diffusional control to which the OER and CER currents comprising the CER selectivity evaluation may be subjected are proposed to render an electrocatalytic material with a penchant for selective oxygen evolution in the presence of the chloride ion even in the thermodynamically contentious acidic conditions. This advancement propels the utility of a ubiquitous seawater electrolyte for water electrolysis and the applicability of the hydrogen energy carrier as a sustainable solution to meet the critical needs of our increscent societies.